Modelling the dynamics and boundary processes of Svalbard glaciers

Ward van Pelt

Author: Ward van Pelt
ISBN: 978-90-393-6068-2
Printing: Proefschriftmaken.nl, Uitgeverij BOXPress

Institute for Marine and Atmospheric research Utrecht (IMAU)
Department of Physics and Astronomy
Faculty of Science
Utrecht University

Modelling the dynamics and boundary processes of Svalbard glaciers

Het modelleren van de dynamica en randprocessen van gletsjers op Spitsbergen

(met een samenvatting in het Nederlands)

PROEFSCHRIFT

ter verkrijging van de graad van doctor aan de
Universiteit Utrecht op gezag van de rector magnificus,
prof. dr. G.J. van der Zwaan, ingevolge het besluit van
het college voor promoties in het openbaar te
verdedigen op

woensdag 8 januari 2014 des middags 4.15 uur

door

Ward Jan Jacobus van Pelt

geboren op 10 maart 1985 te Vlissingen

Promotor: Prof. dr. J. Oerlemans

Contents

Samenvatting

Hoewel het merendeel van landijs op Aarde ligt opgeslagen in de grote ijskappen van Groenland en Antarctica, zijn het de gletsjers en ijskappen buiten Antarctica en Groenland die tot op heden het meest bijdragen aan zeespiegelstijging als gevolg van klimaatverandering. Dit komt doordat kleine gletsjers gevoeliger zijn voor schommelingen in het klimaatsysteem. Extra kwetsbaar zijn gletsjers in het Arctisch gebied, waar een sterkere opwarming wordt waargenomen dan in de rest van de wereld, hetgeen kan worden toegeschreven aan het terugtrekken van zee-ijs en versterkte absorptie van zonlicht. Dit proefschrift focust op gletsjers in Spitsbergen, een eilandengroep ten noorden van Noorwegen, gelegen aan de zuidelijke rand van het zee-ijs in de winter. De verwachte opwarming in dit gebied heeft mogelijk grote gevolgen voor de evolutie van gletsjers en ijskappen, die momenteel 60% van het landschap bedekken.

Om het gedrag van gletsjers in een variabel klimaat beter te kunnen begrijpen en nabootsen wordt veel gebruik gemaakt van computermodellen. De geometrische ontwikkeling van een gletsjer wordt enerzijds bepaald door de interactie tussen atmosfeer en gletsjeroppervlak door middel van smelt en neerslag, en anderzijds door het bewegen van ijs onder de invloed van de zwaartekracht. Het laatstgenoemde hangt nauw samen met de thermische, sedimentologische en hydrologische condities aan de bodem van het ijs, welke de mate van het glijden van het ijs over de bodem beïnvloeden. Een goede beschrijving van zowel randprocessen en interne fysica als interacties tussen de verschillende componenten in een gletsjersysteem is nodig om de ontwikkeling van gletsjers in een veranderend klimaat te kunnen begrijpen en simuleren. In dit proefschrift ligt de focus op het vergroten van ons begrip van zowel bodem- als oppervlakteprocessen in de context van gletsjers op Spitsbergen.

De oppervlaktemassabalans (OMB) van een gletsjer omvat de som van alle positieve en negatieve massabijdragen aan het gletsjeroppervlak. De dominante componenten van de OMB in het Arctisch gebied zijn het afstromen van smeltwater (negatief) en sneeuwaccumulatie (positief). Herbevriezing van smeltwater in de koude sneeuwlaag onder het oppervlak vermindert de afstroming van smeltwater en draagt zodoende positief bij aan de OMB. In Hoofdstuk 2 ligt de focus op het analyseren van de oppervlaktemassabalans van Nordenskiödbreen, een getijdegletsjer in centraal Spitsbergen. Daartoe is een energiebalans model gekoppeld aan een sneeuwmodel. Het energiebalansmodel berekent aan de hand van alle inkomende en uitgaande energiefluxen de hoeveelheid smelt aan het oppervlak, terwijl het sneeuwmodel de ontwikkeling van het sneeuwpakket simuleert. Observaties op de gletsjer spelen een belangrijke rol in zowel het kalibreren van modelparameters als het valideren van de model-

resultaten. Aangedreven met meteorologische data over de periode 1989-2010 berekent het model een sterk negatieve OMB van -0.39 m water equivalent per vierkante meter per jaar. Tezamen met een massaverlies door het afkalven van ijs in het fjord betekent dit dat de gletsjer substantieel kleiner is geworden over deze periode. Herbevriezing draagt 0.27 m water equivalent bij aan de OMB en blijkt daarmee een belangrijke buffer te zijn voor massaverlies. Klimaatgevoeligheidsexperimenten laten zien dat de verwachte mildere toename van temperatuur gedurende de zomermaanden in verhouding tot de wintermaanden een significant lagere gevoeligheid van de OMB tot gevolg heeft. Desalniettemin zal de verwachte temperatuurstijging van 4-6 °C in deze regio tussen 1961-1990 en 2071-2100 leiden tot substantieel massaverlies in de 21ste eeuw.

Als gevolg van variaties in lokale sneeuwval en herverdeling van sneeuw door wind is grote variabiliteit mogelijk in sneeuwdepositie op een gletsjeroppervlak. Nauwkeurige kennis van hoe sneeuwaccumulatie varieert in ruimte en tijd is van groot belang voor zowel het modelleren van de OMB als het interpreteren van lokale OMB-observaties. Radardata geven informatie over de gelaagdheid van het sneeuwpakket en bevatten indirecte informatie over ruimtelijke variabiliteit van sneeuwaccumulatie in het verleden. In hogergelegen delen, waar jaarlijks meer sneeuw valt dan er smelt, kunnen meerdere jaarlijks gevormde lagen worden gedetecteerd. In Hoofdstuk 3 wordt een nieuwe methode toegepast om jaarlijkse accumulatiepatronen voor de periode 2007-2012 uit een radarprofiel af te leiden. De aanpak betreft een inverse methode waarin het gekoppelde model uit Hoofdstuk 2 wordt gebruikt om de gelaagdheid van het sneeuwpakket na te bootsen. Sneeuwaccumulatie, dienend als forcering van het model, wordt langs een 16-km lang radarprofiel op Nordenskiöldbreen stapsgewijs gekalibreerd om overeenstemming tussen modeluitvoer en radardata te bereiken. De gepresenteerde methode onderscheidt zich van traditionele methodes door het expliciet modelleren van de evolutie van het sneeuwpakket en vermijdt daarmee grove aannames ten aanzien van sneeuwdichtheid, waterconcentratie en massatransport tussen verschillende lagen. De afgeleide accumulatiepatronen laten grote ruimtelijke variabiliteit zien (13-27%) en patronen zijn in beperkte mate consistent van jaar op jaar. Een analyse van neerslagpatronen in relatie tot wind karakteristieken en geometrische parameters laat zien dat sneeuwdepositie het meest voorkomt op steile hellingen in de luwte van fluctuaties in het terrein. De niet-lineaire respons van de OMB op verstoringen van accumulatie zorgt voor een netto negatief OMB effect door kleinschalige variabiliteit in neerslag van gemiddeld -0.08 m water equivalent per jaar in lagergelegen delen. Dit demonstreert het belang van het in ogenschouw nemen van kleinschalige neerslagvariabiliteit op de grootschalige OMB.

Vanaf Hoofdstuk 4 verschuift de focus van oppervlakteprocessen naar bodemcondities. De complexe interactie tussen krachten, thermodynamica, hydrologie, topografie en sediment bepaalt niet alleen de snelheid waarmee ijs over de bodem beweegt ('sliding'), het creëert ook terugkoppelingseffecten die kunnen leiden tot periodiek gedrag van ijssnelheden en gletsjergeometrie. Zulke oscillaties staan los van door het klimaat geforceerde geometrische veranderingen. Een voorbeeld hiervan is het 'surge'-gedrag van gletsjers op Spitsbergen,

waarbij korte periodes met zeer hoge ijssnelheden en vooruitgang van de gletsjertong worden afgewisseld door lange periodes met lage ijssnelheden en terugtrekking van de tong. Veel is nog onduidelijk over hoe zulke oscillaties kunnen worden verklaard en welke condities bijdragen aan het voorkomen van dit cyclische gedrag. In Hoofdstuk 4 geven numerieke experimenten met een drie-dimensionaal ijsstroommodel (PISM) inzicht in hoe het samenspel van krachten, thermodynamica en water kan leiden tot het optreden van verschillende types oscillaties. Waar de herverdeling van water aan de bodem een cruciale rol speelt in hoog-frequente oscillaties, zijn laag-frequente oscillaties afhankelijk van veranderingen in de thermische structuur van de bodem. De keuze van modelparameters die de relatie tussen bodemweerstand, waterdruk en sliding beschrijven is bepalend voor het al dan niet optreden van cyclisch gedrag. Zo blijkt een lage materiële weerstand van de bodem een vereiste voor het optreden van oscillaties.

Hoofdstuk 5 beschrijft een methode om de bodemtopografie onder gletsjers te reconstrueren. Accurate kennis van de bodemtopografie is niet alleen belangrijk voor het schatten van het ijsvolume, maar is ook van groot belang voor het nauwkeurig dynamisch modelleren van de tijdsevolutie van gletsjers. Directe metingen van de bodemtopografie zijn vaak schaars, terwijl oppervlaktehoogtes veel uitgebreider beschikbaar zijn. In Hoofdstuk 5 wordt een inverse methode getest waarin een drie-dimensionale bodemtopografie stapsgewijs wordt aangepast om een zo goed mogelijke overeenstemming tussen gemodelleerde en geobserveerde oppervlaktehoogtes te bereiken. Bij het aanpassen van de bodem wordt de resterende fout tussen gemodelleerde en geobserveerde oppervlaktehoogtes direct toegepast om de bodem te corrigeren. Testexperimenten met een geïdealiseerde geometrie laten zien dat de methode convergeert. In een volgende stap is de inverse methode toegepast op Nordenskiöldbreen. Hierbij is het model iteratief gedraaid over de periode 1300-2007, geforceerd met een tijds- en hoogte-afhankelijke klimaatforcering. Vroegtijdige beëindiging van het iteratieve proces voorkomt ruis in de gereconstrueerde bodemtopografie. Een vergelijking van de gereconstrueerde bodem met schaarse observaties laat een goede overeenkomst zien. Naast het afleiden van bodemtopografie, kan de inverse methode ook worden gebruikt om ijsstroommodellen te initialiseren. Degelijke initialisatie geeft een geometrie en thermodynamische toestand van een gletsjer die consistent is met de klimaatforcering in het verleden en reduceert fouten in toekomstruns.

In Hoofdstuk 4 en 5 wordt duidelijk dat onnauwkeurigheid in de beschrijving van bodemcondities, zoals de rol van wateropslag en transport, een belangrijke bron van onzekerheid is in de modelresultaten. De mate van wrijving dat het ijs ondervindt aan de bodem hangt af van de opwaartse druk die het water uitoefent op het ijs. Nauwkeurig simuleren van ruimtelijke en tijdafhankelijke variaties in de waterdruk vereist kennis over de manier waarop het water aan de bodem beweegt en hoe het afwateringssysteem zich aanpast aan veranderende watertoevoer. In Hoofdstuk 6 wordt een watermodel gepresenteerd, geanalyseerd en getest wat enerzijds watertransport en opslag aan de bodem berekent en anderzijds uitwisseling tussen het hydrologische systeem aan de bodem en open ruimtes in het gletsjerijs simuleert. Het

inachtnemen van wateropslag in het poreuze ijs zorgt voor een aanzienlijke vereenvoudiging van de numerieke implementatie. Numerieke experimenten zijn uitgevoerd op het grid van Nordenskiöldbreen. Simulaties met een constante watertoevoer illustreren de gevoeligheid van de waterdruk en waterhoeveelheid ten opzichte van fysische parameters. De verdeling van de waterdruk blijkt ongevoelig voor de poreusheid van het ijs. Tests met een seizoensafhankelijke watertoevoer laten zien dat de poreusheid van het gletsjerijs een directe maat is voor de snelheid waarmee waterdrukveranderingen kunnen optreden, terwijl de rekentijd omgekeerd evenredig afhangt van de poreusheid. Het voorgaande motiveert het gebruik van de poreusheid als een regularisatieparameter, welke kan worden gekozen aan de hand van het gewenste detail in de evolutie van de waterdruk. In toekomstig werk zal het watermodel in Hoofdstuk 6 gekoppeld worden aan het ijsstroommodel PISM.

1 Introduction

1.1 Svalbard glaciers & climate

Over the past few decades, the potential impact of a warming climate on global sea level and the ecologic system, as well as the related socio-economic consequences, received considerable attention. The recognition of ice masses in the Earth's system as indicators of climate change and as potential contributors to sea level rise has stimulated cryospheric research substantially. Despite the relatively small ice volume stored in small glaciers and ice caps compared to the large ice sheets of Greenland and Antarctica, mass loss of quickly responding small ice masses is expected to contribute significantly to sea-level rise in the 21st century [*IPCC*, 2007]. Of particular interest is the Arctic region, where amplified warming, referred to as 'Arctic amplification', is observed and expected to continue in the near-future [*ACIA*, 2005].

In this thesis, I focus on the archipelago of Svalbard (Figure 1.1), first discovered by the Dutch explorer Willem Barentsz in 1596 during his fatal trip in search for a northern route between Europe and eastern Asia. Since 1920 Norway has full sovereignty over Svalbard as established in the Svalbard Treaty. The main island of the archipelago is Spitsbergen, which is home to the largest settlement Longyearbyen with about 2,000 inhabitants. Svalbard is among the largest repositories of small glaciers and ice caps, covering an estimated area of 36,600 km^2, representing about 6% of the Earth's total glacier area. Glaciers and ice caps cover about 60% of the total land area of Svalbard and contain an estimated volume of 7,000 km^3 or 0.02 m of sea-level equivalent [*Hagen*, 1993; *Hagen et al.*, 2003].

The Svalbard archipelago is situated at the northern end of the Atlantic warm water current, causing the climate to be relatively mild compared to other regions at similar latitude. In winter and spring, sea ice in the Arctic Ocean and Barentsz Sea extends to the northern and eastern part of Svalbard and in the event of northeasterly winds cold/dry air is advected over the archipelago. In contrast to summer conditions, winter/spring temperatures and precipitation are hence intimately related to sea ice extent and exhibit strong inter-annual variability [*Day et al.*, 2012]. This is confirmed by instrumental data from Longyearbyen, which reveal markedly larger annual variability in winter/spring temperatures than in summer/autumn

Figure 1.1: *Ice cover map of Svalbard. The location of Longyearbyen and the glacier Nordenskiöldbreen (Section 1.2) are indicated in red. The inset map shows the Arctic region centred around the North Pole and the geographic position of the Svalbard archipelago.*

since 1912 (Figure 1.2). Additionally, retreat of sea ice extent around Svalbard since the mid 19th century [*Divine and Dick*, 2006] is thought to have caused amplified temperature increase with respect to the global mean [*Serreze and Francis*, 2006; *Serreze et al.*, 2009]. Since 1912, annual mean temperatures in Longyearbyen have risen by 0.27 K per decade with more pronounced warming in winter/spring (0.38 K per decade) than in summer/autumn (0.16 K per decade). This preferential warming in winter/spring is expected to continue in the 21st century [*Førland et al.*, 2011]. Observed enhanced heat transport from the Atlantic Ocean into the Arctic Ocean through Fram Strait in response to changing temperature conditions [*Walczowski and Piechura*, 2006] may act to further amplify near-future sea ice retreat around Spitsbergen. Large regional differences in future warming are expected for Svalbard with a projected increase of 3°C in the south-west and 8°C in the north-east between 1961-1990 and 2071-2100, based on regional climate model ensemble experiments with a B2

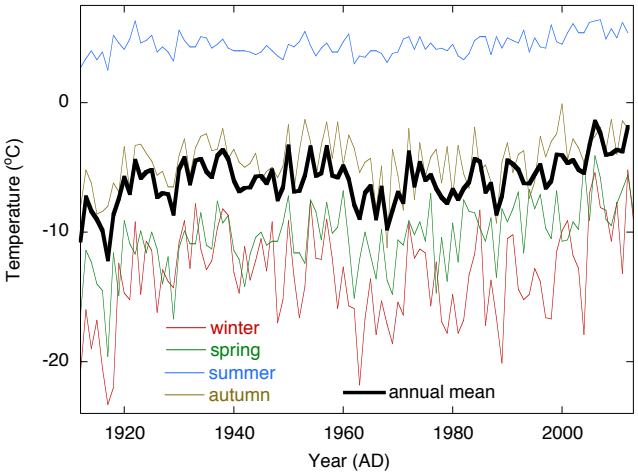

Figure 1.2: *Time-series of seasonal and annual mean temperatures at the Svalbard Airport weather station over the period 1912–2012 [Hanssen-Bauer et al., 2009].*

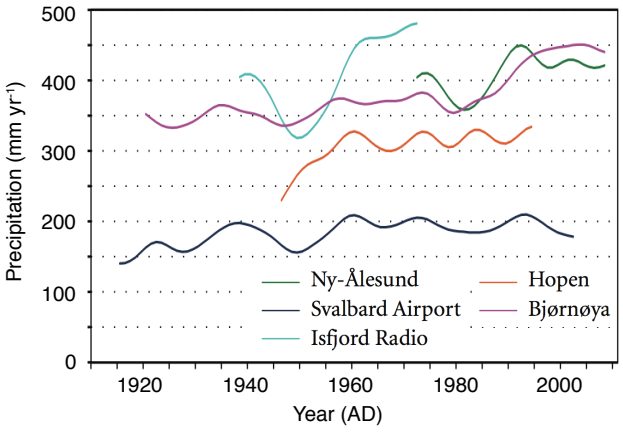

Figure 1.3: *Time-series of annual precipitation at multiple sites in Svalbard. Figure taken and modified from Førland et al. [2011]. A 7-year smoothing filter was applied.*

emission scenario [*Førland et al.*, 2011; *Nakicenovic et al.*, 2000].

Precipitation has been recorded at multiple sites in Svalbard during the past century (Figure 1.3). Despite substantial measurement uncertainty and local-scale variability, positive trends are found for all sites [*Førland et al.*, 2011] and have been ascribed to variations in the atmospheric circulation [*Hanssen-Bauer and Førland*, 1998]. Future projections indicate an estimated increase between 1981–1990 and 2071–2100 ranging from a few percent in the

southwest of Svalbard to more than 40% in the northeast [*Førland et al.*, 2011]. This is in line with IPCC projections for the Arctic region indicating a precipitation increase of $< 5\%$ over the northern Atlantic and between 30 and 40% over the Arctic Ocean [*IPCC*, 2007].

Under the influence of gravity glacier ice flows from areas with a positive mass balance higher up, referred to as the accumulation zone, to areas with a negative mass balance, referred to as the ablation zone, lower down. About 60% of glaciers in Svalbard terminate in the sea and experience additional mass loss by calving of ice bergs at the glacier front [*Blaszcyk et al.*, 2009]. As a result of climatic variability, glaciers are in a continuous state of transition in response to past surface climate conditions, affecting surface melt and accumulation. As the glacier geometry adapts gradually, i.e. with a certain response time, to changing surface conditions, the current geometric state of a glacier does not reflect present-day climate conditions. More information on whether a glacier is currently in balance with the imposed climate can be extracted from spatial patterns of ice thinning or thickening. Recent studies comparing distributed high-resolution surface height data of multiple Svalbard glaciers at two points in time, obtained using airborne/satellite laser altimetry and/or aerial photography, reveal marked thinning in the lower ablation areas and smaller changes higher up over the past few decades [*Nuth et al.*, 2010; *James et al.*, 2012]. On average, *James et al.* [2012] found an average thinning of -0.59 m a^{-1} for six glaciers in Svalbard between 1961 and 2005, with enhanced thinning since 1990 of -0.76 m a^{-1}. More rapid thinning in the ablation area can be ascribed to a higher sensitivity of surface melt to rising air temperature at lower altitudes, whereas the ice thickness in the accumulation zone is only slowly affected by a low melt sensitivity and enhanced drawdown of ice to the ablation zone.

As a dynamic response to overall glacier thinning in response to warming since the mid 19th century [*Divine et al.*, 2011], glaciers in Svalbard have shrunk by 7% of their total area during the past 30 years for a sample of $\sim$400 glaciers [*Nuth et al.*, 2013]. From a longer-term perspective, geological evidence indicates that the mid 19th century glacier extent (at the end of the 'Little Ice Age') was unprecedented since at least 2,500 years BP and that during the early and mid-Holocene (11,650$-$2,500 years BP) glaciers in Svalbard were much smaller or absent [*Svendsen and Mangerud*, 1997]. Additionally, morainal information reveals that, in contrast to glaciers in western Europe, Svalbard glaciers were likely smaller during the cold Younger Dryas period (12,850$-$11,650 years BP) than during the Little Ice Age, which has been ascribed to a lack of precipitation [*Mangerud and Landvik*, 2007].

Independent of the climate induced temporal variability in ice dynamics and geometry, glaciers may exhibit periodic behaviour, characterised by alternating short periods of rapid ice flow and frontal advance and longer periods of slow ice movement and retreat. This oscillatory flow behaviour, referred to as surging, has been ascribed to internal feedbacks within a glacier system arising from the interplay of stresses, thermodynamics and hydrology. Surge-type behaviour is limited to certain clusters around the world, suggesting the relevance of regional conditions on its occurrence [*Hamilton and Dowdeswell*, 1996; *Jiskoot et al.*, 2000]. Surging of glaciers in Svalbard is very common and has been linked to periodic melting/refreezing

of the base of polythermal ice resting on an easily-deformable sediment layer [*Murray et al.*, 2000; *Fowler et al.*, 2001; *Murray et al.*, 2003; *Dunse et al.*, 2011]. Alternatively, surging of temperate glaciers in Alaska has been related to a hydrological instability arising from a switch in the subglacial drainage system [*Kamb et al.*, 1985; *Kamb*, 1987]. The recurrence period of Svalbard surges is relatively long (50-500 years) with a surge phase lasting 3-15 years [*Dowdeswell et al.*, 1991]. As the geometry and mass budget of surge-type glaciers evolve independently of the climate forcing, surge behaviour poses a major challenge to interpretation of mass balance and surface height measurements [*Hagen et al.*, 2005].

1.2 Nordenskiöldbreen

The main purpose of this thesis is to improve our understanding of surface and basal boundary processes of Svalbard glaciers. Much of the modelling work will focus on the glacier Nordenskiöldbreen (78°40'N, 17°15'E), situated in central Spitsbergen (Figure 1.1). Nordenskiöldbreen is named after the Finnish explorer and geologist Adolf Erik Nordenskiöld (1832−1901). The glacier can be classified as a tidewater glacier, as it flows from the Lomonosovfonna ice plateau into the Adolfbukta bay, which is part of the fjord Billefjorden (Figure 1.4). Despite frontal retreat since the end of the Little Ice Age, Nordenskiöldbreen still has an active calving front with an estimated width of 3 km [*Rachlewicz et al.*, 2007]. The Lomonosovfonna ice field, covering an approximate area of 600 km^2, additionally feeds the outlet glaciers Mittag-Lefflerbreen and Tunabreen and numerous smaller glaciers. Ice flows from an altitude of about 1200 m a.s.l. down to sea-level along the main flowline between Terrierfjellet and De Geerfjellet. Two tributary glaciers, located to the south of the main flow between Terrierfjellet, Ferrierfjellet and Minkinfjellet, are considered as part of Nordenskiöldbreen in the context of this thesis. Along the main flowline annual mean surface velocities up to 60 m yr^{-1} are observed, with velocities peaking up to 90 m yr^{-1} at the start of the melt season [*Den Ouden et al.*, 2010]. Much faster ice flow is likely to prevail towards the calving front (Figure 1.5), where severe crevassing is a sign of flow acceleration (Figure 1.6).

During a drilling campaign in May 1997, a 121-m long ice core was drilled at the top of the Lomonosovfonna ice plateau (1255 m a.s.l.). The isotopic composition and densities of the core samples together with observed borehole temperatures reveal information about historical climate conditions at this site [*Isaksson et al.*, 2001]. Based on borehole temperatures, *Van de Wal et al.* [2002] concluded temperatures have risen over the 20th century by 2-3 K. Using the δ^{18}O isotopic signal from this core in combination with instrumental temperature data from the Svalbard Airport weather station, *Divine et al.* [2011] reconstructed winter air temperatures back to 800 AD for Longyearbyen. These time-series reveal a minimum in temperature around 1850 AD and confirm that the Little Ice Age ended towards the end of the 19th century. During the medieval period, winter temperatures were found to be comparable

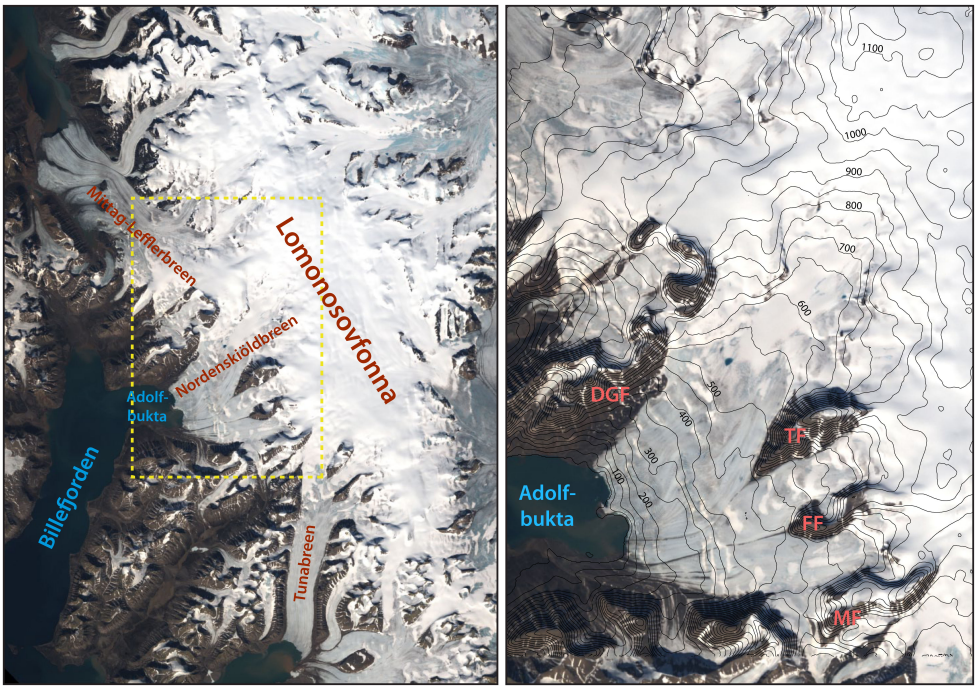

Figure 1.4: *Left: satellite map of Lomonosovfonna and outlet glaciers Tunabreen, Mittag-Lefflerbreen and Nordenskiöldbreen. Right: satellite map zooming in on Nordenskiöldbreen (dashed yellow box in left figure). The right figure is overlain by a height contour map from the SPOT5 DEM [Korona et al., 2009]. Abbreviations: DGF = De Geerfjellet, TF = Terrierfjellet, FF = Ferrierfjellet, MF = Minkinfjellet. Satellite maps are from NASA Landsat imagery taken on 13 July 2002.*

to or even higher than present-day. Temporal accumulation variability has been reconstructed back to 1715 AD by *Pohjola et al.* [2002a] and recently a reanalysis of the data resulted in an extended reconstruction dating back to 1598 AD [D. Divine, personal communication, 2013; Chapter 5]. Spatial variability in accumulation has been analysed by *Pälli et al.* [2002], indicating substantial variability in the higher parts of Nordenskiöldbreen, with reconstructed annual mean accumulation of 0.54 m w.e. yr^{-1} (1963-1999) and 0.71 m w.e. yr^{-1} (1986-1999) along a GPR transect.

Geological evidence indicates Nordenskiöldbreen was likely much smaller than its present-day extent during the Holocene. Based on reconstructed sediment deposition rates, Nordenskiöldbreen only reached the fjord around 1000 BC after which it may have retreated again before advancing to a maximum Neoglacial extent at the end of the Little Ice Age around 1900 AD [*Svendsen and Mangerud*, 1997; *Plassen et al.*, 2004]. Ever since, the glacier has been retreating and based on a combination of aerial photographs, satellite imagery and geomorphological indicators, *Rachlewicz et al.* [2007] computed mean retreat rates varying

Figure 1.5: *The calving front of Nordenskiöldbreen. Photograph taken in April 2012.*

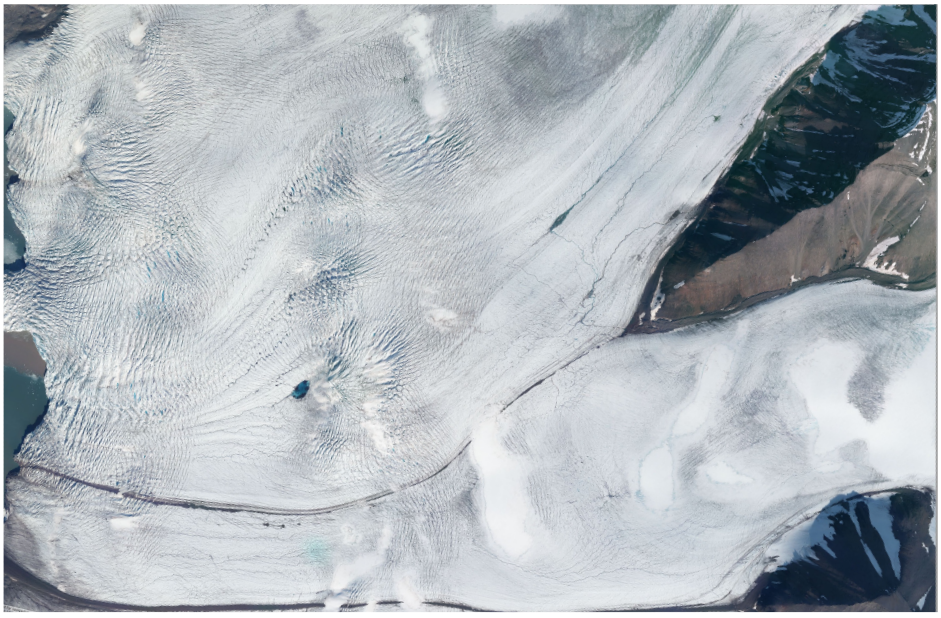

Figure 1.6: *Aerial photograph of the lower ablation area and front of Nordenskiöldbreen in summer. Photo provided by the Norwegian Polar Institute (NPI).*

Figure 1.7: *Photographs showing the automatic weather station (left), a stake mounted with a GPS (middle) and a snow pit in preparation (right). Photos taken during fieldwork in spring 2011 and 2012.*

between 15 and 35 m yr^{-1} for different parts of the calving front.

Jiskoot et al. [2000] argued that Nordenskiöldbreen may have surged during the 20th century based on observed heavy crevassing and elongated moraine loops in 1936 and 1948. It seems however more likely that the glacier is not of surge-type, since there are no signs that the glacier is building up towards a new surge, as confirmed by a negligible change in geometry observed between 1991 and 1997 [*Hagen et al.*, 2005]. Heavy crevassing seems to be a consistent characteristic of the glacier surface and may well be explained by the impact of tensile and compressive forces induced by sliding ice flow over a highly irregular bed (Figure 1.6).

Observed annual mean 10-m subsurface temperatures below melting point in the ablation area [`http://www.projects.science.uu.nl/iceclimate/aws/arctic_oper.php`] and annual 10-m firn temperatures at melting point in the accumulation zone [S. Marchenko, personal communication, 2013] demonstrate the polythermal structure of Nordenskiöldbreen. Temperate firn conditions in combination with low air temperatures in the accumulation area indicate a substantial role of refreezing of percolating melt water on the thermal structure and mass budget; an effect which is quantified in Chapter 2. A polythermal structure, exhibiting cold near-surface temperatures in the ablation area and temperate firn conditions in the accumulation is common for Svalbard glaciers [*Pettersson*, 2004].

Owing to several field campaigns on Nordenskiöldbreen over the years a wealth of observational data has been collected (Figure 1.1), which helps in numerous ways to facilitate numerical modelling exercises in the upcoming chapters. Both observational data and regional climate modelling output have been used either as model input, as a means of calibrating uncertain model parameters or to validate model results. An overview of data used in the different parts of this thesis is given in Table 1.1. For more information and details on the

Table 1.1: *Overview of data used in this thesis gathered at or near Nordenskiöldbreen. Purposes are divided into three categories: C = calibration, V = validation and I = input. Other abbreviations used: RACMO = Regional Atmospheric Climate MOdel, WRF = Weather Research and Forecasting model, DEM = digital elevation model, AWS = automatic weather station and GPR = ground-penetrating radar.*

Variable	Equipment/tool	Chapter	Purpose	Reference
Ice velocity	GPS	5	V	*Den Ouden et al.* [2010]
Mass balance	Stake	2	V	
Snow depth	Probe	2	C	
Snow density	Snow pit	2, 3	C, V	
Snow temperature	Snow pit	2, 3	C, V	
Surface height	SPOT5 DEM	2, 3, 5, 6	I, C	*Korona et al.* [2009]
	Sonic ranger	2	C	
Radiative fluxes	AWS	2	C, V	
Wind speed / dir.	AWS	3	V	
	WRF	3	V	*Claremar et al.* [2012]
Air temperature	RACMO (11-km)	2, 3	I	*Ettema et al.* [2010]
Rel. humidity	RACMO (11-km)	2, 3	I	*Ettema et al.* [2010]
Cloud cover	Svalbard Airport	2, 3	I	Norwegian Meteorological Institute
Precipitation	Svalbard Airport	2, 3	I	Norwegian Meteorological Institute
Bed height	GPR (deep)	5	V	
Reflection horizons	GPR (snow)	3	C	
Deep temperatures	Ice core	2	C	*Van de Wal et al.* [2002]
Deep densities	Ice core	2	C	*Pohjola et al.* [2002b]
Shallow temperatures	Firn core	3	V	S. Marchenko, pers. comm., 2013
Shallow densities	Firn core	3	V	S. Marchenko, pers. comm., 2013

measurements the reader is referred to the indicated chapter(s).

1.3 A glacier as a coupled system

Simulating the evolution of glaciers in space and time requires a proper treatment of what happens within a glacier as well as at the boundaries, either at the surface, base and calving front. Although useful insights can be gained by looking at individual parts of a glacier system, coupling of individual components is ultimately required to understand interactions and identify possible feedbacks. A glacier can be viewed as a coupled system where the ice geometry evolves by interaction between stresses, thermodynamics, hydrology and mass/energy exchange at the boundaries (Figure 1.8).

Regarding ice as an incompressible substance, ice flow and boundary mass fluxes collectively determine the thickness evolution by means of mass continuity. Where melt and accumulation dominate the mass flux at the glacier surface, basal melting may occur at the ice-bed interface and calving of ice bergs removes mass at the glacier front. Ice flows down gradients in gravitational potential by internal creep deformation and basal movement through sliding over the underlying bed and/or deformation of basal sediment [*Paterson*, 1994]. Basal movement

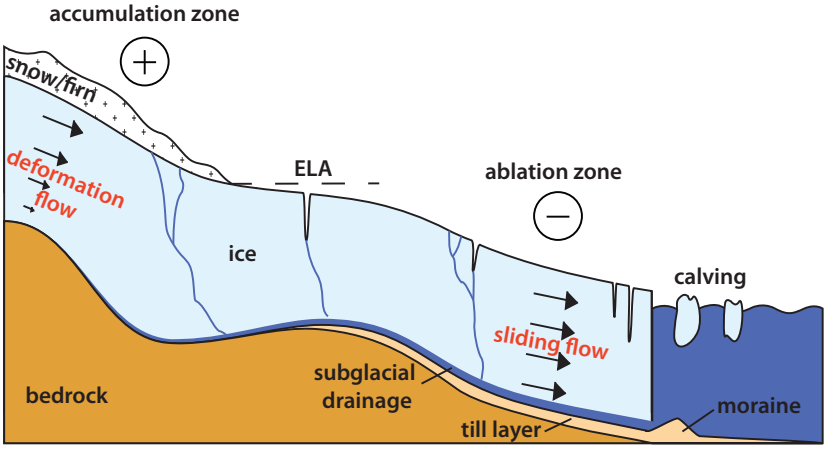

Figure 1.8: *Schematic cross-sectional view of a tide-water glacier.*

is intimately related to friction experienced at the bed, determined by the strength of basal material and the possible presence of water in case of a temperate bed, reducing the effective pressure of the overlying ice [*Clarke*, 2005]. Subglacial water, horizontally transported along gradients in fluid potential, originates from basal melting as well as vertical transport of surface melt water to the bed through moulins, crevasses and cracks in the ice. Surface melt in turn is determined by heat exchange of the surface with the atmosphere and the underlying firn or ice, while firn processes may affect the timing and rate of water input into the englacial system. Although the above gives only a simplified and incomplete description of a glacier system, it does illustrate how the different components in a glacier system interact.

As a result of interactions, feedbacks may arise inducing unstable behaviour. In the field of glaciology, well-known examples of such instabilities are the 'height−mass balance feedback' and the 'ice−albedo feedback'. The height−mass balance feedback is a direct consequence of the dependence of surface air temperature (decreasing with altitude) and precipitation (increasing with altitude) on surface height and may induce accelerated melt in case of surface lowering [*Oerlemans*, 2001]. The term 'ice−albedo feedback' is often used to explain amplified warming in the Arctic, where in a warming climate a reduction in sea ice lowers the surface reflectivity (albedo) and enhances absorption of solar radiation, inducing warming and a further reduction of sea ice [*Kellogg*, 1975; *Curry et al.*, 1995]. On a glacier scale, a similar feedback arises as in response to warming, more snow with a high albedo melts, exposing more ice with a low albedo, thereby enhancing absorption of solar radiation and accelerating melt. In a similar fashion, enhanced dust concentrations in response to surface melt amplify solar radiation absorbance and surface melt [*Oerlemans et al.*, 2009].

Oscillatory flow behaviour of glaciers, such as observed in surges, may only exist by virtue

of instabilities, arising from the interaction of sliding, thermodynamics and hydrology. Such feedbacks act to prevent relaxation to a steady-state geometry in a constant climate. A 'thermal instability' arises when enhanced sliding promotes basal friction and increases basal melt water production, effectively reducing basal shearing, thereby inducing further flow acceleration [*Robin*, 1955; *Clarke*, 1976]. This flow enhancing mechanism has been linked to the occurrence of surges in Svalbard [*Fowler*, 2001; *Murray et al.*, 2003; *Dunse et al.*, 2011]. In Chapter 4, numerical experiments illustrate different types of surge-type behaviour arising from such instabilities and the role of parameters that determine the rate of sliding is discussed.

1.4 Surface processes

1.4.1 Surface mass balance and firn processes

The surface mass balance of a glacier, determined by interactions of the surface layer with the overlying atmosphere and underlying snow/firn, has been acknowledged as the critical link between glaciers and climate [*Meier*, 1965]. Whereas the surface mass balance includes processes adding or removing mass at the surface, the total mass balance of a glacier additionally accounts for changes in the total ice volume related to calving and basal melting. In this thesis, the term surface mass balance refers to the specific mass balance, which describes the accumulated exchange of mass per unit area over a period of time. It is the sum of accumulation by precipitation and riming and ablation by runoff of melt water and sublimation (Figure 1.9). Runoff is the amount of water that actually leaves the snow/firn pack and does not necessarily equal surface melt, as percolating water may be stored or may refreeze in the snow/firn pack. The surface mass balance hence collectively describes the mass budget determined by surface and near-surface processes.

Whereas in situ surface height observations, usually done with stakes drilled in the snow/ice, provide point estimates of the local surface mass balance, numerical models are useful to analyse the temporal evolution and spatial distribution of the surface mass budget [*Arnold et al.*, 1996; *Klok and Oerlemans*, 2002; *Reijmer and Hock*, 2008]. Mass balance models can further be used as predictive tools to study the climate sensitivity of glaciers [*Oerlemans et al.*, 1998; *Raper and Braithwaite*, 2006; *Hock et al.*, 2007]. Among simpler models to compute the surface mass balance are degree-day models, which link the ablation rate directly to the number of days with positive air temperature [*Braithwaite*, 1995]. More accurate and physically-based simulation of the surface temperature and energy involved in melting (Q_{melt}) requires solving the surface energy budget, determined by the sum of all energy fluxes at the surface (Figure 1.10):

$$Q_{\mathrm{melt}} = SW_{\mathrm{net}} + LW_{\mathrm{net}} + Q_{\mathrm{sens}} + Q_{\mathrm{lat}} + Q_{\mathrm{rain}} + Q_{\mathrm{sub}}\,, \tag{1.1}$$

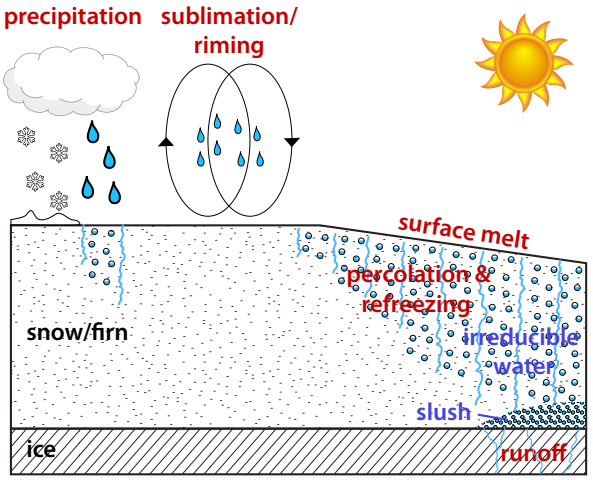

Figure 1.9: *Schematic view of the mass flux components that compose the surface mass balance.*

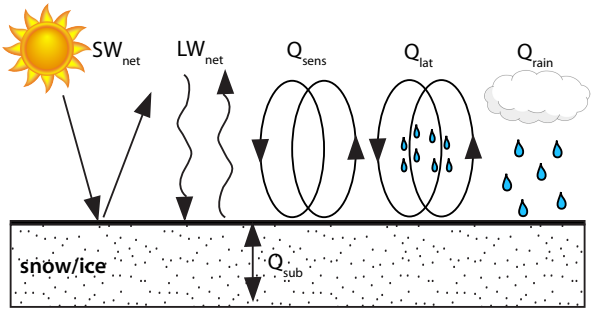

Figure 1.10: *Schematic view of the energy fluxes that determine the surface energy budget.*

where SW_{net} is the net shortwave (solar) radiation, LW_{net} is the net longwave radiation, Q_{sens} and Q_{lat} are the turbulent sensible and latent heat flux, Q_{rain} is the heat transfer by rainfall and Q_{sub} is the subsurface heat flux. Melt water produced at the surface may percolate into the snow/firn (if present), where it may either refreeze, be stored in capillary pore spaces, accumulate on top of the impermeable ice to form a slush layer or leave the firn/snow pack as runoff (Figure 1.9).

Refreezing occurs in non-temperate firn/snow, increasing the density and rapidly raising subsurface temperatures, and is most pronounced in spring or early-summer when melt water percolates in cold winter snow. Additionally, water trapped in pore spaces at the end of summer may refreeze in winter when a cold wave penetrates into the firn [*Pfeffer et al.*, 1991]. Overall, refreezing contributes substantially to the surface mass balance [*Schytt*, 1949; *Ko-*

erner, 1970]. The process of internal accumulation, referring to refreezing below the summer surface of the previous year, received considerable attention as this term is ignored by traditional mass balance measurements in the accumulation zone [*Schneider and Jansson*, 2004; *Reijmer and Hock*, 2008]. Heat release after refreezing has a pronounced impact on the thermal structure of glaciers [*Greuell and Oerlemans*, 1989; *Jania et al.*, 1996]. In Svalbard, preferential refreezing in the accumulation zone commonly induces a thermal structure exhibiting temperate subsurface conditions in the accumulation zone and cold near-surface conditions in the ablation area [*Blatter and Hutter*, 1990; *Pettersson*, 2004]. As subsurface percolation, storage and refreezing effectively reduces and delays runoff of melt water, firn processes influence the timing and rate of input in the englacial drainage system [*Fountain*, 1996; *Jansson et al.*, 2003]. In a warming climate, refreezing and melt water storage in firn pore space may initially act as a buffer against ice mass loss and subsequent sea-level rise [*Bugnion and Stone*, 2002], while accelerated mass loss may occur in case of saturation of temperate firn [*Van Angelen et al.*, 2013].

As firn processes strongly influence the surface energy and mass budget, a coupled modelling approach is desired, simultaneously solving the surface energy budget and modelling the evolution of firn properties (density, temperature and water content). In Chapter 2, a coupled surface energy balance - snowpack model is applied to the distributed grid of Nordenskiöldbreen, Svalbard, to simulate the spatio-temporal evolution of melt, refreezing and runoff for the period 1989−2010. Observational surface and subsurface data, as well as regional climate model output, play a crucial role in model forcing, initialisation, calibration and validation (Section 1.2).

1.4.2 Snow accumulation

For Arctic glaciers, the dominant components of the surface mass balance are mass gain by precipitation and mass loss by runoff of melt water, as latent mass exchange by sublimation and riming is generally small. Precipitation falling as snow directly accumulates at the surface, while precipitation falling as rain may percolate in the firn where it may be stored or refreeze (Figure 1.9). Hence, both snow fall and rain fall may contribute to the mass balance. Whereas surface melt can be computed by solving the surface energy budget (or with simpler approaches), precipitation needs to be prescribed as input, using (scarcely) available data. Models simulating the glacier mass balance usually rely on precipitation input, based on local measurements and a fixed linear precipitation - height gradient [e.g., *Klok and Oerlemans*, 2002; *Hock and Holmgren*, 2005; *Reijmer and Hock*, 2008; *Giesen and Oerlemans*, 2010] or interpolated low-resolution regional climate model output [*Reichert et al.*, 2001; *Rye et al.*, 2010]. Both approaches suffer from a lack of small-scale spatial variability in precipitation forcing, which not only affects the spatial variability in the modeled mass balance, but also influences the spatial mean mass balance, responding nonlinearly to changes in precipitation [*Giesen*, 2009].

Figure 1.11: *Left panel: alternating patches of snow and bare ice in the ablation area. Right panel: wind driven snow redistribution during a storm. Photos taken on Nordenskiöldbreen in April 2011.*

Snow deposition on a glacier surface may vary substantially from one place to another (Figure 1.12). In general, accumulation variability depends on two factors: 1) variations in where the snow falls and 2) horizontal redistribution of the snow by wind. Orographic precipitation in mountainous regions induces enhanced precipitation with altitude [*Sevruk*, 1997]. On a smaller scale, variability in local vertical wind speeds, resulting from divergence/convergence of wind patterns and strongly controlled by the local surface topography, substantially affect precipitation rates [*Lehning et al.*, 2008; *Mott et al.*, 2010]. In the event of strong winds, uplift of already deposited snow and subsequent transport through saltation and suspension may occur, inducing a redistribution of snow [*Pomeroy and Gray*, 1990]. Additionally, sublimation of drifting snow particles may act as a mass loss term [*Lenaerts et al.*, 2010]. Undulations in the terrain have a pronounced impact on the rate of erosion and deposition by wind, effectively leading to enhanced erosion of slopes directed towards the wind and enhanced deposition in the lee of undulations [*Liston and Sturm*, 1998; *Clifton and Lehning*, 2008]. The observed dependence of snow drift on terrain features has led to the development of parameterizations relating snow deposition after redistribution to terrain-based parameters, such as slope and curvature [*Liston et al.*, 2007; *Gascoin et al.*, 2013]. A current lack of observational constraints on spatial accumulation variability limits development of increasingly complex physically-based snow models and hinders improving our understanding of processes involved in shaping the snow cover. A greater understanding of spatial variability in accumulation would help to reduce uncertainty in the interpretation of point-wise annual winter balance measurements with stakes as well as long-term records from ice cores [e.g.,

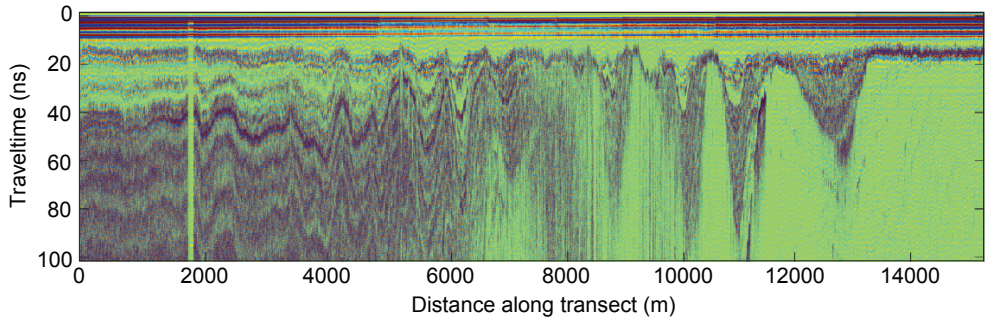

Figure 1.12: *Radargram of GPR measurements along a 15-km transect on Nordenskiöldbreen, collected in April 2012.*

Pohjola et al., 2002a; *Bales et al.*, 2009].

Ground-penetrating (GPR) provides a useful tool to map accumulation variability along a radar transect. Enhanced crystallisation of snow near the surface, related to melt-freeze cycles, vapour transport and radiation transfer, induces elevated near-surface densities at the end of summer, subsequently being buried by low-density snow in winter [*Colbeck*, 1986]. In the accumulation zone, this may produce an alternating annual pattern of high-density summer surfaces and low-density snow/firn in between, resulting in a radargram (Figure 1.12) exhibiting an alternating pattern of high and low reflectivity [*Kohler et al.*, 1997]. The associated two-way travel time (TWT) of highly-reflective layers collectively depends on the depth of the reflective layer as well as on the mean density of the firn/snow [*Robin et al.*, 1969; *Kovacs et al.*, 1995] and water content [*Looyenga*, 1965; *Stacheder*, 2005]. When density and water content profiles are known from observations, TWTs of summer surfaces, bounding annually formed layers, can be converted into depths and annual layer masses using conversion relations. When mass exchange between annual layers is negligible, reconstructed annual layer mass along a radar transect represents annual accumulation patterns. Such an approach has previously been used to extract spatial accumulation variability from GPR data along transects in Antarctica [e.g., *Richardson et al.*, 1997; *Spikes et al.*, 2004; *Fujita et al.*, 2011], Greenland [*Dunse et al.*, 2008; *Miège et al.*, 2013], the Alps [*Machguth et al.*, 2006] and Svalbard [*Pälli et al.*, 2002; *Taurisano et al.*, 2007].

Accurate conversion of TWTs into accumulation requires knowledge of vertical density profiles along the transect. Traditional approaches usually rely on a few point-measurements from snow pits and/or shallow firn cores along the transect and do not reasonably capture horizontal variations in density. Additionally, in areas with substantial melt and refreezing in the firn, there may be significant mass exchange as percolating melt water is exchanged between buried annual layers, reducing the representativeness of annual layer mass as annual accumulation. Finally, the possible presence of water in the firn, altering dielectric properties

of the medium, further increases uncertainty in extracting accumulation from GPR data. To circumvent these issues, an inverse approach can be applied, using a forward model to simulate surface melt and the subsurface evolution of temperature, density and water content, thereby accounting for percolation, storage, refreezing and runoff of melt water. The inverse problem consists of iteratively tuning precipitation, serving as input for the model, such that modelled firn layering and TWTs of buried modelled summer surfaces match with TWTs of reflection horizons in the GPR data. In Chapter 3, this novel approach is applied to reconstruct and analyse accumulation variability along a GPR transect on Nordenskiöldbreen, Svalbard.

1.5 Subglacial processes

Whereas a wealth of observational data of surface processes is available, the inaccessibility of the glacier bed complicates direct observations of subglacial conditions. This has led to a current lack of understanding of subglacial processes, which is unfortunate given the crucial role of processes acting at the ice-bed interface on the evolution of ice masses. Much of our current knowledge of subglacial processes is based on indirect observational data, such as measurements of seasonal surface velocity variations (induced by basal sliding variability), surface uplift (indicating changes in subglacial water pressures) and discharge (influenced by the efficiency of the drainage system). More direct observations come from borehole instrumentation and sampling as well as ground-penetrating radar (GPR) data, collectively providing information on basal sediment properties, bedrock topography, thermal structure, the subglacial drainage system and the presence of subglacial lakes [*Clarke*, 2005]. In recent years, the role of subglacial hydrology has received considerable attention in particular to explain seasonal variability in observed ice velocities of fast-flowing glaciers in response to melt input in Greenland [*Zwally et al.*, 2002; *Van de Wal et al.*, 2008; *Bartholomew et al.*, 2010; *Sundal et al.*, 2011] and Svalbard [*Nuttall and Hodgkins*, 2005; *Den Ouden et al.*, 2010; *Dunse et al.*, 2012]. A greater understanding of basal processes is ultimately needed to understand possible longterm impact of enhanced surface melt in a changing climate on ice dynamics and mass loss [*Sole et al.*, 2013].

Modelling the evolution of fast-flowing glaciers relies crucially on the description of sliding, which is known to depend on basal sediment properties, thermal structure of the bed and the possible presence and transport of water at the ice-bed interface. On the other hand, as surface features are often intimately related to basal properties and models exist that simulate surface behaviour given prescribed basal conditions (parameters), these models can be used in an inverse manner to better constrain basal parameters, like bed topography and slipperiness [*Gudmundsson*, 2011].

1.5.1 Basal topography

Knowledge of the bedrock topography underneath glaciers, ice caps and ice sheets is of high relevance, mainly for two reasons. First of all, when surface heights are known, bed heights are required to estimate the ice thickness distribution and to enable computation of the volume contained in an ice mass or a large sample of ice masses. This is of importance for accurate estimation of the potential contribution of disappearing ice masses to sea-level rise. Secondly, detailed knowledge the bed topography and thickness distribution is relevant for accurate modelling of the evolution of ice masses in a changing climate. In prognostic experiments, the ice evolution depends crucially on the initial (present-day) thickness distribution. Hence, proper initialisation is desired and should result in an initial ice geometry and thermodynamic state consistent with past surface climate conditions. This is required to avoid 'model drift' at the start of time-dependent experiments.

Observational data of subglacial topography are scarce and usually limited to sparse tracks of GPR data on a glacier surface. Whereas 2-D mapping with GPR is an expensive and laborious task, direct interpolation of these tracks is undesired due to the resulting lack of detail of bedrock features. This has stimulated the development of alternative numerical methods to inversely determine basal topography from surface data. Among the simplest approaches are methods that assume a perfectly-plastic ice rheology and compute the ice thickness from surface slope and a constant basal yield stress [e.g., *Nye*, 1951; *Oerlemans*, 1997; *Paul and Svoboda*, 2010; *Li et al.*, 2012]. To reduce uncertainty related to the constant yield stress assumption, extensions of this method additionally require mass balance input and couple the previous method to the mass conservation equation [*Farinotti et al.*, 2009; *Clarke et al.*, 2013]. Other mass conservation approaches rely on ice velocity fields to obtain thickness estimates [*Morlighem et al.*, 2011; *McNabb et al.*, 2012]. Additionally, adjoint-based and bayesian inference methods, requiring velocity and surface height data, have been applied to ice-streams to simultaneously retrieve basal slipperiness and topography [*Thorsteinsson et al.*, 2003; *Gudmundsson and Raymond*, 2008; *Raymond and Gudmundsson*, 2009; *Raymond Pralong and Gudmundsson*, 2011; *Goldberg and Heimbach*, 2013].

Given a map of surface height data, a time-dependent mass balance forcing and an ice flow model, an alternative inverse approach can be applied in which the bed topography is calibrated such that the surface height field at the end of time-dependent model runs matches observed values. This requires an iterative method in which the ice flow model is run multiple times, while information of the surface height misfit after every model run is used to adjust bed heights. A very simple but efficient way to correct the bed after every model iteration is to directly use the surface height error as a negative (and scaled) correction of the bed. Such an approach has previously been applied in a flow-line context [*Oerlemans*, 2001; *Leclercq et al.*, 2012; *Michel et al.*, 2013] and importantly provides an ice geometry and thermodynamic structure which is consistent with the past climate. Hence, the method not only reconstructs basal topography, it simultaneously provides an initialisation method for

forecasting experiments. In Chapter 5, we extend the approach to three dimensions, test its functionality in synthetic experiments and apply and validate the method in a real application on Nordenskiöldbreen.

1.5.2 Basal sliding & hydrology

Sliding at the ice-bed interface may contribute substantially to the flow of glaciers. The thermal structure of the bed plays a decisive role in whether basal sliding may occur as on temperate beds the presence of water reduces resistance experienced by the basal ice, whereas on cold beds resistance is high and ice flow is dominated by internal deformation. In line with this, 'sub-melt' sliding laws have been developed for numerical modelling purposes that link the basal shear stress to subglacial temperature [*Hindmarsh and Le Meur*, 2001; *Greve*, 2005]. More commonly used sliding laws account for the role of water in reducing basal resistance and distinguish between sliding over hard beds, consisting of crystalline bedrock, and soft beds, composed of fine granular material (sediment).

Early work mainly focussed on sliding over hard beds, which occurs by a combination of regelation (melting/refreezing around obstacles), enhanced creep deformation (acceleration around obstacles) and cavitation (reducing the contact area of ice and bed) [e.g., *Weertman*, 1957; *Nye*, 1969, Figure 1.13]. The need for direct formulations linking basal friction and sliding for modelling purposes, stimulated the development of hard-bedded 'sliding laws', relating the basal shear stress in a power-law formulation to sliding velocity and effective pressure (i.e. ice overburden pressure minus water pressure) [*Budd et al.*, 1979; *Fowler*, 1987]. More recently, *Schoof* [2005] argued that hard-bedded basal shearing should have an upper bound as ice loses contact with the bed and proposed a new sliding law.

A different type of sliding occurs over soft beds, where basal movement is achieved through till deformation rather than slip [*Iverson et al.*, 1998; *Tulaczyk et al.*, 2000a]. Soft-bedded sliding occurs when the applied stress exceeds an ultimate strength ('yield stress') of the granular material and starts to deform. If the applied stress is smaller than the yield stress, ice flows solely by internal deformation, whereas when the applied stress exceeds the yield stress, longitudinal stresses come into play to maintain a stress balance. Sliding laws using a Coulomb-plastic formulation, are independent of sliding velocity and are proportional to the effective pressure [*Clarke*, 2005; *Bueler and Brown*, 2009].

Ice sheet models, simulating the evolution of ice masses, require sliding laws to couple the basal shear stress to other model variables, such as sliding velocity, water pressure and/or subglacial temperature. For reasons of easing implementation and reducing numerical effort current ice sheet models either ignore the role of water transport [*Greve*, 2005; *Gagliardini et al.*, 2013] or rely on simplified descriptions of water transport and water pressure [*Bueler and Brown*, 2009]. On the other hand, substantial progress has been made recently in modeling the seasonal evolution of water pressures at glacier scale in relation to water transport and

Figure 1.13: *Photograph illustrating the transition from subglacial till to glacier ice. The shown structure illustrates a mixture of sediment and ice and is likely influenced by basal melting/refreezing and the process of regelation (ice melts upstream of a bed bump due to high pressure, while melt water refreezes in the lee of the obstacle). Photograph taken at the glacier front of Nordenskiöldbreen in April 2013.*

evolving drainage system characteristics [e.g., *Schoof*, 2010; *Pimentel and Flowers*, 2011; *Hewitt et al.*, 2012; *Hewitt*, 2013]. In these studies, physical processes determine the evolution of the drainage system capacity, while water flows along fluid potential gradients. Distributed drainage occurs in a linked-cavity system for low to moderate water input, whereas water flow concentrates in a few large channels in case of high water input. Although it would be desirable to have similar subglacial hydrology physics in fully-coupled ice sheet models, this is currently problematic for several reasons. First of all, as ice sheet models are designated to model the evolution of ice masses at a wide range of temporal and spatial scales, the chosen hydrology model should be applicable at different spatial and temporal resolutions. A disadvantage of explicit modelling of channelized drainage (in combination with sheet-like drainage) is that channels can only form at prescribed locations, which hinders robustness of results at different spatial resolutions. Secondly, model time-steps for pressure evolution in more complete hydrology models are generally much smaller than time-steps for ice dynamics. Detailed modelling of hydrology hence implies substantial increases in computational effort, which is a limitation for long time-scale experiments. Thirdly, including more complete physics in a hydrology model usually goes at the expense of adding more poorly-constrained parameters to the system. Given the limited amount of observational data, a hydrology model is desired with only a limited number of uncalibrated parameters. Altogether, ice sheet models require a hydrology component that: 1) includes reasonable physics

of water transport and drainage system evolution, 2) is applicable to a wide range of spatial and temporal scales, 3) can be constrained given scarcely available data.

In Chapter 6, first steps are presented towards implementation of a new hydrology model in the thermo-mechanically coupled ice sheet model PISM [Parallel Ice Sheet Model; *Bueler and Brown*, 2009, available at `www.pism-docs.org`]. A distributed linked-cavity drainage model is coupled to englacial storage and tested in synthetic experiments with transient melt input on Nordenskiöldbreen. Accounting for englacial storage is shown to substantially ease implementation, whereas the englacial porosity acts as a regularisation parameter reducing runtime at the expense of accuracy of the pressure evolution. This effectively opens the door to application at a wide range of time-scales, requiring different degrees of detail in pressure evolution.

1.6 Thesis outline

Processes acting at the boundaries determine to a large extent the shape and time-dependent behaviour of glaciers. Mass loss/gain at the surface depends ultimately on interactions with the atmosphere and underlying firn, while at the bed sliding velocities evolve as a product of interactions between stresses, thermodynamics and hydrology. The main aim of this thesis is to improve our understanding of both surface and basal conditions in the context of Svalbard glaciers. The remainder of this thesis can roughly be divided into two parts discussing surface processes (Chapters 2 and 3) and subglacial conditions (Chapters 4, 5 and 6).

Chapter 2 focusses on the surface mass budget of Nordenskiöldbreen over the period 1989–2010. A surface energy balance model is coupled to a multi-layer snow model and used to study distributed patterns of melt, runoff and refreezing. We analyse spatio-temporal variability in the components of the mass and energy budget and show the evolution of firn density, temperature and water content. The substantial impact of refreezing on the surface mass balance and firn temperatures is quantified and discussed. Climate perturbation experiments are done to study the sensitivity of the mass balance to seasonally inhomogeneous changes in climate.

Local weather conditions as well as geometric factors affecting the redistribution of snow by wind can lead to significant variability in snow deposition over short distances. Accurate knowledge of how snow accumulation, the dominant mass source at the glacier surface, varies in space and time is of high relevance for both mass balance modelling as well as interpretation of local mass balance observations from stakes and ice-core profiles. In Chapter 3, we use the coupled surface energy balance - snow model in an inverse procedure to extract snow accumulation variability from internal layering in the firn pack as detected in a ground-penetrating radar profile on Nordenskiöldbreen. We analyse annual patterns of spatial accumulation variability along the transect between 2007-2012 and discuss the relevance of inverse modelling in comparison to traditional methods. Spatial variability in accumulation

is discussed in relation to terrain characteristics and wind properties. Finally, the effect of small-scale variability in accumulation on the mean surface mass balance is quantified.

From Chapter 4 onwards the focus shifts from surface to subglacial conditions. In Chapter 4, numerical simulations are performed with a thermo-mechanically coupled ice flow model (PISM) to gain insight into how the interplay of stresses, thermodynamics and hydrology may result in cyclic flow patterns, such as have been observed in Svalbard-type surging. We identify multiple types of oscillations, arising from internal feedbacks at the ice base, keeping the ice mass out of an internal equilibrium. The crucial role of sliding law parameters on oscillatory behaviour is analysed. Finally, the impact of climate feedbacks on cyclic flow characteristics is investigated.

Chapter 5 focusses on reconstructing subglacial topography. Accurate estimates of basal topography are on the one hand needed to estimate ice volume contained in glaciers and on the other hand for detailed modelling of the (future) evolution of glaciers with an ice dynamical model. As direct observations of bed heights are scarce, inverse techniques serve as useful tools to infer information about the bed from surface data. In Chapter 5, an inverse modelling approach is presented in which bed heights, serving as a lower boundary in an ice dynamical model, are iteratively adjusted to minimise the discrepancy between modelled and observed surface heights. A simple regularisation technique is used, which directly uses the surface misfit to correct the bed. The inverse approach is applied in synthetic steady-state experiments, using PISM as a forward model, to verify robustness of the method when recovering distributed beds. In a next step, we reconstruct the basal topography of Nordenskiöldbreen, by fitting surface height data from a DEM and applying a time- and height-dependent surface climate forcing. Early termination of the iterative procedure is discussed to avoid fitting noise in the surface data. Reconstructed bed heights are validated against scarce radar data. In addition to recovering basal topography, the inverse approach provides a useful means to initialise ice flow models for forecasting experiments.

Chapter 6 presents ongoing research towards development and implementation of an improved subglacial hydrology model in PISM. A linked-cavity hydrology model is coupled to an englacial storage model, which enables simulating spatio-temporal water pressure variations in response to transient melt input, subglacial water transport and an evolving drainage system capacity. We analyse steady-state behaviour of the hydrology model and discuss the decisive role of englacial storage on the pressure evolution. Accounting for englacial storage is shown to ease numerical implementation and we demonstrate the englacial porosity can effectively be used as a regularisation parameter, which opens the door to application at a wide range of time-scales.

2

Simulating melt, runoff and refreezing on Nordenskiöldbreen

A distributed energy balance model is coupled to a multi-layer snow model in order to study the mass balance evolution and the impact of refreezing on the mass budget of Nordenskiöldbreen, Svalbard. The model is forced with output of the regional climate model RACMO and meteorological data from Svalbard Airport. Extensive calibration and initialisation are performed to increase the model accuracy. For the period 1989-2010, we find a mean net mass balance of -0.39 m w.e. a^{-1}. Refreezing contributes on average 0.27 m w.e. a^{-1} to the mass budget and is most pronounced in the accumulation zone. The simulated mass balance, radiative fluxes and subsurface profiles are validated against observations and are generally in good agreement. Climate sensitivity experiments reveal a non-linear, seasonally dependent response of the mass balance, refreezing and runoff to changes in temperature and precipitation. It is shown that including seasonality in climate change, with less pronounced summer warming, reduces the sensitivity of the mass balance, refreezing and the equilibrium line altitude (ELA) in a future climate.

This chapter is based on: Van Pelt, W., J. Oerlemans, C. Reijmer, V. Pohjola, R. Pettersson, and J. van Angelen (2012), Simulating melt, runoff and refreezing on Nordenskiöldbreen, Svalbard, using a coupled snow and energy balance model, *The Cryosphere*, *6*(3), 641–659

2.1 Introduction

The mass balance has been acknowledged as the critical link between glaciers and climate [*Meier*, 1965]. Numerical models capable of simulating the surface mass balance have proved useful in analysing the temporal evolution and spatial distribution of the mass budget of ice masses in more detail than provided by observations only [*Greuell*, 1992; *Hock*, 1999]. Additionally, mass balance models have been used as predictive tools to study the sensitivity of glaciers to climate change [*Oerlemans et al.*, 1998; *Braithwaite and Zhang*, 1999; *De Woul and Hock*, 2005; *Raper and Braithwaite*, 2006; *Hock et al.*, 2007]. Distributed mass balance models that solve the surface energy balance to compute melt have been shown to be capable of simulating spatial melt patterns and their variability [*Arnold et al.*, 1996; *Klok and Oerlemans*, 2002; *Hock and Holmgren*, 2005].

Refreezing of percolating and stored water in snow and firn contributes significantly to the mass balance of glaciers [*Schytt*, 1949; *Koerner*, 1970] and has a pronounced impact on the thermal structure [*Greuell and Oerlemans*, 1989; *Jania et al.*, 1996]. Refreezing of percolating water is most pronounced in spring when low subsurface temperatures and the presence of a snow pack increase the potential for refreezing. During the melt season, superimposed ice may form when percolating water accumulates to form a slush layer on top of the impermeable ice and refreezes [*Wadham and Nuttall*, 2002; *Obleitner and Lehning*, 2004; *Wright et al.*, 2005]. After the melt season, water trapped in pore spaces is subject to refreezing when a cold wave penetrates into the snow/firn pack [*Pfeffer et al.*, 1991]. The latent heat release after refreezing raises subsurface temperatures and hence affects the heat flux towards the surface. Refreezing below the previous year's summer surface in the accumulation zone, referred to as internal accumulation, has received considerable attention, since this term is disregarded by traditional mass balance observations [*Trabant and Mayo*, 1985; *Schneider and Jansson*, 2004; *Reijmer and Hock*, 2008]. Other studies show the significance of refreezing on the timing and rate of englacial water transport [*Pfeffer et al.*, 1991; *Fountain*, 1996; *Jansson et al.*, 2003].

Coupling of a surface energy balance model to a snowpack model, simulating the subsurface evolution of temperature, density and water content, is required to accurately simulate ice melt, refreezing and runoff, and to study the relative impact of refreezing on the mass budget of a glacier. In this study, a distributed energy balance model, developed along the lines presented by *Klok and Oerlemans* [2002], is coupled to a multi-layer snow model based on the SOMARS model [Simulation Of glacier surface Mass balance And Related Subsurface processes; *Greuell and Konzelmann*, 1994]. This is then used to simulate the spatial distribution and temporal evolution of the mass balance on Nordenskiöldbreen, Svalbard. Gridded meteorological input fields are constructed from output of the regional climate model RACMO [Regional Atmospheric Climate MOdel; *Van Meijgaard et al.*, 2008] and weather station data from Svalbard Airport. Extensive calibration is performed to obtain values of poorly-constrained model parameters, whereas initialisation is done to attain subsurface profiles at

the start of the simulation. The model is run over the period 1989–2010 and we discuss the surface mass and energy budget in connection with evolving subsurface conditions. Sensitivity experiments are performed to investigate the sensitivity of the model output to the parameter setup, initial subsurface conditions and climate perturbations.

Mean surface temperatures at Svalbard Airport have risen by 0.22 °C per decade since 1912 and regional climate model projections for the 21st century predict a warming from 1961–1990 to 2071–2100 ranging from 3 °C in the southwest of Svalbard to 8 °C in the northeast [*Førland et al.*, 2009, 2011]. Temperature increase is expected to be less pronounced in summer than during the winter season. Regional differences and seasonal inhomogeneity in climate change both have a substantial impact on the sensitivity of the mass balance. We performed sensitivity tests with both seasonally homogeneous and inhomogeneous climate variations and discuss the relevance of accounting for seasonal variability in climate change on future mass balance projections.

2.2 Nordenskiöldbreen

Nordenskiöldbreen is a large outlet glacier, situated in central Spitsbergen and connected to a large ice plateau, Lomonosovfonna (Figure 2.1). Ice flows around two rock formations, Terrierfjellet and Ferrierfjellet, into the Adolfbukta bay. Despite retreat of the glacier since the end of the Little Ice Age around 1900 AD, Nordenskiöldbreen still has an active calving front with an estimated width of 3 km [*Rachlewicz et al.*, 2007]. Calving of the retreating front is likely to remain significant in the near-future, as ground-penetrating radar (GPR) observations, performed during fieldwork in spring 2010, indicate bedrock heights below sea-level upstream of the current glacier front.

A digital elevation model (DEM) of the glacier and its surroundings with a 40-m spatial resolution is derived from stereoscopic optical images gathered in 2007 and provided by the SPIRIT project [SPOT 5 stereoscopic survey of Polar Ice: Reference Images and Topographies, *Korona et al.*, 2009]. Post-processing of the DEM is done to remove erroneous spikes in the surface profile. The resulting gaps were filled using interpolation techniques. A contour plot of the surface topography is shown in Figure 2.1.

The area of Nordenskiöldbreen, bounded by the black line in Figure 2.1, is chosen to extend up to the estimated position of the ice divide, where horizontal ice flow is likely to be small. It can therefore be assumed that the total mass budget of the selected grid is merely the sum of the surface mass balance and a negative mass flux by calving. The selected grid covers a total area of 193 km^2 and spans an altitudinal range of 0 to 1195 m a.s.l.. The highest point of the Lomonosovfonna ice cap is located at 1237 m a.s.l.. Highest ice velocities are found along the main flow line between Terrierfjellet and De Geerfjellet, where annual mean surface velocities are typically in the range of 40-60 m a^{-1} [*Den Ouden et al.*, 2010]. GPR observations indicate an ice thickness of more than 600 m at some locations along the flow

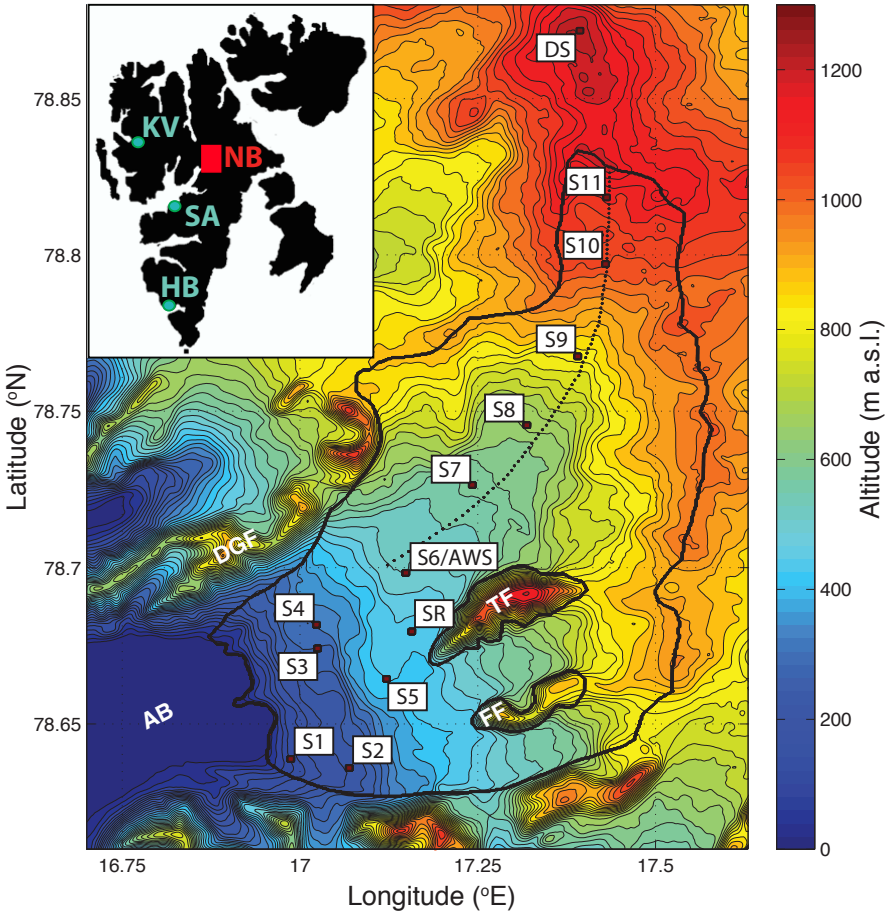

Figure 2.1: *Contour plot of the surface topography. The glacier outline is indicated by the thick black line. Dark red squares mark the position of the stake sites (S1-11), the Automatic Weather Station (AWS), the Sonic Ranger (SR) and the ice core drilling site (DS). The location of De Geerfjellet, Terrierfjellet, Ferrierfjellet and the Adolfbukta fjord are denoted by DGF, TF, FF and AB respectively. The dashed black line indicates the main flowline and cross-sectional subsurface profiles along this line are shown and discussed in Section 2.5.2. In the inset contour map of Svalbard, the locations of Nordenskiöldbreen (NB), Hansbreen (HB), Kongsvegen (KV) and Svalbard Airport (SA) are indicated.*

line. The mean surface temperature and amount of precipitation measured at Svalbard Airport (27 m a.s.l.), situated ∼55 km to the southwest of the glacier snout, over the period 1980-2010 are equal to −6.7 °C and 190 mm per year, respectively. Owing to the high latitude, seasonality in the temperature cycle is strong, with monthly mean temperatures at Svalbard Airport ranging from −16.7 °C in February to +5.9 °C in July.

2.3 Data

In this study, data are used to: 1) construct meteorological input to force the surface energy balance model (Section 2.3.1), 2) calibrate poorly-constrained model parameters (Section 2.4.4) and 3) validate model results (Section 2.5.3). Continuous measurements with an automatic weather station (AWS) at an altitude of 524 m a.s.l. on the glacier (Figure 2.1), operated by the Institute for Marine and Atmospheric research Utrecht (IMAU) since March 2009, are employed for both calibration and validation purposes.

2.3.1 Meteorological input

Two sources of meteorological data are used to construct gridded spatial patterns of air temperature, humidity, precipitation, cloud cover and air pressure: 1) output of the Regional Atmospheric Climate MOdel (RACMO) and 2) meteorological data from Svalbard Airport (SA), Longyearbyen.

Cloud cover and precipitation estimates are constructed from meteorological time-series at Svalbard Airport. Cloud cover observations with a 6-hourly resolution are downscaled to the 3-hour model resolution by interpolation, whereas 3-hourly values of the precipitation rate are constructed by homogeneous distribution of observed 12-hourly precipitation totals in time. We assume cloud cover to be spatially invariant, whereas precipitation increases linearly with height at a calibrated rate of 370 mm per km (see Section 2.4.4). The precipitation rate at 27 m a.s.l. is set equal to the precipitation rate at Svalbard Airport and above an altitude of 971 m a.s.l. the precipitation rate is assumed to be constant. The altitude of 971 m a.s.l. is chosen such that the parameterised mean maximum precipitation rate is equal to observed mean maximum precipitation of 540 mm per year found by *Pälli et al.* [2002] on Nordenskiöldbreen for the period 1963-1999.

Gridded 3-hourly air temperature, pressure and specific humidity input is constructed from output at a 11-km resolution of the Regional Atmospheric Climate Model (RACMO), as presented by *Ettema et al.* [2010]. RACMO is forced at the boundaries with ERA-Interim reanalysis data, provided by the European Centre for Medium-Range Weather Forecasts (ECMWF), for the period 1989-2010. We use data from two RACMO grid points located within 2 km from the grid at altitudes of 461 and 957 m a.s.l.. Every model time-step, altitudinal gradients

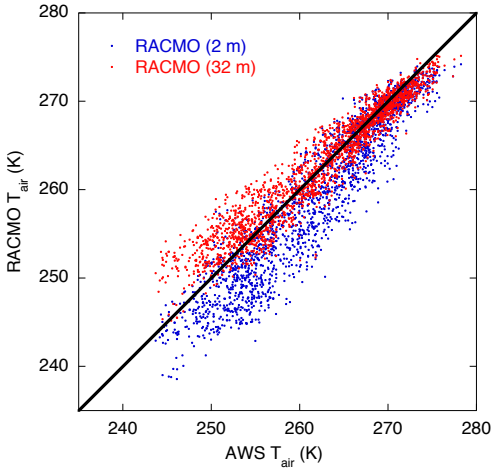

Figure 2.2: *Scatterplot of 3-hourly RACMO air temperatures at heights of 2 m (blue) and 32 m (red) versus observed air temperatures at ∼4 m above the surface at the AWS site for the period March 2009 to November 2010.*

of air temperature, specific humidity and potential temperature between the two RACMO grid points are computed and used to linearly inter- and extrapolate these variables onto the computational grid with a 40-m resolution. Gridded air pressure is then computed using gridded fields of air temperature and potential temperature. The sensible and latent heat flux formulations in the surface energy budget specifically require temperature and specific humidity input that is unaffected by the glacier's microclimate [*Oerlemans and Grisogono*, 2002]. Therefore, RACMO humidity and temperature estimates at 32-m altitude above the glacier surface are used in the calculation of turbulent fluxes. Additionally, RACMO 32-m temperatures are adopted in the computation of the incoming long wave radiation component. A comparison of 3-hourly gridded air temperatures at two altitudes and observed temperatures at ∼4 m above the surface at the location of the AWS is shown in Figure 2.2. The observations since 2009 unfortunately do not cover the melt season due to data logger problems. High correlations are found between the observed values and RACMO 32-m (R=0.96) and 2-m (R=0.94) temperatures, which demonstrates that temperature variations are well replicated in the RACMO dataset. The high correlations indicate the potential to use regional climate model data to construct input fields in regions where observations are scarce.

2.3.2 Stake measurements & snow profiles

Since 2006, stake measurements have been made at multiple sites on the glacier (S1-11 in Figure 2.1). Stake readings were done once a year in early spring and provide estimates of surface height variations. Furthermore, snow depth measurements at the stake locations were

done in order to quantify the relative contribution of ice melt to the change in surface height. Snow pits were dug at several sites in 2008 and 2009 to obtain vertical profiles of density and temperature. The mean observed snow density of 372 kg m^{-3} is used in combination with the change in snow depth to convert the observed surface heights into mass balance estimates. Continuous surface height measurements with a Sonic Ranger in 2007 are used for model calibration, as described in Section 2.4.4.

In May 1997, a 121-m long ice core was drilled near the summit of the Lomonosovfonna (DS in Figure 2.1). From this core, a 36-m deep vertical density profile was constructed and presented by *Pohjola et al.* [2002b]. Borehole temperatures were measured down to the bottom of the ice core, and have been analysed by *Van de Wal et al.* [2002]. The role of these vertical temperatures in the derivation of initial subsurface conditions at the start of the simulation is discussed in Section 2.4.5.

2.4 Model setup

In this study, a distributed energy balance model is coupled to a snow model and applied to Nordenskiöldbreen. The two models are coupled in the sense that melt water production at the surface serves as input for the multi-layer snowpack model, which simulates storage and refreezing of percolating water. Furthermore, the models are coupled through the subsurface heat flux, which affects the surface energy budget and depends on evolving vertical profiles of temperature and density.

The specific mass balance of a certain grid cell on the glacier is defined as the accumulated exchange of mass per unit area over a period of time. It is the sum of accumulation by precipitation and riming and ablation by runoff and sublimation. Ice melt only influences the mass budget if the produced melt water runs off and does not refreeze in the underlying snow or firn pack. Refreezing of rain water below the surface provides an additional contribution to the glacier's mass budget. Accurate computation of the mass balance of a glacier therefore involves treatment of both surface and subsurface mass fluxes.

2.4.1 Surface energy balance model

Forced with meteorological input the energy balance model calculates all energy fluxes that contribute to the surface energy budget. The sum of all fluxes is equal to the energy available for melting (Q_{melt}):

$$Q_{melt} = SW_{net} + LW_{net} + Q_{sens} + Q_{lat} + Q_{rain} + Q_{sub}\,, \tag{2.1}$$

where SW_{net} is the net shortwave radiation, LW_{net} is the net longwave radiation, Q_{sens} and Q_{lat} are the turbulent sensible and latent heat flux, Q_{rain} is the heat transfer by rainfall, and Q_{sub}

is the heat flux into the ice. Fluxes directed towards the surface are defined as positive. In the model, energy fluxes are formulated such that the surface temperature is the only unknown, which is found by iteratively solving Equation (2.1) with the left-hand-side set to zero. In case the computed surface temperature is above melting point, the surface temperature is set to melting point and energy fluxes are recomputed. In that case the sum of fluxes is positive and melting will occur. Next, a brief description of all fluxes contributing to the surface energy budget will be given. Since the surface model has been developed along the lines presented by *Klok and Oerlemans* [2002], the reader is referred to this study for further details.

The amount of solar radiation impinging on the surface depends on multiple factors: the top-of-atmosphere radiation, the transmissivity of the atmosphere, shading by the surrounding terrain, the slope aspect and gradient of the grid cell, the reflectivity of the surrounding terrain and the diffusivity of the sky. Input of cloud cover, air pressure and specific humidity is required to explicitly compute the atmospheric transmissivity due to Rayleigh scattering and gaseous absorption [*Kondratyev*, 1969], water vapour absorption [*McDonald*, 1960] and attenuation by aerosols and clouds [*Houghton*, 1954]. The model distinguishes between direct, diffuse and reflected solar radiation, coming from the surrounding terrain, and determines whether a grid cell is shaded by the surrounding topography. The computed amount of outgoing solar radiation is controlled by the formulation of the surface albedo. A parameterisation developed by *Oerlemans and Knap* [1998] has been adopted, in which the albedo is expressed as a function of the time since the last snow fall event and the snow depth. The calculated amount of incoming longwave radiation from the sky is expressed as a function of cloud cover, air temperature and specific humidity [*Konzelmann et al.*, 1994]. The Stefan-Boltzmann law, describing thermal emittance of a blackbody, is used to compute the outgoing longwave radiation. The turbulent sensible and latent heat flux formulations depend on the large-scale temperature and humidity, following expressions in *Oerlemans and Grisogono* [2002]. In contrast to the Monin-Obukhov similarity theory, in this approach no knowledge is required of near-surface air temperature, humidity and wind characteristics; quantities which are strongly influenced by the glacier surface. Despite its small impact on the energy budget, the heat supplied by rain at the glacier surface is also considered in the surface energy budget. Finally, the glacier heat flux, which depends on the conductivity of the medium and the vertical temperature gradient, is computed by extrapolation of subsurface heat transport in the two uppermost firn layers to the surface.

2.4.2 Subsurface model

The evolution of vertical profiles of temperature, density and water content is simulated with a subsurface model, which is loosely based on the SOMARS model developed by *Greuell and Konzelmann* [1994]. SOMARS has been coupled to a distributed energy balance model before by *Bougamont et al.* [2005] and *Reijmer and Hock* [2008].

The subsurface temperature evolution is described by the thermodynamic equation:

$$\rho c_p(T)\frac{\partial T}{\partial t} = \frac{\partial}{\partial z}\left(\kappa(\rho)\frac{\partial T}{\partial z}\right) + \frac{RL}{d}, \tag{2.2}$$

where ρ is the layer density, T is the layer temperature, $c_p(T)$ is the heat capacity of snow/ice, z is the vertical coordinate, $\kappa(\rho)$ is the effective conductivity, R is the refreezing rate, L the latent heat of melting (3.34×10^5 J kg^{-1}) and d the layer thickness. Expressions for $\kappa(\rho)$ and $c_p(T)$ are taken from *Sturm et al.* [1997] and *Yen* [1981] respectively:

$$\kappa(\rho) = 0.138 - 1.01 \times 10^{-3}\,\rho + 3.23 \times 10^{-6}\,\rho^2 \tag{2.3}$$

$$c_p(T) = 152.2 + 7.122\,T \tag{2.4}$$

The first term on the right hand side of Equation (2.2) represents heating by a vertical diffusive heat flux, whereas the second term describes heat production by refreezing of water within a layer. Since penetration of shortwave radiation in the upper snow layers is neglected, no subsurface melting can occur. This implies that all water in the snow pack originates from percolation of surface melt or rain water.

The densification equation describes the time-evolution of subsurface densities:

$$\frac{\partial \rho}{\partial t} = K_g(\rho, T) + \frac{R}{d}. \tag{2.5}$$

Here, $K_g(\rho, T)$ represents gravitational densification, computed using a formulation developed by *Arthern et al.* [2010], based on in situ measurements of Antarctic snow compaction, and recently modified by *Ligtenberg et al.* [2011]:

$$K_g(\rho, T) = C(b)\,b\,g\,(\rho_{ice} - \rho)\exp\left(-\frac{E_c}{R_d\,T} + \frac{E_g}{R_d T_{avg}}\right), \tag{2.6}$$

where b is the accumulation rate (in mm a^{-1}), g is the gravitational acceleration (9.81 m s^{-2}), ρ_{ice} is the density of ice (917 kg m^{-3}), R_d is the universal gas constant, and E_c (60 kJ mol^{-1}) and E_g (42.4 kJ mol^{-1}) are the activation energies associated with creep by lattice diffusion and grain growth respectively. T_{avg} denotes the temporal mean subsurface temperature and is computed every model time-step by taking the mean subsurface temperature of the preceding year. *Ligtenberg et al.* [2011] introduced the dependence of C on the accumulation rate b, which yields the following formulations of $C(b)$:

$$C(b) = \begin{cases} 0.0991 - 0.0103\log(b), & \text{if } \rho < 550\,\text{kg/m}^3 \\ 0.0701 - 0.0086\log(b), & \text{if } \rho \geq 550\,\text{kg/m}^3 \end{cases}. \tag{2.7}$$

In case a snow/firn pack is present, the available amount of water at the surface, originating from ice melt and rainfall, percolates downwards. Refreezing of the percolating water raises

subsurface temperatures and densities. The density cannot exceed the density of ice, whereas the temperature cannot be raised above melting point, which exposes two constraints on the maximum amount of refreezing. In case not all the available percolating water refreezes in a layer, a small amount of water, called irreducible water, will be held by capillary forces and the remaining water percolates into the next layer. In accordance with *Schneider and Jansson* [2004], an empirical relation has been used to compute the maximum irreducible water content of a layer θ_{mi}, i.e. the ratio of the mass of irreducible water to the total mass of the layer. θ_{mi} is expressed as a function of the porosity n, i.e. the ratio of pore space to the total volume of the snow layer, as follows:

$$\theta_{mi} = 0.0143 \exp(3.3\, n)\,. \tag{2.8}$$

Downward percolation of water continues until an ice layer is reached. On top of the impermeable ice, water may be stored in the remaining pore space to form a slush layer. In contrast to the irreducible water content, slush water runs off gradually, resulting in an exponential decay of the slush water content S in time:

$$S(t) = S(t - \Delta t) \exp\left(-\frac{\Delta t}{t^*}\right), \tag{2.9}$$

where Δt is the model time-step. The time-scale t^* controls the efficiency of the runoff and is expressed as a function of the surface slope β as follows [*Zuo and Oerlemans*, 1996]:

$$t^* = C_1 + C_2 \exp(-C_3 \tan\beta)\,, \tag{2.10}$$

where C_1, C_2 and C_3 are constants for which values of respectively 0.5, 200 and 133 are chosen in line with *Reijmer and Hock* [2008]. Consequently, the runoff timescale t^* takes values of 200, 20 and 0.5 days for surface slopes of 0, 1 and 5 degrees, respectively. Surface runoff occurs when either bare ice is exposed at the surface or when the slush water level in the firn pack equals the surface height. In both circumstances, excess water is assumed to run off instantly. Note that a snow/firn pack effectively delays runoff of melt water produced at the surface, and hence the vertical transport of water into the englacial drainage system. Horizontal transport from one grid cell to another is not considered in the model, since this requires explicit treatment of supraglacial water flows and vertical drainage through moulins, which is beyond the scope of this study.

2.4.3 Numerical setup

Numerical experiments are performed on a grid containing 825x646 grid points with a 40-m horizontal grid spacing. Of these points only 23%, corresponding to 120,671 grid cells, are assigned to the glacier (Figure 2.1). Prior to the start of the time-loop, in which the surface energy balance and subsurface profiles are modelled with a 3-hour time-step, terrain param-

eters are determined following a procedure described by *Dozier and Frew* [1990]. These topographical parameters include the terrain view factor, i.e. the fraction of the overlying hemisphere covered by terrain, and the ice fraction, i.e. the fraction of the surrounding visible terrain covered by ice. Both parameters are required in the calculation of incoming solar radiation coming from the surrounding terrain and depend strongly on the orientation and location of the grid cell. Topographic shading is time-dependent and evaluated with a half-hour time-step. Note that the glacier geometry is assumed to be invariant in time. Incorporating an evolving geometry would require coupling of the mass balance model to an ice dynamical model. By not considering the geometric evolution, we, among other effects, disregard the impact of the mass balance - height feedback, which enhances surface height fluctuations and may become significant over longer periods of time.

The snow model contains a total of 17 vertical layers extending 47 m below the surface, with layer depths increasing exponentially from 0.10 m just below the surface to about 10 m for the lowermost layer. After a change in the surface height due to snow fall, gravitational densification, ice melt or sublimation/riming, vertical profiles will shift and layer properties are updated accordingly. Diffusion of heat in the snow pack is computed by applying an explicit method, in which forward differencing of the time derivative and second-order central differencing of the space derivative is used. A sufficiently small time-step of one hour is used to assure stability and convergence of the heat diffusion method in the thin uppermost layers. At the lower boundary of the snow model, no heat transport can occur and the vertical density gradient is set to zero. Fresh snow is added at the surface with a density ρ_{fs} of 300 kg per m^3.

2.4.4 Calibration

The set of model formulations contains several poorly-constrained parameters. Observations on the glacier provide valuable information that can help to reduce the uncertainty in these parameters. In this study, radiative flux observations at the AWS site, Sonic Ranger measurements, snow depth at two stake sites and precipitation data from Svalbard Airport are used to calibrate the model.

In order to calibrate the modelled incoming solar radiation (SW_{in}), AWS measurements in 2009 and 2010 are employed. Observed half-hourly SW_{in} is corrected for the tilt angle of the sensor and averaged to obtain 3-hourly estimates. Two steps are taken to tune modelled SW_{in}: 1) calibration of the aerosol transmissivity under clear-sky conditions, and 2) finding an expression for the cloud transmissivity as a function of the cloud cover. The aerosol transmissivity τ_a can be expressed as a function of the pressure-corrected optical air mass m, following *Houghton* [1954]:

$$\tau_a = k^m \,, \tag{2.11}$$

where k is a constant, for which values are typically in the range 0.87-1.00, depending on the

geographic position [*Davies and McKay*, 1989]. We found a value for k of 0.97 by matching the observed SW_{in} under clear-sky conditions to simulated values over the calibration period. The cloud fraction at the AWS site is estimated using a method described by *Van den Broeke et al.* [2004, 2006] and *Kuipers Munneke et al.* [2008]. This method assumes that at a certain air temperature, LW_{in} is linearly related to the cloud fraction. Following *Klok and Oerlemans* [2002], the cloud transmissivity τ_{cl} is computed by taking the ratio of the observed SW_{in} and the modelled clear-sky SW_{in}. The resulting values of τ_{cl} are assumed to be a function of the cloud fraction and similar to the procedure described by *Greuell et al.* [1997], a fit has been made to find the following expression for the cloud transmissivity as a function of the cloud fraction n:

$$\tau_{cl} = 1.00 - 0.128\,n - 0.346\,n^2\,. \tag{2.12}$$

Comparing Equation (2.12) to the expression found by *Greuell et al.* [1997] for an Alpine glacier, shows that τ_{cl} in Equation (2.12) depends less strongly on the cloud fraction, which might be related to geographical differences in the prevailing cloud type and associated optical depth.

The incoming long wave radiation flux, $LW_{in} = \varepsilon\sigma T_a^4$, depends on the emissivity of the sky ε, which is formulated as a function of the cloud fraction n after *Konzelmann et al.* [1994]:

$$\varepsilon = \varepsilon_{cs}\,(1 - n^2) + \varepsilon_{cl}\,n^2\,, \tag{2.13}$$

with ε_{cl} a constant and ε_{cs} a function of the vapour pressure e_a and air temperature T_a [*Greuell and Konzelmann*, 1994]):

$$\varepsilon_{cs} = 0.23 + b\left(\frac{e_a}{T_a}\right)^{\frac{1}{8}}\,, \tag{2.14}$$

where b is a constant. In this study, LW_{in} is calibrated by finding values for the constants b and ε_{cl} for which discrepancies in the modelled LW_{in} are minimised in respect to observed values. Due to data logger problems during the melt season in 2009 and 2010, only longwave radiation measurements outside the melt season are available for comparison. Note that ε_{cl} and b can be determined independently by considering cloud-free and fully cloudy conditions. A value for ε_{cl} of 0.990 was found by comparing modelled and observed overcast (cloud fraction >95%) incoming longwave radiation. A comparison of simulated and observed LW_{in} under clear-sky conditions (cloud fraction <5%) led to a value for b of 0.447. These values agree well with estimated values for ε_{cl} and b of 0.984 and 0.433 by *Klok and Oerlemans* [2002] for the Morteratsch glacier in Switzerland.

The observed albedo at the AWS site, derived by taking the ratio of reflected and incoming shortwave radiation, is employed to constrain values of the ice albedo α_{ice} (0.32), fresh snow albedo α_{fs} (0.87) and to estimate a threshold snow fall rate P_{fs} (0.04 mm w.e. per hour) above which the albedo is set to the albedo of fresh snow.

The relative amount of liquid and solid precipitation in the model is determined by the local

air temperature. A threshold air temperature $T_{s/r}$ for which precipitation is assumed to be half rain and half snow, is derived from time-series of precipitation type and the corresponding air temperature at Svalbard Airport since the year 2000. The resulting value for $T_{s/r}$ is 274.6 K. Around this threshold value the relative fraction of snow fall with respect to the total precipitation is assumed to decrease linearly from 100% at $T_{s/r} - 1$ K to 0% at $T_{s/r} + 1$ K.

Snow depth measurements at the sonic ranger site and the AWS site in March 2007 and 2008 are used to tune the altitudinal precipitation gradient, γ_p. This resulted in a yearly mean value for γ_p of 370 mm per km. With this gradient, the average maximum precipitation of 540 mm w.e. per year [*Pälli et al.*, 2002] is reached at 971 m a.s.l..

The turbulent flux formulations, adopted from *Oerlemans and Grisogono* [2002], include a background exchange coefficient C_b, associated with turbulence generated by the large-scale wind. Lacking direct observations of turbulent fluxes, a value for C_b of 0.0028 has been estimated by matching simulated snow and ice melt in 2007 to observations at the Sonic Ranger site. Note that calibration of C_b and γ_p should be done after calibration of the other tuning parameters since ice melt and snow depth do not vary independently of the setup of the other tuning parameters. We chose to tune γ_p before calibrating C_b, since the influence of C_b on snow depth is much less pronounced than the impact of γ_p on ice melt.

2.4.5 Initialisation

Subsurface profiles of density, temperature and water content depend strongly on the history of subsurface processes and climate forcing. Due to the significance of vertical advection and diffusion in mass and heat transport, the response time of subsurface variables increases rapidly with distance from the source of variability (mainly at the surface). At a depth equivalent to the maximum depth in the snow model of 47 m, the response time is typically on the order of a few decades. It is therefore important to have properly initialised subsurface profiles at the start of the model run in 1989. To do so, observed snapshots of the vertical borehole temperatures at the drill site in May 1997 [*Van de Wal et al.*, 2002] are used as a benchmark against which the initial profiles are calibrated. The strategy of the initialisation procedure is to loop the model over the period 1989-1997 as often as is required to resemble the observed borehole temperature profile. Note that the drill site is not part of the selected grid of Nordenskiöldbreen, where the surface energy budget and vertical profiles are computed every model time-step (Figure 2.1). Nevertheless, for initialisation purposes the surface energy balance and evolution of the snow pack have been simulated for the grid point nearest to the drill site as well. At the start of the first loop of initialisation, linear vertical density profiles are prescribed, whereas vertical temperatures are set equal to an arbitrary constant value of -8 °C. The initial snow depth is set to increase linearly with altitude from 0 m at 700 m a.s.l. to 25 m at the altitude of the drill site (1237 m a.s.l.).

Figure 2.3 shows subsurface densities and temperatures at the location of the drill site after

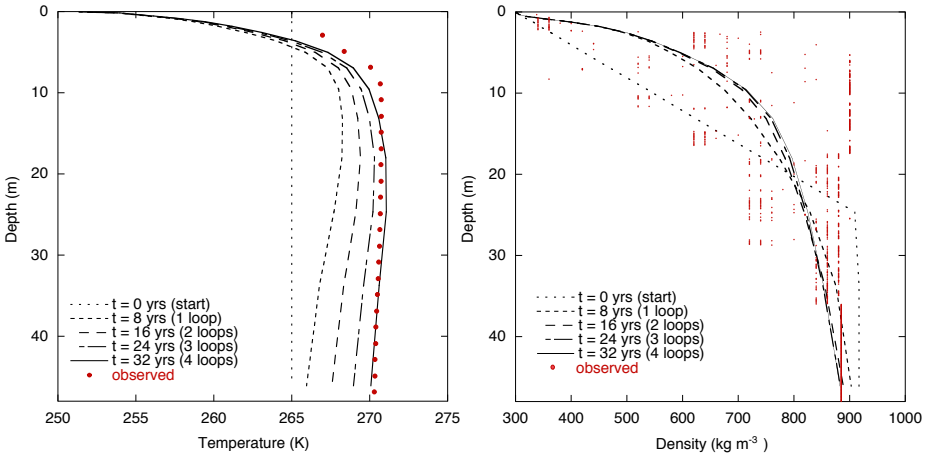

Figure 2.3: *Initialisation of the subsurface temperature (top panel) and density (bottom panel) at the ice core drill site. Observed vertical temperatures are taken from Van de Wal et al. [2002], whereas observed densities are adopted from Pohjola et al. [2002b].*

every 8-year loop of the initialisation procedure. Observed subsurface temperatures [*Van de Wal et al.*, 2002] and densities [*Pohjola et al.*, 2002b] at the drill site in May 1997 are also shown. Best agreement between modelled and observed subsurface temperatures is found after 32 years of initialisation. This implies 24 years of initialisation is done to produce initial conditions for the entire grid in 1989. In contrast to the simulated densities, the observed density profile shows a large variability between the different layers (Figure 3b). Simulating small-scale density variations would require a more detailed treatment of the evolution of the snow microstructure in response to melt water percolation and refreezing. More discussion on this is included in Chapter 3.

2.5 Standard run: 1989-2010

Starting from initialised subsurface profiles, a 21-year simulation is performed covering the period from October 1989 to October 2010. In this section, we present the temporal evolution and spatial distribution of the mass and energy balance and discuss these in relation to evolving subsurface properties.

2.5.1 Mass and energy budget

Figure 2.4 presents contour plots of the annual mean mass balance, refreezing and runoff averaged over the full simulation period. Spatial variations in the mass balance (Figure 2.4a)

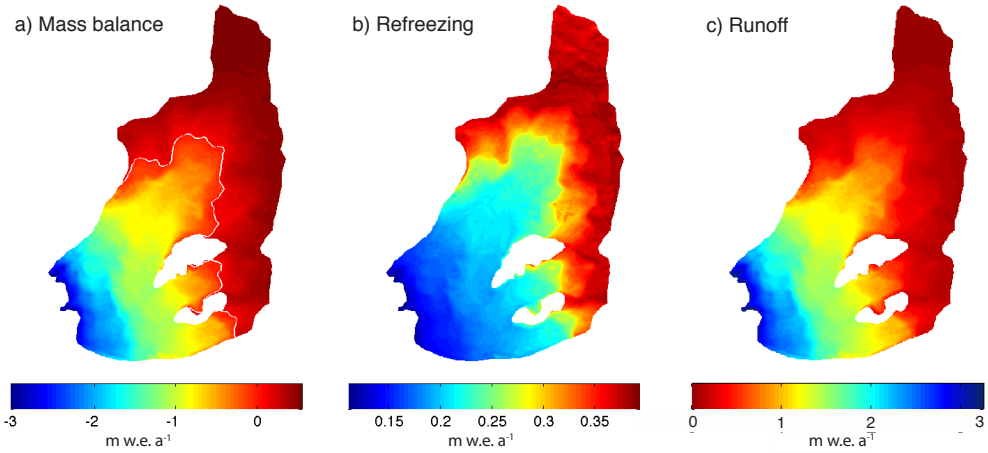

Figure 2.4: *Contour plots of the annual mean mass balance (a), refreezing (b) and runoff (c), averaged over the period 1989-2010. The white line in (a) marks the position of the equilibrium line.*

are to a large extent explained by a combination of altitudinal differences in air temperature and precipitation, spatial gradients in the surface albedo and local variations in the amount of refreezing. Local mass balance variations by topographic effects are only significant in the immediate vicinity of steep valley walls. The equilibrium line altitude over the simulation period is on average 719 m a.s.l.. Over the period spanned by the stake measurements (2006-2010), the estimated observed ELA is $\sim$600 m a.s.l.. This is slightly lower than the simulated ELA over the same period of 631 m a.s.l.. The spatial mean net mass balance for 1989-2010 is -0.39 m w.e. per year. In Section 2.5.3, simulated specific mass balance at the stake sites is validated against observations. As grid boundaries are selected along the ice divide, no ice is assumed to flow into the model domain. In order to compute the actual mass budget of the glacier, the negative contribution of calving should be considered in the mass budget as well. Estimating the mass loss by calving is hindered by the absence of frontal velocity and ice thickness estimates during the active calving phase. Nevertheless, a positive surface mass balance would have been required to balance calving losses, which indicates the glacier experienced substantial thinning over the simulation period.

Refreezing of subsurface water (Figure 2.4b) is most significant in the accumulation zone, where percolating and stored water refreezes down to tens of meters below the surface. In the accumulation zone, low snow temperatures at the start of the melt season increase the potential for refreezing, whereas the amount of melt water production can be a limiting factor. A maximum in the amount of refreezing is found around 1000 m.a.s.l.. Despite high melt rates in the ablation zone, refreezing is limited by the disappearance of snow during the melt season. On average, refreezing contributes 0.27 m w.e. per year to the mass budget. Hence, 25% of all melt water (1.05 m w.e. a^{-1}) and rain water (0.05 m w.e. a^{-1}) at the surface

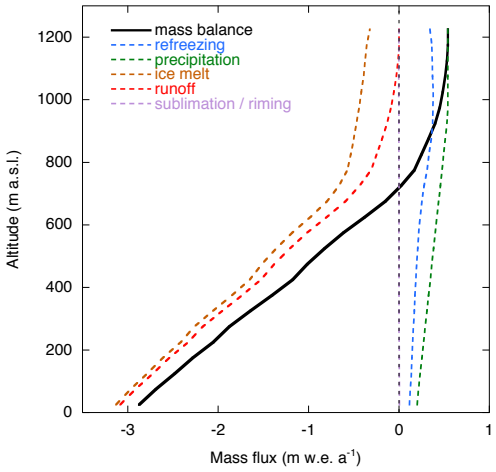

Figure 2.5: *Elevation profiles of the mass balance, refreezing, precipitation, ice melt, runoff and the mass flux by sublimation and riming. Data are divided into 25-m bins and averaged over the simulation period 1989-2010.*

refreezes in the snow pack. Refreezing is equivalent to 69% of snow accumulation during a year. The spatial pattern of runoff (Figure 2.4c) is mainly controlled by the melt rate and the amount of refreezing. In the accumulation zone, a large fraction of the available water at the surface refreezes in the snow pack, thereby limiting the amount of runoff of slush water. Averaged over the glacier, the net runoff is 0.82 m w.e. a^{-1}, implying a total discharge of 1.58×10^8 m^3 a^{-1}.

The surface mass balance is a product of precipitation, runoff and latent transport by sublimation and riming. Figure 2.5 shows elevation profiles of the mass budget and its defining components. The mass exchange with the atmosphere by sublimation and riming is negligibly small, so the sum of precipitation and (negative) runoff determines the mass budget. High up in the accumulation zone, melt occurs while runoff goes to zero, which implies that all melt water refreezes. Precipitation dominates the mass budget at high altitudes, whereas ice melt dominates the mass budget in the ablation zone. The mean altitudinal mass balance gradient in the ablation zone is 4.1 mm w.e. a^{-1} m^{-1}, which is close to the average found for Svalbard by *Hagen et al.* [2003].

Contour-plots of the components that comprise the energy budget are shown in Figure 2.6. The sum of all the incoming and outgoing fluxes, which is equivalent to the energy involved in melting (Figure 2.6a), decreases with altitude and is small in the accumulation zone, although melting occurs even at the highest point on the grid. The net shortwave flux (Figure 2.6b) is the main source of energy and its spatial pattern is to a large extent controlled by the surface albedo. Generally, the effect on the shortwave budget of shading near valley walls is

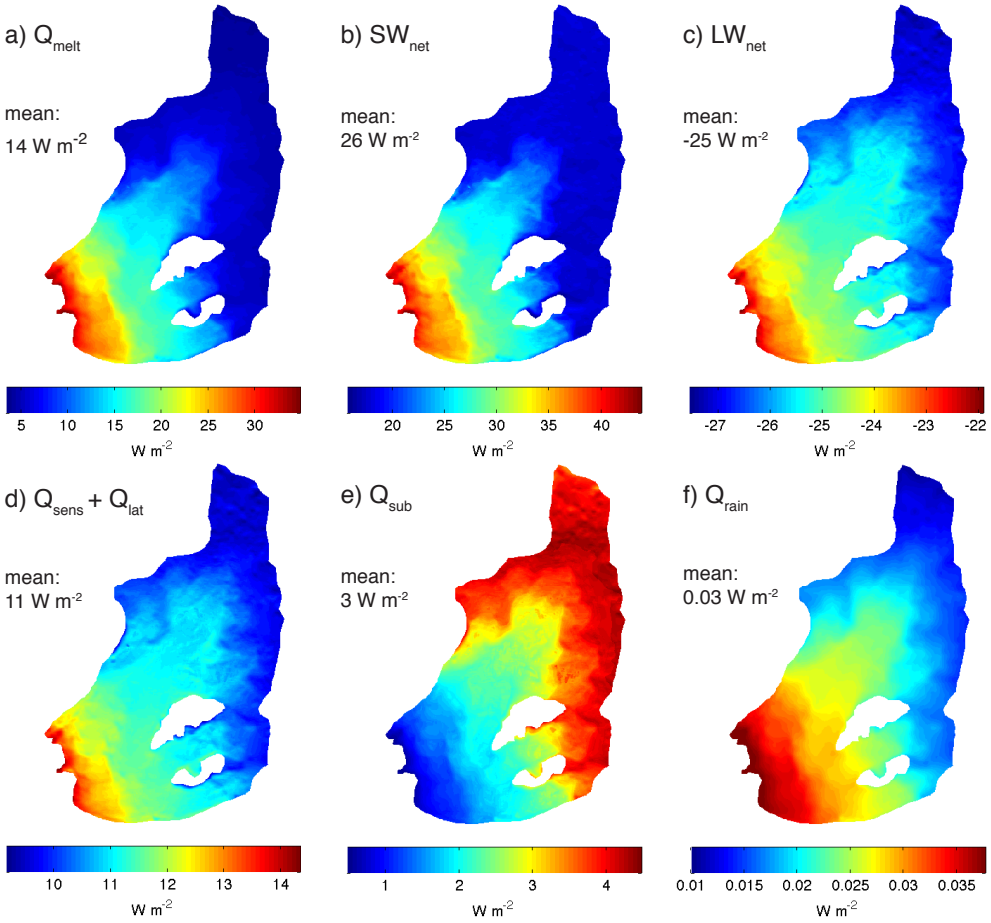

Figure 2.6: *Contour plots of the melt energy (a), net shortwave radiation (b), net longwave radiation (c), turbulent heat transport (d), the subsurface heat flux (e) and the heat supplied by rain (f), averaged over the period 1989-2010.*

relatively small. The net longwave flux (Figure 2.6c) is the main energy sink and is strongly dependent on the temperature deficit at the surface, which increases with altitude. Regarding the turbulent fluxes (Figure 2.6d), the sensible heat flux contributes substantially to the energy budget, whereas the latent heat flux is small. Due to refreezing, the subsurface heat flux (Figure 2.6e) is positive and contributes significantly to the surface heat budget, especially in the accumulation zone where refreezing is most pronounced and surface temperatures are low. Surface heating by rain fall (Figure 2.6f) is of negligible magnitude.

Time-series of the net mass balance, runoff and precipitation are shown in Figure 2.7a. Over the simulation period, two positive mass balance years occurred (1992 and 1996), which are

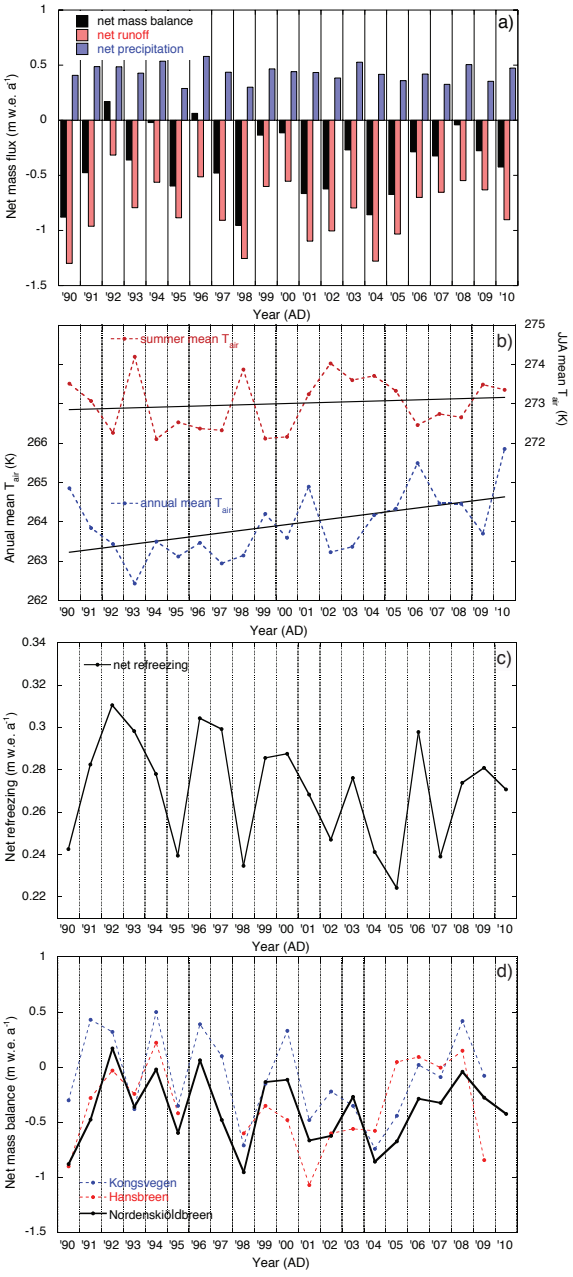

Figure 2.7: *Time-series over the period 1989-2010 of the net mass balance, precipitation and runoff (a), spatially averaged annual and summer (JJA) mean air temperatures (b), net annual refreezing (c), and the net mass balance for Nordenskiöldbreen, Kongsvegen and Hansbreen (d). The years on the horizontal axis represent mass balance years starting at the 1st of October of the preceding year. The location of Kongsvegen and Hansbreen is indicated in Figure 2.1.*

also the years with lowest runoff. The large inter-annual variability is explained by strong year-to-year variations in both summer melt and annual accumulation. The most negative net mass balance of -0.95 m w.e. a^{-1} is found in 1998, which is related to high summer temperatures in combination with limited snow fall during the preceding cold season. Trends in the annual and summer mean temperatures in Figure 2.7b are tested for significance by taking the ratio of regression slope and the standard error of the slope to find t-scores of 2.21 and 0.61 respectively. Consequently, only the trend in annual mean air temperatures since 1989 is significant at a 95% confidence level. This finding is in line with observed seasonal temperature trends at Svalbard Airport since 1912, which reveal a preferred warming outside the summer months [*Hanssen-Bauer et al.*, 2009]. Correlations of -0.66 and 0.64, significant at a 99%-confidence level, exist between net mass balance and summer mean air temperature and annual precipitation, respectively. A correlation of only -0.10 is found between the net mass balance and annual mean temperatures, which demonstrates the insignificance of temperature variations outside the melt season on the mass budget. Winter snow fall is important, owing to both its direct effect on the surface mass budget and the impact on the period of bare ice exposure. Time-series of the annual amount of refreezing in Figure 2.7c reveal a modest year-to-year variability over the simulation period. The variability results mainly from fluctuations in annual snow fall, having a major impact on refreezing in the ablation area, and air temperature, which affects the cold content of the snow pack and the amount of melt available for refreezing in the accumulation zone. Figure 2.7d shows a comparison of the net mass balance time-series with observed mass balance records for Kongsvegen (western Svalbard) and Hansbreen (southern Svalbard), provided by the World Glacier Monitoring Service (WGMS). Correlations of 0.79 and 0.56 are found between the simulated mass balance and records at Kongsvegen and Hansbreen, respectively. The simulated mean mass balance for Nordenskiöldbreen is 0.30 m w.e. a^{-1} lower than observed on Kongsvegen and 0.05 m.w.e. a^{-1} lower than observed on Hansbreen.

2.5.2 Subsurface variables

Figures 2.8a-b show time-series of the vertical temperature and density distribution for the period 1989-2010 at stake site S9, which is located in the accumulation zone (just above the ELA). Furthermore, focussed time-series for the year 2009, additionally showing the irreducible and slush water content, are presented in Figure 2.8c-f. Surface melt percolates into the snow pack and subsequent refreezing heats the snow to melting point in summer. This continues until the percolating water encounters the impermeable ice and starts to form a slush layer. Heat diffuses into the underlying cold ice and after the melt season a cold wave penetrates into the firn pack from above, causing the stored slush water and irreducible water to refreeze gradually. Subsurface temperatures remain at melting point until the water content of a layer is entirely depleted. The inter-annual variability in refreezing at S9 is quite large and determined by both surface melt water production and the cold content of the snow

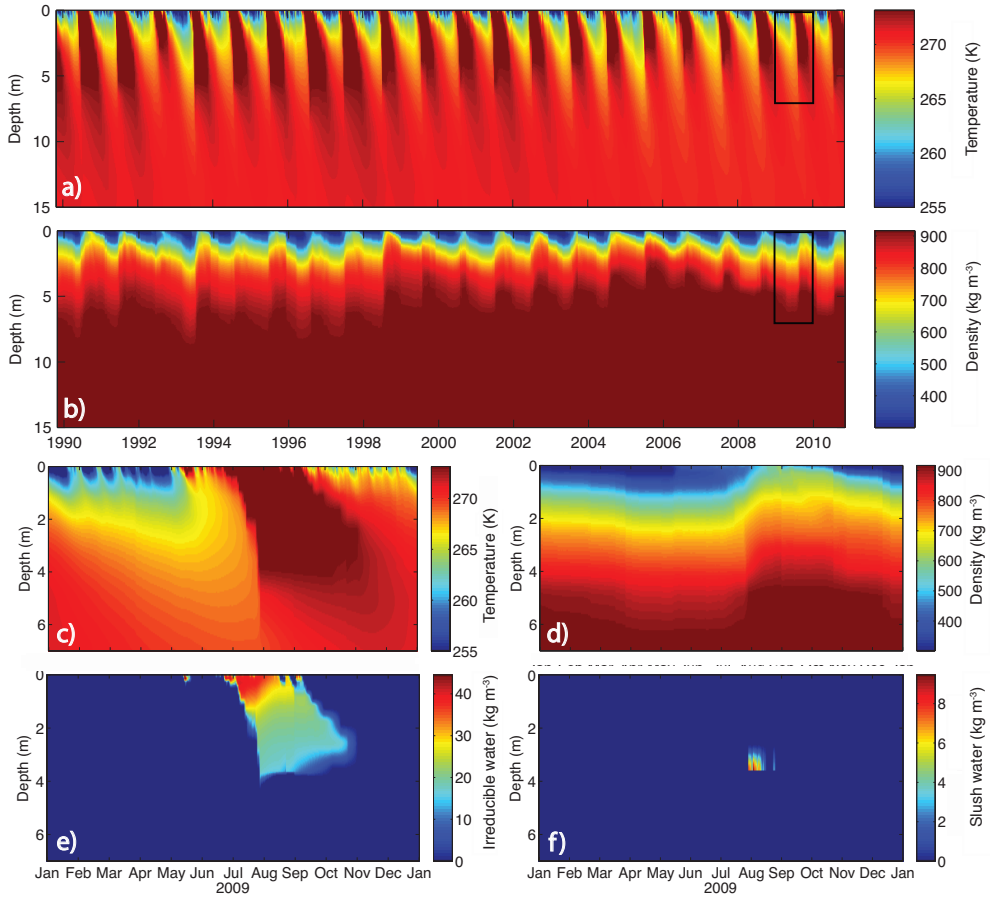

Figure 2.8: *The upper two panels show time-series of the simulated subsurface temperatures (a) and densities (b) at stake site S9 over the period 1989-2010. The lower four panels focus on the temperature (c), density (d), irreducible water (e) and slush water content (f) evolution in 2009 over the time and depth range marked by the black box in the upper two panels.*

pack. Note that the firn depth reaches a minimum between 2004 and 2006, thereby limiting the amount of refreezing during this period. Figure 2.8 also shows the delayed response of ice temperatures with depth to the forcing at the snow-ice interface.

An example of simulated runoff time-series at S6 in the ablation zone for the year 2010 is shown in Figure 2.9. Surface melting starts in early May and until early June all melt water refreezes and runoff is absent. From then on, a slush layer is formed and water runs off gradually until the snow pack has fully melted. Clearly, the snow pack has a buffering effect on the amount of runoff; when the snow pack is all gone, all available water at the surface runs off immediately, inducing a clear diurnal cycle. A snow fall event in August shuts down

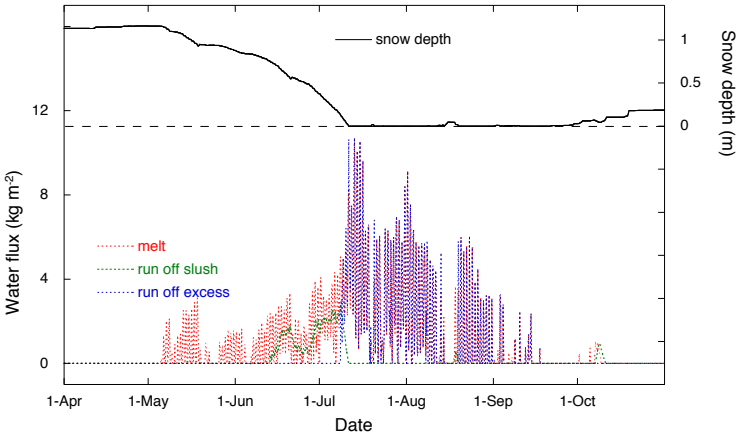

Figure 2.9: *Time-series of the snow depth, melt and runoff at S6 in the ablation zone for the year 2010.*

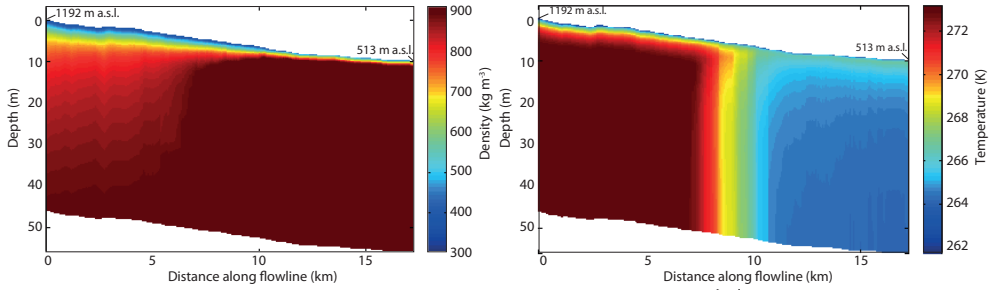

Figure 2.10: *Cross-sectional vertical profiles of the 2009-2010 mean subsurface temperature (left panel) and density (right panel) along the main flow line marked in Figure 2.1. A vertical shift of the profiles is applied to show altitudinal differences along the cross-section.*

ice melt and runoff for several days, which has a remarkable impact on the mass budget. A limited amount of snow fall in summer leads to a major increase in the albedo and thus effectively reduces the amount of absorbed solar radiation and thus melt.

Along the flow line marked in Figure 2.1, vertical profiles of mean subsurface temperatures and densities over the final year of simulation (2009-2010) are presented in Figure 2.10. Around the ELA, a clear transition from cold ice in the ablation area to temperate snow/firn in the accumulation zone is seen. In the accumulation zone, heating by refreezing dominates advection and diffusion of lower surface temperatures at depths >5 m. In the ablation area, refreezing in the shallow snow pack during the melt season raises near-surface temperatures. It should be noted that a zero energy flux at the lower boundary of the vertical domain might be a crude assumption in the ablation area where likely warmer ice gets advected from below.

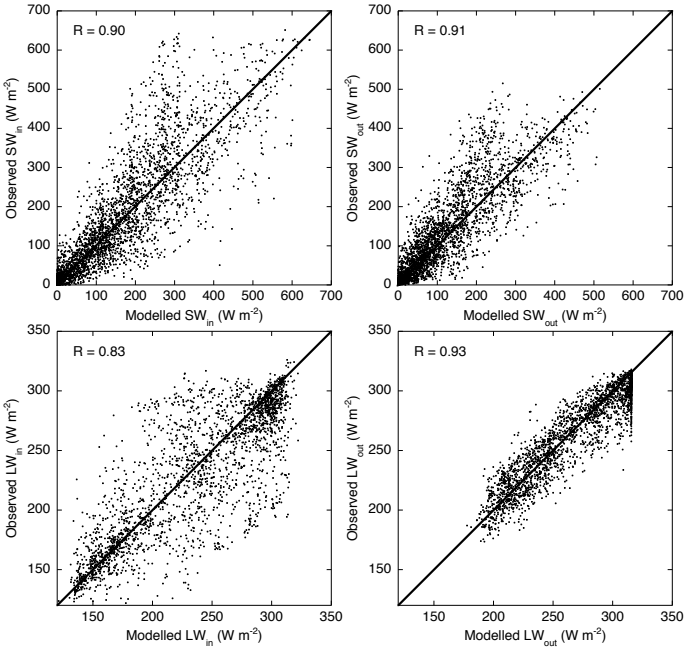

Figure 2.11: *Scatter plots showing observed (3-hourly) vs. modelled incoming solar radiation (a), reflected solar radiation (b), incoming longwave radiation (c) and outgoing longwave radiation (d) for the period from March 2009 to November 2010.*

Note that inclusion of horizontal advection of ice by ice flow would lead to a horizontal shift, increasing with depth, of the vertical profiles in Figure 2.10. A near-surface temperature distribution with temperate ice in the accumulation zone and cold ice near the surface in the ablation zone is typical for glaciers in Svalbard [*Blatter and Hutter*, 1990; *Pettersson*, 2004].

2.5.3 Comparison with observations

As discussed in Section 2.4.4, observed SW_{in}, SW_{out} and LW_{in} at the AWS between March 2009 and November 2010 are used to calibrate modelled fluxes. Scatter plots of these fluxes, presented in Figure 2.11, show a good agreement between the modelled and measured values with correlation coefficients between 0.83 and 0.91. Discrepancies between observed and simulated SW_{in} result mainly from errors in the estimated cloud cover, which also accounts for discrepancies between observed and simulated LW_{in}. Recall that due to data-logger problems we lack observations of longwave fluxes during the melt season. The net shortwave and longwave budgets are on average overestimated by 1.6 W m^{-2} and 1.9 W m^{-2}, respectively. The only non-calibrated flux is the outgoing longwave radiation. Modelled values of LW_{out}

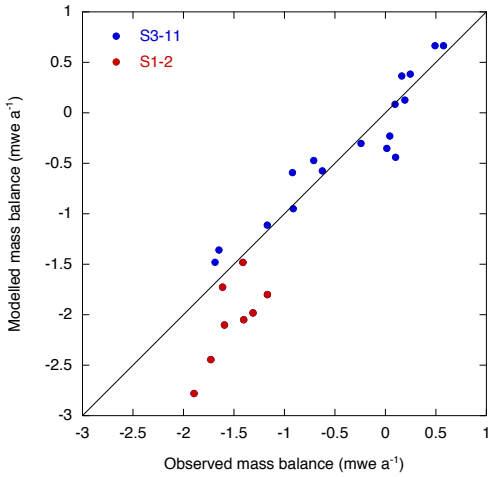

Figure 2.12: *Scatter plot of simulated mass balance values versus mass balance estimates derived from stake height observations over the period 2006-2010 at sites S1-11.*

agree well with observations (R = 0.93), which is an indication that modelled surface temperatures are accurate. Recall that the surface temperature is the only unknown in the energy balance equation.

Validation of the surface mass balance is performed by comparing modelled values to stake observations. As mentioned, the observed surface height variations are converted into mass changes by employing the mean observed snow density in snow pits. Figure 2.12 reveals a good agreement between measured and simulated mass balance values for S3-11. At S1 and S2, the model overestimates mass loss, which could be related to wind-driven snow transport accumulating mass in this area. Figure 2.1 illustrates that, in contrast to S3-11, stakes S1 and S2 are positioned close to the southern edge of the ice grid in the vicinity of steep valley walls. *Berthier et al.* [2010] show that redistribution of snow by wind may lead to accumulation of snow in concave areas near the margins.

Finally, we compare observed snow temperatures and densities in snow pits in spring 2008 and 2009 with simulated values. For this purpose, seven observed vertical profiles in the ablation area are used and vertically averaged values are compared to modelled mean values. Two additional snow pit profiles were available but not used due to a lack of data points (two or less). The mean measured snow temperature of 256.2 K is only 0.5 K lower than the simulated mean. The mean measured snow density of 367 kg m^{-3} is 18 kg m^{-3} higher than simulated. Besides uncertainty in the simulated densification rate, this discrepancy may also be related to an underestimation of the fresh snow density.

Table 2.1: *Overview of the mass balance sensitivity (δMB), refreezing sensitivity (δRE) and runoff sensitivity (δRU) to perturbations of a selection of model parameters. Sensitivities are given in mm w.e. a^{-1}.*

Parameter	Value	+/-	δMB	δRE	δRU
C_b	0.0028	+0.0010	−6.1	−7.0	−2.8
		−0.0010	0.3	7.5	−3.1
γ_p [m/km]	0.370	+0.050	67.2	5.1	33.6
		−0.050	−74.4	−5.9	−40.7
a_{max} [m w.e.]	0.54	+0.10	4.2	0.2	−0.1
		−0.10	−41.7	7.3	−1.0
ε_{cl}	0.990	+0.01	−87.5	−0.6	−85.7
		−0.01	81.0	−0.5	79.1
b	0.447	+0.010	−25.6	−3.0	−24.6
		−0.010	24.6	3.0	23.6
k	0.97	+0.01	−53.3	−0.7	−52.8
		−0.01	50.2	0.5	49.7
ρ_{fs} [kg/m^3]	300	+25	−7.8	2.5	−7.7
		−25	2.3	−4.9	2.2
α_{ice}	0.32	+0.03	24.1	0.1	24.1
		−0.03	−24.3	−0.1	−24.2
α_{fs}	0.87	+0.03	118.0	−0.8	116.1
		−0.03	−138.9	−2.1	−137.2
C_{ro}	1	×2	−0.7	0.8	−0.7
		/2	0.6	−0.6	0.5
$T_{s/r}$ [K]	274.6	+0.5	32.3	1.6	32.2
		−0.5	−40.7	−1.3	−40.6
P_{fs} [mm/hr]	0.04	+0.01	−52.3	−1.5	−51.9
		−0.01	40.9	1.1	40.7

2.6 Sensitivity experiments

Additional experiments are performed to test the model's sensitivity to changes in model parameters (Section 2.6.1), initial conditions (Section 2.6.2) and the climate forcing (Section 2.6.3).

2.6.1 Parameter sensitivity

A set of 5-year runs over the period 2005-2010 is performed to investigate the robustness of the model output to changes in model parameters. An overview of the sensitivity of the mass balance, refreezing and runoff averaged over the glacier to perturbations of selected model parameters is given in Table 2.1. The simulated mass balance and runoff is most sensitive to changes in parameters that affect the net shortwave budget (α_{ice}, α_{fs}, k, γ_p, P_{fs} and $T_{s/r}$) and longwave budget (ε_{cl} and b). The sensitivity to perturbations of the fresh snow albedo (α_{fs})

is particularly high, due to the large relative impact on the net shortwave budget. The amount of refreezing is mainly sensitive to changes in parameters that affect the surface temperature (C_b), snow thickness (γ_p) and snow density (ρ_{fs}). The rate at which slush water runs off is controlled by the parameter C_{ro}, which is a scaling factor for the runoff time-scale. Despite its impact on the runoff rate, perturbing C_{ro} has only a limited effect on the net mass balance, refreezing and runoff. A clear nonlinear response of the mass balance to changes in the maximum accumulation rate a_{max} is explained by a nonlinearity in the area affected by a change in a_{max} (fewer gridpoints towards higher altitudes).

2.6.2 Initialisation sensitivity

The benefit of extensive initialisation is investigated by perturbing initial subsurface temperatures. For this purpose, two simulations over the period 2004-2010 are performed with the initial water content in the snow pack set to zero in both simulations and the subsurface temperature reduced by 3 K in one of the runs. The initial water content has been set to zero to avoid immediate refreezing when lowering subsurface temperatures. Reducing the subsurface temperatures by 3 K increases the mass balance by 27 mm w.e. after 1 year and by 60 mm w.e. between 2-6 years after the start of the experiment. It can be concluded that lowering subsurface temperatures has only a modest but long-term effect on the mass balance, thereby indicating the relevance of proper initialisation for high-precision mass balance modelling.

2.6.3 Climate sensitivity

Statistical downscaling of an ensemble of GCM future climate scenarios for Svalbard has indicated a strong seasonal variability in climate change with more pronounced warming in winter and spring [*Benestad*, 2008; *Førland et al.*, 2009]. We perform one set of runs, with T and P perturbations identical for all seasons, whereas in a second set of experiments perturbations include a seasonal dependence. The degree of seasonal variability in T and P perturbations is derived from projections of T and P changes per season at Svalbard Airport from 1981-2010 to 2071-2100 [*Førland et al.*, 2009], based on the A1b-emission scenario [*IPCC*, 2001]. We compute the relative change per season with respect to the annual mean change leading to scaling factors for projected temperature change in winter, spring, summer and autumn of 1.48, 1.45, 0.39 and 0.68, respectively. Scaling factors for seasonal precipitation change are 1.61 (winter), 1.06 (spring), 1.07 (summer) and 0.27 (autumn).

In order to study the mass balance sensitivity to future changes in climate, we performed multiple runs with perturbed air temperature (T) and precipitation (P) over the period 2000-2010. Experiments with and without seasonally scaled T and P perturbations are performed and mass balance, refreezing and ELA sensitivities are given in Table 2.2. Altitudinal mass balance sensitivity profiles for eight of the seasonally invariant climate change experiments

Table 2.2: *Overview of the mass balance sensitivity (δMB), refreezing sensitivity (δRE) and ELA sensitivity (δELA) to changes in air temperature T and precipitation P. Sensitivities are given in m w.e. a^{-1} for the mass balance and refreezing sensitivity and m a.s.l. for the ELA sensitivity. The non-seasonal δELA in the run with $T+4$ K could not be resolved since the ELA in this scenario is above the highest point on the grid. Mass balance, refreezing and ELA values in the unperturbed climate run are -0.448 m w.e. a^{-1}, 0.259 m w.e. a^{-1} and 724 m a.s.l., respectively.*

Run	No seasonality			With seasonality		
	δMB	δRE	δELA	δMB	δRE	δELA
$T-4$ K	+0.78	−0.046	−402	+0.51	+0.012	−150
$T-3$ K	+0.68	−0.014	−285	+0.41	+0.013	−120
$T-2$ K	+0.52	+0.008	−169	+0.30	+0.011	−86
$T-1$ K	+0.29	+0.013	−90	+0.16	+0.006	−44
$T+1$ K	−0.36	−0.017	+103	−0.21	−0.005	+34
$T+2$ K	−0.79	−0.034	+225	−0.46	−0.009	+102
$T+3$ K	−1.27	−0.047	+366	−0.77	−0.010	+175
$T+4$ K	−1.79	−0.056		−1.18	−0.015	+236
$P-40\%$	−0.55	−0.051	+175	−0.56	−0.053	+183
$P-30\%$	−0.38	−0.033	+134	−0.39	−0.035	+132
$P-20\%$	−0.27	−0.029	+110	−0.24	−0.022	+86
$P-10\%$	−0.11	−0.009	+37	−0.11	−0.010	+38
$P+10\%$	+0.10	+0.008	−19	0.10	+0.009	−17
$P+20\%$	+0.19	+0.015	−48	0.19	+0.016	−45
$P+30\%$	+0.27	+0.022	−75	0.27	+0.024	−73
$P+40\%$	+0.34	+0.028	−100	0.34	+0.030	−94

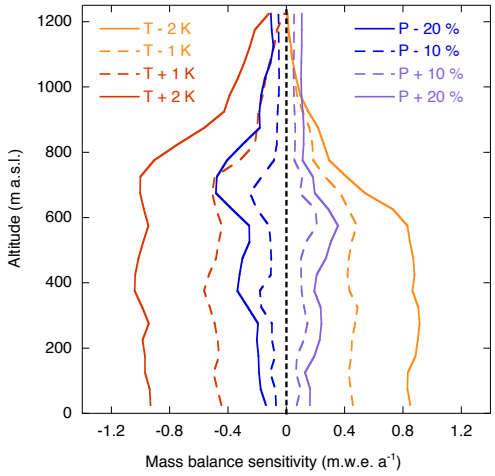

Figure 2.13: *Height profiles of the mass balance sensitivity to seasonally invariant changes in air temperature T and precipitation P.*

are shown in Figure 2.13. Clearly, the mass balance responds nonlinearly to changes in T and P. Figure 2.13 illustrates that the mass balance is mainly sensitive to climate variations in the ablation zone, where changes in the surface albedo in response to temperature changes amplify the melt sensitivity. Climate perturbations lead to a shift in the ELA (Table 2.2) and thus the extent of the ablation zone, thereby explaining the nonlinearity. On average, a 1-K temperature change can be offset by a 32% change in precipitation of similar sign in case of seasonally uniform perturbations. On the other hand, in the case of seasonally scaled climate change, a 1-K change in temperature is balanced by a much smaller change in precipitation of 17% as a result of a lower temperature sensitivity (Table 2.2). Since the mass balance is mainly determined by melt in the summer months (and year-round precipitation), the relatively small increase of summer temperatures in case of seasonally scaled perturbations reduces the mass balance sensitivity in a changing climate. This stresses the importance of considering climate change on a seasonal scale in regions like the Arctic where temperature increase is expected to be less pronounced during the melt season. Note that including seasonality has only a minor effect on the mass balance sensitivity to precipitation perturbations. This is related to the fact that precipitation changes in winter, spring and autumn all affect the snow depth at the start of the melt season in a similar fashion.

Table 2.2 also shows that the amount of refreezing is not very sensitive to changes in temperature and modestly sensitive to changes in precipitation. Changes in precipitation affect the snow thickness and its 'cold content', which is a measure for the refreezing potential. A change in temperature influences the cold content at the start of the melt season and affects the amount of precipitation falling as snow, which leads to an inverse dependence of refreezing on changes in temperature. It should be noted that the mass balance and refreezing effect of longterm trends ($>$10 years) in subsurface conditions is not captured in the relatively short period of the sensitivity experiments.

In order to put the mass balance period 1990-2010 into a longer term perspective, we first used output of additional runs to construct 'seasonal sensitivity characteristics' [SSC, *Oerlemans and Reichert*, 2000]. In these model experiments, running over the period 2000-2010, T or P are perturbed for one season, while unperturbed values are used for the other seasons. In this way the sensitivity of the annual mass balance to seasonal climate variations can be estimated and the sensitivities do not depend on changes during the other seasons (affecting snow depth and subsurface conditions). Figure 2.14 shows the mass balance sensitivity to various seasonal T and P changes. The mass balance sensitivity to T variations is pronounced in summer, whereas in winter the impact is negligible. Seasonal P perturbations have a year-round impact on the annual mass balance. We derived time-series of seasonal mean T and P values from monthly composite time-series at Svalbard Airport [*Hanssen-Bauer et al.*, 2009]. Mean seasonal temperatures and precipitation totals at Svalbard Airport were computed for the period 1912-1989 and 1990-2010 and indicate an increase in annual mean temperature and annual precipitation of 1.8°C and 11 mm (6.2%) respectively. When looking at the seasonal pattern in temperature change, the increase in summer is much less

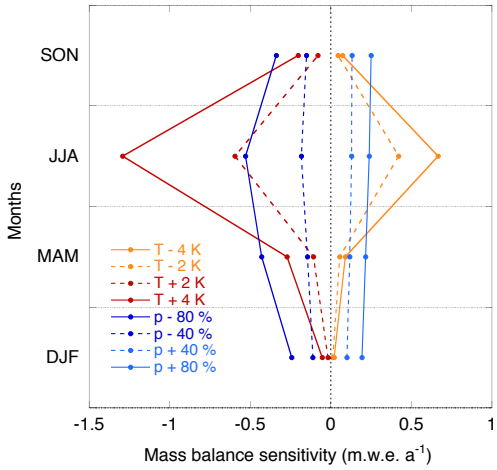

Figure 2.14: *Annual mass balance sensitivity to seasonally perturbed temperatures (red) and precipitation (blue) over the period 2000-2010.*

pronounced (1.0°C) than in winter (2.3°C), which is in line with the aforementioned future projection for this region [*Førland et al.*, 2009]. Nevertheless, from Figure 2.14 it can be concluded that the modest increase in summer temperatures had a larger impact on the mass balance than strongly rising winter temperatures. Furthermore, the decrease in mass balance related to temperature changes is only partly compensated by a precipitation increase. From the above, we conclude that the mass balance was more positive during the period 1912-1989 than during the simulation period (1990-2010). We purposely do not present absolute values or time-series of the mass balance over the period 1912-1989 or in the future, since an evolving ice geometry increases uncertainty in mass balance estimates over longer periods of time. Factors not taken into account include the mass balance - altitude feedback and changes in glacier area and grid orientation (affecting absorbance of solar radiation).

2.7 Conclusions & discussion

In order to simulate the surface mass budget of Nordenskiöldbreen, a distributed surface energy balance model is coupled to a multi-layer snow model. Gridded climate input is generated from regional climate model (RACMO) output in combination with meteorological time-series from Svalbard Airport. An optimal parameter setup is found after calibration with observations on the glacier. Prior to the actual simulation over the period 1989-2010, extensive initialisation of subsurface profiles is performed to find initial subsurface conditions that evolve to observed borehole profiles in 1997.

Over the period 1989-2010, the simulated net surface mass balance is -0.39 m w.e. a^{-1} with extrema of $+0.17$ and -0.95 m w.e. a^{-1} for mass balance years 1992 and 1998, respectively. Year-to-year variations are explained by fluctuations in summer air temperatures and year-round snow fall and variability largely resembles patterns observed on Kongsvegen and Hansbreen. Refreezing of subsurface water amounts to 0.27 m w.e. a^{-1}, which is equivalent to 69% of the annual snow accumulation. The mean simulated ELA is 719 m a.s.l.. The net runoff per unit area is the sum of discharge of slush water and surface runoff and is equal to 0.82 m w.e. a^{-1}. Refreezing delays and reduces runoff especially in the accumulation zone, where refreezing is most pronounced, thereby raising annual mean subsurface temperatures to melting point at depths >5 m. Substantial refreezing in the accumulation zone is linked to low winter/spring temperatures, providing a large cold content in the snow/firn pack at the start of the melt season, in combination with significant melt during the summer season. In the ablation area annual snow accumulation mainly controls the amount of refreezing, inducing a positive trend with altitude.

Modelled energy fluxes are validated against AWS measurements on the glacier and a generally good agreement is found. A comparison of mass balance estimates from stake observations to simulated values shows a good agreement, except for the two lowest stake locations. We hypothesise this is related to the effect of wind driven snow transport, which is not considered by the model. Snow pit profiles in the ablation zone indicate that simulated snow temperatures correlate well with observations, whereas the density is slightly underestimated, which is shown to have a very limited impact on the mass balance.

Parameter sensitivity experiments show a high sensitivity of the mass balance and runoff to parameters affecting the shortwave and longwave radiative budget. The amount of refreezing is sensitive to changes in parameters that affect the surface temperature, snow thickness and snow density. Experiments with perturbed initial subsurface conditions show that the simulated mass balance is modestly affected by changes in initial subsurface temperatures.

Multiple climate perturbation experiments are performed and show a non-linear response of the mass balance, refreezing and runoff to changes in temperature and precipitation. Scaling climate perturbations per season, based on a future climate scenario for Svalbard Airport, reduces the mass balance sensitivity, mainly as a result of less pronounced summer warming. Seasonal sensitivity characteristics confirm that the mass balance is particularly sensitive to temperature changes in summer, whereas the seasonal variability in mass balance sensitivity to precipitation changes is relatively small. Based on computed sensitivities and observed seasonal trends in temperature and precipitation, we conclude that the surface mass balance during the simulation period (1990-2010) was more negative than during the period 1912-1989.

In addition to uncertainty related to inaccurate model physics and parameter calibration, we expect much of the uncertainty in our results can be ascribed to inaccurate climate input. An example of this is the lack of spatial variability in snow accumulation. In the model, the

accumulation rate increases linearly with height (at a rate γ_p) and maximises at a_{max}. In reality, wind patterns will have a major impact on the spatial distribution of accumulation. As discussed by *Berthier et al.* [2010], a redistribution of snow by wind often leads to enhanced thinning rates along the centreline and additional accumulation in concave areas near the margins. Reconstructed accumulation rates along a horizontal profile in the accumulation zone of Nordenskiöldbreen, presented by *Pälli et al.* [2002], confirm that accumulation rates vary significantly over short distances. Regarding air temperature input, a comparison of observed air temperatures at the AWS site and RACMO derived temperatures shows a high correlation and systematic errors for this specific site are found to be small. In absence of sufficient meteorological time-series near the glacier, output of RACMO therefore provides valuable data to force the model. The use of regional climate model output to force mass balance models opens the door to mass balance modelling in areas with a lack of meteorological data from weather stations.

3

Snow accumulation variability along a radar transect on Nordenskiöldbreen

We present an inverse modelling approach to reconstruct annual accumulation patterns from ground-penetrating radar (GPR) data. A coupled surface energy balance - snow model is used to simulate surface melt and the evolution of subsurface density, temperature and water content. The inverse problem consists of iteratively calibrating accumulation, serving as input for the model, by finding a match between modelled and observed radar travel times. Accounting for melt water percolation, refreezing and runoff facilitates accumulation reconstruction in temperate firn. The inverse method is applied to a 16-km long GPR transect on Nordenskiöldbreen, Svalbard, yielding annual accumulation patterns for 2007-2012. Accumulation patterns contain substantial spatial variability, with annual standard deviations of 13 to 27% of the mean, and show considerable year-to-year variations. Compared to traditional methods, accounting for horizontal density variability along the transect is shown to dampen spatial variability in reconstructed accumulation, whereas incorporating irreducible water storage reduces absolute values. Correlating normalised accumulation to terrain characteristics in the dominant wind direction indicates a strong preference of snow deposition on leeward slopes. The impact of small-scale accumulation variability ('noise') on the mean net mass balance is quantified, yielding a negligible impact in the accumulation zone and a negative impact of -0.08 m w.e. a^{-1} in the ablation area.

This chapter is under review as: Van Pelt, W., R. Pettersson, V. Pohjola, S. Marchenko, B. Claremar, and J. Oerlemans (2013a), Inverse estimation of snow accumulation variability along a snow radar transect on Nordenskioldbreen, Svalbard, *submitted to Journal of Geophysical Research: Earth Surface*

3.1 Introduction

Understanding the processes that determine variability of snow accumulation in space and time is of great importance for both mass balance modelling as well as interpretation of local mass balance measurements and ice core derived accumulation rates. Spatial variability in accumulation not only induces local variations of the surface mass budget, it also affects the area-averaged surface mass balance due to the non-linear response of the mass balance to changes in accumulation. Glacier mass balance models, requiring accumulation input, usually rely on interpolated local observations [e.g., *Klok and Oerlemans*, 2002; *Reijmer and Hock*, 2008, Chapter 2] or low-resolution climate model output [e.g., *Reichert et al.*, 2001; *Rye et al.*, 2010], thereby ignoring the role of small-scale accumulation variability.

Spatial variability in snow accumulation is controlled by both local variability in precipitation as well as redistribution of the snow by wind. In mountainous regions, on a larger scale precipitation variability has been linked to changes in altitude [e.g., *Sevruk*, 1997], whereas on a smaller scale variations in local vertical wind speeds associated with flow divergence/convergence become significant [*Lehning et al.*, 2008; *Dadic et al.*, 2010; *Mott et al.*, 2010]. The uplift of already deposited snow by wind depends on the local wind speed and direction relative to the ground, which is known to vary significantly in space due to undulations in the terrain. Slopes directed towards the wind suffer from erosion, whereas deposition occurs in the lee of undulations [*Liston and Sturm*, 1998; *Clifton and Lehning*, 2008]. Modelling efforts to simulate the redistribution of snow by wind with snow models indicate the necessity of detailed modelling of local wind fields and snow drift processes [*Mott et al.*, 2010; *Lehning et al.*, 2008], which is complex and computationally expensive. Other modelling attempts rely on parameterisations built on correlations between snow deposition and terrain-based parameters [*Gascoin et al.*, 2013; *Liston et al.*, 2007].

Observational data, providing constraints on spatial accumulation variability, are valuable for validation of snow model output, as well as to improve our understanding of processes involved in shaping the snow cover. While ice-cores provide point estimates of temporal accumulation variability [e.g., *Pohjola et al.*, 2002a; *Bales et al.*, 2009], GPR has been extensively used to reconstruct spatial accumulation variability along radar transects in Antarctica [e.g., *Sinisalo et al.*, 2003; *Frezzotti et al.*, 2007; *Fujita et al.*, 2011], Greenland [e.g., *Kanagaratnam et al.*, 2004; *Dunse et al.*, 2008; *Miège et al.*, 2013], the Alps [*Machguth et al.*, 2006] and Svalbard [*Pälli et al.*, 2002; *Taurisano et al.*, 2007]. In the accumulation zone of a glacier enhanced crystallisation near a summer surface, related to melt-freeze cycles, vapor transport and radiation transfer, produces annual layers with elevated density in the firn pack [*Colbeck*, 1986], associated with a high reflectivity of the GPR signal [*Kohler et al.*, 1997]. Accretion on top of these elevated density layers as a result of refreezing of percolating melt water in subsequent years, may further enhance the density contrast [*Dunse et al.*, 2008]. These highly-reflective layers are referred to as internal reflection horizons (IRHs). The observed two-way travel time (TWT) of the radar signal traveling between the surface and an

IRH depends not only on the depth of the IRH, but also on the electric permittivity of the medium. In a cold firn pack, the electric permittivity is determined mainly by the density of the firn, and empirical relations have been developed relating TWTs to firn density and depth [*Robin et al.*, 1969; *Tiuri et al.*, 1984; *Kovacs et al.*, 1995]. Unfortunately, information about vertical densities is usually limited to a few point measurements from firn core profiles and do not reasonably capture spatial variability along the radar transect. In temperate firn, the presence of water, stored in pore spaces in the firn, significantly increases the electric permittivity [*Looyenga*, 1965; *Waldner et al.*, 2001; *Stacheder*, 2005]. Hence, information on the vertical water content is required when converting TWTs in temperate firn into annual layer masses [*Pettersson et al.*, 2004].

Inverse methods have regularly been applied in the field of glaciology to determine model parameters from observations. Inverse methods can effectively be used to indirectly obtain information about variables that are not well constrained by measurements, including basal slipperiness, basal topography and/or ice viscosity [e.g. *Joughin et al.*, 2004; *Gudmundsson and Raymond*, 2008; *Arthern and Gudmundsson*, 2010, Chapter 5]. The concept of inverse estimation of accumulation from radar layering has previously been illustrated in an ice dynamical framework by *Waddington et al.* [2007] and *Steen-Larsen et al.* [2010], who inversely determined longterm mean accumulation along a transect in Antarctica, using a forward model to describe ice flow and data of a deep isochrone in an ice-penetrating radar profile.

In this study, we present a novel inverse approach to extract spatial and temporal accumulation variability from GPR data. A coupled surface energy balance - snow pack model computes surface melt and subsequent percolation, storage, refreezing and runoff of water in order to simulate the subsurface evolution of density, temperature and water content. Accumulation, serving as input for the coupled model, is iteratively adjusted to find a match between modelled and observed TWTs. The method is applied to a GPR data-set, obtained along a transect on Nordenskiöldbreen, Svalbard. Selection of annual IRHs allows reconstruction of accumulation per year between 2007 and 2012. The reconstructed accumulation variability along the transect forms the basis for a further analysis of the pattern in relation to terrain characteristics and wind, as well as a discussion and quantification of the negative impact of short-scale accumulation variability on the overall surface mass budget.

In contrast to traditional methods, the firn water content and density distribution is explicitly modelled along the transect, which is shown to have a substantial impact on reconstructed accumulation. Additionally, with the use of the inverse method post-depositional processes (melt, refreezing and runoff) are taken into account, inducing discrepancies between accumulation and mass stored in annual layers, i.e. between two IRHs. Traditional methods only extract annual layer mass, implying substantial errors in accumulation estimates in areas with significant melt percolation, refreezing and runoff.

Our main objective in this work is to reconstruct and analyse spatio-temporal accumulation

variability on an Arctic glacier from GPR data. A brief description of the study area is given in Section 3.2. In Section 3.3, we present the GPR data, the inverse approach and discuss relevant features of the coupled model. Output of model sensitivity experiments is discussed in Section 3.4. We present, validate and analyse reconstructed accumulation in Section 3.5.

3.2 Study area

Nordenskiöldbreen is a tidewater glacier in central Svalbard, connected to a large ice plateau, Lomonosovfonna (Figure 3.1). The glacier covers an altitudinal range from sea level to $\sim$1200 m a.s.l. and flows into the Adolfbukta fjord, where the glacier front is actively calving along part of its width. Continuous GPS data reveal annual mean ice velocities up to $\sim$60 m per year in steeper parts and decreasing velocities towards the ice plateau [*Den Ouden et al.*, 2010]. Annual mean temperatures rising at a rate of 0.22 K per decade since the start of the instrumental record at Svalbard Airport in 1912 [*Førland et al.*, 2009] have enhanced surface ablation and explain the observed ongoing retreat of the glacier tongue since the end of the 19th century [*Plassen et al.*, 2004].

In May 1997, a 120-m deep ice core was drilled on top of the Lomonosovfonna ice plateau, providing a record of accumulation back to 1598 AD [*Pohjola et al.*, 2002a, Chapter 5]. A previous study by *Pälli et al.* [2002], using low-frequency GPR data from the upper accumulation zone (above 1000 m a.s.l.) on Nordenskiöldbreen, discusses longterm trends in accumulation between 1963-1997. In contrast to *Pälli et al.* [2002], the GPR transect in this study covers not only the upper part of the accumulation area, but also lower parts of the accumulation zone, subject to significant refreezing and runoff, as well as part of the ablation area.

3.3 Data & methods

3.3.1 GPR

On 17 April a GPR profile was gathered along a 16-km transect of Nordenskiöldbreen using a Malå ProEx impulse GPR system with a 500 MHz antenna (Figure 3.2). Traces were collected every 0.3 seconds and each trace was stacked 8 fold. The antenna was dragged $\sim$5 m behind a snowmobile at a speed of $\sim$10 km hr^{-1} giving a trace spacing of 0.8 m. The GPR transect is located along the main flow line, spanning from 1198 to 550 m a.s.l. (Figure 3.1), and is gently sloping with a mean and maximum slope of 2.4° and 5.7° respectively. The profile was positioned using kinematic carrier-phase differential GPS mounted on the snowmobile. The position of the GPR antenna was determined by interpolation along the

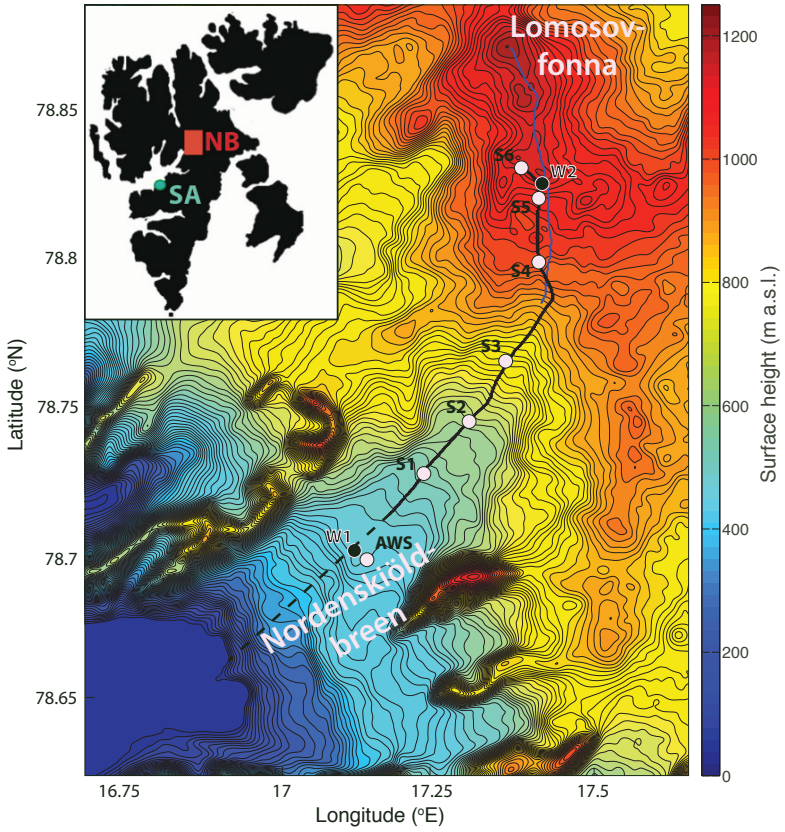

Figure 3.1: *Contour map of Lomonosovfonna and Nordenskiöldbreen. Height contours come from a DEM, gathered in 2007 as part of the SPIRIT project: SPOT 5 stereoscopic survey of Polar Ice: Reference Images and Topographies [Korona et al., 2009]. The inset map shows the position of Nordenskiöldbreen (NB) and Svalbard Airport (SA) on the Svalbard archipelago. The black line marks the position of the GPR profile collected in April 2012. The blue line indicates the position of the GPR data collected by Pälli et al. [2002]. Snow pit profiles obtained in April 2011 and 2012 are labeled S1-S6 and the position of the automatic weather station is marked (AWS). Continuous GPS measurements at S1-S5 provide surface velocity estimates. A shallow ice/firn core has been drilled on 13 April 2012 on the ice plateau near S6. W1 and W2 mark the position of simulated wind fields with the atmospheric model WRF for 2009-2010, further discussed in Section 3.5.6. The dashed black line marks the extended transect used to quantify the impact of spatial accumulation variability on the mass balance in Section 3.5.7.*

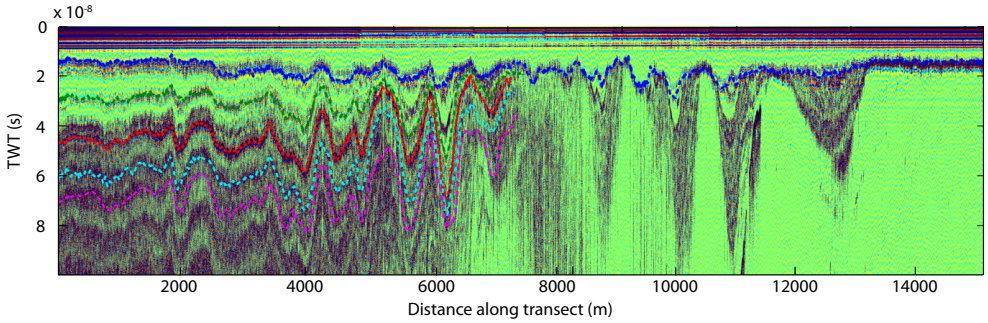

Figure 3.2: *GPR radargram along the transect. Selected IRHs are indicated by the coloured dashed lines [2011 = dark blue, 2010 = green, 2009 = red, 2008 = light blue, 2007 = magenta].*

travelled trajectory. The horizontal and vertical accuracy of the antenna position is estimated to be less than 0.1 m.

Processing of the GPR profile includes band-pass filtering to remove high frequency noise, applying a SEC gain function to compensate for attenuation and geometrical spreading of the radar signal and application of a normal-move-out to compensate for antenna-offset. Continuous layers of high reflectivity (IRHs) were manually picked. The accuracy of picking of the IRHs TWT was estimated at 1.1×10^{-9} s based on repeated picking of the IRHs. Starting from the highest point on the grid, five IRHs could be traced with confidence continuously for the first 7.3 km of the GPR transect. For the remaining part of the profile (in the lower accumulation and ablation area) excessive signal diffusion and/or absence of a firn pack enabled tracing of only the uppermost IRH.

Based on the distinct and clear character if the IRHs we assume that they are annual rather than multi- or intra-annual [*Spikes et al.*, 2004; *Eisen et al.*, 2006; *Miège et al.*, 2013]. However, there is an uncertainty in the annual character of the picked IRHs [*Brown et al.*, 2011] and this will be validated and discussed in Section 3.5.3.

3.3.2 Subsurface data

For validation purposes, snow pit profiles obtained during field campaigns in April 2011 and 2012, as well as data from a 12-m shallow firn-core, drilled near the start of the transect (S6) in April 2012, were employed (Figure 3.1). Snow pits were dug at multiple sites along the transect in 2011 (S4 and S6) and 2012 (S1, S2, S3 and S5). Modelled vertical temperature and density profiles, as well as snow mass, are validated against observations in Section 3.5.3.

3.3.3 Coupled model

We use a coupled surface energy balance - snow pack model to simulate surface melt and subsequent percolation, storage, refreezing and runoff of melt water. Here, we give only a brief description of relevant model features. For a more elaborate overview of both the surface energy balance model and the multi-layer snow model, as well as the meteorological input, the reader is referred to Chapter 2 and references therein. The surface energy balance model explicitly computes all the energy fluxes (i.e. short-wave, long-wave, turbulent and subsurface heat fluxes) and solves the surface energy budget for the surface temperature:

$$Q_m = Q_s + Q_l + Q_t + Q_r + Q_g \,, \tag{3.1}$$

where Q_m, Q_s, Q_l, Q_t, Q_r and Q_g denote the melt energy, short-wave radiative flux, long-wave radiative flux, turbulent heat flux, heat supplied by rain and the subsurface heat flux, respectively. A bisectional root-finding method is used to solve Equation (3.1) for the surface temperature. The surface temperature cannot exceed the melting point of ice, in which case excess energy is converted into melt. Meteorological input comes from two grid points of the regional climate model RACMO (air temperature, pressure and specific humidity) and data from a weather station at Svalbard Airport (precipitation and cloud cover), all down-scaled to the 3-hour model resolution [Chapter 2]. The surface model computes snowfall, rainfall, melt and surface temperature, serving as an upper boundary forcing of the subsurface module, which tracks the percolating melt/rain water in the snow/firn pack, while evolving subsurface densities, temperature and water content. Percolating water may refreeze, run off or it may be stored as either irreducible water or as slush water on top of the impermeable ice.

The time-evolution of subsurface temperatures is determined by the thermodynamic equation describing local heating through heat diffusion and refreezing:

$$\rho c_p(T)\frac{\partial T}{\partial t} = \frac{\partial}{\partial z}\left(\kappa(\rho)\frac{\partial T}{\partial z}\right) + \frac{RL}{d} \,, \tag{3.2}$$

where T is the layer temperature, ρ the layer density, $c_p(T)$ the specific heat capacity, $\kappa(\rho)$ the effective conductivity, R the refreezing rate, L the latent heat of fusion and d the layer thickness. Subsurface densities evolve according to the densification equation, describing local density variations induced by gravitational packing $G(\rho, T)$ and refreezing:

$$\frac{\partial \rho}{\partial t} = G(\rho, T) + \frac{R}{d} \,. \tag{3.3}$$

As water percolates in the snow/firn, a small amount of water is held by capillary forces and is referred to as irreducible water. Additionally, when percolating water reaches the impermeable ice, it accumulates on top of the ice, filling the remaining pore space, hence forming a slush layer. Slush water is set to runoff gradually, whereas in case bare ice is exposed, runoff

occurs instantaneously [*Reijmer and Hock*, 2008]. We extended the subsurface model to track the depth of annual summer surfaces, which are defined when the surface height reaches a minimum during the melt season. Summer surface depths are hence modelled independently of the vertical density profile. A limitation of the firn model in this work and other studies is the lack of accounting for variability in vertical propagation speed of the percolating water. In the model vertical water transport is instantaneous and fluxes are controlled by the rate of refreezing and capillary space in different layers. Implementing realistic vertical water transport velocities requires modelling micro-scale processes like piping and impedance of water flow on top of ice lenses [e.g. *Pfeffer and Humphrey*, 1998; *Bell et al.*, 2008], which is currently not realistically feasible given the lack of observational constraints and physics to describe these processes. By ignoring variability in water transport rates we do not model associated micro-scale variability in refreezing rates affecting the density distribution within annual layers.

The subsurface model contains a total of 140 layers, with a grid spacing in the upper 10 m of 0.1 m and a spacing of 1.0 m in the lower 40 m of the vertical grid. In the event of mass addition or removal at the surface, due to melt, accumulation or sublimation/riming, vertical model layers are updated accordingly. Fresh snow is added to the surface with a density set to the observed mean near-surface density (344 kg m^{-3}) in the upper 20 cm of all the snow pits. Calibration of other uncertain model parameters is discussed in Chapter 2.

From simulated subsurface density, water content and summer surface depths, modelled TWTs of a radar signal are computed using a conversion relation. The two-way travel time t of an electromagnetic wave through a medium depends on the travel distance as well as the effective electric permittivity of the medium ε:

$$t = \frac{2D\sqrt{\varepsilon}}{c}\,, \tag{3.4}$$

where D is the depth of the reflective layer and c the speed of an electromagnetic wave in vacuum. The effective electric permittivity ε of a medium consisting of a mixture of water and snow can be determined from [*Looyenga*, 1965; *Stacheder*, 2005]:

$$\varepsilon = \left(F\varepsilon_f^{\frac{1}{3}} + W\varepsilon_w^{\frac{1}{3}}\right)^3\,, \tag{3.5}$$

where ε_f and ε_w are respectively the relative permittivity of firn and water, whereas F and W are respectively the firn and water volume fractions. Whereas a constant value has been used for the relative permittivity of water $\varepsilon_w = 89$ [*Stacheder*, 2005], the effective permittivity of dry firn depends on the air content and has been empirically related to the firn density by *Kovacs et al.* [1995]:

$$\varepsilon_f = \left(1 + 0.845\frac{\rho}{\rho_w}\right)^2\,, \tag{3.6}$$

where ρ_w denotes the density of water (1000 kg m^{-3}). Combining Equations (3.4)-(3.6), the modelled TWT of a radar signal, traveling from the surface to a certain summer surface and back, is determined from modelled vertical densities, liquid water content and the simulated depth of the tracked summer surface.

3.3.4 Iterative inverse approach

The coupled model is used as a forward model in an inverse approach, aiming to find a match between modelled and observed TWTs of the selected annual IRHs. This is done by iteratively adjusting surface accumulation, serving as input for the coupled model. The GPR transect is projected onto the distributed model grid with a 40 m resolution. Since no horizontal coupling between grid points is included in the coupled model, reconstruction of annual accumulation can de done independently for every grid point along the transect.

Intuitively, one might consider starting the reconstruction of surface accumulation with the oldest annual layer, using the deepest two IRHs to calibrate modelled accumulation between the formation of the two summer surfaces. Consecutively, more recent years could be reconstructed, hence going forward in time. Such an approach would function in terms of convergence, but introduces (unnecessary) uncertainty, related to the fact that future melt, percolation and refreezing affect the mass of an annual layer after it has been formed. Since the amount of internal accumulation (refreezing) depends on future surface accumulation, which is in this approach still unknown, this introduces uncertainty in the accumulation reconstruction. To circumvent this problem, we apply a backward reconstruction, which implies reconstructing accumulation associated with the most recently formed layer first, and successively reconstruct older IRHs, hence effectively going back in time. By doing so, future accumulation and melting/refreezing is already known when reconstructing accumulation associated with an older layer.

Reconstructed annual accumulation does not only depend on what happens in subsequent years, but is also slightly affected by the history of the firn pack. For example, heat exchange with deeper layers is affected by the temperature and density profile in underlying firn. Proper spin-up of the firn pack is therefore desired to initialise firn properties. Therefore, the coupled model is run since 1989 till the start of the reconstruction experiment (between 2007 and 2011), forced with accumulation time-series from Svalbard Airport, scaled such that the annual mean accumulation increases linearly with altitude from 0.19 m w.e. a^{-1} at sea level (equivalent to the Svalbard Airport mean for 1989-2010) to 0.61 m w.e. a^{-1} above 850 m a.s.l. (equivalent to the mean maximum annual accumulation found by *Pälli et al.* [2002] for 1963-1999). The relative insensitivity of reconstructed accumulation to initialisation is quantified and discussed in Section 3.4. Firn properties at the start of the spin-up in 1989 were estimated from initialised profiles presented in Chapter 2.

The following steps were taken for every grid point along the transect and every annual layer

(between two IRHs) to reconstruct surface accumulation. Temporal variability of accumulation is taken directly from the Svalbard Airport record, whereas absolute values are scaled per year with the inverse approach. Starting with the reconstruction of the top layer (2011-2012), model iterations run from 1 July 2011 to 17 April 2012, first with an initial guess for the accumulation. Starting at 1 July is early enough to simulate the formation of the summer surface, which usually forms towards the end of the melt season. After every model iteration, a root-finding algorithm is applied to obtain a new annual accumulation estimate. The root-finding method used, called the 'false-position method', uses information of the misfit (modelled minus observed TWT) for older test values of accumulation to estimate a value for the accumulation for the next iteration [*Press et al.*, 1992]. Basically, in case of a negative misfit (m_-) for a low test value of accumulation (a_-) and a positive misfit (m_+) for a high test value (a_+), a new test value (a_{new}) can be computed by drawing a straight line between m_+ and m_- and determining the root of this line. Hence, the new accumulation is computed according to:

$$a_{new} = a_- - \frac{m_-(a_+ - a_-)}{m_+ - m_-} \,. \tag{3.7}$$

The method converges indefinitely, since the TWT of an IRH increases continuously with accumulation. Hence, only one solution for accumulation exists for which modelled and observed TWTs are in agreement. In case the TWT (and hence the misfit) would depend linearly on accumulation, only one step would be sufficient to achieve convergence. In all experiments, we stop iterating after 7 iterations, which is enough to achieve a mean accuracy of the reconstructed accumulation of 0.04 mm w.e. a^{-1}. After reconstructing the uppermost layer, reconstruction of the second layer (2010-2011) involves running the model between 1 July 2010 and 17 April 2012, with previously determined accumulation between 1 July 2011 and 17 April 2012 and iteratively updated accumulation between 1 July 2010 and 1 July 2011. In the same spirit, annual accumulation associated with the third, fourth and fifth layer has been reconstructed. In the end, we have (scaled) surface accumulation estimates for all grid points and every year (starting 1 July), as well as dates of summer surface formation. From this, we compute annual surface accumulation between the formation of two IRHs. In the remainder of this chapter, annual accumulation is defined over the period between the formation of two summer surfaces.

3.4 Parameter sensitivity

All uncertainties in the inverse approach related to model initialisation, uncertain modelling physics, inaccurate conversion of subsurface properties into TWTs and uncertainty in the climate forcing contribute to the total error in the reconstructed accumulation patterns. Here we test the robustness of the reconstructed accumulation to changes in parameter settings. We compare mean accumulation for a one-year (2009-2010) and a five-year period (2007-2012). Results are shown in Table 3.1.

Table 3.1: *Reconstructed accumulation sensitivity (ΔAcc.) for 2007-2012 and 2009-2010 after perturbations of the initialisation accumulation (A_{init}), firn permittivity (ε_f), maximum pore space (m_{liq}), fresh snow density (ρ_f), vertical grid spacing (Δz), air temperature (T_{air}) and reference date (t_{ref}). ΔAcc. is given in m w.e. a^{-1}.*

Parameter	Unit	Standard value	+/−	ΔAcc. (2007-2012)	ΔAcc. (2009-2010)
A_{init}	m w.e. a^{-1}	$0.45-0.61$	$+0.10$	$+0.000$	-0.001
			-0.10	-0.001	-0.001
ε_f	-	Eq. 3.6	$+10$ %	-0.029	-0.029
			-10 %	$+0.030$	$+0.029$
m_{liq}	-	0.0143	$+10$ %	-0.004	-0.007
			-10 %	$+0.004$	$+0.005$
ρ_f	kg m^{-3}	344	$+25$	$+0.026$	$+0.022$
			-25	-0.028	-0.029
Δz	m	$0.1-1.0$	$\times 2$	-0.004	$+0.004$
			$/2$	$+0.003$	-0.002
T_{air}	K	RACMO output	$+0.5$	$+0.022$	$+0.022$
			-0.5	-0.019	-0.018
t_{ref}		1 July	-90 days	-0.000	-0.004

Perturbing the spin-up accumulation pattern homogeneously by 0.10 m w.e. a^{-1} is shown to have only a minor impact (up to 0.001 m w.e. a^{-1}) on reconstructed accumulation, indicating a small effect of firn properties below the layer(s) to be formed. This additionally motivates the use of the backward reconstruction, rather than going forward in time introducing large errors related to unknown future accumulation.

Conversion of simulated subsurface densities and summer surface depths into TWTs relies on a empirical relation developed by *Kovacs et al.* [1995], based on Antarctic firn measurements. Uncertainty in the associated firn permittivity ε_f (Equation (3.6)) directly affects computed TWTs and indirectly accumulation, which is calibrated to minimise the misfit with observed TWTs. We find that perturbing ε_f by 10% induces a substantial error of 0.030 m w.e. a^{-1} (3.8%) in accumulation. Although there is no indication that the mixing model, described by Equations (3.5) and (3.6) is not applicable to the firn pack in this study, different mixing models exist, yielding slightly different relations between permittivity, firn density and water content. A detailed comparison of mixing models and their impact on computed TWTs would be needed to estimate uncertainty involved in the choice of a mixing model.

Another empirical relation has been used to compute the maximum pore space in the firn pack available for storage of irreducible water [*Schneider and Jansson*, 2004]. A 10%-perturbation of the maximum pore space, affecting the water content distribution in the firn pack is shown to have a small impact on reconstructed accumulation of on average 0.005 m w.e. a^{-1} (0.5%).

The fresh snow density ρ_f directly affects the mean density of the firn pack and hence modelled summer surface depths, thereby indirectly influencing reconstructed accumulation. Per-

turbing ρ_f by 25 kg m^{-3} induces a significant change in accumulation of on average 0.027 m w.e. a^{-1} (3.4%).

Whereas accumulation input is calibrated, errors in the air temperature input still lead to uncertainty in the simulated surface energy budget, melt, firn properties and summer surface depths, thereby affecting reconstructed accumulation. In Chapter 2, we describe the use of regional climate model (RACMO) output to construct height-dependent 3-hourly temperatures and show the good agreement of model temperatures in comparison to independent AWS data. A mean bias between modelled and observed values of 0.4 K was found. Perturbing air temperature in the model by 0.5 K results in an average shift in reconstructed accumulation of 0.020 m w.e. a^{-1} (2.5%).

The chosen starting date (1 July) of the iterations influences the temporal accumulation distribution (rather than the total accumulation) between the formation of two IRHs. A sensitivity experiment with the reference date perturbed by 90 days illustrates the minor influence of the choice of reference date on the accumulation reconstruction.

Finally, sensitivity experiments with perturbed vertical grid resolution, multiplied and divided by a factor two, are performed. Results show the relative insensitivity of reconstructed accumulation on the vertical grid resolution. These results indicate there is little improvement to be gained by a further decrease of the vertical grid spacing, which would go at the expense of an increase in computational cost.

3.5 Results & discussion

3.5.1 Annual accumulation patterns 2007-2012

Applying the inverse approach results in annual accumulation patterns back to 2007 for a total of 495 grid points along the GPR transect. Figure 3.3 shows reconstructed accumulation patterns per year (panels a-e) and a composite pattern (panel f). For $x > 7300$ m, where x is the distance along transect, only one IRH could reasonably be identified in the collected GPR data (Figure 3.2). Hence only reconstructed accumulation for 2011-2012 covers the full extent of the transect. Comparing annual patterns reveals distinct year-to-year variability in the mean, slope (mean horizontal gradient) and standard deviation. Reconstructed annual mean values range from 0.66 to 0.88 m w.e. a^{-1} with a 2007-2012 average of 0.78 m w.e. a^{-1}. We find substantial year-to-year discrepancies in the degree of spatial variability with standard deviations ranging from 0.103 (2008-2009) to 0.217 m w.e. a^{-1} (2009-2010), corresponding to 13 to 27% of annual mean accumulation. A minimum accumulation of 0.35 m w.e. a^{-1} is found for 2007-2008, whereas a maximum of 1.51 m w.e. a^{-1} occurred in 2010-2011. Despite altitude decreasing with distance along the transect (spanning an altitudinal range of $\sim$550-1200 m a.s.l.), we find very weak trends in both the 2011-2012 pattern and the 2007$-$2012 mean. Spatial slope of the annual patterns varies substantially in both

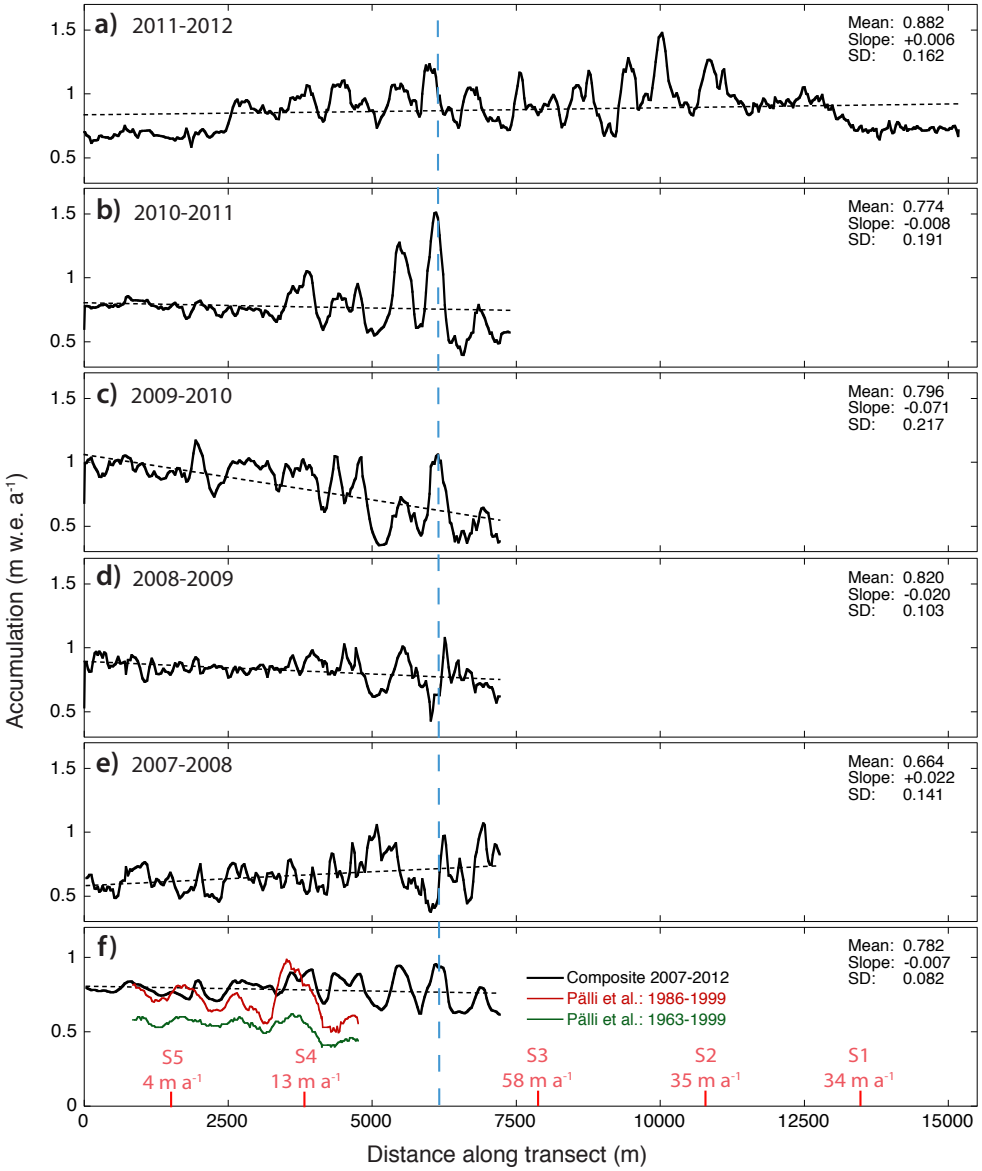

Figure 3.3: *Reconstructed accumulation distributions for 2007-2012 (a-e). In panel f), a composite accumulation record is shown and compared to reconstructed accumulation variability by Pälli et al. [2002] (Figure 3.1). Annual mean observed surface velocities at S1-S5 are indicated in red in panel f). A dashed blue vertical line is shown to illustrate the significance of an ice velocity induced phase shift in reconstructed accumulation.*

magnitude and sign with values ranging from -0.07 (2010-2011) to $+0.02$ m w.e. a^{-1} km^{-1} (2007-2008). Spatial variability is much larger for $4000 < x < 7300$ m than in the upper accumulation area. In Section 3.5.6 we further analyse spatial variability and correlate accumulation patterns to terrain parameters (surface slope, curvature and wind sheltering) and wind properties.

When interpreting consistency of annual accumulation patterns, one should keep in mind that ice is transported down the transect. In the case of substantial ice velocities, this leads to a horizontal shift with depth of variability along the transect [*Arcone et al.*, 2005]. Continuous GPS velocities obtained at multiple sites along the transect (S1-S5 in Figure 3.1; *Den Ouden et al.* [2010]) for the period 2010-2012 are included in Figure 3.3f. Velocities reveal substantial spatial variability with highest flow speeds in the steepest part of the flow line (Figure 3.1) and rapidly decreasing speeds towards the ice plateau. Given observed velocities up to 58 m a^{-1}, we expect a maximum shift of an accumulation anomaly in the order of 200-300 meters between the 2011-2012 and the 2007-2008 layer. The dashed blue line in Figure 3.3 coincides with peaks in the composite accumulation pattern and illustrates that a phase shift is apparent in the lower part of the accumulation area. As a result of this phase shift, systematic variability in the composite pattern is partly suppressed in regions with high flow velocities. Due to the lack of spatial detail in the velocity observations, no attempts have been made to correct annual patterns for a possible phase shift. It can be seen in Figure 3.3 that, despite slight phase shifts, major peaks in the lower accumulation zone are still well represented in the composite pattern. It should be noted that in the lower accumulation zone, due to increased difficulty in layer picking of older IRHs (Figure 3.2), uncertainty in reconstructed accumulation increases with depth/age.

As illustrated in Figure 3.1, part of the transect covered by *Pälli et al.* [2002] nearly overlaps with the transect in this study. *Pälli et al.* [2002] presented mean accumulation patterns for the periods 1986-1999 and 1963-1999 of which the lowest 4 km are shown in Figure 3.3f. Reasonable agreement is found between spatial patterns, whereas the mean in our study (0.78 m w.e. a^{-1}) is higher than the averages of 0.71 and 0.54 m w.e. a^{-1} for 1986-1999 and 1963-1999 found by *Pälli et al.* [2002]. This could indicate significantly higher accumulation rates since 2007 relative to the longterm mean. However, in addition to uncertainty in our approach, these discrepancies could very well result from substantial systematic errors involved in dating the 1986 and 1963 layers in *Pälli et al.* [2002] (estimated errors up to 35% for the 1986 layer).

3.5.2 Vertical profiles of density, temperature and water content

Next, we present subsurface properties at the end (17 April 2012) of the final reconstruction experiment with fully calibrated accumulation from the inverse method. Figure 3.4 shows subsurface density, temperature and water content of the first 10 m in the firn/ice along the transect. Depths of the modelled summer surfaces are indicated.

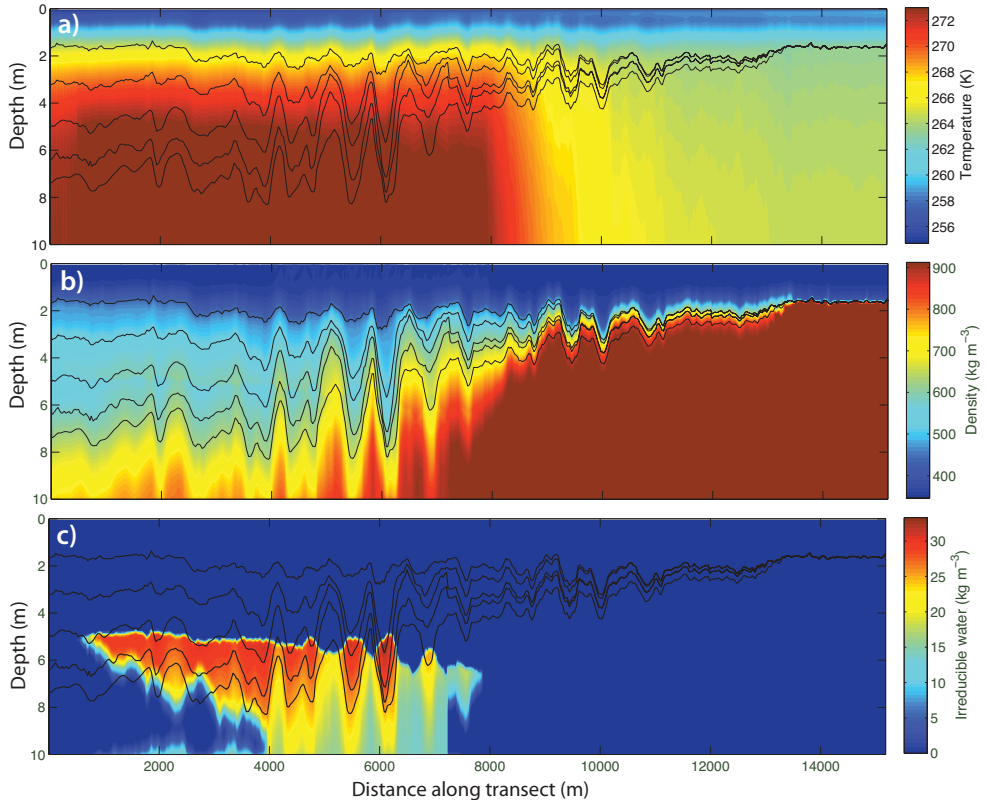

Figure 3.4: *Simulated subsurface temperature (a), density (b) and irreducible water content (c) in the upper 10-m of the firn and/or ice on 17 April 2012. Black lines mark the modelled 2007-2011 summer surface depths.*

Subsurface temperatures at 17 April 2012 in Figure 3.4a show a temperate firn pack below a depth of ∼5 m for a major part of the accumulation area. This can be ascribed to substantial refreezing of percolating melt water, while cold wave penetration during the 2011-2012 winter season induced non-temperate near-surface conditions. In the lower accumulation zone and ablation area heat release by refreezing in permanent firn is small or absent and deep temperatures remain cold. Results also illustrate that the subsurface temperature distribution at the end of the winter season is hardly affected by accumulation variability, indicating that heat diffusion predominates advection.

Subsurface densities in Figure 3.4b illustrate the strong influence of accumulation on the vertical density distribution. Firstly, with high accumulation rates low density snow propagates downward at a faster rate. This effect predominates over enhanced gravitational packing, effectively reducing density at depth. Secondly, faster downward advection of mass reduces

the significance of refreezing in a layer of a certain age, implying a lower density. The sum of these two effects cause a strong dependence of the vertical density gradient on the accumulation rate as seen in Figure 3.4b.

The simulated subsurface water content in Figure 3.4c shows the presence of irreducible water in the firn pack below a depth of $\sim$5 m in a large part of the accumulation zone. The water has been stored in the firn pack during previous melt seasons and has gradually been refrozen from above due to surface cooling during the 2011-2012 winter season. This results in a sharp transition with depth of the water content coinciding with a transition from cold to temperate firn. Only near the start of the transect, winter cooling is sufficient to refreeze all irreducible water and non-temperate conditions prevail. Within temperate firn, variability in the water content can primarily be ascribed to the density distribution affecting the storage limit of irreducible water [*Schneider and Jansson*, 2004].

3.5.3 Validation

As a means of validation, we compare simulated subsurface profiles of density and temperature to firn observations along the transect. Observational data comprise density and temperature profiles from multiple snow pits along the transect in April 2011 and 2012, as well as a 12-m shallow firn core, drilled at the start of the transect (Figure 3.1). Since modelled values are area-averaged and subsurface characteristics may be prone to substantial small-scale horizontal variability, discrepancies between model output and observations can in part be ascribed to the point-wise character of the observations.

Snow pit profiles

A comparison of the snow pit density and temperature profiles and model output is shown in Figure 3.5. Under real conditions the complex interaction of the surface layer with the atmosphere through e.g. wind compaction, moisture exchange, radiation and precipitation type leads to a vertical density distribution exhibiting substantial small-scale density variability [*Colbeck*, 1986]. On the contrary, in the model a constant fresh snow density is prescribed, resulting in a much smoother density distribution in the snow pack (Figure 3.5a). Mean modelled densities agree well with observations (difference 1 kg m^{-3}), which can in part be ascribed to calibration of the fresh snow density with observed near-surface densities. Due to the linear dependence of TWT at a certain depth on firn density (Equations (3.4)-(3.6)), the degree of variability in density does not affect the radar travel time between two IRHs. Therefore, we expect the lack of modelled small-scale density variability has a negligible impact on reconstructed annual accumulation. Comparing snow pit temperatures with modelled profiles (Figure 3.5b) reveals that the model generally captures vertical variability in subsurface temperatures well. In addition to the local character of observations and uncertainty in modelled

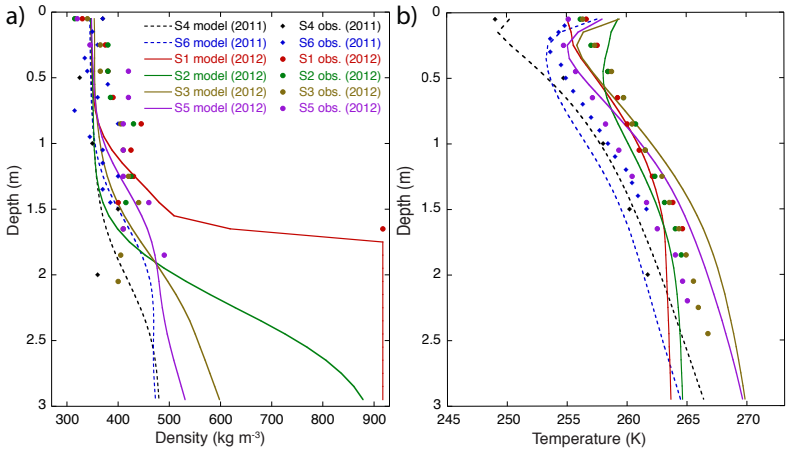

Figure 3.5: *Comparison of subsurface density (a) and temperature (b) profiles in the model output (lines) and observed in snow pits (dots) in April 2011 and 2012 at sites S1-S6 (Figure 3.1).*

heat transport and refreezing, discrepancies can also be attributed to local unresolved surface temperature variability.

Shallow firn core profiles

Shallow firn core densities and temperatures are compared to modelled values in Figure 3.6 indicating a reasonable agreement. As discussed the model does not account for variability in vertical transport rates of percolating water and is therefore unable to produce the observed lower density segments alternating with local dense ice layers. On average, modelled densities for this site are 21 kg m^{-3} higher than observed values. If this error would be systematic, this would imply an uncertainty of $\sim$0.023 m w.e. a^{-1}, estimated from output of the sensitivity experiment with perturbed fresh snow density (Section 3.4). Simulated and observed temperatures (Figure 3.6b) show a similar increase towards temperate conditions at depths $>$ 10 m. Between 2 and 8 m depth, the model slightly overestimates temperatures, possibly due to uncertainty in modelled heat diffusion and refreezing.

Isochronal accuracy

The continuity of the IRHs across the profile in the GPR radargram (Figure 3.2) indicate they are likely isochrones [*Spikes et al.*, 2004; *Eisen et al.*, 2006]. In combination with large accumulation rates, buried coarse-grained high-density summer surfaces, covered by low-density winter snow, produce pronounced IRHs in the GPR radargram. This is apparent for the highest part of the transect. Diffusion and eventually fainting of IRHs following excessive melt

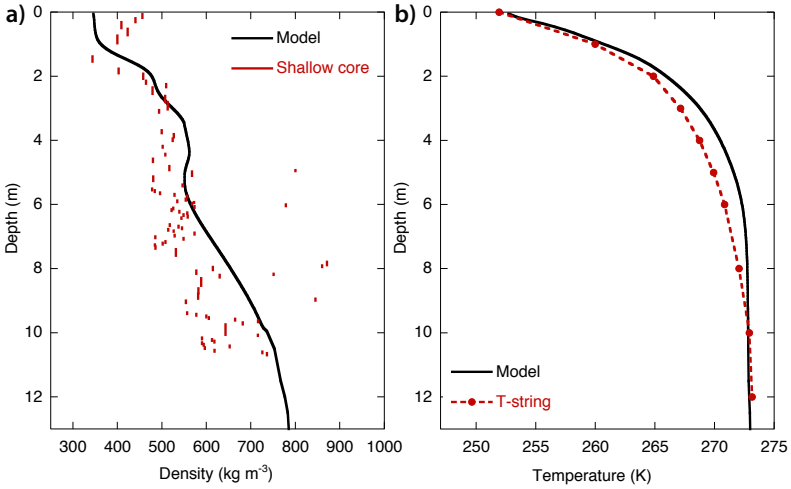

Figure 3.6: *Comparison of subsurface density (a) and temperature (b) profiles in the model output (black) and observed in a 12-m shallow firn core (red), drilled at S6 in April 2012.*

[*Dunse et al.*, 2008; *Brown et al.*, 2011] is apparent beyond ∼5000 m, but is unlikely to cause absence of IRHs higher up. Deep percolation of melt water suggests a possibly important role of accretion on top of existing buried summer surfaces, enhancing the reflectivity contrast of IRHs in subsequent years [*Dunse et al.*, 2008]. In comparable climatic conditions in southeast Greenland, *Miège et al.* [2013] found annual IRHs in the higher part of a transect and fainting of some annual horizons at lower elevation. From the above it seems likely that selected continuous IRHs, starting at the highest point on the grid, bound annual layers. We verify the annual character of the upper two identified IRHs by comparing observed snow mass in snow pits dug in April 2011 and 2012 to simulated values on top of the previous year's summer surface. A scatterplot in Figure 3.7 shows substantial discrepancies between modelled and observed values, which can be ascribed to the aforementioned local character of the observations (e.g. snow depth may vary strongly over short distances). More importantly, the mean snow mass of all snow pits in a single year gives information on possible systematic errors in the dating of a continuous IRH. In case continuous IRHs would bound multi-annual layers, mean modelled values would overestimate snow mass by a factor two or more. Alternatively, selection of multiple IRHs per annual layer would result in a severe underestimation of mean modelled snow mass along the transect. For the snow pits in 2011, we find an average modelled and observed snow mass of 0.78 and 0.74 m w.e. respectively, whereas for 2012, a mean snow mass of 0.71 (modelled) and 0.75 m w.e. (observed) is found. From this we conclude that the upper two IRHs likely represent summer surfaces and bound annual layers. Direct means to confirm the annual character of the deeper layers are lacking.

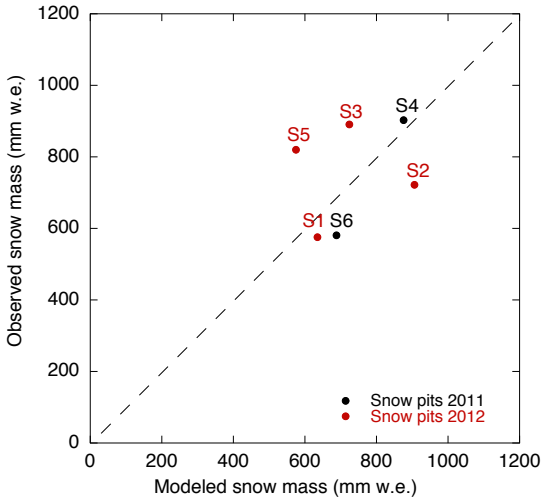

Figure 3.7: *Modelled versus observed snow mass in snow pits dug in April 2011 (black) and 2012 (red).*

3.5.4 Accounting for melt, refreezing and runoff

The use of a coupled model allows us to decompose the mass budget along the transect into mass fluxes by surface accumulation, melt, latent transport, refreezing and runoff. With the inverse method, post-depositional processes are modelled and we are able to distinguish between surface accumulation and mass stored in annual layers. Traditional direct approaches convert GPR travel times into annual layer mass, which is assumed to equal accumulation. These approaches hence only provide a suitable method for reconstruction of surface accumulation in cold firn where internal mass transport through melt water percolation and refreezing is negligible.

We analyse the mass budget along the transect in the final model experiment, with fully calibrated annual accumulation from the inverse method, covering the period from 1 July 2007 to 30 June 2012 (Figure 3.3). The time-frame is extended to cover a full five-year period (with reconstructed 2011-2012 accumulation pattern assumed for the period 17 April - 30 June 2012). In Figure 3.8a, the total mass budget and its components are shown for 2007-2012 (solid lines) as well as for 2011-2012 (dashed lines). In the upper part of the accumulation zone ($x < \sim 4000$ m) runoff is absent and all melt refreezes in the firn pack. The refreezing potential is limited by two factors: 1) the amount of water available for refreezing and 2) the cold content of the firn. Towards lower altitudes, the available melt water increases, whereas the cold content decreases, implying increased significance of the cold content as a limiting factor for refreezing. We find refreezing is nearly constant in the accumulation area and decreases gradually towards the ablation area. The amount of refreezing is hardly affected

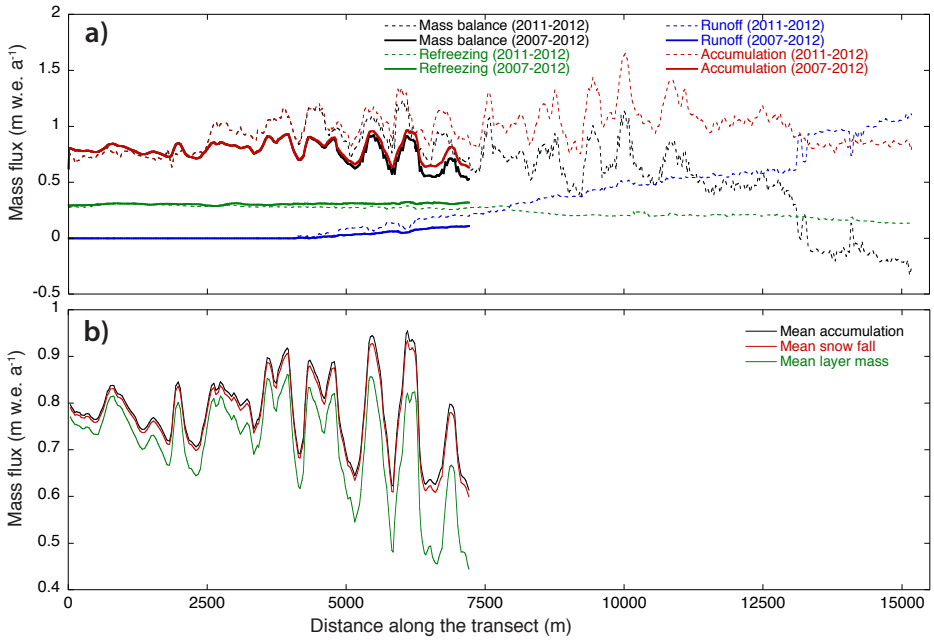

Figure 3.8: *Panel a) shows the simulated mass balance, refreezing , runoff and accumulation along the transect for 2007-2012 (solid lines) and 2011-2012 (dashed lines). In panel b) a comparison of mean annual accumulation, snowfall and layer mass is shown.*

by variability in accumulation, due to the minor influence of accumulation on subsurface temperatures and surface melt.

In case during the period 2007-2012 percolating water refreezes or runs off below the oldest IRH under consideration (2007), this mass is lost for annual layers formed since 2007. The water flux through the oldest IRH is therefore a measure for the discrepancy between surface accumulation and annual layer mass. In Figure 3.8b we show five-year mean surface accumulation, snowfall and layer mass. The difference between snow fall and accumulation indicates the small fraction of total accumulation falling as rain. The discrepancy between accumulation and layer mass increases towards lower altitudes as mass exchange in the firn pack becomes more prominent. Even at the highest grid point, some refreezing below the IRH formed in 2007 occurs, resulting in a reduced mean layer mass with respect to accumulation. For $x < 7300$ m, we find a discrepancy between accumulation and layer mass ranging from 0.03 to 0.17 m w.e. a^{-1}. This directly quantifies errors made when assuming annual layer mass equals accumulation, as in traditional methods.

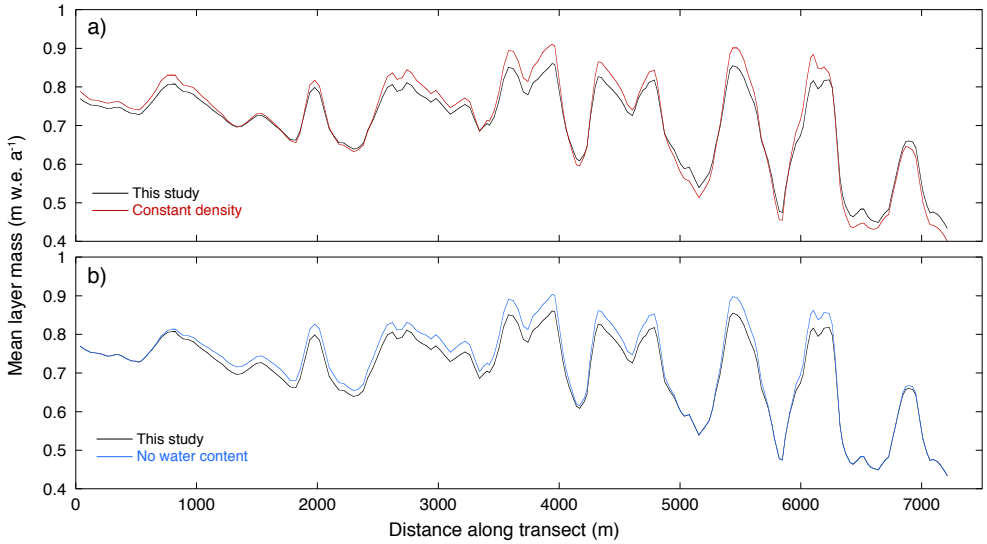

Figure 3.9: *Assessment of the impact of ignoring density variability (a) and water content (b) on annual mean reconstructed layer mass for 2007-2012 and $x < 7300$ m.*

3.5.5 Accounting for density and water content variability along the transect

In a next step, we quantify the impact of accounting for density variability and water content of the firn pack on reconstructed accumulation. Comparing our results with alternative traditional approaches, often disregarding horizontal density variability and firn water content, gives an idea of the relevance of explicit modelling of density and water content variability along the transect.

In order to quantify the impact of accounting for density variability along the transect, we calculated the layer mass that would be obtained from observed TWTs by assuming a vertical density profile equivalent to the mean for $x < 7300$ m. This is equivalent to traditional methods using a composite density record to directly convert TWTs into layer mass. This is compared to the mean layer mass in our approach in Figure 3.9. It can be seen that accounting for density variability along the transect effectively reduces the degree of variability in reconstructed annual layer mass. This dampening can be understood by looking at the dependence of the TWT on density ρ (Equation (3.4)). Two counteracting effects play a role here: 1) the permittivity ε_f increases with ρ, and 2) the summer surface depth D decreases with ρ. Using that the summer surface depth D is inversely proportional to ρ, it follows from Equation (3.4)

that:

$$\begin{aligned} t &\sim \frac{C_1}{\rho}(C_2 + C_3\rho) \\ &\sim \frac{C_1 C_2}{\rho} + C_1 C_3 , \end{aligned} \tag{3.8}$$

where C_1, C_2 and C_3 are positive constants. The derivative of the TWT with regard to ρ is then given by:

$$\frac{\partial t}{\partial \rho} \sim -\frac{C_1 C_2}{\rho^2} . \tag{3.9}$$

From this we can conclude that a perturbation of ρ is accompanied by a change of the TWT of opposite sign. The dominant effect controlling the sensitivity of the TWT to changes in accumulation is the direct shift in summer surface depth associated with changes in the surface mass flux. The above analysis shows that this background effect is amplified by the effect of a change in accumulation on the density. E.g., a positive perturbation of accumulation leads to a direct downward shift of the summer surface depth and hence an increase in the associated TWT. At the same time, a drop in density occurs, which induces an additional increase in TWT, according to Equation (3.9). This illustrates that accounting for density variability in our approach leads to a stronger dependence of TWT on accumulation. From this it can be understood that smaller adjustments of accumulation relative to the mean are needed to find a match between the modelled and the observed TWT pattern, thereby explaining the reduced variability in Figure 3.9a. Not accounting for density variability along the transect (as in traditional approaches) leads to an increase of the standard deviation in the reconstructed layer mass of 19%. This indicates the high relevance of accounting for density variability when extracting spatial accumulation patterns from GPR data. On average, the absolute discrepancy is 0.021 m w.e. a^{-1}.

Although the firn water content may only comprise a small fraction of the total firn volume, the impact of firn water on the effective permittivity can be substantial due to the large relative permittivity of water. Water in pore spaces hence attenuates the radar signal, thereby affecting TWTs and indirectly reconstructed accumulation. In order to quantify the impact of neglecting water in the firn pack on reconstructed layer mass we first calculate mean layer mass from observed TWTs and the modelled density distribution while assuming a zero water content (as in traditional approaches). These results are then compared with modelled layer mass in which the effect of irreducible water on TWTs is taken into account. Figure 3.9b illustrates that neglecting the impact of irreducible water on TWTs leads to an overestimation of reconstructed layer mass. Accounting for water increases modelled TWTs, which needs to be compensated by a lower accumulation rate. In high-accumulation areas annual layers extend deeper in the firn pack and reconstructed layer masses experience a larger influence of water (Figure 3.4c). On average we find a discrepancy of 0.017 m w.e. a^{-1}. Note that the GPR data were gathered in spring, where the water content in the firn pack exhibits a

minimum. More substantial errors can be expected when collecting data in other seasons.

3.5.6 Spatial variability vs. terrain parameters

Previous work has demonstrated that the interaction of wind and terrain features controls the distribution of snow deposition. Snow redistribution by wind is known to erode snow on the windward side of ridges, whereas increased deposition occurs in the lee [*Dadic et al.*, 2010; *Clifton and Lehning*, 2008]. Additionally, reduced wind velocities on the leeward side of undulations may result in preferential precipitation [*Lehning et al.*, 2008]. Collected DGPS data of the surface elevation along the GPR profile allow us to link accumulation variability to terrain parameters.

Before quantifying correlations between terrain features and accumulation, it is important to know the prevailing wind direction relative to the transect orientation. For that purpose observational and simulated wind data are employed. Wind velocity and direction at $\sim$4 m height are recorded every 10 minutes at the AWS in the Nordenskiöldbreen valley (Figure 3.1). The wind rose and histogram of all observations between March 2009 and August 2012 are shown in Figure 3.10e-f, and show a clear prevalence of winds blowing from the north-east. Recent modelling of wind fields at a 2.7 km resolution using the atmospheric model WRF [*Claremar et al.*, 2012] resulted in wind roses at points near the AWS and the ice summit (W1 and W2 in Figure 3.1) for one summer (Jun-Aug 2009) and winter season (Dec 2009 - Feb 2010). In agreement with the AWS data, modelled wind roses at W1 in Figure 3.10c-d reveal prevailing winds from the north-east. A similarly consistent simulated pattern is found on the ice plateau at W2 (Figure 3.10a-b). This implies that prevailing winds blow approximately parallel to the down-slope direction of the transect for $x > \sim 4400$ m, whereas for $x < \sim 4400$ m winds blow in the down-slope direction of the transect with a horizontal inclination of $\sim 60°$.

In Figure 3.11a normalised mean accumulation patterns, based on the profiles shown in Figure 3.3, are shown for both the final year (2011-2012), covering the full transect, and the five-year period (2007-2012), covering the upper part of the transect. The notion of preferential accumulation in the lee of ridges has led to parameterisations linking accumulation to surface slope and/or curvature in the direction of the wind (e.g. *Liston et al.* [2007] and *Gascoin et al.* [2013]). Since the wind is shown to be rather consistently blowing parallel to a large part of the transect, the reconstructed accumulation in combination with accurate height data along the transect comprise a useful dataset to verify the dependence of accumulation on terrain features in the dominant wind direction. We correlate normalised accumulation (Figure 3.11a) to terrain curvature (Figure 3.11b), slope (Figure 3.11c) and a so-called "sheltering index" (Figure 3.11d). Curvature is assumed to equal the second derivative of the surface height profile. In line with *Gascoin et al.* [2013], curvature is computed over a length scale, representing one-half the dominant wave length of topographic features. A spectral analysis resulted in an estimated curvature length scale of 700 m. The sheltering index *SI*,

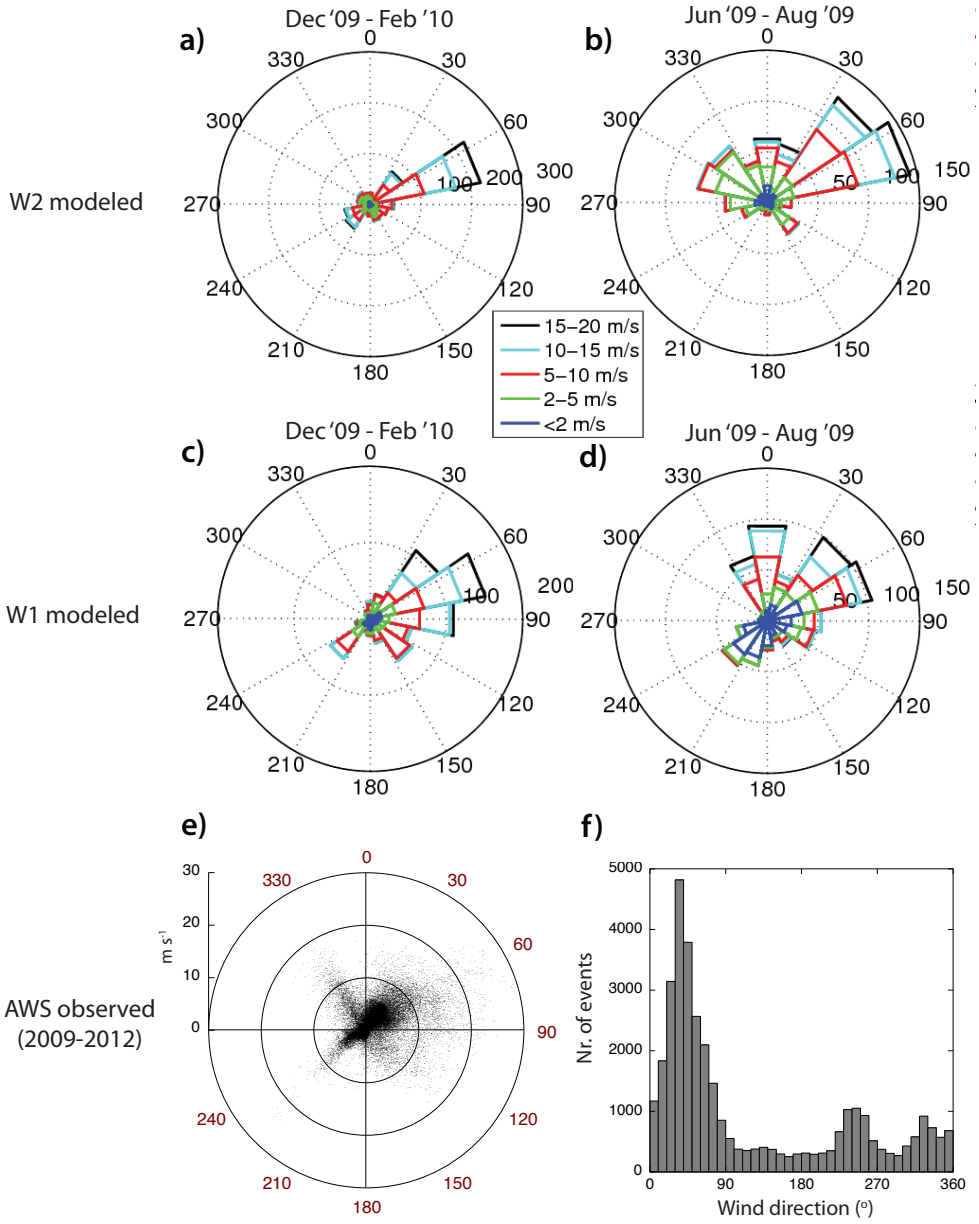

Figure 3.10: *Simulated wind roses on the ice plateau at W2 (a-b) and near the AWS at W1 (c-d) from output of the atmospheric model WRF with a 2.7 km grid resolution. Bottom panels show the observed wind rose (e) and histogram (f) at the AWS, based on half-hourly observations between March 2009 and August 2012. The position of the AWS, W1 and W2 is marked in Figure 3.1.*

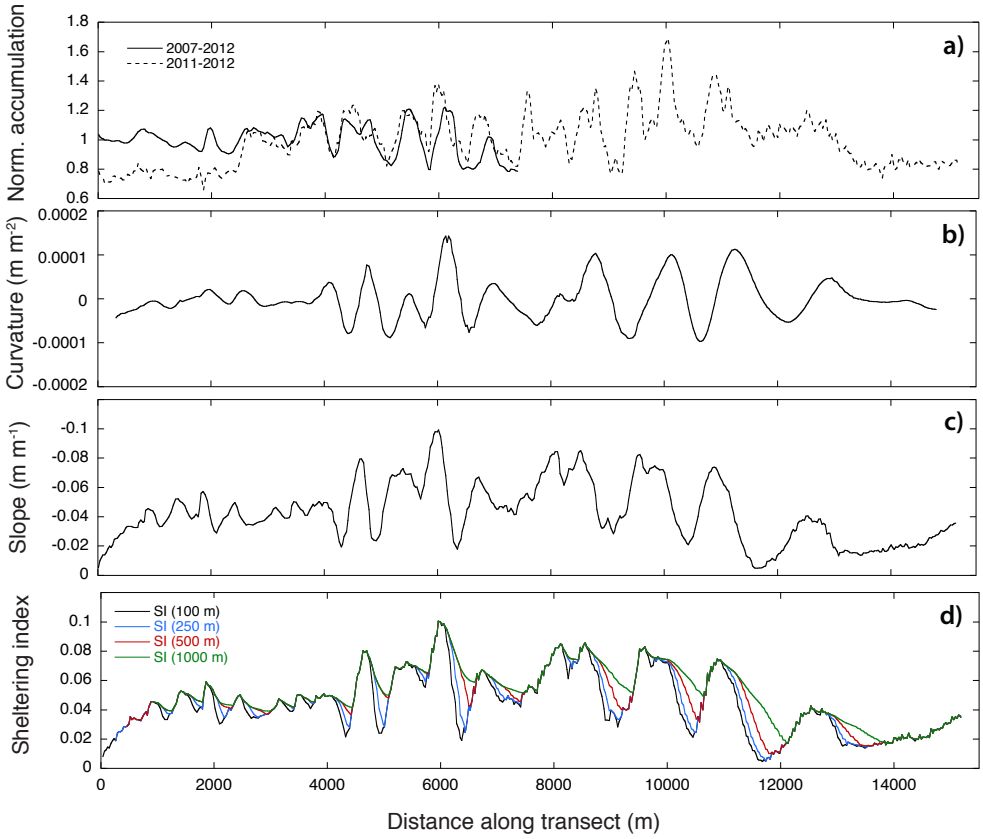

Figure 3.11: *Reconstructed normalised accumulation for 2007-2012 (a) and terrain curvature (b), slope (c) and the sheltering index (d). The sheltering index is shown for search distances ranging between 100 and 1000 m.*

developed by *Winstral et al.* [2002], determines the degree of wind sheltering of a certain grid cell by searching for the maximum slope of a line leaving the grid cell and intersecting with terrain in the dominant wind direction:

$$SI = \max\left[\tan\left(\frac{z(x_s) - z(x_i)}{x_s - x_i}\right)\right], \tag{3.10}$$

where z is surface height, x_s is the position of the shelter-defining cell and x_i denotes the position of the cell of interest. Calculated SI profiles for maximum search distances $d_{\max}$ ranging from 100 to 1000 m are shown in Figure 3.11d. Note that for small $d_{\max}$, SI will approximate the local slope (Figure 3.11).

Table 3.2 presents correlations of normalised accumulation and terrain curvature, slope and sheltering for the full transect (2011-2012), for $x < 7300$ m and $x < 4400$ m (2007-2012 and

Table 3.2: *Correlations between normalised accumulation for the periods 2007-2012 (A07 − 12) and 2011-2012 (A11 − 12) and terrain curvature, slope and the sheltering index. Correlations significant at a 99% confidence level are marked in bold.*

	A11-12 (full transect)	A11-12 ($x < 7300$ m)	A11-12 ($x < 4400$ m)	A07-12 ($x < 7300$ m)	A07-12 ($x < 4400$ m)
Curvature	**+0.18**	+0.12	+0.16	**+0.40**	−0.07
Slope	**−0.52**	**−0.59**	−0.22	−0.08	−0.04
SI (100 m)	**+0.53**	**+0.60**	+0.18	+0.16	+0.07
SI (250 m)	**+0.53**	**+0.59**	+0.07	**+0.24**	+0.08
SI (500 m)	**+0.53**	**+0.59**	−0.02	+0.16	+0.00
SI (1000 m)	**+0.53**	**+0.53**	−0.24	+0.13	+0.02

2011-2012). For the full transect, we find highly significant absolute correlations between accumulation and slope and *SI*. Given the large number of data points along the full transect ($N = 495$), correlation coefficients $r > 0.12$ are significant at a 99% confidence level. The anti-correlation between accumulation and local slope confirms preferred snow deposition on steep slopes directed away from the dominant wind direction. Along the full transect we find a much weaker, yet still significant, correlation between accumulation and curvature. Local slope variations directly affecting the degree of wind sheltering cause preferential snow deposition on the upwind side of concave surface depressions. This explains a downwind phase shift of variability in local curvature relative to accumulation in Figure 3.11a-b. Correlating accumulation to *SI* does not substantially improve *r*-coefficients in comparison to slope correlations.

For $x < 4400$ m, we find relatively weak correlations between normalised accumulation and slope or curvature for both 2007-2012 and 2011-2012 (Table 3.2). The horizontal inclination of the wind in this area relative to the transect direction in combination with the lack of pronounced surface features on the plateau explain a lack of high correlations. For $x < 7300$ m, normalised accumulation for 2011-2012 anti-correlates strongly with slope ($r = -0.59$), whereas for the 2007-2012 pattern a strong correlation with curvature ($r = 0.40$) is found. Comparing patterns in Figure 3.11a for $4400 < x < 7300$ m illustrates that similar patterns of variability in accumulation are found for 2007-2012 and 2011-2012, yet with a phase shift, which has earlier been ascribed to the effect of ice flow on reconstructed accumulation. The low correlation between slope and 2007-2012 accumulation can likely be ascribed to this phase shift. Moreover, by definition a 90° phase shift is apparent between curvature and slope, with curvature being the first derivative of slope. From this, it can be understood that the phase error in 2007-2012 accumulation (unrealistically) increases the correlation with curvature.

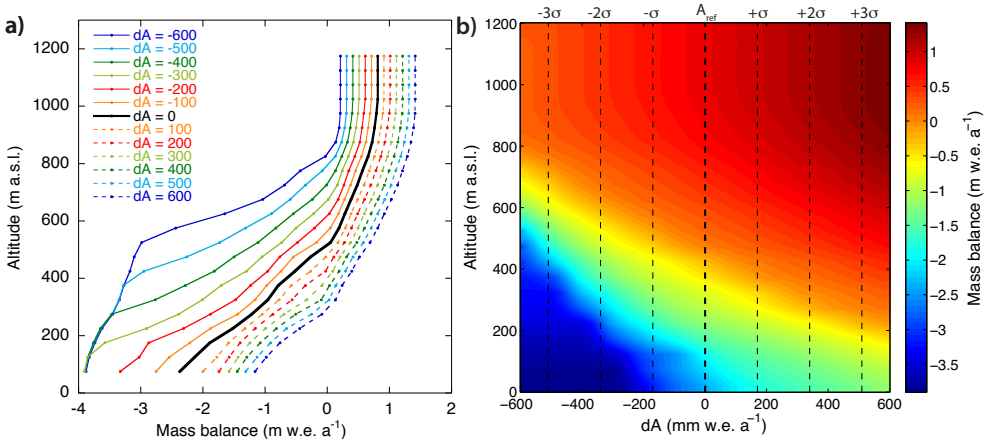

Figure 3.12: *Annual mean net mass balance vs. height constructed from output of sensitivity experiments with perturbed accumulation (dA in mm w.e. a^{-1}) in panel a). Panel b) shows an interpolated contour-plot of the mass balance in a two-parameter space spanned by altitude and accumulation perturbations (dA). Black dashed lines mark the mean annual standard deviation ($\sigma = 0.17$ m w.e. a^{-1}) of reconstructed accumulation, representing spatial 'noise' in annual accumulation.*

3.5.7 Impact of spatial variability on net mass balance

The response of the surface mass balance to a change in accumulation is non-linear, due to interactions within the coupled model of accumulation and snow depth with the surface albedo and subsurface properties. Effectively, these interactions amplify the sensitivity of the mass balance to changes in accumulation. Moreover, the sensitivity of the mass balance may vary for positive and negative perturbations of accumulation, implying that the mass balance will depend on the degree of spatial accumulation variability.

In order to quantify the effect of accumulation variability on the net mass balance, we first extend the model transect down to the calving front (dashed line in Figure 3.1). Temporal accumulation variability once again comes from the Svalbard Airport record. We define a smooth scaled reference accumulation pattern (A_{ref}), which is linearly increasing with altitude up to 850 m a.s.l., above which accumulation is constant and scaled such that the annual mean accumulation matches the reconstructed mean of 0.78 m w.e. a^{-1} (Figure 3.3). We perform multiple model experiments over the period 2007-2012 with perturbed accumulation ($-600 < A - A_{\text{ref}} < 600$ mm w.e. a^{-1}) and divide the simulated annual mean mass balance into 50-m height bins. Resulting height profiles are shown in Figure 3.12a. In the accumulation zone, the mass balance responds approximately linearly to changes in accumulation, whereas in the ablation area the mass balance is more sensitive to negative accumulation perturbations. For very negative accumulation perturbations below 500 m a.s.l., annual accumulation becomes zero and the mass balance is insensitive to further reductions.

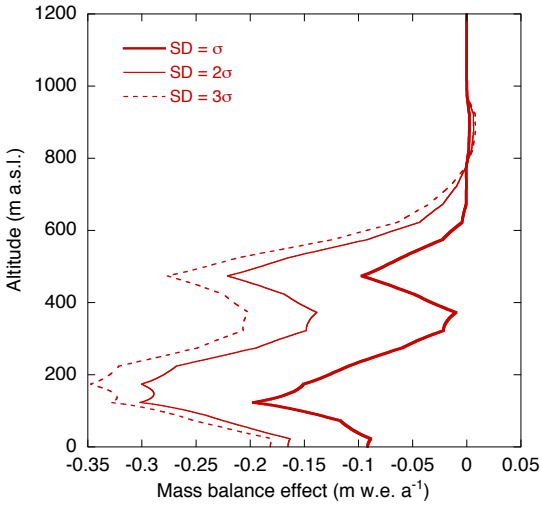

Figure 3.13: *Impact of spatial variability with a standard deviation of 1, 2 and 3σ on the mass balance as a function of altitude.*

Figure 3.12b shows the mass balance vs. altitude for a range of accumulation perturbations. The contour-map consists of vertical lines, adopted from output in Figure 3.12a, and is completed by means of spring-metaphor interpolation between these lines. In subsequent steps, we 1) subtract the reference mass balance in Figure 3.12b, 2) set the standard deviation of accumulation variability, 3) apply a normal probability density function around A_{ref} and 4) integrate over dA for every altitude. This results in a height profile of the net mass balance effect of spatial accumulation variability, given a certain standard deviation σ, representing the mean degree of accumulation variability (or noise) along the transect. We set σ to the mean of the annual standard deviations of reconstructed accumulation for $x < 7300$ m for 2007-2012 (Figure 3.3), yielding $\sigma = 0.17$ m w.e. a^{-1}. Figure 3.13 shows the net mass balance effect of small-scale spatial variability with a standard deviation of 1, 2 and 3σ and clearly illustrates the net negative mass balance effect of accumulation variability in the ablation area. In case of a standard deviation equivalent to the annual mean for $x < 7300$ m, this induces a mean mass balance effect of -0.041 m w.e. a^{-1} for the entire grid. In the ablation area, the relatively strong nonlinear response of the mass balance to accumulation changes induces a reduction of -0.081 m w.e. a^{-1} below 600 m a.s.l.. Perturbations of accumulation have a major impact on the mass balance if changes from ablation to accumulation area or vice versa occur. This affects the non-linearity in the net mass balance sensitivity and explains extrema found at $\sim$400 and 500 m a.s.l.. The decline of the net mass balance effect below $\sim$100 m a.s.l. can be ascribed to the aforementioned absence of accumulation for very negative perturbations. In the accumulation zone, accumulation variability hardly affects the net mass balance, since the surface albedo is rather insensitive to accumulation changes.

3.6 Conclusions

A novel approach is presented and applied to extract spatial and temporal accumulation variability from GPR data. The method uses a coupled surface energy balance - snow model in an inverse approach and aims to find a match between simulated and observed TWTs by iteratively adjusting accumulation, serving as input for the coupled model. The coupled model computes surface melt and subsequent percolation, storage, refreezing and runoff of water in order to simulate the subsurface evolution of density, temperature and water content. The use of a model in the determination of accumulation rates from a GPR dataset has several benefits. Firstly, since the model accounts for mass exchange between annual layers and runoff, we can distinguish between annual surface accumulation and layer mass. In contrast to traditional approaches, this enables reconstructing accumulation in areas with substantial melt percolation, refreezing and runoff if IRHs can reasonably be defined. Secondly, by using a model to simulate density variability and water content along the transect, we avoid making rough assumptions on these variables affecting accumulation estimates.

The inverse approach is applied to a GPR transect, obtained along a 16 km transect on Nordenskiöldbreen, Svalbard. Reconstructed annual accumulation patterns for 2007-2012 are shown to be partly consistent from year-to-year. Spatial variability is substantial with an annual standard deviation ranging from 13 to 27% of annual accumulation of on average 0.78 m w.e. a^{-1}. Considerable ice velocities in the lower accumulation area induce a downward shift of accumulation peaks in time, thereby dampening the magnitude of reconstructed variability somewhat. An analysis of the mass budget illustrates the significance of melt water percolation and refreezing below the previous year's summer surface, leading to a discrepancy between annual layer mass and surface accumulation becoming more substantial towards lower altitudes. Explicit modelling of density variability along the radar transect, which is among other factors strongly affected by the accumulation rate itself, leads to dampening of spatial variability in reconstructed layer mass by 19% compared to traditional approaches assuming a horizontally constant density distribution. Accounting for water content in the firn pack is shown to have a limited impact (0.017 m w.e. a^{-1}) on reconstructed layer mass in this study, but would be more substantial if GPR data were gathered during other seasons. The demonstrated prevalence of winds blowing along the transect enabled correlating accumulation variability to terrain features. Very strong correlations are found between slope and accumulation, indicating preferential deposition of snow on leeward slopes due to wind shading. Generally weaker correlations are found between accumulation and terrain curvature. Mass balance sensitivity experiments along an extended transect illustrate the non-linear dependence of the mass balance on accumulation, implying a nonzero mass balance sensitivity to spatial 'noise' in accumulation. This effect is only substantial in the ablation area, resulting in an estimated mean reduction of the surface mass balance of -0.04 m w.e. a^{-1} along the full height-range and -0.08 m w.e. a^{-1} in the ablation area.

Sensitivity experiments illustrate that uncertainty in reconstructed accumulation stems mainly

from uncertainty in the chosen fresh snow density, air temperature input and inaccuracy of the conversion relation used to compute TWTs from subsurface profiles. Results are nearly insensitive to the chosen vertical grid resolution and firn initialisation. Another source of uncertainty comes from dating of the manually selected IRHs, which could potentially bound multi-annual or intra-annual layers. Snow mass observations rule this out for the upper two annual layers.

The lack of modelling physical processes causing small-scale vertical density variability in the firn pack is argued to have only a limited impact on reconstructed accumulation. Nevertheless, some improvement of accumulation rates can be expected when processes affecting local vertical water transport rates in the firn, like piping and attenuation of water flow on ice lenses, can be included in a physical or parameterised way. At the moment, the lack of observational data and physical understanding of these processes limit the feasibility of implementation in a densification model. Inclusion of such processes is however certainly needed when aiming to describe small-scale density variability observed in snow pits and drilled firn cores.

The inverse method used in this study to extract accumulation rates from GPR data requires a model simulating the subsurface evolution, a spatially dependent surface melt rate and detected and dated IRHs in a GPR dataset. Here an energy balance model, forced with spatially dependent climate input is used, but application of the inverse approach is not constrained to this type of melt model. Similarly, using alternative snow models might be desirable in other applications. Altogether, with this study we hope to set an example how inverse methods can help to improve the accuracy of reconstructed accumulation from GPR data.

4

Cyclic behaviour in the Parallel Ice Sheet Model (PISM)

Numerical experiments are conducted on a synthetic topography with a three-dimensional thermo-mechanically coupled ice-sheet model, the Parallel Ice Sheet Model (PISM). Within the model, combined stress balances are connected to evolving thermodynamics and hydrology. The sensitivity of cyclic behaviour to changes in sliding-law parameters and the climate input is studied. Multiple types of oscillations were found with strong variations in both amplitude and frequency of ice volume and sliding velocities. A physical description is given in which these variations and transitions from one oscillation type to another are linked to the interplay of stresses, heat transport and hydrology at the ice-bed interface. High-frequency oscillations are linked to interaction of sliding and a redistribution of water at the base. Low-frequency cycles additionally rely on changes in the thermal regime, thereby mimicking surging of 'Svalbard-type'. Oscillation characteristics are shown to be strongly sensitive to changes in sliding-law parameters and inclusion of a surface height dependent mass balance.

This chapter is based on: Van Pelt, W., and J. Oerlemans (2012), Numerical simulations of cyclic behaviour in the Parallel Ice Sheet Model (PISM), *Journal of Glaciology*, *58*(208), 347–360

4.1 Introduction

Climatic variations are known to exert an external control on the dynamic evolution of glaciers and ice sheets. However, not all observed changes in ice movement and geometry evolution can be ascribed to changes in the climate system. Ice sheets evolve as a product of the interplay of geometry, thermodynamics and hydrology. Hence, accurate simulation of ice evolution requires proper treatment of both internal and external conditions. Irrespective of the climate forcing, periodic changes in ice geometry and flow velocities may occur.

Numerical modelling of periodic behaviour in ice masses has helped to provide insight into how internal instabilities may trigger oscillatory flow. *Budd* [1975] was the first to link basal sliding velocities to the thermal regime in a numerical model and simulated surging behaviour. Later work by *Oerlemans* [1983] has illustrated the relevance of explicit treatment of basal water and including temperature advection in the heat equation. A "binge/purge" mechanism, proposed by *MacAyeal* [1993], relates periods of excessive ice advance to changes in the thermal regime. *Payne* [1995] demonstrated that the interaction of basal dynamics and the basal heat budget may lead to limit cycles in the basal thermal regime. Based on a similar mechanism, multi-millennial oscillations were found in a three-dimensional (3-D) model, developed by *Marshall and Clarke* [1997], in studies by *Calov et al.* [2002] and *Papa et al.* [2006]. Results of the Heinrich Event INtercOmparison (HEINO) as part of the Ice-Sheet Model Intercomparison Project (ISMIP), summarised in *Calov et al.* [2010], demonstrate the ability of ice sheet models to simulate Heinrich-type oscillations. Heinrich events are periods of excessive iceberg calving from the Laurentide ice sheet during the last ice age, for which observational evidence originates from layers of ice-rafted debris in deep-sea sediment cores [*Heinrich*, 1988; *Bond et al.*, 1992]. They are thought to be related to periodic ice stream surging in Hudson Strait [*Clarke et al.*, 1999].

Surging of valley glaciers is an example of periodic ice movement, in which one cycle is characterised by a long period of quiescent flow, followed by a shorter period of high ice velocities. Theoretical work has emphasised the crucial role of basal conditions, facilitating sliding of the ice, in the occurrence of surging [*Clarke et al.*, 1984; *Clarke*, 1987]. Several mechanisms have been proposed to explain surging, of which changes in the efficiency of the drainage system [*Kamb et al.*, 1985] and a thermally controlled surging mechanism [*Murray et al.*, 2000; *Fowler et al.*, 2001] are most widely accepted. *Murray et al.* [2003] concluded, based on observed regional differences between surge dynamics, that at least two distinct surge mechanisms exist. Understanding the interaction between basal resistance to ice flow, the basal hydrological system and melting conditions near the base is required to address mechanisms causing surge-like behaviour.

Runaway feedback mechanisms arising from the interaction of basal thermodynamics, water production and basal shearing have been linked to flow variations of ice streams along the Siple Coast, West Antarctica [*Payne and Dongelmans*, 1997; *Tulaczyk et al.*, 2000b; *Anandakrishnan et al.*, 2001], observed in satellite imagery of the Ross ice shelf and its tributaries

[*Bindschadler and Vornberger*, 1998; *Fahnestock et al.*, 2000; *Jacobel et al.*, 2000]. *Payne and Dongelmans* [1997] and *Payne* [1999] address the role of a feedback between internal shearing and ice viscosity [*Clarke et al.*, 1977] in ice-stream flow. Flow variability of connected ice streams is linked to changes in the drainage basin extent of the individual ice streams. *Tulaczyk et al.* [2000b] use an undrained plastic-bed model [*Tulaczyk et al.*, 2000a] to show that an instability arising from the interaction of frictional heating, water storage and sliding velocities may lead to transient ice-stream behaviour. This instability has been proposed as a possible mechanism for the shutdown of Kamb Ice Stream (formerly Ice Stream C), which occurred $\sim$160 years ago [*Rose*, 1979; *Retzlaff and Bentley*, 1993; *Bougamont et al.*, 2003]. *Alley et al.* [1994] and *Anandakrishnan and Alley* [1997] argue that the stoppage of Ice Stream C may have been caused by a topographic change leading to enhanced water flow to the neighboring Alley Ice Stream (formerly Ice Stream B2).

In this study, a 3-D thermo-mechanically coupled ice sheet model, the Parallel Ice Sheet Model (PISM), is used to simulate ice flow on a synthetic valley-shaped basal topography. Within the model, combined stress balances, a detailed energy conservation scheme and an evolving basal hydrology interact within a single framework. Coupling of these model components in a 3-D framework allows for a detailed study of mutual interactions and provides new insights into the processes involved in oscillations. This study aims to physically describe different types of oscillations that appear in the model output in order to identify the role of internal destabilising feedback mechanisms in maintaining oscillations. This involves a discussion of the interplay of stresses, heat fluxes and basal water. In simulations of Austfonna, Svalbard, using SICOPOLIS (SImulation COde for POLythermal Ice Sheets), the choice of specific sliding-law parameters was shown to facilitate characteristic dynamics of outlet glaciers, ranging from steady fast flow to cyclic surge behaviour [*Dunse et al.*, 2011]. In line with *Dunse et al.* [2011], we study the dependence of the occurrence and characteristics of periodic behaviour on parameters controlling the basal resistance to sliding flow (Section 4.3.1). In contrast to SICOPOLIS, PISM incorporates hybrid stress equations and explicitly models the evolution of basal water, with substantial implications for simulated cyclic behaviour. The role of the height-dependence of the surface mass balance and temperature is studied separately (Section 4.3.2). Finally, model robustness under grid refinement is verified (Section 4.3.3).

4.2 Model & setup

Numerical experiments are conducted with an open source ice dynamical model, PISM. Within the model, ice flow is simulated as a product of mechanical, thermodynamical and hydrological processes. A more complete description of the model is given in *Bueler and Brown* [2009]. Here, only model properties relevant to the simulated cyclic behaviour are discussed.

4.2.1 Model description

PISM combines two shallow (small depth to width ratio) stress balances, namely the Shallow Ice Approximation (SIA) and the Shallow Shelf Approximation (SSA), which are computationally efficient schemes to simulate ice flow by internal deformation and ice-stream flow, respectively. The widely used non-sliding SIA [*Hutter*, 1983; *Morland and Johnson*, 1980] is a stress balance in which the driving stress is balanced solely by internal vertical shearing:

$$\tau_{xz} = -\rho g H \frac{\partial h}{\partial x} \tag{4.1}$$

$$\tau_{yz} = -\rho g H \frac{\partial h}{\partial y} \tag{4.2}$$

where (τ_{xz}, τ_{yz}) are horizontal shearing components, H is the ice thickness, h the surface height, ρ the ice density (910 kg m^{-3}) and g the gravitational acceleration (9.81 m s^{-2}). In case basal lubrication significantly adds to the surface velocity, basal friction and membrane stresses can no longer be neglected, in which case the SSA applies. It assumes that the gravitational driving stress is fully balanced by membrane stresses and friction at the ice/bedrock interface [*MacAyeal*, 1989; *Weis et al.*, 1999]:

$$\frac{\partial}{\partial x}\left(4H\nu\dot{\varepsilon}_{xx} + 2H\nu\dot{\varepsilon}_{yy}\right) + \frac{\partial}{\partial y}\left(2H\nu\dot{\varepsilon}_{xy}\right) - \tau_{b,x} = \rho g H \frac{\partial h}{\partial x} \tag{4.3}$$

$$\frac{\partial}{\partial y}\left(4H\nu\dot{\varepsilon}_{yy} + 2H\nu\dot{\varepsilon}_{xx}\right) + \frac{\partial}{\partial y}\left(2H\nu\dot{\varepsilon}_{yx}\right) - \tau_{b,y} = \rho g H \frac{\partial h}{\partial y} \tag{4.4}$$

where ($\dot{\varepsilon}_{xx}$, $\dot{\varepsilon}_{yy}$) denote longitudinal/transverse strain rates, ($\dot{\varepsilon}_{xy}$, $\dot{\varepsilon}_{yx}$) represent horizontal shearing strain rates, ν is the vertical averaged ice viscosity and ($\tau_{b,x}$, $\tau_{b,y}$) = $\vec{\tau}_b$ is the basal shear stress. In PISM, deformational velocities from the SIA and sliding velocities from the SSA are weighted and averaged to achieve a smooth transition from shearing flow to sliding flow. The hybrid implementation of stresses appears to be a powerful tool to deal with the flux matching problem at the boundary between grounded and sliding ice [*Schoof*, 2006; *Bueler et al.*, 2007; *Bueler and Brown*, 2009; *Winkelmann et al.*, 2011; *Goldberg*, 2011]. Furthermore, in terms of computational costs, this shallow model is significantly more efficient than higher-order or full-Stokes alternatives.

An energy conservation scheme, as described by *Aschwanden and Blatter* [2009], computes temperature and liquid water content fields using an 'enthalpy-gradient method' [*Pham*, 1995]. The scheme solves the enthalpy balance equation simultaneously in temperate ice (ice at pressure melting point) and cold ice (ice below pressure melting point) and is therefore particularly suited to model the thermodynamic state of polythermal ice masses. Within the ice, the energy scheme accounts for enthalpy advection, diffusion and production of enthalpy by strain heating. Within the bedrock layer, enthalpy evolves diffusively, with a prescribed lower boundary flux equal to the geothermal heat flux. At the ice/bed interface, frictional

heating occurs as ice slides over the bedrock. When the ice at the base is at pressure-melting point, excess energy is used for melting the ice. A simple diffusion relation describes the evolution of the effective thickness of the water layer, W, at the base [*Bueler and Brown*, 2009]:

$$\frac{\partial W}{\partial t} = S + K\left(\frac{\partial^2 W}{\partial x^2} + \frac{\partial^2 W}{\partial y^2}\right), \tag{4.5}$$

where S denotes the local water production by basal melting and K is a diffusion coefficient (200 $m^2\ a^{-2}$). S may become negative, in which case refreezing of basal water occurs as the basal temperature is below pressure-melting point. The basal water diffusion relation provides a simplified description of water transport, in which water diffuses at a prescribed rate (controlled by K) from high to low effective thickness of the water layer. Clearly, the model does not include changes in the hydrological drainage efficiency, which are often related to Alaskan-type surging behaviour [*Kamb et al.*, 1985]. The basal water pressure p_w is given by

$$p_w = \alpha \rho g H \left(\frac{W}{W_0}\right), \tag{4.6}$$

W_0 denotes the preset maximum value for W (of 2 m) at which till saturation is achieved. α is a factor defining the maximum ratio of porewater pressure (p_w) to overburden pressure ($p_I = \rho g H$), which is achieved in case of till saturation. In this study, we used $\alpha = 0.97$, which is accordance with observations that α is close to 1 [*Luthi et al.*, 2002]. The basal water effective thickness at the ice margin is set to zero.

Sliding velocities in PISM are derived by iteratively solving the SSA, in which the basal shear stress, $\vec{\tau}_b$, has a pseudo-plastic form:

$$\vec{\tau}_b = -\tau_c \frac{\vec{u}_b}{|\vec{u}_b|^{(1-q)} u_0^q}, \tag{4.7}$$

where τ_c denotes the yield stress, u_b is the basal velocity vector, u_0 is a constant threshold velocity (100 m a^{-1}) and q is the pseudo-plasticity exponent, which can take values ranging from 0 (perfectly plastic till) to 1 (linearly viscous till) [*Clarke*, 2005]. In this study, the till is assumed to behave plastically or nearly plastically with values of q ranging from 0 to 0.3. Nearly plastic deformation implies that some, but limited, till deformation occurs when the applied stress is slightly smaller than the yield stress. The yield stress formulation is given by [*Bueler and Brown*, 2009]

$$\tau_c = c_0 + \tan(\phi)\,(p_I - p_w). \tag{4.8}$$

Here c_0 is the till cohesion (set to zero) and ϕ is a material parameter describing the material strength of the till, which is assumed to be spatially invariant, in contrast to *Bueler and Brown* [2009]. Values of ϕ range from 7.5 to 30 degrees for the different experiments. Note that $\alpha = 1$ would imply that the yield stress goes to zero in case of till saturation.

In PISM, ice dynamics, thermodynamics and hydrology are coupled within a single framework. Sliding velocities are computed from the SSA stress equation in which the driving stress is balanced by membrane stresses and basal friction. The basal shear stress is a function of the basal water pressure (Equations (4.7) and (4.8)), while the basal water pressure is in turn affected by basal melting (Equations (4.5) and (4.6)). Basal melting follows from the enthalpy equation, in which frictional heat production depends on the magnitude of sliding velocities. This is an example showing how the different regimes of the model are connected. The interaction between dynamics, thermodynamics and hydrology is crucial in the description of cyclic flow.

4.2.2 Numerical setup

Model experiments were conducted on a synthetic bottom topography (Figure 4.1), using a 88×56 horizontal grid (grid spacing 1.25 km). The basal profile is inclined such that the central flow line is at a 1.0° inclination, thereby forcing the ice to flow to the left in Figure 4.1. An increasingly sloping bed topography towards the edges in the y-direction and upstream in the x-direction prevents ice flow out of the model domain. Consequently, all ice volume variations are due to changes in the total mass balance, related to fluctuations in the extent of the ice cap.

The vertical grid contains 150 unevenly distributed layers (more concentrated near the base). In the bedrock thermal model, a vertical grid containing ten evenly distributed layers extending 50 m into the bed is applied. An adaptive time-stepping scheme selects the largest time-step for which stability of the mass-continuity and energy-conservation scheme is assured, thereby significantly improving computational efficiency [*Bueler and Brown*, 2009].

4.2.3 Experiments

To a large extent, parameters ϕ and q control the area and magnitude of sliding flow, as they directly affect the basal resistance experienced by moving ice. In a first set of experiments, referred to as 'basal parameter experiments', a systematic exploration of the $\phi - q$ parameter space is carried out to study the relation between these parameters and the presence and characteristics of cyclic flow (Section 4.3.1).

Finally, in a second set of experiments, referred to as 'climate feedback experiments', the impact of including a surface-height-dependent mass balance and surface temperature formulation on the oscillation characteristics is studied (Section 4.3.2). In previous experiments, a location dependent surface mass balance and temperature are prescribed. Feedback mechanisms associated with the inclusion of a surface height-dependence of the specific mass balance and ice surface temperature may interfere with other feedback mechanisms active during oscillations, which complicates the analysis of oscillatory flow. Hence, the time-dependent

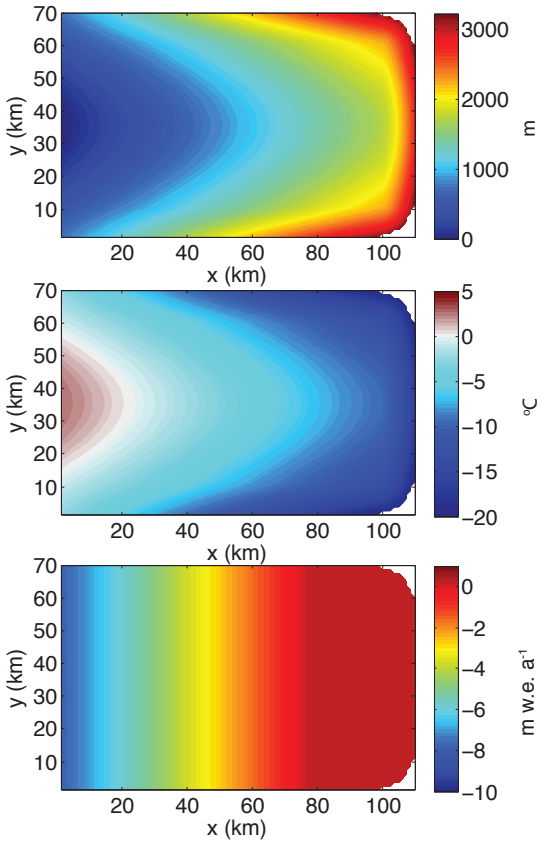

Figure 4.1: *Contour maps of the synthetic bedrock topography (top panel), the prescribed surface temperature (middle panel) and the prescribed surface mass balance (bottom panel). The surface mass balance is given in meters water equivalent per year (m w.e. a^{-1}).*

effect of surface height variations on the surface mass balance and temperature is studied separately.

4.2.4 Climate setup

The prescribed surface mass balance (Figure 4.1) is assumed to increase linearly along the flow line with the height of the bed at a rate of 0.006 m w.e. a^{-1} m^{-1} and has an upper limit of 0.33 m w.e. a^{-1}. A zero mass balance is prescribed at the domain boundaries to prevent ice formation by accumulation at the boundary of the model domain. Forced by the valley shape of the bed profile with steepest slopes near the domain boundaries, ice flow is always directed inward, i.e. away from the domain boundaries, and hence no ice will form at the domain edges. The imposed mass balance distribution together with the valley shaped

bedrock forces the ice mass to form an ablating tongue downstream of a wide accumulation basin.

The prescribed surface temperature (Figure 4.1) is set to increase linearly with height of the bedrock at a rate of 0.007 °C m^{-1}. In the basal parameter experiments (Section 4.3.1), the equilibrium line altitude (E) and the 0°C-surface temperature height (z_{T_0}) correspond to a bedrock height of 1350 m (along the center flowline) and 400 m, respectively.

In the climate feedback experiments (Section 4.3.2) the mass balance and surface temperature are a function of the time-dependent surface height instead of the basal topography. Therefore, E and z_{T_0} are corrected for the altitudinal difference, which is required to obtain an ice cap of approximately similar size as in the corresponding basal parameter experiments. More specifically, values of E and z_{T_0} have been corrected for the mean ice thickness derived from the corresponding run without the height feedback.

In all experiments, the chosen climate setup results in a polythermal ice mass, with temperate ice at the base of the tongue, being surrounded by cold ice upstream. The experimental setup is not designed to replicate one specific type of observed cyclic behaviour, like small-scale surging of valley glaciers or large-scale ice stream flow behaviour, but rather serves the purpose of identifying the processes and interactions involved in multiple types of oscillatory flow. We purposely selected a climate set-up that produces an ice cap with a polythermal basal thermal structure, since previous work has indicated the dependence of a variety of flow instabilities on fluctuations in basal melt conditions. For example, changes in the basal thermal regime have been linked to unstable cessation of ice stream flow [*Tulaczyk et al.*, 2000b], thermally controlled surging [*Clarke*, 1976; *Fowler et al.*, 2001] and have been proposed to explain Heinrich-type oscillations [*MacAyeal*, 1993]. Additionally, the current set-up allows for varying sliding and climate parameters over a wide range of values, while the ice margins do not cross the domain boundaries.

4.3 Results

An underlying assumption in the derivation of the SIA and SSA and higher-order models, based on the Stokes model for a slow flowing fluid [*Fowler*, 1997], is that inertia from flow accelerations can be neglected in the stress equations. This implies that the flow field is determined fully by the ice geometry (thickness and slope), boundary stresses and the ice viscosity. Ice flow at a certain time is therefore not directly affected by the modelled ice velocities of the previous time step. Consequently, oscillatory behaviour of masses based on inertia, e.g. a spring-mass oscillation, is intrinsically infeasible in a "slow" flow model. In case the shape of an ice mass is forced out of its equilibrium state, ice velocities will change such that the surface profile will relax back to its equilibrium shape in a nearly-diffusive way following the mass continuity equation (the SIA is fully diffusive, whereas longitudinal stresses in the SSA allow for ice flow in the across-slope direction). In the absence of feedback mechanisms

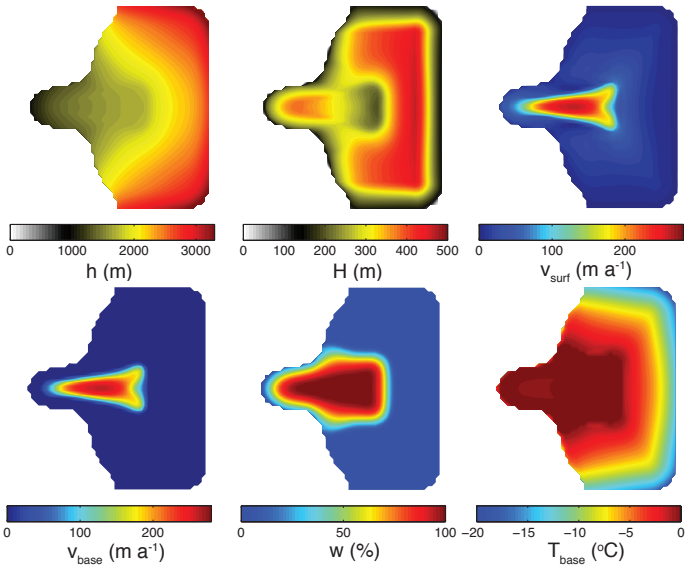

Figure 4.2: *Contour maps of (a) mean surface height, h, (b) ice thickness, H, (c) surface velocity, v_{surf}, (d) basal velocity, v_{base}, (e) water saturation level, w, and (f) and basal temperature, T_{base}, in the basal parameter experiment with (ϕ, q) = (12.5°, 0.0).*

enhancing flow or sliding variations, geometric perturbations will not initiate a sustained oscillation. Cyclic flow behaviour therefore shows up as internal or external feedback processes activate when the ice mass is restoring itself from an out-of-equilibrium situation. The aim of this study is to qualitatively describe possible feedback mechanisms in order to understand the oscillatory behaviour found in simulated ice velocities.

4.3.1 Basal parameter experiments

First, the impact of changes in the parameters controlling the basal shear stress on the presence and characteristics of oscillatory flow is discussed. *Jiskoot et al.* [2000] have illustrated that sediment properties exert a strong control on the occurrence of surging behaviour in Svalbard. In terms of computational costs, it is efficient to start the basal parameter experiments with a fully developed ice mass instead of prescribing ice-free conditions at $t = 0$. Therefore, a 5 kyr initialisation run is performed with (ϕ, q) = (20°, 0.0), which serves as a starting point for the experiments with varying values of ϕ and q. Starting from a fully developed ice mass, model runs with values of the till strength ϕ ranging from 7.5 to 22.5° and values of the sliding exponent q ranging from 0.0 to 0.3 are performed.

Figure 4.2 shows contour plots of temporal mean values of six variables, averaged over the run time, in this case for (ϕ, q) = (12.5°, 0.0). The maps illustrate the formation of an ice

tongue with a sliding zone on a temperate base, partially being saturated with water produced by basal melting. Mean basal ice velocities (up to 280 m a^{-1}) dominate over internal deformation velocities in the sliding zone. In cold-based areas, sliding is absent and surface velocities are much lower. The water saturation level in Figure 4.2 is determined by a balance between generation of water by basal melting and diffusion of water from a high to low saturation level (Equation (4.5)). Along the flowline, this leads to a saturated zone bounded downstream by an unsaturated zone as basal water goes to zero at the ice edge, and bounded upstream by an unsaturated zone under the influence of cold ice advection.

The diagram in Figure 4.3 gives an overview of modelled flow behaviour in the output of model runs with various combinations of ϕ and q. Three types of flow are distinguished: (1) stationary fast (sliding) flow, (2) high-frequency oscillatory fast flow (period 114-169 years) , and (3) low-frequency oscillatory fast flow (period 1000+ years). The till strength is a measure of the material resistance of the bed to the ice flow near the base (Equation (4.7)). Reducing the till strength directly enhances ice velocities in the sliding zone as the gravitational driving stress experiences less resistance by basal friction. On the other hand, the sliding exponent, q, defines to what extent the basal shear stress is proportional to the ice velocity. Increasing the value of q enhances basal resistance and thus lowers ice velocities in the sliding zone. Concerning the different types of flow, Figure 4.3 illustrates that increasing ice velocities (by lowering ϕ or q) at some point leads to a shift from stationary ice flow to high-frequency oscillating flow. Further enhancement of ice velocities at some point leads to a transition from high- to low-frequency cyclic flow. The different flow types, transitions and trends in the oscillation characteristics are analysed in the remainder of this section.

The basal water feedback

As mentioned before, oscillations in the model may only arise when a feedback mechanism, causing flow enhancement, prevents relaxation to a steady-state geometry. To illustrate such a mechanism, we consider a perturbed initial surface slope in the sliding zone which is somewhat steeper than the equilibrium slope. Larger driving stresses cause sliding velocities to increase instantaneously. Higher sliding velocities induce more heat production by frictional heating and consequently more basal melt water production. A higher water saturation level reduces basal resistance to the flow and thus leads to further flow acceleration. This flow enhancing feedback mechanism is further referred to as 'the basal water feedback' and was already described by *Robin* [1955]. Among others, *Clarke* [1976] and *Fowler et al.* [2001] also pointed out the importance of this feedback mechanism and related it to surging. The basal water feedback provides an additional 'push' to the ice flow when recovering from a perturbed geometry in regions with a nearly saturated base. In saturated areas, enhanced basal melting does not lead to a further reduction of the basal shear stress. Next, we will discuss the two types of cyclic behaviour illustrated in Figure 4.3 in which the basal water feedback plays a decisive role.

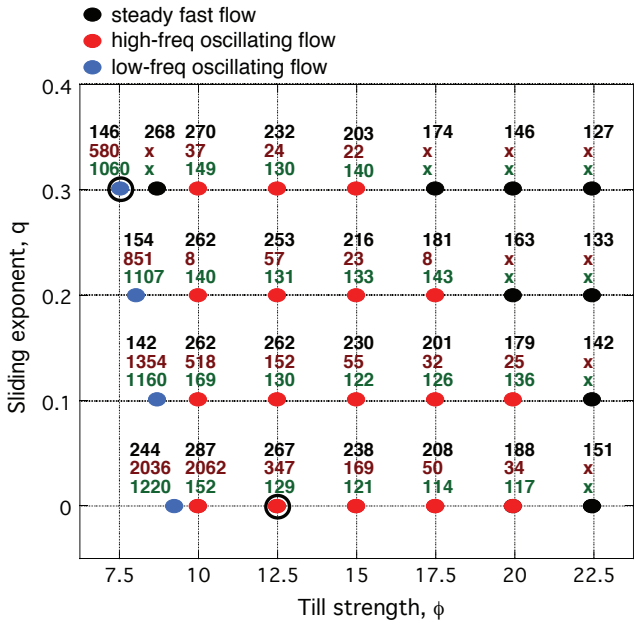

Figure 4.3: *Overview of oscillation features in the basal parameter experiments. The coloured circles indicate the flow type. The value tags represent the mean maximum sliding velocity in m a^{-1} (black), the oscillation amplitude in m a^{-1} (brown) and the oscillation period in years of the maximum sliding velocity (green). Crosses indicate absence of oscillatory behaviour. The periodicity for the high-frequency oscillations ranges from 114 to 169 years. Low-frequency oscillations have a period of 1000+ years. Black circles mark the high-frequency and low-frequency experiments used for further analysis.*

High-frequency oscillations

The two types of oscillations found in the basal parameter experiments both share the property that they exist by virtue of the basal water feedback. Nevertheless, some fundamental differences between the oscillations exist, which explain observed discrepancies in oscillation characteristics (Figure 4.3). First, we focus on one cycle of a high-frequency oscillation, shown for a run with $(\phi, q) = (12.5^\circ, 0.0)$. Temporal mean values of the ice thickness, H, basal velocity, v_{base}, and water saturation, w, of this case are shown in Figure 4.2. Figure 4.4 shows deviations of the latter variables from the temporal mean at four different times t (in yrs) covering one full cycle.

The four snapshots of the thickness deviation indicate oscillatory behaviour of the surface profile with a repetition period of 129 yrs. Steepening of the sliding zone leads to a maximum surface slope in the sliding zone at $t = 35$ yrs, whereas flattening of the surface leads to a minimum at $t = 100$ years. At $t = 0$ years and $t = 70$ years the surface slope in the sliding zone is close to the mean slope. Regarding basal velocities, one may expect extrema to

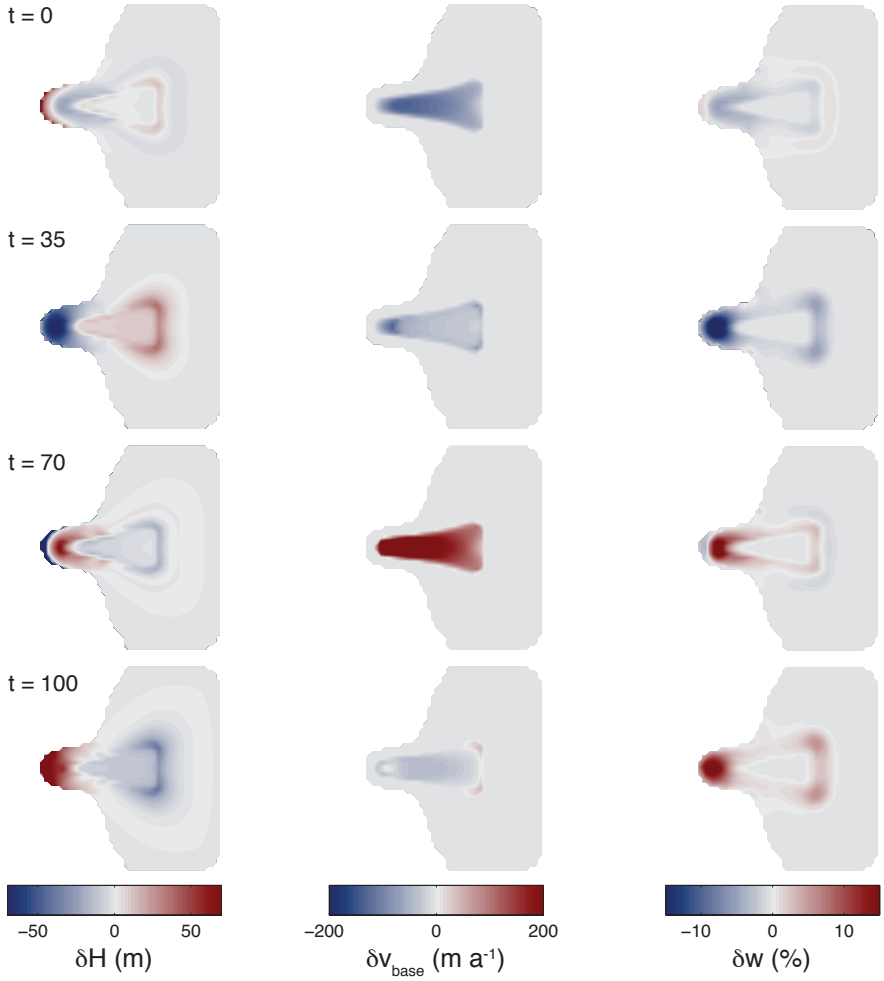

Figure 4.4: *Contour maps of deviations from the mean of (a) the ice thickness, $\delta H = H(t) - H_{\text{mean}}$, (b) the basal velocity, $\delta v_{\text{base}} = v_{\text{base}}(t) - v_{\text{base,mean}}$, and (c) the water saturation level, $\delta w = w(t) - w_{\text{mean}}$ during one cycle of a high-frequency oscillation with (ϕ, q) = (12.5°, 0.0); t is given in years.*

occur simultaneously with extrema in the surface slope and driving stress. However, Figure 4.4 shows that extrema in basal velocities coincide with surface slopes in the sliding zone close to the mean. While the surface is flattening in the sliding zone from $t = 35$ to 70 years, basal velocities continue to increase. This counter-intuitive behaviour is possible as additional basal water production by enhanced velocities leads to a strong enough reduction of the basal resistance near the front of the sliding zone, thereby causing basal velocities to increase and the sliding zone to expand. Conversely, surface steepening in the sliding zone after $t = 100$ yrs is accompanied by a reduction in ice velocities (by amplified reduction of basal water at the front of the sliding zone). Note that the basal water feedback is only effectively changing basal resistance in regions with an unsaturated till, i.e. close to the boundaries of the sliding zone. Flow enhancement by the basal water feedback results in a phase shift of about one-quarter of a period between extrema in the surface slope in the sliding zone and basal velocities and is a necessary ingredient for these oscillations to occur.

The feedback is further illustrated in Figure 4.5, showing deviations from the mean of the driving stress, τ_d, the basal shear stress, τ_b, and the membrane stress, τ_m. The membrane stress comprises the combined effect of longitudinal stresses and transverse shear stresses. The driving stress is mainly controlled by slope variations, whereas the basal water saturation level controls to a large extent the basal shear stress. Between $t = 35$ and 70 yrs, τ_b is reduced by enhanced basal melting. Enhanced sliding velocities lead to flattening of the surface in the sliding area, causing an overall reduction of the driving stress. At the same time, at the upstream and downstream boundary of the sliding zone, enhanced velocity gradients cause the surface to steepen locally and thus lead to a local increase of the driving stress. This local steepening in combination with reduced basal resistance results in enhanced longitudinal stresses at the downstream and upstream boundaries of the sliding zone, which cause the sliding zone to expand even when the driving stress is overall below its mean value. The expansion upstream of the sliding zone is small, since the transition to cold ice hinders growth of the area with a saturated till due to refreezing of basal water.

Figure 4.6 presents time series of ice volume and maximum basal velocity for the basal parameter experiments with $q = 0.1$. Despite the impact of the high-frequency oscillations on the flow velocities, the ice volume is hardly affected. Since in these experiments the mass balance is only location-dependent (not yet a function of surface height), the total mass budget of the ice cap is only affected when the areal extent of the ice mass is altered. High-frequency oscillations tend to have a small impact on the extent of the ice cap and thus on the total mass budget. Termination of ice flow acceleration is primarily caused by reduction of the surface slope rather than advection of cold ice from higher areas. This is reflected in the absence of significant variations in the extent of the temperate base. Note that this type of oscillation therefore relies on variations in the water distribution on a temperate base.

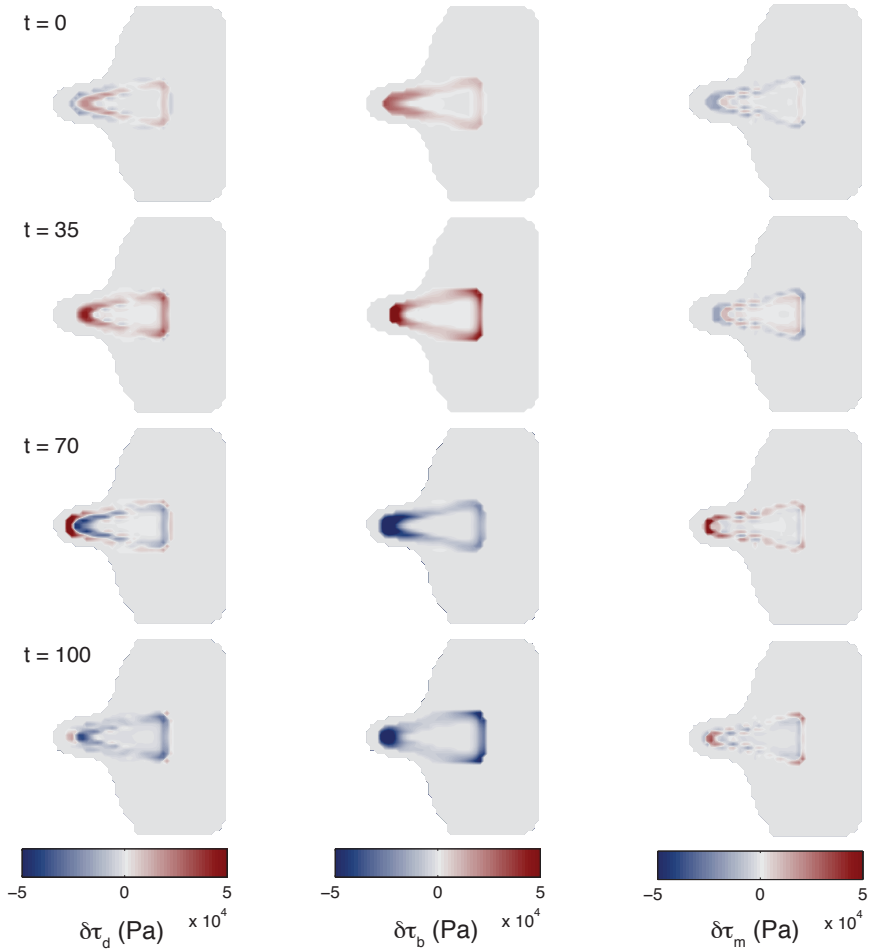

Figure 4.5: *Contour maps of deviations from the mean of (a) the driving stress, $\delta\tau_d = \tau_d(t) - \tau_{d,mean}$, (b) the basal shear stress, $\delta\tau_b = \tau_b(t) - \tau_{b,mean}$, and (c) the membrane stress, $\delta\tau_m = \tau_m(t) - \tau_{m,mean}$ during one cycle of a high-frequency oscillation with (ϕ, q) = (12.5°, 0.0); t is given in years. Values are only shown in regions with a water saturation level greater than 70%.*

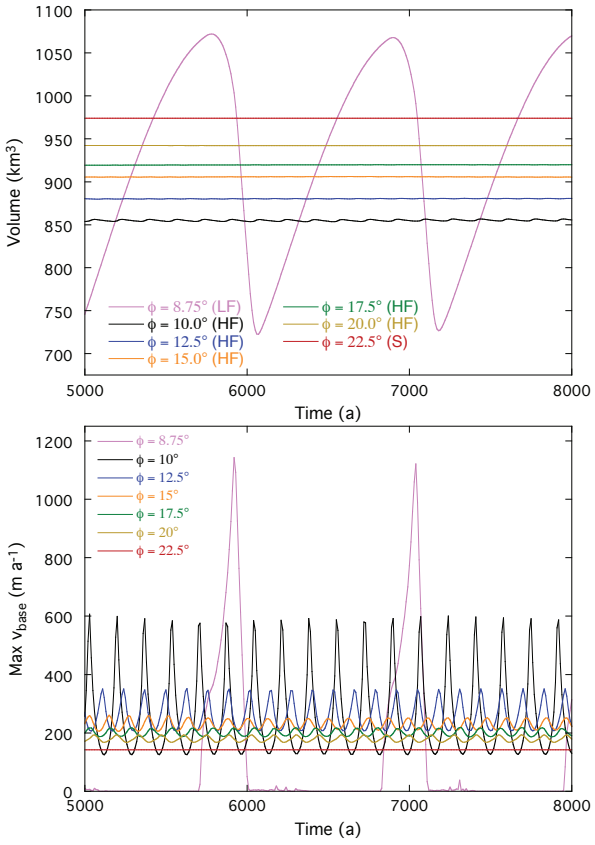

Figure 4.6: *Time series of (a) ice volume and (b) maximum basal velocity for basal parameter experiments with $q = 0.1$ and ϕ ranging from 8.75 to 22.5°; LF, HF and S denote low-frequency, high-frequency and steady fast flow, respectively.*

Low-frequency oscillations

Further reduction of the till strength, ϕ, in the basal parameter experiments at some point leads to a transition to a second type of oscillation, the low-frequency oscillation (Figure 4.3). Figure 4.7 shows snapshots of the ice thickness, sliding velocities, water saturation level and basal temperatures at six different times, t (years), in a cycle for a run with (ϕ, q) = (7.5°, 0.3). At $t = 0$ years, sliding is still absent, while the surface is recovering from a previous tongue advance. Excess energy from strain heating (by internal shearing) and geothermal heating in the temperate zone induces basal melting. Consequently, the water saturation level increases and basal sliding initiates as the yield stress weakens relative to the driving stress. As the tongue advances, the surface of the tongue flattens, thereby reducing the driving stress. Local steepening of the surface occurs down- and upstream of the sliding

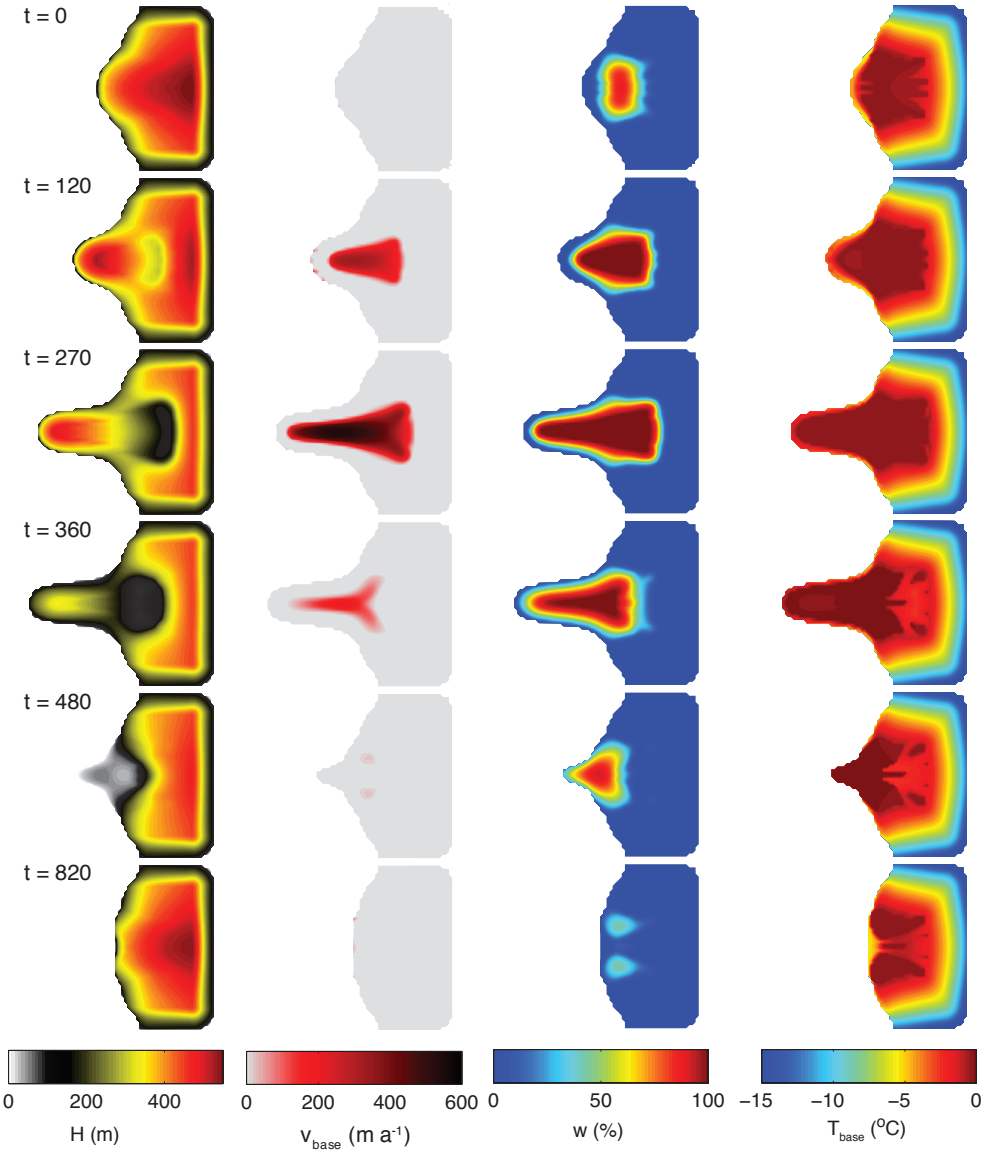

Figure 4.7: *Contour maps of (a) ice thickness, H, (b) basal velocity, v_{base}, (c) water saturation w and (d) basal temperature T_{base}, during one cycle of a low-frequency oscillation with (ϕ, q) = (7.5°, 0.3); t is given in years.*

area. Enhanced driving stresses together with reduced basal resistance, amplified by the basal water feedback, cause flow enhancement and extension of the sliding zone both in the down- and upstream directions. Enhanced strain heating in steep regions promotes basal melting and thickening of the basal water layer. The saturated zone therefore expands in both the downstream and upstream direction, despite refreezing at the transition from temperate to cold basal ice. Greatest sliding velocities are reached at $t = 270$ years. The tongue now extends far into the valley, causing the ice cap to have a negative total mass balance. Further acceleration of the ice stream flow is in part prevented by a limited inflow of ice coming from the accumulation zone and in part by the advection of cold ice into the sliding zone causing basal water to refreeze and the basal shear stress to increase. Consequently, the tongue of the ice cap will thin as surface melting is no longer compensated for by ice inflow. The reduced insulation and basal shear stress after thinning further reduce the available heat at the base and ultimately cause a shutdown of the ice stream. In a similar fashion, *Tulaczyk et al.* [2000b] argued that the interplay of basal shearing, melting and sliding may lead to unstable stoppage of streaming flow. During the recovery phase, a positive mass budget enables ice-cap growth, while strain heating and geothermal heating gradually raise basal temperatures to melting point. This describes a full cycle with a periodicity of 1060 years.

Whereas in a high-frequency cycle the small impact on ice volume shortens the oscillation period, in a low-frequency cycle, the recovery time of the ice geometry (volume) and thermodynamics after a tongue advance is much longer. Figure 4.6 illustrates the difference in volume fluctuations between high- and low-frequency oscillations. As in a high-frequency oscillation, the role of the basal water feedback and local steepening in the low-frequency cycle is again to enhance acceleration and deceleration of ice flow, in that way keeping the ice cap out of a steady state. In contrast to high-frequency cyclicity, significant fluctuations in the extent of the temperate zone arise in low-frequency oscillations, thereby illustrating the important role of cold ice advection. The low-frequency cyclic mechanism described here is to a large extent similar to the 'binge/purge' mechanism proposed by *MacAyeal* [1993] and the thermally-controlled surging mechanism described by *Dunse et al.* [2011], which has been linked to surging in Svalbard *Murray et al.* [2003].

Occurrence and magnitude of oscillations

The description of the high- and low-frequency cycle mechanisms has demonstrated the role of the basal water feedback and local slope variations in maintaining oscillations. The diagram in Figure 4.3 demonstrates that the presence and characteristics of the different types of oscillations depends strongly on the choice of the sliding-law parameters ϕ and q.

Lowering the till strength, ϕ, has the effect of reducing the basal resistance experienced by the sliding ice at the ice/bed interface. As as result, sliding velocities increase and the sliding zone expands. In an environment with overall lower basal shear stresses, flow velocities are more sensitive to fluctuations of the driving stress. Under these conditions, perturbations of

the surface slope have a larger impact on flow velocities. The sensitivity of flow velocity to local slope variations, further amplified by the basal water feedback, is a measure for the amplitude of the oscillations. In this way, the transition from stationary fast flow to oscillatory flow for decreasing values of ϕ can be understood. Stronger variability in ice velocities for lower basal resistance (larger sliding velocities) has also been found by *Dunse et al.* [2011].

Figure 4.3 also shows that high-frequency oscillation amplitudes are inversely proportional to the sliding exponent, q. This is explained by the fact that the basal shear stress, τ_b, is proportional to $|u_b|^q$, which implies that in case $q > 0$, enhanced (reduced) sliding velocities experience enhanced (reduced) basal resistance. For larger values of q, this is a restrictive factor for the effectiveness of flow enhancement. Hence, a more plastic till promotes the occurrence and magnitude of high-frequency oscillations. The opposite was found in *Dunse et al.* [2011], in which an alternative 'sub-melt' sliding law has been used and strongest oscillations arised for a linear sliding law exponent (equivalent to $q = 1$).

A transition to low-frequency cyclicity, in which the ice volume is strongly altered, occurs when local steepening and the basal water feedback are strong enough to expand the temperate zone in the upstream direction. This may only arise in the case of intense flow enhancement, which occurs for very low values of ϕ. Expansion of the temperate zone facilitates a larger inflow of ice into the ablation area, feeding the advancing tongue until cold ice advection shuts down enhanced inflow. The 'activation' of cold ice exposes a major difference between high- and low-frequency cyclic behaviour.

4.3.2 Climate feedback experiments

In the following experiments the prescribed mass balance and surface temperature fields are no longer time-independent. In the climate feedback experiments, the prescribed climate forcing is proportional to the evolving surface height, thereby introducing a time-dependence. Starting without ice, 15 ka model runs were performed for multiple values of ϕ, while fixing q at 0.1. Recall that in previous experiments the surface mass balance and temperature are a function of bedrock height rather than surface height. Therefore, in all experiments a positive correction is applied to the equilibrium line altitude E and 0°C-altitude z_{T_0}, equal to the spatial mean ice thickness in the corresponding basal parameter experiment. In this way, the size of the ice cap and the mean surface temperature in the climate feedback experiments are rather similar in respect to the basal parameter experiments. Nevertheless, a direct (quantitative) comparison of oscillation amplitude and frequency with the outcome of the basal parameter experiments is not feasible.

Mass-balance/height feedback

The dependence of the mass balance on the surface elevation provides an additional feedback mechanism which plays a role in the occurrence of oscillatory flow. Time series of ice volume

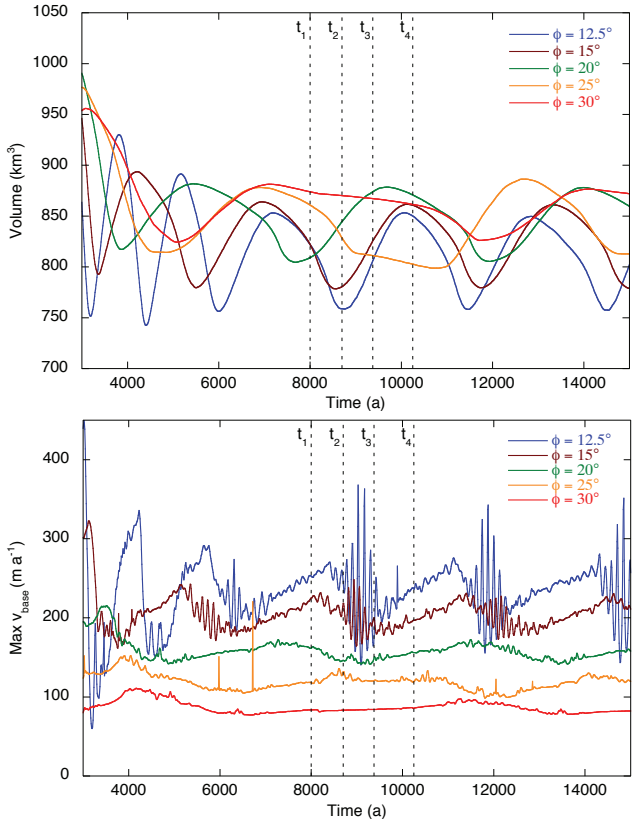

Figure 4.8: *Time series of (a) ice volume and (b) maximum basal velocity in the mass-balance/height feedback experiments with $q = 0.1$ and ϕ ranging from 12.5 to 30.0°. At $t_1 = 8000$ yrs, $t_2 = 8700$ yrs, $t_3 = 9400$ yrs and $t_4 = 10250$ yrs snapshots of the ice thickness in the run with $\phi = 15.0°$ (brown curves) are taken and shown in Figure 4.9.*

and maximum basal velocities for five model runs with different values of ϕ ($q = 0.1$) are shown in Figure 4.8. Figure 4.9 shows maps of the evolution of the ice thickness and basal velocity at four points in time during one cycle in a run with $\phi = 15°$. Only the tongue of the ice cap varies significantly in thickness during a cycle. As shown in Figure 4.8, $t = t_2$ and t_4 correspond to extrema in the ice volume. Extrema in the basal velocities are found during times of intermediate volume ($t = t_1$ and t_3). At $t = t_1$, basal velocities are high since geothermal heating and internal shearing induce more basal melting after a period with large ice volume (Figure 4.9). A large extent of the ice cap causes the total mass balance to be negative, inducing volume loss. Since the mass balance is surface-height dependent, thinning of the ice induces a more negative mass balance, causing more rapid thinning. In this way, the mass-balance/height feedback is 'pushing' the ice out of the mean geometric state. This feedback causes tongue thinning and terminus retreat to a minimum extent at

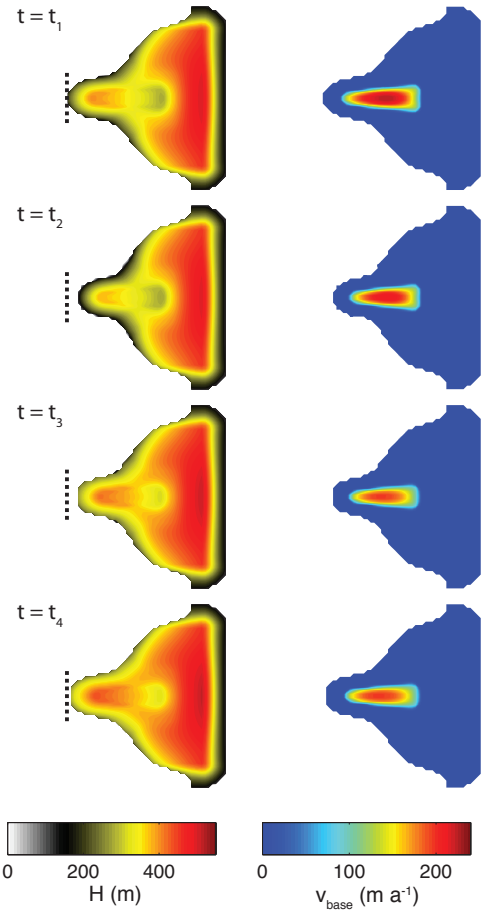

Figure 4.9: *Snapshots of (a) ice thickness and (b) maximum basal velocity in a run with* $(\phi, q) = (15.0°, 0.1)$ *in the mass-balance/height feedback experiments. The times* $t = t_1$ *to* t_4 *refer to the times indicated in Figure 4.8. The dashed lines mark the position of the snout at* $t = t_1$.

$t = t_2$. As the tongue retreats, the total mass budget goes to zero, limiting further retreat of the terminus. Cooling of the thin ice and reduction of the sliding-zone extent result in lower sliding velocities and hence cause the mass budget to become positive after $t = t_2$. The resulting thickening is enhanced by the mass-balance/height feedback, and a delayed response of the ice area cause the mass budget to be positive at $t = t_3$. From $t = t_3$ to t_4, terminus advance initiates and is further enhanced by larger sliding velocities as more heat is available for basal melting. The total mass budget reduces to zero at $t = t_4$, after which thinning sets in. This completes one cycle.

Figure 4.8 illustrates that high-frequency velocity oscillations may coexist with the low-frequency volume cycle described above. These high-frequency cycles seem to be of similar

origin as the high-frequency oscillations in the basal parameter experiments. In line with the basal parameter experiments, the high-frequency oscillations only appear in experiments with low values of ϕ. Whether the low-frequency volume oscillations, forced by the mass-balance/height feedback, occur depends on whether a stable equilibrium state for the ice cap exists. Under stable conditions, a perturbed surface profile induces velocity variations that force the surface back to the equilibrium state. This relaxation effect is then stronger than the mass-balance/height feedback, which tends to enhance ice thickness perturbations. Unstable conditions may thus arise as the relaxation effect is dominated by the mass balance effect. A strong dependence of the mass balance on altitude, i.e. a large balance gradient, directly enhances the strength of the mass-balance/height feedback and thus favours the occurrence of this type of oscillations.

Surface-temperature/height feedback

Next, we introduce a surface height dependence of the surface temperature. Figure 4.10 shows time series of the ice volume and maximum sliding velocity for four model runs with varying till strength. As mentioned above, a quantitative comparison with the basal parameter experiments is not feasible. Nevertheless, qualitatively comparing the results (compare Figures 4.10 and 4.6) indicates very similar behaviour. When the till strength declines, a consecutive shift from stationary fast flow to high-frequency oscillatory flow and from high- to low-frequency cyclic flow occurs. For the chosen set-up, these results suggest that introducing a dependence of the surface temperature on the surface height is not affecting the qualitative characteristics of oscillations.

4.3.3 Resolution experiments

To verify the robustness of the model under grid refinement, the mass-balance/height feedback run with $(\phi, q) = (15^\circ, 0.1)$ was repeated with a grid spacing of 0.83 km (standard /1.5) and 1.88 km (standard $\times 1.5$). In the standard model run, we found two types of oscillatory flow, that is a low-frequency volume cycle and a high-frequency velocity oscillation (Figure 4.8). Adaptive time-stepping assures stability for all experiments. Generally, the model time-step changes with grid resolution following $\Delta t \sim \Delta x^2$. In Table 4.11, mean values of the ice volume, ice thickness, ice area, sliding zone extent and maximum basal velocity are given. Convergence towards a fine grid result is clear for the mean ice volume and thickness. The mean volume shows a decreasing trend towards a higher resolution, with values in the 1.88 km run 4.0% larger and in the 0.83 km run 1.1% smaller than in the standard run. This mainly results from deviations of the mean ice thickness rather than the ice extent. The mean ice area does not converge; however, absolute deviations w.r.t. the standard run are small (up to 1.3% at 0.83 km resolution). The mean sliding-zone extent and maximum basal velocity converge under grid refinement, with absolute deviations from the standard run ranging from

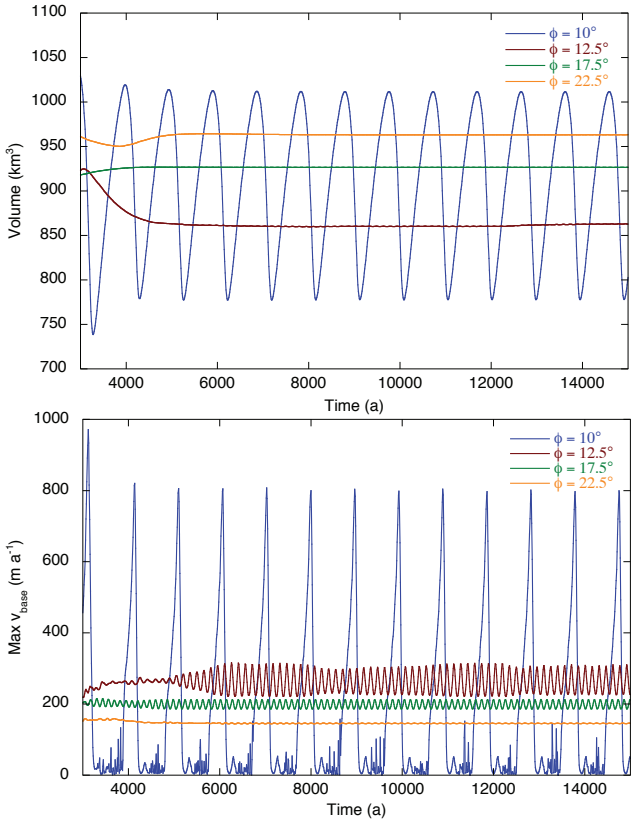

Figure 4.10: *Time series of (a) ice volume and (b) maximum basal velocity in the surface-temperature/height feedback experiments with $q = 0.1$ and ϕ ranging from 10.0 to 22.5°.*

Table 4.1: *Mean volume, V_{mean}, ice thickness, H_{mean}, sliding zone area, S_{mean} and maximum sliding velocity, $v_{\text{base,max}}$, in the mass-balance/height feedback experiment with (ϕ, q) = (15.0°, 0.1) at resolutions of 0.83, 1.25 and 1.88 km*

Grid res. (km)	V_{mean} (km^3)	H_{mean} (m)	A_{mean} (10^3 km^2)	S_{mean} (km^2)	$\bar{v}_{\text{base,max}}$ (m w.e. a^{-1})
1.88	858 (+4.0%)	365 (+4.6%)	2.35 (−0.8%)	225 (−12%)	194 (−4.9%)
1.25	825	349	2.37	255	204
0.83	816 (−1.1%)	340 (−2.6%)	2.40 (+1.3%)	261 (+2.4%)	207 (+1.6%)

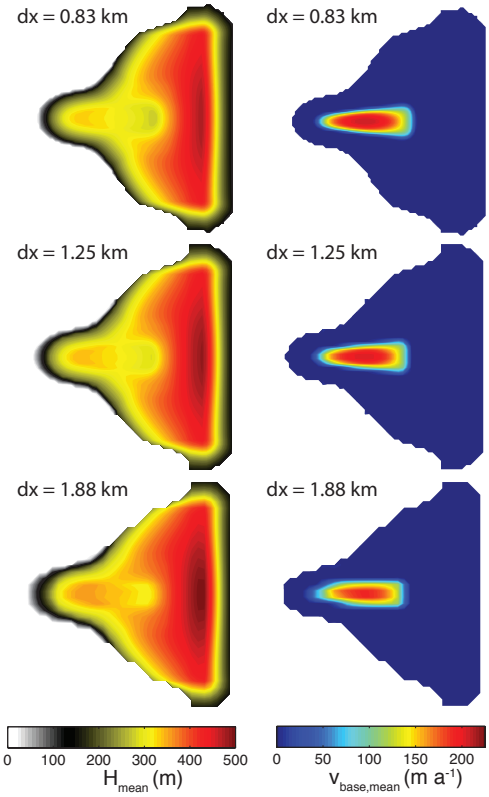

Figure 4.11: *Contour maps of the mean (a) ice thickness, H_{mean}, and (b) maximum basal velocity, $v_{\mathsf{base,max}}$, in the mass-balance/height feedback experiment with (ϕ, q) = (15.0°, 0.1) at resolutions of 0.83 km (top), 1.25 km (middle) and 1.88 km (bottom). Values in parentheses indicate the positive (+) or negative (−) percentage deviations from the standard run*

2.4% (0.83 km) to 12% (1.88 km) and 1.6% (0.83 km) to 4.9% (1.88 km), respectively. Contour maps of the mean ice thickness and mean basal velocity for the three model runs are shown in Figure 4.11. Fluctuations of the ice volume show a decreasing but converging trend towards a finer grid, with an amplitude corresponding to 18% (1.88 km), 10% (1.25 km) and 8% (0.83 km) of the total volume. In terms of oscillation characteristics, the three model runs all show qualitatively similar behaviour with a high-frequency surface oscillation superposed on a low-frequency volume cycle. Generally, we conclude that increasing the grid resolution leads to only minor changes in model behaviour.

4.4 Conclusions & discussion

Model experiments were performed on a synthetic topography to study mechanisms causing oscillatory flow in a thermo-mechanically coupled polythermal ice sheet model (PISM). Oscillatory behaviour in a slow-flow model occurs as internal feedback mechanisms, causing instability, force an ice mass out of an equilibrium state. One of the feedback mechanisms is a basal water feedback, in which the interaction of basal sliding, melting and shearing may effectively enhance velocity fluctuations, thereby avoiding relaxation to a steady state. The basal parameter experiments illustrate that, for a fixed set-up, high-frequency oscillatory flow may initiate if the material till strength is lowered. Further reduction of the till strength amplifies oscillations and at some point leads to a transition to a low-frequency oscillatory flow type. In both oscillation types, flow enhancement by the basal water feedback plays a decisive role in maintaining oscillations. High-frequency oscillations and low-frequency cycles differ significantly in terms of volume fluctuations. In high-frequency oscillations, the surface slope and basal water distribution fluctuates, while the extent of the temperate base is hardly affected. Low-frequency cycles are found to exist by virtue of variations in the polythermal basal structure and the advection of cold ice to the bed. The physical mechanism responsible for low-frequency oscillations in the basal parameter experiments is essentially similar to the oscillatory mechanism discussed by, for example, *Oerlemans and van der Veen* [1984], *MacAyeal* [1993], *Payne* [1995], *Calov et al.* [2002] and *Dunse et al.* [2011]. Low values of the sliding exponent q, implying a nearly-plastic till, favour the occurrence of oscillations, as dampening of perturbed ice flow by related changes in the basal resistance is less pronounced.

Flow enhancement results from the interplay of basal shearing, water production and sliding. We find that oscillatory flow is more likely to occur for lower material resistance of the bed, which is in line with findings that most, if not all, surge-type glaciers are underlain by a layer of easily deformable eroded material [*Murray et al.*, 2000; *Harrison and Post*, 2003]. Although we find oscillations based on variations in of the subglacial water distribution on a temperate bed, due to the simplicity of the water transport model, proposed mechanisms for surging of Alaskan-type caused by transient behaviour of the drainage system's efficiency are not modelled. For example, simulating surge-termination related to a transition between a slow distributed drainage system and a highly conductive conduit system [*Kamb et al.*, 1985; *Kamb*, 1987] would require a more detailed water transport scheme. On the other hand, the proposed mechanism for thermally-controlled soft-bedded surging [*Fowler et al.*, 2001; *Murray et al.*, 2003], often referred to as surges of Svalbard-type, appears to be of the identical origin as the low-frequency oscillations in this study. As in the modelled low-frequency oscillations, flow acceleration during a thermally controlled surge relies on a positive feedback between till weakening and sliding acceleration, whereas termination of flow acceleration is caused by basal refreezing. On a larger scale, *MacAyeal* [1993] used the same principles in a possible explanation for the Heinrich-type oscillations of the Laurentide ice sheet.

The frequency difference between the two oscillation types in the basal parameter experiments is mainly related to the impact of the oscillations on ice volume and the thermodynamic structure. In low-frequency oscillations, the ice volume and basal thermal regime vary significantly during an advance/retreat cycle. The length of the quiescent phase is inversely proportional to the accumulation rate [*Dowdeswell et al.*, 1995; *Eisen et al.*, 2001], which controls the rate of recovery. A more dramatic advance requires a longer recovery time, thereby reducing the oscillation frequency. The periodicity of thermally controlled cyclicity therefore depends strongly on the chosen grid dimensions. Since the experimental setup in this study is not designed to study a specific type of observed cyclic behaviour, we are not able to directly compare simulated timescales of the low-frequency oscillations (1000+ years) with the observed periodicity of Svalbard-type surging (50-500 years) [*Dowdeswell et al.*, 1991] and the frequency of Heinrich-type oscillations ($\sim$7000 years).

Introducing a surface-height dependence of the mass balance may lead to another type of instability in which surface perturbations are enhanced, causing sustained long-term fluctuations in the ice volume. These oscillations become more pronounced with a larger balance gradient. Incorporating a height dependence of the surface temperature does not affect the qualitative aspects of cyclic flow in the chosen set-up of the experiments.

Numerical inconsistencies related to a discontinuous transition of ice flow at the ice stream margin, as discussed by *Fowler* [2001] and *Bueler and Brown* [2009], are tackled in PISM by the hybrid implementation of stress equations, causing a smooth transition from non-sliding to sliding ice flow. Results of ISMIP HEINO [*Greve et al.*, 2006; *Calov et al.*, 2010] have previously demonstrated that oscillatory flow is not confined to models with a sharp transition from sliding to non-sliding flow. Our results confirm this finding.

In all experiments in this study the basal thermal structure was polythermal, with a temperate zone downstream of a cold-based region. It would be interesting to also study flow patterns for different polythermal structures as well as for fully temperate-based ice. Furthermore, rather than using a invariant external climate forcing a time-dependent forcing could be used to study possible interactions of climatic fluctuations and internal flow instabilities.

5

An inverse method to estimate basal topography and initialise ice flow models

We evaluate an inverse modelling approach to reconstruct distributed subglacial topography. The inverse method involves an iterative procedure in which an ice dynamical model (PISM) is run multiple times over a prescribed period, while being forced with space and time-dependent climate input. After every iteration bed heights are adjusted using information of the remaining misfit between observed and modelled surface topography. The inverse method is first applied in synthetic experiments with a constant climate forcing to verify convergence and robustness of the approach in three dimensions. In a next step, the inverse approach is applied to Nordenskiöldbreen, Svalbard, forced with height- and time-dependent climate input since 1300 AD. An L-curve stopping criterion is used to prevent over-fitting. Validation against radar data reveals a high correlation (up to $R = 0.89$) between modelled and observed thicknesses. Remaining uncertainties can mainly be ascribed to inaccurate model physics, in particular uncertainty in the description of sliding. Results demonstrate the applicability of this inverse method to reconstruct the ice thickness distribution of glaciers and ice caps. In addition to reconstructing bedrock topography, the method provides a direct tool to initialise ice flow models for forecasting experiments.

This chapter is based on: Van Pelt, W., J. Oerlemans, C. Reijmer, R. Pettersson, V. Pohjola, E. Isaksson, and D. Divine (2013b), An iterative inverse method to estimate basal topography and initialize ice flow models, *The Cryosphere*, *7*(3), 987–1006

5.1 Introduction

The inaccessibility of the bed underneath glaciers and ice caps limits observational constraints on basal conditions. Surface data are much more abundant and, when linked to basal parameters using a forward model, can be used in an inverse manner to better constrain basal boundary conditions (e.g. *MacAyeal* [1992], *Joughin et al.* [2004] and *Raymond Pralong and Gudmundsson* [2011]). In this study, we focus on reconstructing basal topography. Accurate estimates of the basal topography and ice thickness distribution are needed mainly for two reasons. Firstly, estimates of the ice thickness distribution are required to determine the total ice volume stored in a glacier or ice cap, which is needed to assess the potential contribution to sea-level rise. Secondly, accurate simulation of the future evolution of glaciers and ice caps in a changing climate depends strongly on the initial ice thickness distribution. Proper initialisation of ice flow models should result in an ice geometry and thermodynamic state at the start of a prognostic experiment, which is consistent with the history of the surface climate forcing. The relevance of accurate initialisation has been stressed by e.g. *Oerlemans et al.* [1998], *Huybrechts and de Wolde* [1999] and *Huss et al.* [2008].

Measuring distributed fields of basal topography using Ground Penetrating Radar (GPR) is a laborious and expensive task, hence bed height data sets generally cover the region of interest only partially. This has motivated the development of techniques to indirectly estimate the ice thickness distribution. A first attempt was made by *Nye* [1951], who assumed a perfectly plastic ice rheology in order to compute the ice thickness from the surface slope and a constant yield stress. This method has been used to recover glacier bed topographies by e.g. *Haeberli and Hölzle* [1995], *Oerlemans* [1997] and *Paul and Svoboda* [2010]. Recently, *Li et al.* [2012] extended this method accounting for variable width of the glacier, thereby incorporating the effect of side drag on the stress state. Alternatively, several studies used the mass continuity equation to derive the thickness distribution. *Farinotti et al.* [2009] and *Huss and Farinotti* [2012] applied a mass conservation approach to compute the thickness distribution from surface height data. Other mass continuity approaches rely on velocity data to compute bed heights (e.g. *Morlighem et al.* [2011]; *McNabb et al.* [2012]). Inverse control methods have been applied to Antarctic ice streams to simultaneously recover basal topography and slipperiness, requiring distributed fields of surface topography and velocity [*Thorsteinsson et al.*, 2003; *Raymond and Gudmundsson*, 2009; *Raymond Pralong and Gudmundsson*, 2011]. In *Clarke et al.* [2009], an alternative method is proposed and discussed, which uses neural networks to obtain thickness estimates from surface height data.

In this study, an iterative inverse method is presented to reconstruct distributed basal topography, given a map of surface height data, an ice flow model and a time-dependent surface climate forcing. The approach does not require surface velocity input and aims to minimise the discrepancy between modelled and observed surface heights at the end of time-dependent model runs. In this way, it additionally provides an efficient way to initialise ice flow models for forecasting experiments. In the spirit of a recent studies by *Pollard and DeConto* [2012]

and *Michel et al.* [2013], a simple regularisation method is employed, in which the surface height misfit is directly used to iteratively update the basal topography. In this manner, complex evaluation of cost-function gradients in order to define a search direction is avoided. This study builds on previous applications of such a correction method in a flow-line context [*Oerlemans*, 2001; *Leclercq et al.*, 2012; *Michel et al.*, 2013] and extends the analysis to three dimensions. The real glacier application to Nordenskiöldbreen, with added complexities related to the presence of data errors and climate variability/feedbacks, serves as step-by-step manual for future applications recovering distributed basal topography and/or initialising ice flow models. First, we present the regularisation method and discuss relevant features of the forward model (Section 5.2). Then the approach is applied in a set of synthetic steady-state experiments to evaluate convergence and robustness of the inverse method in three dimensions (Section 5.3). In Section 5.4 the inverse approach is applied to the glacier geometry of Nordenskiöldbreen, Svalbard. Reconstructed beds are validated against radar observations and the significance of errors is discussed.

5.2 Model & method

5.2.1 Model description

The Parallel Ice Sheet Model (PISM) is used as a forward model in the iterative procedure in which the basal topography is adjusted after every iteration. Here we will address relevant features of the model. For a more elaborate description of the model, the reader is referred to *Bueler and Brown* [2009] and *Winkelmann et al.* [2011].

Forced with fields of surface mass balance and near-surface temperature, experiments are performed with PISM to simulate the spatio-temporal evolution of the surface topography. Ice flow in PISM is a combination of ice movement by internal deformation, described by the Shallow Ice Approximation (SIA) [*Morland and Johnson*, 1980; *Hutter*, 1983], and basal sliding, described by the Shallow Shelf Approximation (SSA) [*MacAyeal*, 1989; *Weis et al.*, 1999]. Weighting and averaging of the two velocity components results in a smooth transition from shearing to sliding flow and hence provides a solution to the flux-matching problem at the transition from sliding to non-sliding ice [*Schoof*, 2006; *Bueler and Brown*, 2009]. Effectively, the SSA is used as a sliding law. As a direct consequence of its 'shallowness', the model is significantly more efficient than higher-order or full-Stokes alternatives in terms of computational costs.

The evolution of the internal thermodynamic structure of the ice is modelled using an energy conservation scheme in which an 'enthalpy-gradient approach' is adopted to compute vertical profiles of water content and temperature [*Aschwanden and Blatter*, 2009; *Aschwanden et al.*, 2012]. Enthalpy advection, diffusion and production by strain heating are modelled in a consistent manner in both cold ice (temperature below pressure-melting point) and temperate

ice (temperature at pressure-melting point). Additionally, a bedrock model simulates the diffusive enthalpy transport in the upper hundreds of meters of bedrock underlying the ice. A fixed geothermal heat flux (0.042 W m^{-2}) is prescribed at the lower boundary of the bedrock model. When ice slides over the bed, frictional heating will contribute to the heat budget at the ice/bed interface. In case the bed is at pressure-melting point, excess energy will induce basal melting and local water production. Basal water is stored locally and may refreeze when the basal temperature drops below pressure-melting point. In this simplified water model exchange of water between grid cells is not accounted for. An approximation of the local conservation of energy determines the spatial distribution of temperate and cold ice and the spatial distribution of basal water production. A more realistic water model, incorporating a Darcian transport scheme, surface to bed transport and a transient transmissivity of the system, would be needed to realistically simulate water transport and seasonal variability in water layer thickness and pressures, which is beyond the scope of this work.

The connection between water layer thickness, water pressure and the basal shear stress follows the description of *Bueler and Brown* [2009] and Chapter 4. A pseudo-plastic formulation for the basal shear stress $\vec{\tau}_b$ as a function of the basal sliding velocity $\vec{u}_b$ and the yield stress τ_c is used:

$$\vec{\tau}_b = -\tau_c \frac{\vec{u}_b}{|\vec{u}_b|^{1-q}\,\vec{u}_b^{\,q}} \,. \tag{5.1}$$

A value of the pseudo-plasticity exponent q of 0.4 is used here, which is equivalent to a Weertman-type sliding law exponent of 2.5. The yield stress τ_c depends on the material till strength ϕ and water pressure p_w according to *Clarke* [2005]:

$$\tau_c = \tan(\phi)\,(\rho g H - p_w) \,, \tag{5.2}$$

where ρ is the ice density (900 kg m^{-3}), g is the gravitational acceleration (9.81 m s^{-2}) and H the ice thickness. The water pressure p_w is a fraction of the overburden pressure and depends linearly on the effective water layer thickness as described in *Bueler and Brown* [2009]. Given the simplicity of the determination of the basal shear stress, which is inevitable given our current knowledge of the basal conditions, we accept that a major source of error in the reconstructed basal topography stems from uncertainty in modelling the basal resistance. In Section 5.4 reconstructed beds will be validated against independent ground-penetrating radar data, which enables us to quantify the accuracy of the reconstruction and assess the significance of modelling errors.

5.2.2 Correction method

Our main aim is to develop, test and apply an inverse approach in which bedrock heights are iteratively adjusted in such a manner that the misfit of modelled and observed surface topography is minimised. Here we discuss the regularisation technique used to stabilise the

inverse procedure. In contrast to many previous inverse approaches in glaciology, often aiming to minimise the misfit in surface velocities to reconstruct basal shearing conditions (e.g. *MacAyeal* [1992], *Joughin et al.* [2004]), the correction method used here does not rely on evaluation of cost function gradients to update model parameters. *Pollard and DeConto* [2012] recently presented a correction method in which the local surface height misfit is directly used to iteratively update basal slipperiness. In a similar fashion, we directly use the surface height misfit to iteratively adjust bed heights. Forced at the surface with prescribed mass balance and near-surface temperature input, the ice flow model (PISM) is iteratively run over a specified period of time. At the end of every model iteration, local deviations between modelled surface heights h_{mod} and reference heights h_{ref} are evaluated and directly applied to compute a new bed b

$$b^{n+1} = b^n - K\left(h^n_{mod} - h_{ref}\right) \ , \tag{5.3}$$

where K is a constant, referred to as the relaxation parameter, and n is the iteration number. The magnitude of the bed correction in response to a surface discrepancy hence scales linearly with the relaxation factor K, which needs to be chosen small enough to avoid instabilities due to overcompensation of the bed, and large enough to speed-up convergence of the approach. The same correction method has previously been applied in a flow-line context in *Oerlemans* [2001], *Leclercq et al.* [2012] and *Michel et al.* [2013] and is based on the intuitive principle that a higher bedrock elevation leads to an overall higher surface elevation. In the field of fluid-dynamics *Heining* [2011] studied gravity-driven film flow over an undulating bed and used the correction method to successfully recover basal topography in idealised flow-line experiments. Perturbations of the bed height lead to a non-local surface expression with a transfer amplitude and phase-shift depending on multiple factors including slip ratio and dimensions of the basal perturbation, as shown by *Gudmundsson* [2003] and *Raymond and Gudmundsson* [2005]. Observational verification for many of their theoretical findings has recently been provided by *De Rydt et al.* [2013]. When recovering a single bump in an otherwise flat bed, the surface misfit and hence the bedrock correction will initially be out-of-phase with the actual bump position (when starting from a fully flat bed). We will illustrate in Section 5.3.1 that the interaction of bed adjustments and the surface misfit causes the recovered bump to gradually grow and move into the right position.

5.3 Synthetic experiments

Experiments with a synthetic ice sheet give insight in the functionality of the bedrock reconstruction method and the sensitivity of convergence to the chosen setup of the experiments.

Prior to the iterative procedure to recover the basal topography, reference bedrock and surface height geometries are required. The reference geometries are the geometries we aim to reconstruct with the inverse procedure. A reference bed topography is manually designed and serves as a lower boundary in an initial model run performed to produce a reference surface

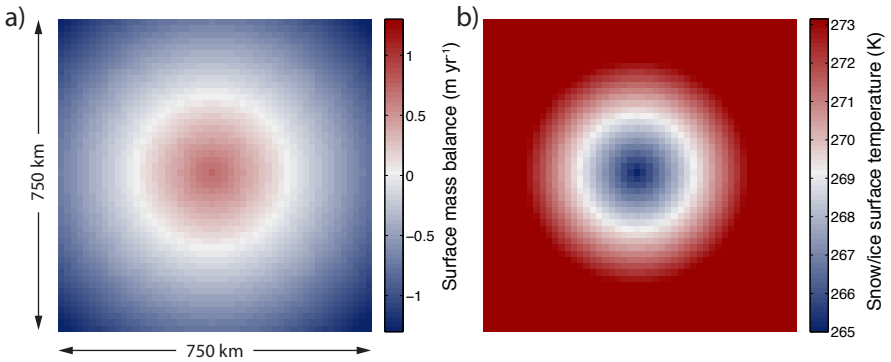

Figure 5.1: *The prescribed surface mass balance (a) and snow/ice surface temperature (b) forcing fields in the synthetic experiments.*

(h_{ref} in Equation 5.3). After the initial run, the designed reference basal topography is 'forgotten' and the iterative recovery starts from a random initial bed (a flat bed in the synthetic experiments) and attempts to gradually recover the reference basal topography. In both the initial and iterative model runs, the model starts without ice and an invariant mass balance and temperature forcing is applied, shown in Figure 5.1. The model runs forward in time over a period of 20 kyrs, which is sufficient to reach a steady state geometry. After every model iteration, the surface height misfit ($h_{mod} - h_{ref}$) is computed and the bed is adjusted accordingly. Both the prescribed mass balance and temperature at the snow/ice interface are constant in time and vary linearly with distance to the domain centre (Figure 5.1). Resulting steady-state geometries are approximately axisymmetric and the velocity field is characterised by an internal deformation dominated centre region and more significant sliding velocities towards the ice margin. In the standard setup the relaxation factor K is set to 1.

Experiments are conducted on a 50 x 50 horizontal grid with a 15 km grid spacing. The vertical grid in the ice contains 100 unevenly distributed layers (more concentrated near the bed). The vertical grid in the bedrock consists of 10 layers extending down to 200 m below the ice-bedrock interface.

The idealised framework of the synthetic experiments allows us to study convergence of the inverse approach in three-dimensions under simplified conditions. Additional complexities related to the presence of noise in the surface height data, height-feedbacks of the climate forcing and non-steadiness of the final surface profile, which are relevant in an application with real data, are addressed in Section 5.4. The experiments in this section are divided into two parts, discussing recovery of a bed containing a single bump ('one-bump' experiment, Section 5.3.1) and a distributed field of bumps ('bump-field' experiment, Section 5.3.2).

5.3.1 'One-bump' experiment

In a first experiment the iterative procedure is used to recover a single bump in an otherwise flat bed. The initial run produces reference surface height and bedrock height profiles shown in Figure 5.2a and 5.2b, respectively. In the iterative bed recovery procedure, an arbitrary total of 40 iterations is performed of which snapshots of the recovered bed are shown in Figure 5.2d. Corresponding snapshots of surface misfit, defined as the modelled minus the reference bed height, are plotted in Figure 5.2c. Surface velocities are dominated by deformation in the interior (up to 13 m a^{-1}) and sliding near the ice margin (up to 48 m a^{-1}).

With the increasing number of iterations the bump in the bed is gradually recovered (Figure 5.2d) and the surface misfit diminishes (Figure 5.2c). The presence of the bedrock bump in the reference bed raises the reference surface upstream of the bump position (and slightly lowers the surface downstream of the bump). At the start of the iterative procedure with a flat bed, the surface misfit is therefore negative upstream of the reference bump position, thereby inducing a positive bed correction. In subsequent iterations the gradually growing bump upstream of the reference bump position affects the surface misfit such that the negative misfit (positive bed correction) gradually shifts in the downstream direction (Figure 5.2c). Consequently the recovered bump slowly moves towards the reference position, while its amplitude increases (Figure 5.2d). It can be shown that for a phase-shift between the reference bed bump and the corresponding surface bump smaller than 180°, the recovered bump position will converge to the reference position. *Raymond and Gudmundsson* [2005] and *Gudmundsson* [2003] illustrate that phase-shifts do not become larger than 90° for a wide range of parameter values. A cross-sectional view of the bed in Figure 5.2e further illustrates the recovered bump movement and growth with the number of iterations. The above experiment demonstrates that despite the non-local surface expression related to a local bed height perturbation, the local recovered bed approaches reference values when applying sufficient iterative corrections. The non-local surface expression in both the along-flow and cross-flow direction is apparent for the entire grid (Figure 5.2c) and reduces with the number of iterations. Note that the bed perturbation of up to 150 m results in a surface perturbation of only up to 10 m (ice thickness $\sim$1000 m), which is indicative of the low transfer amplitude of bed height variability to the surface. A larger transfer amplitude would enhance the growth rate of the recovered bump and hence speed-up convergence. Among other factors, the low mean surface slope (0.3°) in this example limits the bed to surface transfer amplitude [*Raymond and Gudmundsson*, 2005].

5.3.2 'Bump-field' experiment

The previous experiment demonstrates convergence of the bedrock reconstruction method when recovering a single bump. Next, we apply the iterative method to a distributed field of bumps and additionally verify the robustness of the approach when changing: 1) the initial

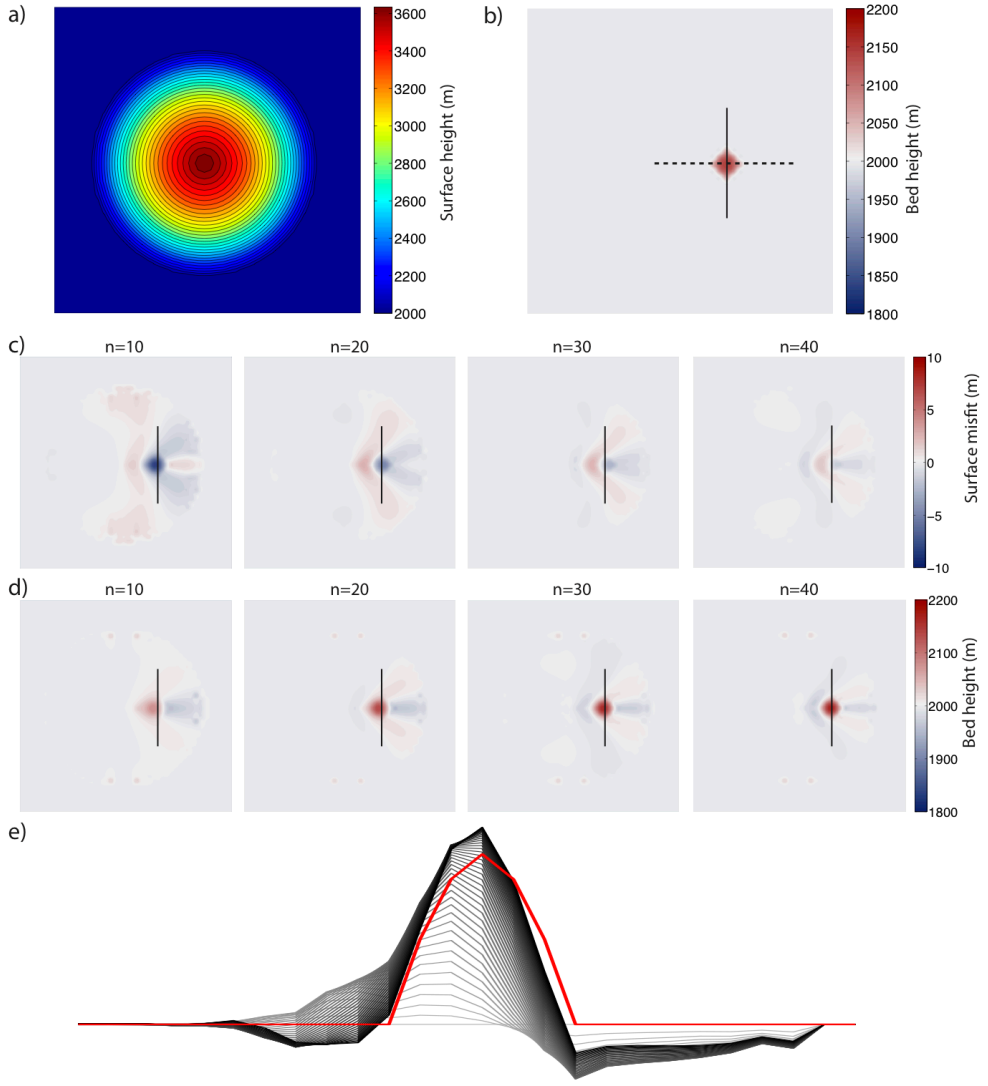

Figure 5.2: *Recovery of a single bump with an amplitude of 150 m in an otherwise flat bed. Panels a) and b) show reference surface and bed heights; c) and d) show snapshots of the surface height misfit and recovered bed height after $n = 10$, 20, 30 and 40 iterations. In e) the gradual recovery if the bed is illustrated along the cross-section marked by the dashed line in b); every line represents the bed after a certain iteration while the grayscale is a measure for the iteration number (low = light grey, high = black); the red line marks the reference bed height. Solid lines in b), c) and d) mark a fixed position to illustrate movement of the recovered bump and surface misfit.*

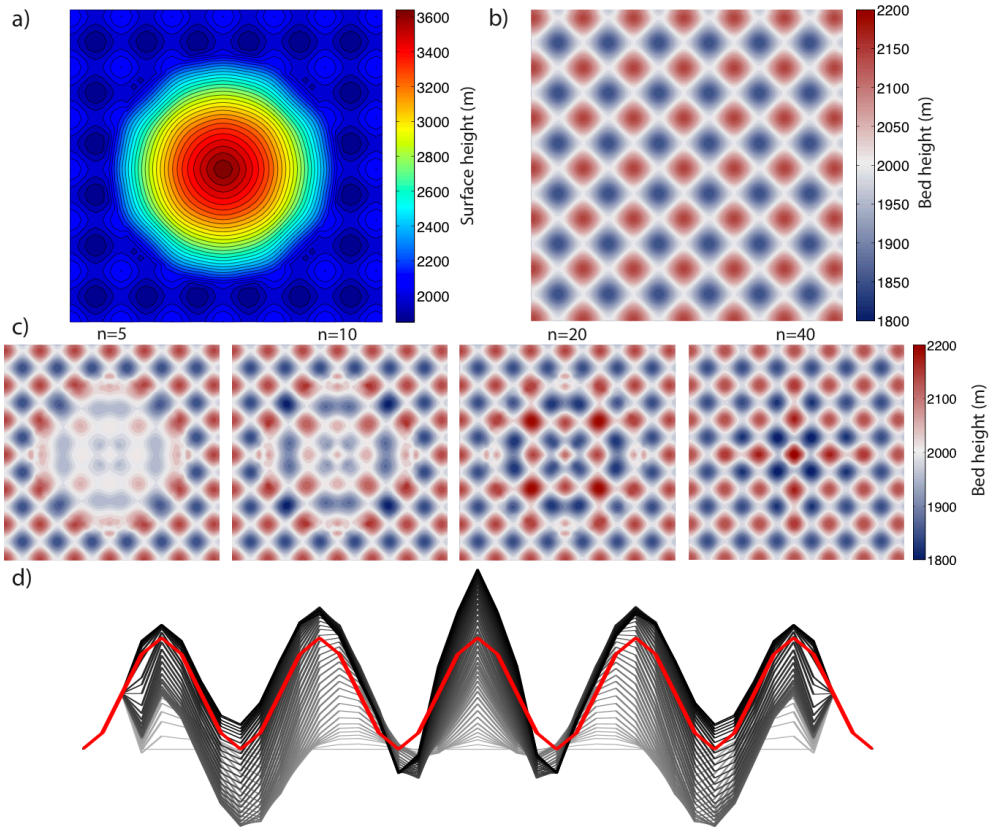

Figure 5.3: *Recovery of a field of bumps with an amplitude of 150 m. The reference surface and bed are shown in a) and b). Panel c) shows snapshots of the recovered bed height after n =10, 20, 30 and 40 iterations. In d) the gradual recovery if the bed is depicted with every line representing the bed after a certain iteration while the grayscale is a measure for the iteration number (low = light gray, high = black); the red line marks the reference bed height.*

bed, 2) the relaxation factor K, 3) the mass turnover and 4) the bump dimensions.

An initial model run produces reference bed and surface heights shown in Figure 5.3a, and 5.3b. The inverse procedure, starting from a flat bed underneath the ice, uses the misfit between the modelled and reference surface heights to iteratively update the bed. Snapshots of the bed during the iterative procedure in Figure 5.3c indicate gradual reduction of the misfit of the reconstructed bed w.r.t. the reference bed. A cross-sectional profile of the bed in Figure 5.3d illustrates convergence with the number of iterations and shows that after 40 iterations errors remain largest near the centre of the ice sheet. *Raymond and Gudmundsson* [2005] showed that the bed to surface transfer amplitude after a bed height perturbation is propor-

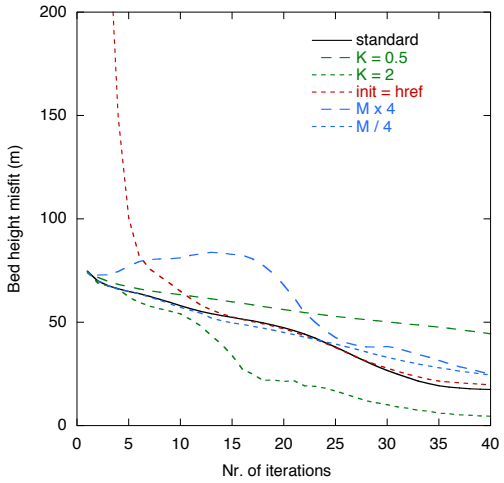

Figure 5.4: *The root-mean-square bed height misfit versus the number of iterations for experiments with varying relaxation factor K (green), initial bed (red) and balance gradient (blue).*

tional to the surface slope and the slip ratio, i.e. the ratio of sliding vs. shearing velocity. In this experiment, enhanced sliding velocities towards the margin and low slopes in the interior lead to an increasing transfer amplitude towards the margin. A higher transfer amplitude implies a stronger surface response to bed height deviations and consequently larger corrections of the bed. From this, lower bed height convergence rates towards the ice sheet centre in Figure 5.3c and 5.3d can be understood.

Figure 5.4 shows the root-mean-square surface misfit versus the number of iterations for multiple sensitivity experiments. The magnitude of the bed correction scales linearly with the relaxation factor K. A low value for K implies slower convergence of the bed. On the other hand, setting K too high might lead to over-correction of the bed. That is, when the surface height is very sensitive to changes of the bed height, the associated large bed corrections might lead to a surface misfit (of opposite sign) larger than its value after the previous iteration, which is a sign of over-compensation of the bed. Consequently, an optimum value for K can be selected, which is small enough to achieve stable convergence and large enough to increase the rate of convergence. Figure 5.4 clearly shows faster convergence for large K.

The sensitivity of the approach to a different bed topography at the start of the first iteration is investigated by performing an additional run in which the initial bed height is strongly overestimated by setting it to the reference surface height. This will lead to a significant overestimation of the surface height in the first few iterations. Figure 5.4 illustrates that, despite a much larger initial bed (and surface) misfit, the misfit after 40 iterations is nearly identical. Final beds after 40 iterations are similar, indicating that the reconstructed bed is not very sensitive to the chosen initial topography after many iterations.

We further investigate the applicability of the method when applying a different mass balance - altitude gradient, implying significant changes in ice dynamics and surface geometry. Before starting the iterative recovery, reference profiles are constructed consistent with the new surface forcing. Figure 5.4 illustrates that convergence is apparent for both a positively (4 times larger) and negatively (4 times smaller) perturbed balance gradient. A larger balance gradient implies larger ice fluxes and a thicker ice mass with steeper slopes near the margin. Steep slopes in combination with a high slip ratio near the margin result in a high bed to surface transfer amplitude. The wavy pattern of the surface misfit for the large balance gradient can be ascribed to overcorrection of the bed near the margin. Setting K to a smaller value would reduce this effect.

In order to study the sensitivity of convergence for varying bump dimensions the inverse approach is applied to recover a bed containing a mixture of two bump sizes (Figure 5.5b). Snapshots of the bed in Figure 5.5c and the bed height misfit series in Figure 5.5d indicate convergence and illustrate that large-scale features are recovered more quickly than smaller-scale features. The recovery of the large-scale bumps leads to a rapid drop in the bed misfit until around 15 iterations. The slower recovery of the small-scale bumps continues until the end of the experiment and is particularly slow in the interior (again as a consequence of the small slope). The slower recovery of smaller sized bumps is in line with studies by *Gudmundsson* [2003] and *Raymond and Gudmundsson* [2005], which show an inverse dependence of bed to surface transfer amplitude with the wavelength of the bed perturbation. The fact that larger features are recovered prior to smaller features is used in Section 5.4 to define a stopping criterion for the iterative procedure, which is required when dealing with actual data (containing noise) and modelling errors.

In the aforementioned experiments reference surface heights were generated with the model prior to the inverse procedure. In that case a bed is known to exist for which the reference surface heights exactly match modelled values. Therefore, the recovered bed continues to improve with the number of iterations. Nevertheless, we hypothesise there is a numerical limitation to the detail in the bed that can be recovered because beyond some point very small bed adjustments may no longer affect surface heights due to numerical rounding/diffusion. In real world applications, surface height data contain a certain amount of error and the model forcing and physics are imperfect. In that case a perfect match between modelled and observed surface heights is not desired. When the iterative procedure is continued for too many iterations, further reduction of small-scale surface errors induce unrealistic adjustments of the recovered bed. Beyond a certain amount of iterations, adjustments of the bed based on the remaining surface misfit are hence no longer an improvement. As discussed in the next section, early termination of the inverse procedure can be applied to prevent contamination of the bed with undesired noise.

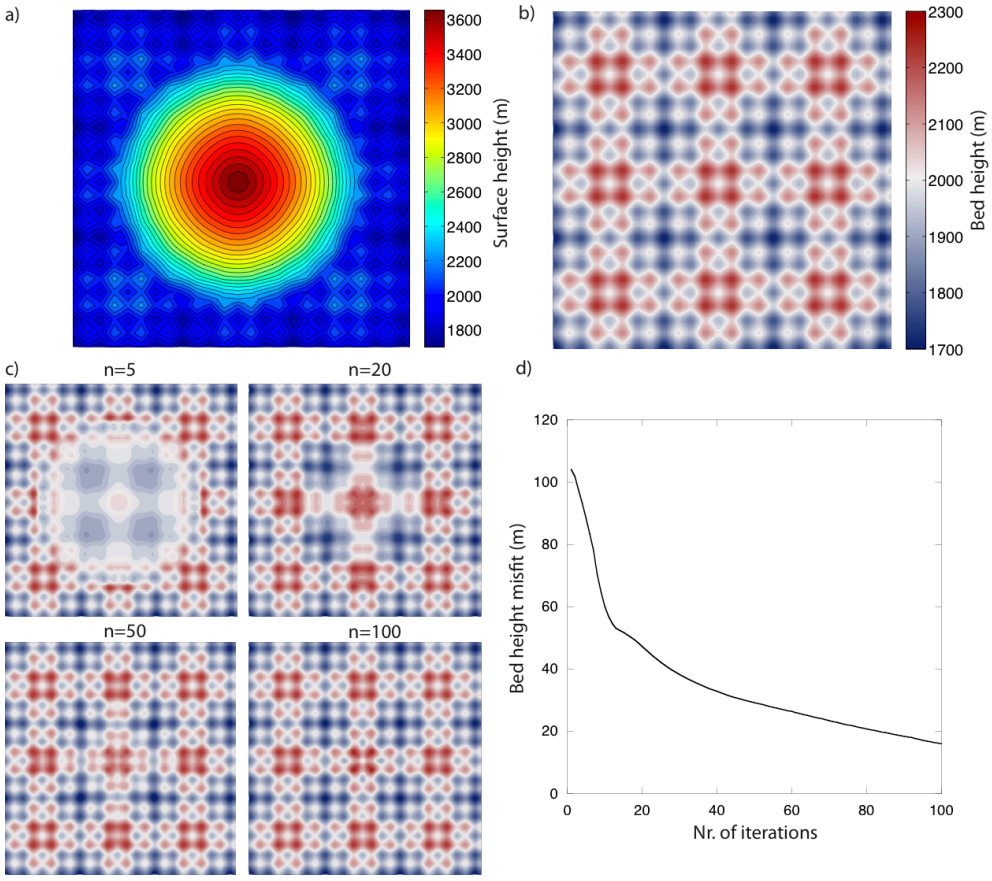

Figure 5.5: *Recovery of a bump field containing mixed bump sizes. The reference surface and bed are shown in a) and b). The reference bed contains a superposition of bumps with an amplitude of 150 m and a bump-width varying by a factor 4. Panel c) shows snapshots of the recovered bed height after n =5, 20, 50 and 100 iterations. d) shows the bed height misfit as a function of the number of iterations.*

5.4 Application to Nordenskiöldbreen, Svalbard

The experiments in the previous section have illustrated that the inverse approach enables recovering basal topography in an idealised setting. Next, the applicability of the approach in a real world situation is investigated. The inverse method is applied to the geometry of Nordenskiöldbreen, Svalbard, for which we have an accurate set of surface height data from a DEM [*Korona et al.*, 2009] and some bed height data, gathered using Ground Penetrating Radar (GPR). The DEM will serve as a reference surface, whereas the bed height data are used for validation of the reconstructed bed. Compared to the idealised examples in the previous

section application to Nordenskiöldbreen poses some additional challenges. First of all, as mentioned before, the presence of data and modelling errors suggest the need for termination of the iterative procedure before fitting the modelled surface to unrealistic features. Hence, a stopping criterion is used to minimise the significance of over-fitting. Secondly, in contrast to the synthetic experiments, the glacier is not in steady state at the end of an iteration. A time-dependent surface climate forcing since 1300 AD is prescribed and the effect of surface height changes on the mass balance and surface temperature is taken into account, as outlined in Section 5.4.2 .

5.4.1 Nordenskiöldbreen

Nordenskiöldbreen is a tidewater glacier in central Svalbard, connected to a large ice plateau, Lomonosovfonna. After recent retreat the ice front has partly retreated on land and the significance of frontal calving has declined [*Plassen et al.*, 2004]. GPS observations of ice movement along the flow line since 2006 reveal annual mean surface velocities up to 60 m yr^{-1} [*Den Ouden et al.*, 2010]. Nordenskiöldbreen has a polythermal thermodynamic structure with cold annual mean near-surface temperatures in the ablation area and a nearly-temperate snow pack in the accumulation zone as a result of significant melt water refreezing [Chapter 2]. This type of structure is common for Svalbard glaciers [*Pettersson*, 2004]. A 40 m resolution DEM of the glacier and its surroundings, obtained in 2007 as part of the SPIRIT (*SPOT 5 stereoscopic survey of Polar Ice: Reference Images and Topographies*) project [*Korona et al.*, 2009], is shown in Figure 5.6a. Some post-processing has been done to remove inconsistent data. The black line in Figure 5.6a marks the extent of the selected grid of Nordenskiöldbreen, including two side-flows between Terrierfjellet, Ferrierfjellet and Minkinfjellet, merging with the main flow further downstream. GPR bed height data along the track shown in Fig 5.6b, gathered using a 500-MHz radar during a field campaign in 2010, reveal bed heights below sea level upstream of the current frontal position. The bed data are used to validate the reconstructed bed.

5.4.2 Climate forcing

In this section, the strategy employed to obtain a time- and altitude-dependent surface forcing is described. Given a winter air temperature reconstruction for Svalbard Airport, Longyearbyen, [*Divine et al.*, 2011] and an annual accumulation record for Lomonosovfonna, a climate reconstruction for Nordenskiöldbreen back to 1300 AD has been made. The climate sensitivity of the mass balance and subsurface temperature, constituting the surface forcing, is computed with a coupled energy balance - snow model.

The winter air temperature record is used in combination with temperature data from the Longyearbyen weather station to obtain annual temperature estimates. The instrumental

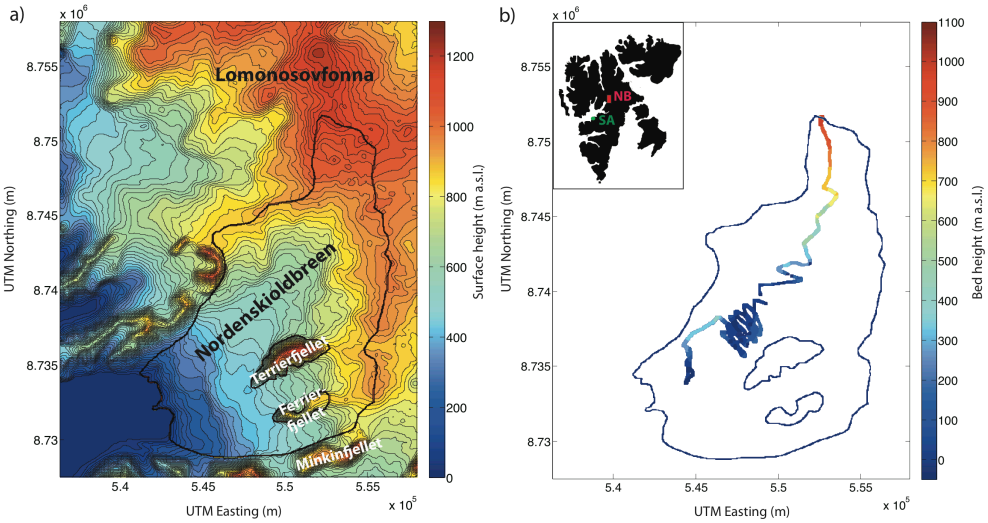

Figure 5.6: *Observed surface heights from a DEM (a) and bed heights from radio-echo sounding (b). The black line marks the extent of Nordenskiöldbreen, connected along the ice divide to the Lomonosovfonna ice plateau. The location of mountain ridges Terrierfjellet, Ferrierfjellet and Minkinfjellet is indicated. The inset figure in b) shows the Svalbard archipelago with the position of Svalbard Airport (SA) and Nordenskiöldbreen (NB).*

record for Longyearbyen since 1912 reveals a much stronger year-to-year variability in winter than in summer temperatures. Additionally, over the instrumental period summer temperatures show a much smaller positive trend (0.011 K yr^{-1}) than winter temperatures (0.024 K yr^{-1}). In line with this, future climate scenarios for this region predict a higher sensitivity of winter temperatures in a changing climate [*Førland et al.*, 2009]. We compute the mean ratio of trends in winter temperatures and annual mean temperatures over the instrumental period (since 1912) and subsequently use this ratio to convert the winter temperature record, derived from a composite δ^{18}O record from two ice cores in Svalbard [*Divine et al.*, 2011], into annual mean temperature estimates back to 1300 AD. Figure 5.7 shows smoothed temperature anomalies w.r.t. the reference period 1989-2010. These anomalies are directly used to describe temperature variability for Nordenskiöldbreen since 1300 AD.

An accumulation history, derived from an ice core drilled at the top of the Lomonosovfonna plateau in 1997, provides estimates back to 1598 AD. An accumulation record back to 1715 AD, based on the similar ice core data set, is presented in *Pohjola et al.* [2002a] The time-series are extended to cover the period 1997-2010, using precipitation estimates from the Longyearbyen weather station (computing precipitation anomalies w.r.t. to the period 1960-1996 and applying these to the Lomonosovfonna record since 1997). For the period 1300-1598, accumulation data were lacking and values are set to the mean accumulation over the

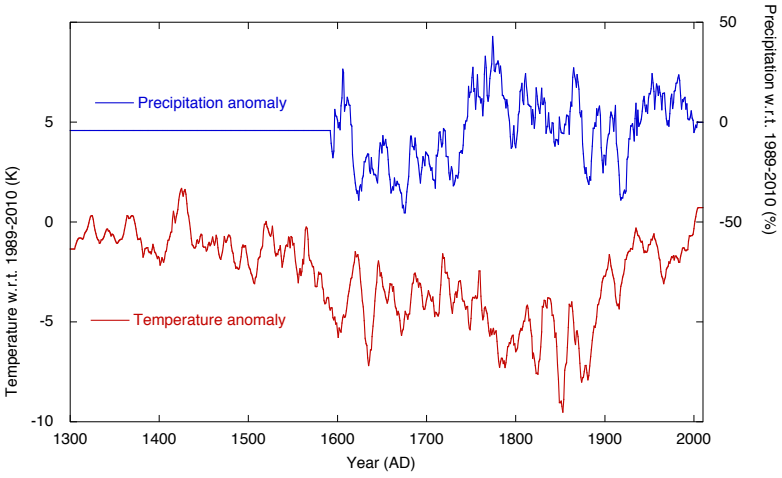

Figure 5.7: *Time-series of reconstructed air temperature (red) and precipitation (blue) relative to the mean over the reference period 1989-2010. A 10-year smoothing filter is applied. Precipitation anomalies are given in percentages, whereas temperature anomalies are absolute deviations.*

period 1598-2010. The resulting smoothed record of accumulation anomalies since 1300 is shown in Figure 5.7.

The ice flow model requires input of the surface mass balance and subsurface temperature (at the snow-ice interface) as surface forcing. Both the mass balance and subsurface temperature depend on air temperature and accumulation. A coupled distributed energy balance - snow model, presented in Chapter 2, solves the surface energy budget and simulates melt water percolation, refreezing and runoff in the firn pack. The coupled model is applied to the grid of Nordenskiöldbreen to quantify the mass balance and subsurface temperature sensitivity by performing multiple model experiments with perturbed accumulation and air temperature over the period 1989-2010. Based on the previously discussed trends in the Longyearbyen instrumental record temperature perturbations are defined per season, e.g. a 1 K temperature perturbation in winter corresponds to a 0.47 K summer temperature perturbation. In this way, seasonality in climate change is taken into account. Seasonal differences in observed precipitation trends are much less pronounced [*Førland et al.*, 2009] and therefore not accounted for in the coupled model experiments. Temporal variability in the climate forcing in the sensitivity runs is based on 3-hourly climate input from a regional climate model RACMO (temperature and specific humidity) and the Longyearbyen weather station (precipitation and cloud cover). From distributed output fields of the sensitivity experiments altitudinal profiles of the annual mean mass balance and snow/ice-surface temperature are computed for every climate perturbation. In order to enable selection of the mass balance and snow/ice-surface temperature for every altitude and climate perturbation, curve fitting per height bin and fur-

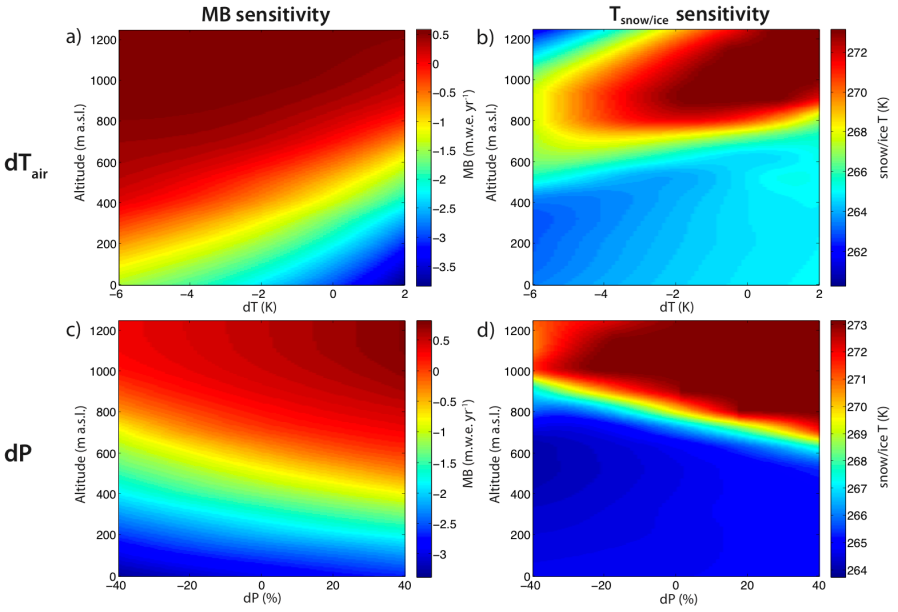

Figure 5.8: *Diagrams showing the surface mass balance sensitivity as a function of altitude for changes in air temperature (a) and precipitation (c). The sensitivity of the snow/ice temperature as a function of altitude for changes in air temperature and precipitation is shown in b) and d) respectively. Sensitivities were obtained from output of sensitivity experiments with a coupled energy balance - snow model, ran over the period 1989-2010. Temperature and precipitation anomalies are defined w.r.t the mean over the period 1989-2010. More details can be found in Chapter 2.*

ther interpolation are performed to complete the diagrams, which are shown in Figure 5.8.

The diagrams in Figure 5.8 serve as look-up tables for the mass balance and snow/ice-surface temperature given the current altitude of the grid cell and the reconstructed temperature and precipitation anomaly. Hence, while running the ice dynamical model forward in time, mass balance and subsurface temperature values can be selected dynamically for every grid point by considering the current air temperature and precipitation anomaly (Figure 5.7. With this approach, altitudinal feedbacks of the mass balance and subsurface temperature are implicitly taken into account.

5.4.3 Setup

Model iterations are performed on a grid with a 500 m resolution, containing a total of 3432 grid points. Every model iteration starts with an initialisation run over the period 500-1300

AD, forced with constant-in-time, height-dependent climate input (Section 5.4.2) to initialise the ice geometry and its thermodynamics (approaching a steady-state in 1300). The prescribed surface climate during initialisation corresponds to the mean climate for the period 1300-2007. Initialisation is followed by a run over the period 1300-2007 with the model being forced with reconstructed time- and height-dependent climate input (Section 5.4.2). The difference between modelled and observed surface heights in 2007, referred to as the surface misfit, is used to correct the bed after every iteration.

Outside the grid of Nordenskiöldbreen, the ice is allowed to evolve in a limited sense. A 'force-to-thickness' mechanism is applied there, which involves prescription of an artificial mass balance required to force the surface height to approach present-day (DEM) values. The resulting slightly smoothed surface outside the grid resembles present-day surface heights and avoids severe time-stepping restrictions, i.e. very short model time-steps, related to steep surface gradients. The grid of Nordenskiöldbreen is selected along the present-day ice divide, implying negligible ice flow across the grid boundary. The limited ice thickness evolution at the ice divide and its fixed position increase uncertainty in the reconstructed bed near the ice divide. Moreover, low surface slopes and small ice fluxes limit the bed to surface transfer amplitude and hence bed heights cannot meaningfully be determined. Therefore, Equation 5.3 is not applied to adjust the bed at the estimated position of the ice divide and bed heights are determined by nearest-neighbour interpolation between iteratively adjusted bed heights on the grid and fixed bed heights outside the grid. Outside the Nordenskiöldbreen grid bed heights are determined by means of the perfect-plasticity assumption [*Nye*, 1951], assuming a constant applied stress equal to the mean determined from thickness and surface slope estimates at GPR bed data locations. A minimum slope of 0.025 is used to avoid unrealistically large ice thicknesses. Additionally, some measures are taken to prevent inconsistent corrections near the margins. This includes: 1) interpolating the bed for grid points that are directly connected to ice-free grid cells, 2) interpolating the bed for modelled ice-free grid cells that are ice-covered in the reference surface from the DEM, 3) not adjusting the bed for grid cells which are ice-free in the reference surface and ice-covered at the end of a model iteration. Interpolation involves application of a spring metaphor to estimate unknown bed heights by interpolating between surrounding bed heights from inverse modelling (on the grid) and/or fixed bed heights (outside the grid).

In these experiments, ice is set to calve of at the present-day position of the calving front and hence the glacier front is not allowed to move beyond its present-day position. This implies some uncertainty in ice flow near the glacier front, in particular further back in time. The current lack of proper physics in the model to deal with calving and movement of the grounded calving front obliged us to use this simplifying assumption.

A value for the relaxation factor K of 0.25 has been used in these experiments and leads to stable convergence of the inverse method. It is worth mentioning that climate feedbacks, like the mass balance - altitude feedback, enhance deviations of the surface height after a bedrock adjustment. This is one of the reasons to use a smaller K than in the synthetic experiments.

We start the first iteration with an initial bed generated through interpolation between known bed heights from the GPR data set and from the DEM (ice-free regions). Note that the data cover only a very small part of the grid, leading to a relatively smooth interpolated initial bed. For the tributary glaciers a constant initial ice thickness has been assumed to derive basal topography. The sensitivity of the reconstruction to the initial bed is discussed in Section 5.4.4. When validating reconstructed bed, we discuss a possible bias introduced by including GPR data in the initial bed at the start of the inverse method.

As mentioned, modelling errors and surface data noise may lead to undesired corrections of the bed. A stopping criterion is needed to terminate the iterative procedure before the reconstructed bed gets too severely contaminated by unphysical variability. Synthetic experiments have indicated that with the number of iterations the rate of improvement of the surface misfit declines as smaller scale-bed features are recovered. The relative significance of modelling errors, as well as surface height data errors, hence increases with the number of iterations. *Habermann et al.* [2012] indicated that for problems involving both data and modelling errors, a so-called 'L-curve criterion' can be used to define a reasonable point of termination [*Aster et al.*, 2005]. The L-curve criterion is based on the principle that the iterative method should stop when further reduction of the surface misfit comes at the expense of (unrealistically) large adjustments of the bed. In order to define the point of termination, the residual norm, i.e. the square-root of the summed squared surface misfit, is plotted versus the model norm in a log-log plot. The L2-model norm is used, which is the square-root of summed squared deviations of the reconstructed bed height relative to the initial bed. A bending point in this graph represents the critical point beyond which over-fitting is likely to occur and hence defines a reasonable point to stop the iterative method (Figure 5.10). Note that an alternative stopping criterion could be to stop the inverse procedure when the misfit between modelled and observed bed heights minimises. With the L-curve criterion we illustrate a stopping principle that can be applied in presence and absence of (scarce) bed data. In other inverse modelling studies reconstructing basal conditions underneath glaciers, iterative procedures are often terminated when the surface misfit falls below a certain predefined tolerance ['discrepancy principle'; *Maxwell et al.*, 2008; *Arthern and Gudmundsson*, 2010] or when the rate of change of the residual norm drops below a predefined threshold ['recent-improvement principle'; *Joughin et al.*, 2006; *Sergienko et al.*, 2008] . In problems involving both modelling and data errors, it is generally hard to define the tolerance required in the discrepancy principle. On the other hand, the recent-improvement criterion depends strongly on the predefined value of the threshold, for which constraints are lacking.

5.4.4 Results

Next, we present results of application of the inverse method on Nordenskiöldbreen. In a first set of experiments (Section 5.4.4), the approach is applied to a bed allowed to freely evolve everywhere, whereas in a second experiment (Section 5.4.4), an alternative approach

is applied in which the bed is fixed at locations where radar data are available.

Experiment I: unconstrained bed

First, we discuss results of the application of the inverse method to an unconstrained bed, i.e. the ice-covered bed is not constrained by any radar observations during the iterative method. The sensitivity of the reconstructed bed to modelling errors is studied by performing experiments with a perturbed 1) till strength, 2) initial bed and 3) surface climate forcing.

Both spatial variability in the basal shear stress and bedrock topography exert an influence on the surface height and velocity distribution. The basal shear stress depends on the presence of water, lubricating the bed, as well as the material till strength, which is known to be high for glaciers underlain by hard crystalline bedrock and much lower for soft-bedded glaciers underlain by sediment [*Clarke*, 2005]. The till strength directly affects the amount of basal lubrication, which implies a strong influence on the ice thickness distribution. Since we lack observational constraints on the sediment distribution underneath Nordenskiöldbreen, we prescribe a spatially invariant material till strength in our experiments. Any surface height variability related to a non-uniform distribution of the material till strength is therefore not taken into account and is acknowledged as a source of uncertainty in our approach.

The sensitivity of the reconstructed bed to changes in the material till strength is investigated by performing runs with different values for the material till strength ϕ (Equation 5.2) with values ranging between 11 and 15°. Snapshots of the reconstructed bed and the surface misfit for the $\phi = 13°$ experiment after 1, 5, 10 and 23 iterations are shown in Figure 5.9. Clearly, the surface misfit reduces with the number of iterations, indicating convergence of the approach. Starting from a relatively smooth initial bed, the reconstructed bed gradually acquires more smaller-scale features. In accordance with the GPR data (Figure 5.6b) an overdeepening is apparent in the main flow with minimum bed heights around sea-level. Figure 5.10a shows the RMS surface misfit as a function of the number of iterations. A log-log plot of the smoothed residual norm (Figure 5.10b) versus the model norm is used to define a point beyond which further iterations are likely to deteriorate the recovered bed. The bending point, corresponding to the point of maximum curvature is found here after 23 iterations. In all experiments discussed in this section the stopping point was found between 22 and 25 iterations. The surface misfit remains largest near the margins, where the modelled ice thickness is very sensitive to the applied surface forcing leading to uncertain bed corrections. This was the main reason to interpolate the bed in the immediate vicinity of the margin.

Figure 5.11 shows the reconstructed bed height and bed discrepancy for the sensitivity experiments with perturbed till strength (1st and 2nd column) and perturbed initial beds (3rd and 4th column). The bed discrepancy is computed relative to the final bed height in the $\phi = 13°$ experiment. Perturbing the material till strength affects mean sliding velocities and the ice thickness. A lower till strength enhances basal velocities, thins the ice and hence raises the

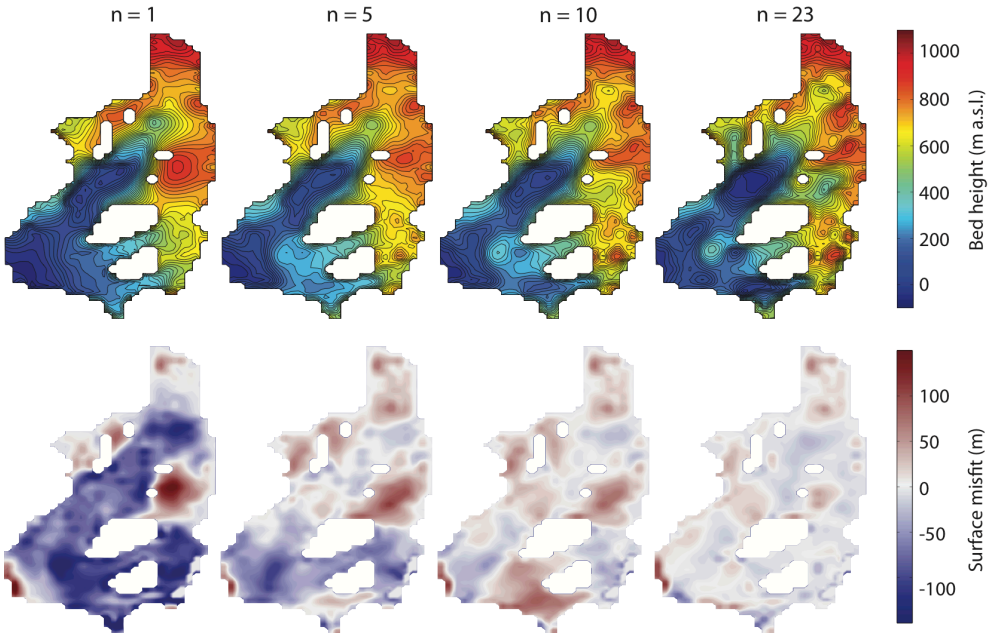

Figure 5.9: *Snapshots of the recovered bed (1st row) and surface height misfit (2nd row) after n =1, 5, 10 and 23 iterations in the experiment with* $\phi = 13^\circ$.

reconstructed bed in regions where sliding is significant. Largest bed discrepancies arise in locations where the surface slope is large, due to a higher sensitivity of sliding to changes in the basal shear stress. In cold-based higher regions the reconstructed bed is only slightly affected by a change in the till strength.

Regardless of the initial bed at the start of the first iteration, with the number of iterations the reconstructed bed always seems to converge to a similar bed profile, as illustrated in the synthetic experiments (Figure 5.4). This is only approximately true in the current experiment, where a small misfit will always remain in the surface heights since the model is unable to produce an exact match of the surface heights in the DEM. The stopping criterion forces early termination of the inverse method, which implies that the recovered bed at the stopping point may still be influenced by the chosen initial bed profile. Figure 5.11 (column 3) illustrates that, when repeating the $\phi = 13^\circ$ experiment with an initial bed, which is uniformly lowered by a 100 m, the remaining absolute bed discrepancy after 23 iterations is relatively small (on average 11 m). We performed an additional experiment to test the sensitivity of the reconstruction to an initial bed with perturbed spatial variability. For that purpose, an initial bed was constructed using the perfect plasticity assumption with a relatively high slope threshold (discussed in more detail later in this section). The initial bed is shown in Figure 5.14c and

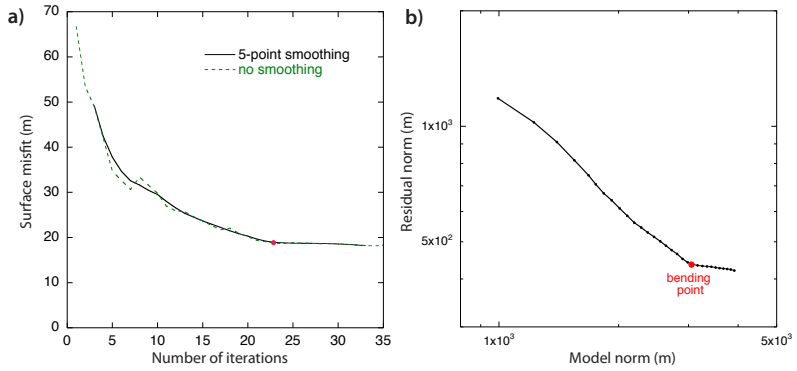

Figure 5.10: *Plots showing the surface misfit vs. the number of iterations (a) and the residual norm vs. the model norm (b) for the $\phi = 13^\circ$ experiment. A bending point in the L-curve, used to define a stopping point for the iterative method, is marked in red. Five-point smoothing of the residual norm series facilitates selecting a bending point in b).*

lacks prominent features like the over-deepening along the main flow line. The reconstructed basal topography and the bed discrepancy is shown in Figure 5.11 (column 4) and shows similar variability as in the $\phi = 13^\circ$ experiment. E.g. the over-deepening is apparent in the reconstruction. Remaining absolute deviations are on average 17 m (was 85 m at the start of the experiment). These results indicate convergence to a similar bed profile after many iterations for both experiments with perturbed initial beds. Nevertheless, due to preliminary stopping of the inverse procedure we can conclude that an initial bed estimate with a realistic spatial pattern and mean bed height does increase the accuracy of the final reconstructed bed.

We also study the sensitivity of the reconstructed bed to perturbations of the climate forcing. In a first sensitivity experiment, the $\phi = 13^\circ$ experiment is repeated with a constant-in-time surface forcing, using an air temperature and accumulation rate equivalent to the mean since 1300 AD. The resulting bed discrepancy w.r.t. the time-dependent forcing experiment is shown in Figure 5.12 (1st column). This illustrates that applying a constant surface forcing raises the bed in higher regions (thinner ice) and lowers the bed in lower regions (thicker ice). The temperature time-series (Figure 5.7) reveal relatively high temperatures since 1900 AD, preceded by a relatively cold period since around 1600 AD. In the non-constant climate experiment the ice thickens significantly over the entire grid for the period 1600-1900 AD, due to a positive mass balance as well as a reduction of ice velocities, which is related to a drop in surface temperatures (advection of colder ice to the bed). Since around 1900 AD, relatively high temperatures induce more melting particularly in the lower regions, locally thinning the ice (Figure 5.12). As a result of surface steepening, enhanced ice velocities gradually lead to thinning of higher regions as well. Since this dynamical thinning process is slow, relatively thick ice is still present in 2007 in the time-dependent climate experiment. The relatively

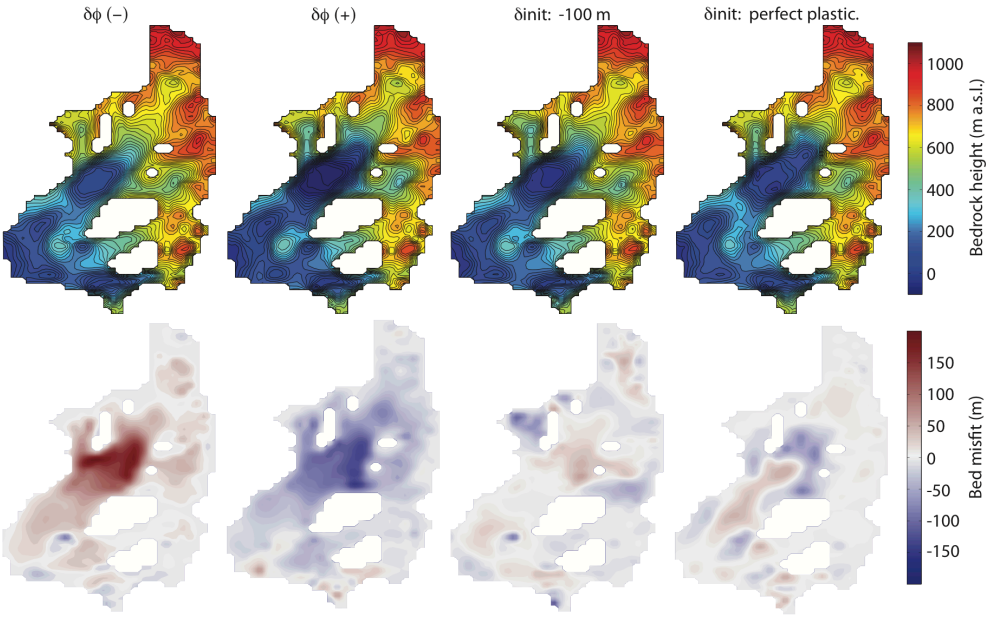

Figure 5.11: *Final recovered basal topography (1st row) and the corresponding bed discrepancy (2nd row) w.r.t. to the $\phi = 13^\circ$ experiment with a negative perturbation of the material till strength ($\delta\phi(-)$, 1st column), a positive till strength perturbation ($\delta\phi(+)$, 2nd column), a uniformly lowered initial bed (3rd column) and an initial bed from perfect plasticity (4th column).*

large and systematic bed discrepancy found when ignoring the time-dependence of the surface forcing indicates the relevance of accounting for temporal variability when recovering basal topography or initialising ice flow models for forecasting experiments. In a second climate perturbation experiment, the air temperature forcing for the spin-up period 500-1300 AD has been lowered by 1 K. The bed misfit in Figure 5.12 (2nd column) indicates a very small influence of the spin-up climate on the final reconstructed bed. Finally, we perturb the air temperature for the period 1300-2007 AD by -1 K (Figure 5.12, 3rd column) and find a more pronounced effect on the bed misfit.

Next, the reconstructed beds in the sensitivity experiments are validated against observed bed heights, obtained using GPR along a track near the main flow line (Figure 5.6b). A scatterplot of observed bed heights (a) and ice thicknesses (b) versus reconstructed values for the experiments with varying till strength is shown in Figure 5.13. As mentioned, changing the material till strength affects the mean ice thickness and induces a shift in the mean bed height in areas where sliding is significant. Figure 5.13 illustrates that much of the variability in the observed bed heights and ice thickness is recovered by the model. Nevertheless, significant local errors in the bed remain, which can be ascribed to multiple factors. In fact, the bed height discrep-

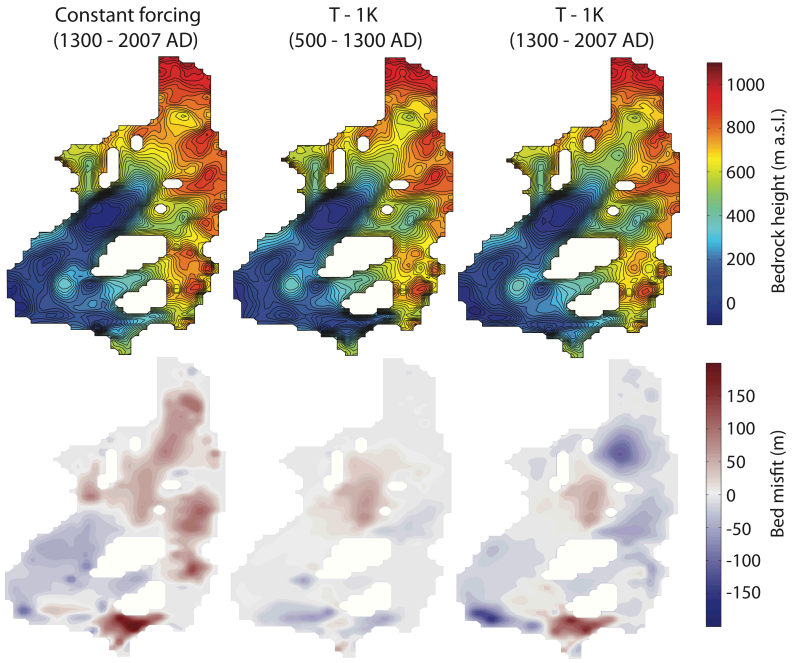

Figure 5.12: *Final recovered basal topography (1st row) and the corresponding bed discrepancy (2nd row) w.r.t. to the $\phi = 13^\circ$ experiment using a constant climate forcing for 1300-2007 AD (1st column) and negative temperature perturbation for 500-1300 AD (2nd column) and for 1300-2007 AD (3rd column).*

ancies in the scatterplot reflect the sum of all uncertainties involved in the inverse approach, including uncertainties in the model physics, climate forcing, surface data, bed data and the stopping criterion. Differences in mean thickness, the RMS thickness misfit, the mean thickness misfit and the correlation coefficient are computed for all sensitivity experiments and presented in Table 5.1. The lowest RMS misfit and a high correlation coefficient are found for the $\phi = 13^\circ$ experiment, which can hence be regarded as the best estimate. Perturbing the initial bed affects the correlation coefficient and RMS misfit only slightly, indicating robustness of the approach for different initial beds. Although best results are found for the $\phi = 13^\circ$ experiment, the perturbed initial bed experiments also indicate that a possible bias related to the inclusion of the GPR data in the initial bed topography at the start of the first iteration is small. Applying a constant surface forcing leads to a lower agreement between modelled and observed ice thicknesses, indicating the relevance of using a time-dependent climate forcing. Perturbing the spin-up temperature has a very minimal effect on the quality of the reconstruction, whereas the effect of a perturbation of the 1300-2007 AD temperature on the reconstructed bed is more pronounced. It is noteworthy that the bed misfit in Figure

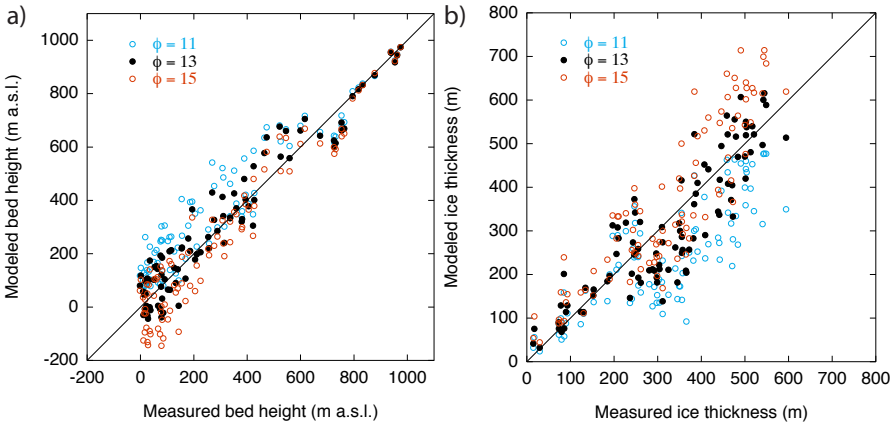

Figure 5.13: *Scatterplots showing the modelled bed height vs. the observed bed heights from radar (a) and modelled vs. measured ice thickness (b). Results are shown for sensitivity experiments with varying material till strength. The corresponding correlation coefficients, RMS misfit, bias and mean error are given in Table 5.1.*

5.13a) changes sign around an altitude of ∼600 m a.s.l., which is likely to related to inaccuracy of the modelled position of the cold to temperate ice transition, which has a substantial impact on the ice thickness distribution.

Additionally, a comparison of observed ice thicknesses with theoretically-derived values, based on the perfect-plasticity assumption, is made. In the perfect-plasticity assumption [*Nye*, 1951], the local ice thickness H is directly computed from the surface slope s, while assuming a constant yield stress τ_0:

$$H = \frac{\tau_0}{\rho g s}\,, \tag{5.4}$$

where g is the gravitational acceleration and ρ the density of ice. The perfect-plasticity method computes unrealistically large ice thicknesses when the surface slope approaches zero. Therefore, a minimum slope is defined, below which the ice thickness is not computed and determined by interpolation. Local yield stresses have been computed for all GPR grid points, using observed ice thicknesses and slopes from the DEM. The mean of the local yield stresses is used as the constant yield stress in the perfectly-plasticity method. Beds were reconstructed for three different slope thresholds (0.015, 0.02 and 0.04) and the resulting beds are shown in Figure 5.14. A high slope threshold (Figure 5.14c) implies that bed heights cannot be determined for a large part of the grid and are hence determined by interpolation. On the other hand, with a low slope threshold (Figure 5.14a) ice thicknesses are computed for a larger part of the grid, but the larger thicknesses are more uncertain. Comparing the derived beds in Figure 5.14 to the final bed in the $\phi = 13°$ experiment (Figure 5.9) reveals quite significant discrepancies. It should be noted that the perfect plasticity assumption is

Table 5.1: *Comparison of modelled and theoretically derived ice thicknesses with observations along the radar track (Figure 5.6b). δH_{mean} is the discrepancy between modelled and observed mean thickness (2nd column). The 3rd, 4th and 5th column present the root-mean-square error (RMSE), the mean absolute difference and the correlation coefficient (R), respectively. The mean observed ice thickness is 322 m.*

Experiment	δH_{mean} (m)	RMSE (m)	Mean diff. (m)	R
$\phi = 11°$	−78	118	96	0.80
$\phi = 13°$	−14	75	61	0.88
$\phi = 15°$	+41	93	76	0.89
Initial bed −100 m	−24	79	65	0.87
Initial bed perfect-plasticity	−9	82	64	0.86
Climate: const. forcing (1300 - 2007)	−20	90	72	0.84
Climate: $T - 1$ K (1300 - 2007)	−25	84	69	0.85
Climate: $T - 1$ K (500 - 1300)	−11	77	64	0.86
Perfect-plasticity (slope> 0.015)	−0.1	116	94	0.69
Perfect-plasticity (slope> 0.02)	+18	107	90	0.71
Perfect-plasticity (slope> 0.04)	+106	162	140	0.67

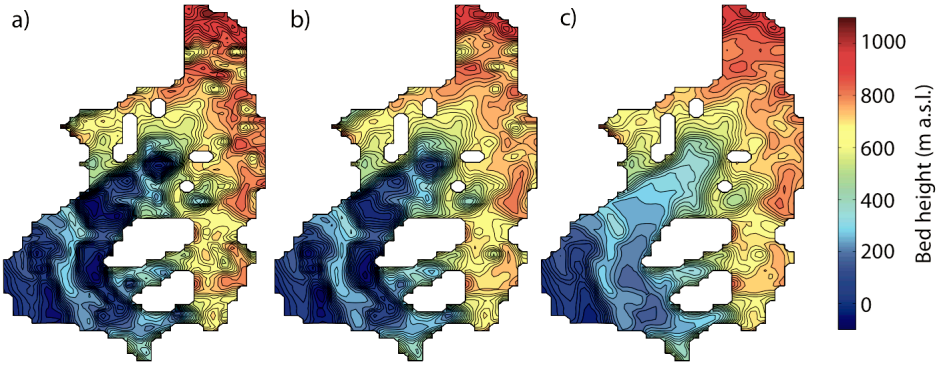

Figure 5.14: *Bed heights computed using the perfect-plasticity assumption using minimum slope thresholds of 0.015 (a), 0.02 (b) and 0.04 (c).*

a simplified form of the shallow ice approximation (all shear is concentrated at the base) in which longitudinal stresses are ignored. The approach is therefore unlikely to perform well in areas of significant sliding. Correlating the perfectly-plastic beds against the radar observations (Table 5.1) reveals markedly lower correlation coefficients with values ranging between 0.67 and 0.71.

In *Den Ouden et al.* [2010], surface velocity data over the period 2006-2009 gathered using GPSs at multiple locations on Nordenskiöldbreen are presented. Figure 5.15a shows a

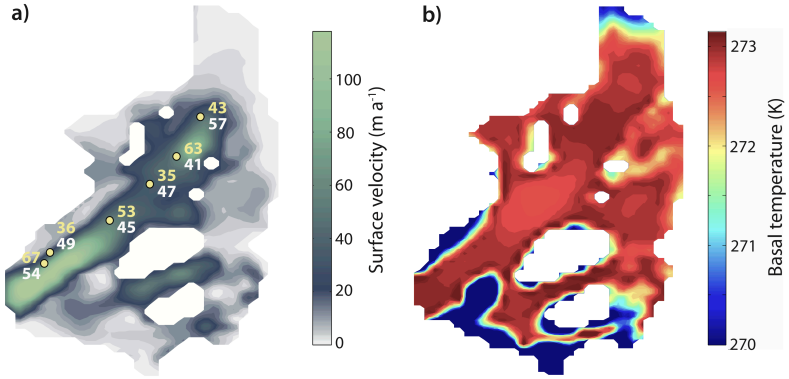

Figure 5.15: *Distributed map of simulated ice velocities (a) and basal temperatures (b) in 2007 for the $\phi = 13°$ experiment. At the locations of velocity observations, reported in Den Ouden et al. [2010], observed velocities (white) and simulated velocities (yellow) are indicated. Only basal temperatures higher than 270 K are shown.*

distributed map of modelled final annual mean ice velocities in 2007 in the $\phi = 13°$ experiment. The approximate GPS positions are marked and modelled (yellow) and observed (white) annual mean values are shown. Modelled and observed velocities agree reasonably well, although some of the spatial variability in observed surface velocities is not present in the modelled values. Discrepancies can be ascribed to many factors, including 1) the lack of modelled small-scale bed and surface height features, 2) the lack of spatial variability in till strength, 3) uncertainty in the position of the temperate to cold base transition, 4) the fact that point measurements are compared with gridded model velocities and 5) possible unmodelled temporal variability in ice velocities over the relatively short period of observations. Simulated basal temperatures in Figure 5.15b reveal a temperate base for most of the grid. Due to substantial refreezing in the accumulation zone surface temperatures are substantially higher in the accumulation area than in the ablation zone (Figure 5.8). A transition from temperate to cold basal ice occurs around a bedrock height of 600 m a.s.l.. In the ablation area, simulated subglacial temperatures depend mainly on cold ice advection, strain heating and frictional heating from sliding and cause the base to be temperate in areas with substantial ice fluxes and sliding and cold in areas near the grounded margin. This is a common pattern for polythermal glaciers in Svalbard [*Pettersson*, 2004].

Experiment II: constrained bed

In the previous experiments, bed height data were not used to constrain the bed and were only used for validation purposes. Next, we present an alternative approach in which the bed is held fixed in locations where bed heights are known from GPR observations. The iterative

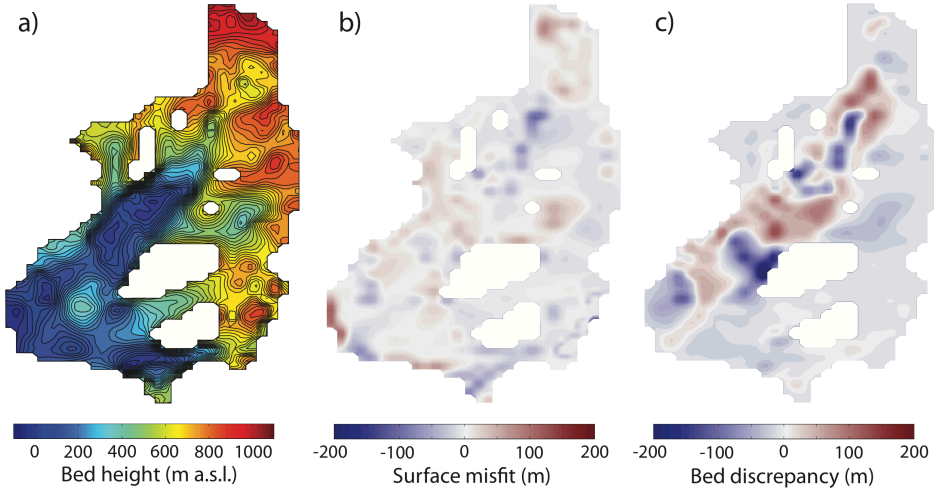

Figure 5.16: *Reconstructed bed with bed heights fixed when radar observations are available in panel a). The corresponding remaining surface misfit is shown in panel b). Panel c) shows the bed discrepancy w.r.t. to the basal topography in the unconstrained experiment with* $\phi = 13°$.

method then attempts to recover the bed for the remainder of the grid. This approach hence provides an alternative method that could be used when scarce bed data are available and the main goal is to estimate the bed for the grid not covered by the observations.

We repeat Experiment I with $\phi = 13°$, with the only difference being the fixed bed at radar grid points. The L-curve stopping criterion indicates a knick point around 25 iterations and the iterative method is terminated at this point. The reconstructed bed, the remaining surface misfit and the difference between the reconstructed topography and the bed in Experiment I with $\phi = 13°$ are shown in Figure 5.16. Comparing the surface misfit distribution in Figure 5.16b to the pattern in Figure 5.9 reveals that the misfit remains larger in regions close to the GPR data grid points (Figure 5.6). This is expected as the bed is not freely evolving in these areas. The difference between the reconstructed bed in Experiment I and II (Figure 5.16c) illustrates that bed heights of the grid points in the vicinity of the fixed bed grid points tend to compensate for the absence of adjustments of the fixed grid cells. This explains the alternating bed discrepancy pattern, visible in Figure 5.16c, with an average bed discrepancy close to zero. Far away from the fixed grid cells, the effect on the reconstructed bed is very limited. It is hard to say whether fixing the bed at bed data locations leads to an improved bed reconstruction in comparison with Experiment I, since means to validate the unconstrained part of the reconstructed bed are lacking. One might argue that in Experiment II the bed is more reliable at the GPR locations, but somewhat less reliable in the vicinity of the GPR locations, due to the aforementioned over-compensation of the bed.

5.5 Conclusions & discussion

In this study, a simple bed height recovery method is discussed and applied in synthetic experiments and in a real-world setting (Nordenskiöldbreen, Svalbard). The inverse method can effectively be used to reconstruct distributed bed heights when direct observations are scarce or lacking. Requirements for the method include a distributed surface height dataset, an ice flow model and a history of surface climate forcing. The thermo-mechanically coupled ice flow model PISM has been used as a forward model in time-dependent experiments. Ice flow in PISM is determined using combined stress balances in which the rate of sliding is determined by the SSA with the basal shear stress controlled by the material till strength and basal thermodynamics. The iterative correction method aims to reduce the discrepancy between modelled and observed surface topography by directly using the surface height misfit to update bed heights.

Idealised experiments with a synthetic ice geometry and a temporally constant surface forcing show convergence and robustness of the inverse method in three dimensions. It is illustrated that local bed adjustments, despite its non-local surface expression, lead to effective reduction of the surface misfit and recovery of the reference bed with the number of iterations. The robustness of the method when changing the initial bed, relaxation factor, mass balance forcing and bump dimensions has been investigated. Main findings include that: 1) results are shown to be insensitive to the initial bed, 2) an optimum value for the relaxation factor can be selected for which fastest stable convergence occurs and 3) larger bumps are more easily resolved than smaller ones.

In contrast to the synthetic experiments, application of the method to Nordenskiöldbreen involves dealing with time- and height-dependent climate input, leading to a non-steady final geometry, and dealing with modelling and data errors, implying a risk of over-fitting. A time- and height-dependent surface forcing was constructed using reconstructed temperature and accumulation over the period 1300-2007 in combination with output from sensitivity experiments with a coupled distributed energy balance - snow model. An L-curve stopping criterion has been used to minimise contamination of the bed with undesired variability related to data and modelling errors. Bed height data along a radar track are used for validation of the modelled bed topography. Sensitivity experiments on an unconstrained bed all indicate convergence of the inverse iterative method. We find that 1) the chosen material till strength parameter significantly affects the mean modelled bed height in the sliding zone, 2) the initial bed has a small impact on the bed reconstruction, and 3) a constant-in-time surface forcing reduces the quality of the reconstructed bed. While all errors in the approach related to uncertainty in the model physics, termination of the correction method, surface height data and surface forcing, are absorbed in the reconstructed bed, we find correlations up to $R = 0.89$ when comparing reconstructed ice thicknesses with observations. The best estimate of the bed has a mean absolute deviation of 61 m (mean ice thickness 322 m). The remaining unexplained variability in bed heights can mainly be ascribed to uncertain model physics,

particularly in the description of sliding. The approach in this study is shown to produce more accurate bed estimates for this glacier than obtained using the perfect-plasticity assumption (using different minimum slope thresholds). In a final experiment, the bed was held fixed in locations where bed heights were known from the radar data. Here, the inverse method provides a tool to interpolate the bed between known bed heights. However, reconstructed bed heights in the immediate vicinity of fixed bed heights are likely over-compensating for the lack of movement of the fixed grid cells.

A better agreement between modelled and observed bed heights could be obtained by more precise selection of a constant material till strength or including a spatial dependence of the till strength. Furthermore, extending the subglacial model with a water transport scheme would allow for detailed modelling of spatio-temporal variability in subglacial water pressures and basal lubrication. This is however beyond the main scope of this work, in which we aim to demonstrate convergence and applicability of the inverse method. The application to Nordenskiöldbreen sets an example of how the method can be used on a real glacier geometry. Application of the inverse approach is not constrained to a single model or glacier, although the accuracy of the reconstructed bed does depend on the choice of model and the reliability of the prescribed surface forcing. As this method can potentially be applied to estimate the thickness distribution of larger sets of glaciers and ice caps, e.g. to estimate ice volume, one could decide to use a computationally inexpensive ice flow model at the expense of detail in the reconstructed bed.

A major advantage of the approach is that, in addition to reconstructing basal topography, it directly provides a means to spin-up ice flow models for forecasting experiments, since the method searches for a bed for which modelled surface heights approach DEM values and thermodynamics are initialised. Alternatively, in case an accurate map of basal topography would already be available from observations, an approach as in *Pollard and DeConto* [2012], iteratively using the surface height misfit to update the sliding coefficient, could be used as a means of initialisation. However, for many glaciers and ice caps, bedrock data are scarce or absent and the current approach provides a reasonable method for spin-up.

The L-curve stopping criterion provides a means to terminate the iterative procedure before the recovered bed gets too severely polluted with undesirable noise. Whether adjustments of the bed are still an improvement depends on the relative significance of modelling errors in respect to the bed to surface transfer amplitude. Both the magnitude of modelling errors and the transfer amplitude may vary significantly from one place to another, implying that at the stopping point some areas are prone to over-fitting, whereas in other places under-fitting is likely to occur. In this study, a constant relaxation factor K has been used and no attempt has been made to apply weighted bed corrections, with stronger corrections in areas where bed corrections are more likely an improvement and weaker corrections in regions where over-fitting is apparent. Assigning spatially dependent values to K seems only feasible when a distribution of the magnitude of modelling errors as well as the bed to surface transfer amplitude can reasonably be defined, which is not straightforward. Examples of a possible spatial

dependence of K could include gradually weaker corrections towards the margins, where modelling errors become more significant, and stronger corrections in high-sloping regions, where the bed to surface transfer amplitude is large. Since the inverse method performs best when the bed to surface transfer amplitude is large, the accuracy of the bed reconstruction is likely to be higher for glaciers with a larger slope and/or a higher slip-ratio.

In future work the presented approach could be used as a spin-up method for prognostic experiments on Nordenskiöldbreen or other glaciers. Proper initialisation avoids abrupt changes ('model drift') at the start of prognostic experiments related to the lack of spin-up of internal thermodynamics and the ice thickness distribution, which is inevitably needed to accurately simulate the near-future evolution of glaciers and ice caps.

6

Towards an improved subglacial hydrology model for PISM

This chapter provides first steps towards implementation of a more realistic subglacial hydrology model in the Parallel Ice Sheet Model (PISM). Ice flow by sliding of the ice over the bed is known to depend strongly on the presence and evolution of subglacial water. In particular, sliding laws link the basal shear stress to subglacial water pressure. To model water pressures ice sheet models require a hydrology component that: 1) incorporates reasonable physics of water transport and evolving drainage morphology, 2) is applicable at a wide range of spatial and temporal scales, 3) contains a limited number of poorly-constrained constants. With this in mind, we developed and tested a subglacial hydrology model connecting distributed drainage to englacial water storage and discuss its potential for implementation in ice sheet models. The model is applied to the geometry of Nordenskiöldbreen, Svalbard. We analyse steady-state behaviour with respect to model parameter choices and discuss the crucial role of englacial transport on the pressure evolution in transient summer melt conditions. Steady-state experiments indicate a high sensitivity of model output to poorly-constrained parameters affecting cavity opening and closure as well as parameters affecting melt input and transmissivity of the drainage system. Transient experiments show the strong dependence of pressure variability on englacial porosity and motivate the use of the porosity as a regularisation parameter.

This work is done in collaboration with Ed Bueler, University of Alaska Fairbanks.

6.1 Introduction

Whereas internal deformation determines slow ice movement of cold glaciers and in the interior of ice sheets, pronounced sliding of the ice occurs on temperate-bedded outlet and mountain glaciers. The presence of water at the ice-bed interface lubricates the till and reduces the contact area between ice and bedrock, thereby reducing frictional resistance and allowing for slip of the ice. Observational studies have shown the direct connection between sliding velocities and melt input [e.g., *Zwally et al.*, 2002; *Bartholomaus et al.*, 2007; *Van de Wal et al.*, 2008; *Bartholomew et al.*, 2010; *Sundal et al.*, 2011], and relationships have been developed linking the basal shear stress to sliding velocity and water pressure [*Budd et al.*, 1979; *Fowler*, 1987; *Schoof*, 2005; *Clarke*, 2005]. Modelling the spatial and temporal evolution of water pressure not only requires knowledge of changes in local water supply, but also a physical description of water transport and evolution of the geometry of the subglacial system. Water flows along gradients in the fluid potential, whereas local capacity is determined by a balance between opening through cavitation and wall melt and closure due to creep. Additionally, water is exchanged with a porous englacial system, in which the water level is a measure for the subglacial water pressure [*Bartholomaus et al.*, 2011; *Hewitt*, 2013]. Ultimately, in order to understand and quantify the response of the mass budget of glaciers and ice sheets to climate change, ice dynamical models, solving stress equations, need to be coupled to surface models (melt/runoff), englacial models (thermodynamics) and subglacial models (hydrology and basal sliding). Current ice sheet models commonly use a sliding description, either directly linking basal shearing to subglacial temperature ["submelt sliding laws"; e.g., *Dunse et al.*, 2008; *Pattyn*, 2010; *Pollard and DeConto*, 2012] or applying a simplified water production/transport model [e.g., *Bueler and Brown*, 2009].

This chapter focusses on developing a hydrology model, suitable for implementation in the 3-D thermo-mechanically coupled ice sheet model PISM [Paralllel Ice Sheet Model; *Bueler and Brown*, 2009]. As discussed in Chapter 1 ice sheet models require a hydrology component that: 1) includes reasonable physics of water transport and drainage system evolution, 2) is applicable to a wide range of spatial and temporal scales, 3) has a limited number of poorly-constrained parameters that can be constrained given scarcely available data. With this in mind, we extended a distributed linked-cavity subglacial model, developed along the lines presented in *Schoof et al.* [2012], with an englacial storage model as in *Bartholomaus et al.* [2011]. As in the *Schoof et al.* [2012] model, cavities open by sliding of the ice over bedrock bumps and close by creep under the influence of gravity. The model tested here is in essence similar to the distributed part of the model described in *Hewitt* [2013]. Here we discuss its potential for implementation in large-scale ice sheet models. Our aim is to provide insight in steady-state behaviour and to illustrate the role of englacial storage on the pressure evolution. It will be shown that accounting for englacial transport has a reducing effect on computational effort at the expense of detail in the pressure evolution. We motivate the use of the englacial porosity as a regularisation parameter, which opens the door to application at a wide range of

time-scales, requiring different degrees of detail in pressure evolution.

Many further extensions to the model are possible, such as accounting for channelised drainage or adding a till storage model. Although some model extensions may be desirable for specific applications, in general further extensions will interfere with the above mentioned goals of applying the hydrology model, as part of an ice sheet model, at a wide range of spatial and temporal scales and to limit the amount of uncalibrated parameters as much as possible. The process of opening by wall melt and the related transformation of the subglacial system into a conduit system for large water fluxes is hence not considered here, mainly because existing theory requires prescribed fixed positions where channels can form [*Schoof*, 2010; *Pimentel and Flowers*, 2011; *Hewitt et al.*, 2012; *Hewitt*, 2013], limiting robustness of results under grid refinement. We are currently investigating possibilities to include characteristic features of channelised flow in a qualitative way.

Explicit modelling of the simultaneous evolution of capacity of the drainage system, horizontal water transport and exchange with the englacial water system enables resolving the water thickness and pressure evolution in space and time without requiring a pre-defined parameterisation relating water pressure to water thickness. Such parameterisations do not always satisfy bounds on the water pressure [*Schoof et al.*, 2012] and are typically unsuitable for application in non-steady conditions due to transient water input.

In contrast to the distributed hydrology model presented in *Schoof et al.* [2012] we assume the glacier has a certain finite porosity, determined by cracks, moulins, empty pockets and pore space. Water is assumed to move efficiently between subglacial and englacial storage, while the water level within the porous glacier is a measure for the water pressure at the subglacial connection. Incorporating englacial water storage is not only important in computing subglacial storage, pressure and transport, it also substantially eases implementation and numerical solving. In non-porous medium model, instantaneous adjustment of subglacial capacity and water pressure is needed to accommodate changes in water input. On the contrary, in a porous medium approach a change in the water input only leads to a gradual (non-discrete) change in the water pressure and subglacial drainage system capacity as transport from and to englacial storage is needed to adjust the englacial water level. Effectively, a finite porosity is shown to reduce "stiffness" of the pressure evolution equation, thereby simplifying implementation and reducing numerical cost. The buffering effect of englacial water storage on subglacial water pressures has previously been discussed in a lumped framework by *Bartholomaus et al.* [2011].

In this chapter, we summarise the hydrology model (Section 6.2), discuss the role of englacial transport (Section 6.3), analyse steady-state behaviour (Section 6.4) and perform basic tests on the real glacier geometry of Nordenskiöldbreen, Svalbard (Section 6.5).

6.2 Model

In this section, we give a model description and discuss physical principles behind the model equations. This involves a discussion of how water pressure and water thickness evolve in relation to water transport, subglacial and englacial storage and the capacity of the drainage system.

6.2.1 Mass conservation

Water in the hydraulic system is divided into two components representing water storage at the ice-bed interface (W) and water stored in englacial pore space (W_{en}). The total effective thickness of water (W_{tot}) in a vertical column is therefore

$$W_{\text{tot}} = W + W_{\text{en}} \, . \tag{6.1}$$

An efficient connection is assumed between the subglacial hydraulic system and englacial storage space, consisting of crevasses, cracks, moulins and empty pockets and pore space. The total amount of water is incompressible and evolves according to the mass continuity equation:

$$\frac{\partial W_{\text{tot}}}{\partial t} + \nabla \cdot \mathbf{q} = \frac{m}{\rho_w} \, , \tag{6.2}$$

where $\mathbf{q}$ is the water flux, m is the water input and ρ_w is the density of fresh water (1000 kg m^{-3}). Equation 6.2 describes water transport in a mass conserving manner and the water thickness changes when there is an imbalance between the water input and the flux divergence. The water input (m) at the bed is the sum of sources and sinks resulting from both subglacial production and englacially transported surface melt water. The basal heat budget, comprising englacial heat transport, geothermal heating and frictional heating by sliding of the ice over the bed, determines the rate of melting or refreezing of basal ice. As sliding velocities depend on the water pressure, this motivates a coupled interactive treatment of basal sliding, ice thermodynamics and subglacial water. However, for the sake of understanding the uncoupled behaviour of the drainage system, we prescribe a passive (i.e. uncoupled) spatially distributed time-dependent melt input.

6.2.2 Water flow

A Darcian type water transport scheme is used to move water between grid-cells. Water flow is described by a generic form of the Manning / Darcy-Weisbach flux formulation:

$$\mathbf{q} = -k W^{\alpha} |\nabla \psi|^{\beta - 2} \nabla \psi \, . \tag{6.3}$$

Here k is the effective hydraulic conductivity, ψ is the hydraulic potential and α and β are power-law constants. In line with *Hewitt et al.* [2012] we use $\alpha = 5/4$ and $\beta = 3/2$. The hydraulic potential is given by:

$$\psi = P + \rho_w g\,(b + W)\,, \tag{6.4}$$

where P denotes the water pressure, g is the gravitational acceleration and b is the bedrock height. Equations 6.3 and 6.4 describe water flow from high to low fluid potential, where the fluid potential is determined by water pressure (P) and the gravitational potential of the top of the water layer ($z = b + W$). Effectively, water is forced down gradients in water pressure (proportional to the ice thickness), bed height and water thickness. The water pressure P is non-negative and cannot exceed the overburden pressure, in which case the ice starts to float. The hydrostatic overburden pressure is given by:

$$P_o = \rho_i g(h - b)\,, \tag{6.5}$$

with ρ_i the density of ice (910 kg m^{-3}) and h the ice surface height.

By considering the hydraulic potential at the top of the water layer ($z = b + W$), any model with mass conservation (Equation 6.2) and Darcian flux (Equation 6.3) gives diffusive evolution for W. Many previous studies disregard this diffusive transport by considering the hydraulic potential at the bed height ($z = b$). In case of a constant distributed pressure field this leads to undesired unlimited growth of water thickness in local minima of the hydraulic potential. Decomposing the flux into advective and diffusive components leads to:

$$\mathbf{q} = \mathbf{V}W - D\nabla W\,, \tag{6.6}$$

where the advective velocity $\mathbf{V}$ and diffusion coefficient D are given by:

$$\mathbf{V} = -K\nabla\,(P + \rho_w g b) \tag{6.7}$$

$$D = \rho_w g K W\,. \tag{6.8}$$

Substantial diffusion may arise near lows of the geometric potential $\psi_0 = \rho_i g H + \rho_w g b$ in cases where sliding is small and the water thickness has built-up.

6.2.3 Capacity evolution

In a linked-cavity system the evolution of the bed separation Y is determined by the difference between opening by ice sliding over bumps in the bed $\mathscr{O}_{\text{cav}}$ and closure by creep under the influence of gravity $\mathscr{C}_{\text{cr}}$ [*Hewitt*, 2011]:

$$\frac{\partial Y}{\partial t} = \mathscr{O}_{\text{cav}} - \mathscr{C}_{\text{cr}}\,. \tag{6.9}$$

As in *Schoof et al.* [2012] cavitational opening is proportional to the absolute sliding velocity $|\mathbf{v}_b|$:

$$\mathscr{O}_{\text{cav}} = C_1 |\mathbf{v}_b| (W_r - Y)_+ \,. \tag{6.10}$$

Here W_r is a typical roughness height of basal topography and C_1 is a constant. The $(...)_+$ notation enforces positivity of $\mathscr{O}_{\text{cav}}$. Equation (6.10) illustrates opening increases with the rate of sliding and decreases when the capacity Y increases as the contact area between ice and bed reduces. Creep closure is expressed as a function of water pressure P and capacity Y [*Schoof*, 2010; *Hewitt*, 2011; *Schoof et al.*, 2012]:

$$\mathscr{C}_{\text{cr}} = C_2 A \, (P_o - P)^3 \, Y \,, \tag{6.11}$$

where A is the ice softness and C_2 is a constant. Collectively, Equations (6.9) - (6.11) describe how the capacity of the drainage system Y and water pressure P are related. A change in Y induces a temporary imbalance between opening and closure (non-zero $\frac{\partial Y}{\partial t}$) and a pressure change of similar sign will occur. Hence, in a linked-cavity system pressure increases with cavity size. In steady state, $\frac{\partial Y}{\partial t} = 0$ and water pressure P can be expressed as a function of Y, which is further discussed in Section 6.4.

6.2.4 Englacial storage

Equation 6.3 describes horizontal transport of water available at the ice-bed interface. Hence, only water at the ice-bed interface is horizontally exchanged between grid cells. In additional to subglacial water storage, in a porous glacier part of the available water is stored englacially and assumed to be efficiently connected in the vertical to subglacial storage [*Bartholomaus et al.*, 2011; *Hewitt*, 2013]. The subglacial water pressure P experienced at the bottom of the vertical column, i.e. at the subglacial connection, equals the hydrostatic pressure of the lowest englacial water. Hence, P can be expressed as a function of the height of the top of the water table z_{en} within the glacier:

$$P = \rho_w g z_{\text{en}} \,. \tag{6.12}$$

As $P \leq P_o$, the englacial water level $z_{\text{en}} \leq \frac{\rho_i}{\rho_w}(h-b)$, which implies the maximum water level is 91% of the ice thickness $H = h - b$, in which case flotation occurs. Assuming the glacier has a certain constant porosity ϕ, the water pressure P can be expressed in terms of the amount of englacial water W_{en}:

$$P = \frac{\rho_w g}{\phi} W_{\text{en}} \,. \tag{6.13}$$

From equation 6.13 it can be seen that the magnitude of a change in P, simultaneous with a change in W_{en}, depends inversely on the porosity of the medium ϕ. In Sections 6.3 and 6.5,

we illustrate and discuss the important role of a finite value for ϕ on reducing stiffness of the pressure evolution, thereby easing numerical implementation.

6.2.5 Closure

In previous sections we described the separate elements of the subglacial hydrology model. Mass conservation determines how the total water thickness $W_{\text{tot}} = W + W_{\text{en}}$ evolves in relation to the water pressure P. The cavity evolution model (Equations 6.9 - 6.11) describes how cavity size Y and P are related. Finally, the englacial water model relates water pressure P to the amount of englacial water W_{en}. At this point, combining Equations (6.1), (6.9) and (6.13) leads to the following set of equations:

$$\frac{\partial W}{\partial t} + \frac{\partial W_{\text{en}}}{\partial t} = -\nabla \cdot (\mathbf{q}(P,W)) + \frac{m}{\rho_w} , \tag{6.14}$$

$$\frac{\partial Y}{\partial t} = C_1 |\mathbf{v}_b| (W_r - Y)_+ - C_2 A (P_o - P)^3 Y , \tag{6.15}$$

$$P = \frac{\rho_w g}{\phi} W_{\text{en}} , \tag{6.16}$$

with $\mathbf{q}(P,W)$ given by Equations (6.3) and (6.4). As the above three equations contain four unknowns (W, W_{en}, Y and P) the system is underdetermined. To produce a solvable model an additional closure is needed.

To close the model we assume cavities to be full at all times, hence $Y = W$ [*Schoof et al.*, 2012; *Hewitt*, 2013]. This disables the underpressure case in which cavities become partially filled. Underpressure occurs when cavity closure (at $P = 0$) cannot keep up with a drop in the water level. By disallowing partially filled cavities we potentially overestimate water thickness in case of sudden drops in water input, as well as for very low water input, which is further discussed in Section 6.4.

With the full-cavity closure, the system of state equations can be rewritten as:

$$\frac{\partial W}{\partial t} + \frac{\partial W_{\text{en}}}{\partial t} = -\nabla \cdot (\mathbf{q}(P,W)) + \frac{m}{\rho_w} , \tag{6.17}$$

$$\frac{\partial W}{\partial t} = C_1 |\mathbf{v}_b| (W_r - W)_+ - C_2 A (P_o - P)^3 W , \tag{6.18}$$

$$\frac{\partial W_{\text{en}}}{\partial t} = \frac{\phi}{\rho_w g} \frac{\partial P}{\partial t} , \tag{6.19}$$

6.3 Role of englacial storage

Combining equations (6.17) - (6.19) yields the following pressure evolution equation:

$$\underbrace{\frac{\phi}{\rho_w g}\frac{\partial P}{\partial t}}_{\text{I}} = \underbrace{-\nabla\cdot(\mathbf{q}(P,W))}_{\text{II}} + \underbrace{\frac{m}{\rho_w}}_{\text{III}} + \underbrace{C_2 A (P_o - P)^3 W}_{\text{IV}} - \underbrace{C_1 |\mathbf{v}_b| (W_r - W)}_{\text{V}} \tag{6.20}$$

In order to understand the behaviour of the water pressure P in response to variable melt input m, we examine the terms I–V.

We first consider the case without englacial storage ($\phi = 0$), i.e. term I is zero, so Equation 6.20 is elliptic (in particular, has no time-derivative). A similar non-porous medium approach is applied in *Schoof et al.* [2012]. In case of a sudden shift to a larger constant melt input m, the water pressure P increases instantaneously, which on the one hand enhances transport out of the grid cell (term II) and on the other hand causes cavities to grow as creep closure (term IV) decreases. As W increases in subsequent time-steps, cavitational opening (term V) decreases and eventually balances with creep closure again at larger W. At the same time, a new balance between melt input (term III) and flux divergence (term II) is achieved. In a similar fashion, a sudden drop in the melt input requires an instantaneous lower water pressure P to attract more water from surrounding grid cells and accelerates creep closure. After some time a new balance between opening and closure, as well as between melt input and flux divergence, is then found at lower W.

In the porous medium case ($\phi > 0$) the pressure P no longer responds instantaneously to changes in the melt input. A sudden change of m is now initially balanced by an increase of term I, implying a non-zero $\frac{\partial P}{\partial t}$ and a gradual change of P rather than an instantaneous adjustment. From a physical point of view, the left-hand side of Equation (6.19) is equivalent to the change in the amount of englacially stored water $\frac{\partial W_{\text{en}}}{\partial t}$. A sudden change in m leads to a gradual change of the englacial water level and thereby also the water pressure. In case of a constant melt rate, P and W converge to equivalent values in both the porous and non-porous medium case. The porosity ϕ is a measure for how rapid the englacial water level and hence the water pressure responds to changes in m. Values for the porosity of a glacier will be higher for glaciers consisting of temperate ice than for cold ice sheets. Values used in literature are in the range $\phi = 10^{-4} - 10^{-1}$ [*Huss et al.*, 2007; *Bradford et al.*, 2009; *Hewitt*, 2011].

Accounting for englacial storage ($\phi > 0$) reduces stiffness of the pressure evolution equation (Equation (6.19)). Stiffness arises as the time-scales for pressure evolution are relatively short compared to water thickness evolution time-scales. The non-porous pressure equation ($\phi = 0$) contains no time-derivative and can be regarded as "infinitely stiff". [*Schoof et al.*, 2012] presents such a model, which at each time-step solves an instantaneous pressure balance by means of an elliptic variational inequality. Solving the porous-medium equation (6.19), including a pressure time-derivative, avoids solving instantaneous pressure changes, which

substantially eases numerical implementation and parallelisation.

6.4 Steady states

In case melt input is constant, the water pressure P and water thickness W converge to a steady state. In steady state, time-derivatives vanish and mass conservation and cavity evolution essentially become decoupled:

$$0 = -\nabla \cdot \mathbf{q} + \frac{m}{\rho_w} , \tag{6.21}$$

$$0 = C_1 |\mathbf{v}_b| (W_r - W)_+ - C_2 A (P_o - P)^3 W . \tag{6.22}$$

From Equation (6.22), a direct relation can be constructed linking water pressure P to water thickness W in steady state:

$$P(W) = P_o - \left(\frac{C_1 |\mathbf{v}_b|}{C_2 A} \right)^{1/3} \left(\frac{(W_r - W)_+}{W} \right)^{1/3} . \tag{6.23}$$

The water pressure reaches overburden $P = P_o$ for $W \geq W_r$. Since P cannot become negative, we can also define a critical $W = W_c$ below which underpressure occurs and Equation (6.22) no longer applies. Using that in case of underpressure $P = 0$, a critical water cavity size W_c can be derived from Equation (6.22):

$$W_c = \frac{W_r}{\frac{C_2 A}{C_1 |\mathbf{v}_b|} P_o^3 + 1} \tag{6.24}$$

In order to satisfy $P \geq 0$ the water thickness $W \geq W_c$. The critical water thickness W_c represents a minimum cavity size resulting from a balance of cavitational opening and creep closure at zero water pressure. In principle, the water thickness W could become smaller than this minimum cavity size, leaving the cavity partially filled. As a consequence of the full-cavity closure, we do not model this effect, thereby slightly overestimating water thickness in case of underpressure. Nevertheless, values of W_c are typically smaller than a few percent of W_r indicating a minor effect on simulated W.

Equation (6.23) gives useful insight in how steady-state pressures depend on model parameters. The independence of the steady-state P on ϕ confirms that the porosity only affects the rate of change of P after variations in the melt input, rather than steady values of P (and W).

It is noteworthy that we are only able to construct a $P(W)$ relation by assuming a steady state. In non-steady conditions, mass conservation and cavity evolution are no longer decoupled, impeding construction of such a $P(W)$ expression. Modelling both the cavity evolution and water transport provides a way to solve for both P and W without having to specify an

additional parameterisation relating for $P(W)$ [*Schoof et al.*, 2012]. This is a major advantage over previous approaches as in *Flowers and Clarke* [2002] and *Pimentel and Flowers* [2011], applying a similar mass conservation equation, but with a direct $P(W)$ power-law relation based on scarce observational data. Such parameterised $P(W)$ relations may be useful to predict $P(W)$ in steady state but are unlikely to produce reasonable results in non-steady conditions, i.e. for transient melt input.

6.5 Results

In this section, we show results of application of the stand-alone hydrology model to the grid of Nordenskiöldbreen, Svalbard. With these test experiments we aim to: 1) verify sensitivity of steady-state P and W to perturbations of uncertain model parameters, 2) test robustness under grid refinement, and 3) study the role of ϕ on the evolution of P and W in transient melt conditions.

6.5.1 Setup

We perform experiments on a 31 by 24 km grid with a standard grid spacing of 500 m. The bed height and surface height are constant in time and shown in Figure 6.1a and b. The hydrology model is passively forced with a constant sliding velocity field (Figure 6.1c). For the steady-state experiments in Section 6.5.2 an idealised height-dependent melt input is prescribed, representing mean summer surface runoff based on altitudinal profiles in Chapter 2 (Figure 6.2a). The prescribed time- and height-dependent melt input for the transient experiments (Section 6.5.3) is shown in Figure 6.2b, representing a typical seasonal melt cycle.

An overview of model parameters and physical constants is given in Table 6.1. The model equations contain several often poorly constrained parameters, for which we selected values used in previous work. This is referred to as the standard setup. Calibration of uncertain parameters can potentially be done in a coupled ice dynamical / hydrology modelling approach by matching simulated and observed surface velocities, which is left for future work. Here, we study the role of parameter choices on model behaviour.

6.5.2 Steady-state experiments

First, we focus on steady-state behaviour of water pressure P and thickness W after perturbing the conductivity K, the creep closure constant C_2, the melt rate m and the sliding velocity $|\mathbf{v}_b|$. The resulting steady-state P and W distributions are compared to the standard patterns in Figure 6.3. Pressure is shown as a fraction of the overburden pressure, i.e. $P_{\text{frac}} = P/P_0$.

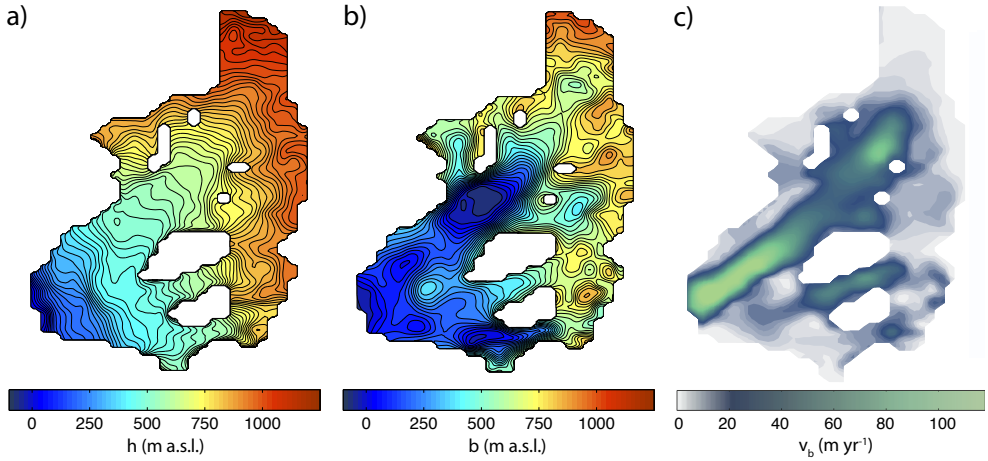

Figure 6.1: *Distributed maps of surface topography h (a), basal topography b (b) and sliding velocity $|\mathbf{v}_b|$ (c). A SPOT5 DEM [Korona et al., 2009] provides surface heights; bed heights and sliding velocities result from an iterative inverse estimation procedure, described in Chapter 5.*

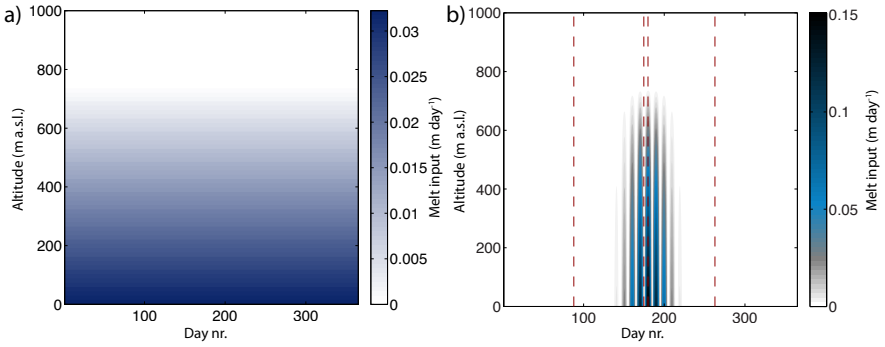

Figure 6.2: *Melt input for the steady-state experiments (a) and the transient experiments (b). In the transient experiments, a background melt rate of 0.05 m yr^{-1} (1.4×10^{-4} m day^{-1}) is prescribed. Days 91, 177, 182, and 273 are indicated by dashed vertical lines; compare Figure 6.5.*

Table 6.1: *Physical constants and model parameters.*

Name	Default Value	Units	Description
g	9.81	$\mathrm{m\,s^{-2}}$	acceleration of gravity
ρ_i	910	$\mathrm{kg\,m^{-3}}$	ice density [*Greve et al.*, 2006]
ρ_w	1000	$\mathrm{kg\,m^{-3}}$	fresh water density [*Greve et al.*, 2006]
A	3.1689×10^{-24}	$\mathrm{Pa^{-3}\,s^{-1}}$	ice softness
α	$5/4$		power in flux formula [*Hewitt et al.*, 2012]
β	$3/2$		power in flux formula [*Hewitt et al.*, 2012]
C_1	0.500	$\mathrm{m^{-1}}$	cavitation coefficient [*Hewitt et al.*, 2012]
C_2	0.158		creep closure coefficient
ϕ	0.001		porosity of englacial system
k	0.01	$\mathrm{m^{2\beta-\alpha}\,s^{2\beta-3}\,kg^{1-\beta}}$	conductivity coefficient [*Hewitt et al.*, 2012]
W_r	0.1	m	roughness scale [*Hewitt et al.*, 2012]

Much of the demonstrated behaviour in these experiments can be understood by looking at Equations (6.21) - (6.23).

Perturbing the melt input m affects fluxes in the mass conservation equation. In steady state, Equation (6.21) applies and a larger water input implies a larger outflow (i.e. a larger flux divergence). This occurs for larger W, which according to Equation (6.23) implies a higher pressure P. Hence, both P and W increase with m. Strongest deviations of the spatial pattern are seen towards lower altitudes where absolute changes in m are largest.

Sliding velocities $|\mathbf{v}_b|$ directly affect the rate of cavity opening by cavitation. Larger sliding velocities imply stronger cavity opening, which is associated with a lower water pressure P, according to Equation (6.23). At the same time, larger cavities hold more water, which tends to increase steady-state P and partly offsets the pressure lowering. Perturbing the creep closure coefficient C_2 has exactly the opposite effect. From Equation (6.23), it follows that enhanced creep tends to increase water pressures, while a lower water thickness partly offsets this effect.

The hydraulic conductivity k directly alters the efficiency of the drainage system. In a slow drainage system water accumulates yielding larger W. According to Equation (6.23) this implies an increase in steady-state pressure P. Conversely, in case of a high conductivity k, water is more efficiently transported out of the drainage system, resulting in low W and P in steady state.

To verify robustness under grid refinement, the unperturbed experiment is repeated with a doubled horizontal resolution. A comparison of P_{frac} and W at 250-m and 500-m resolution is shown in Figure 6.4. Results indicate consistency of the distributions for finer grids.

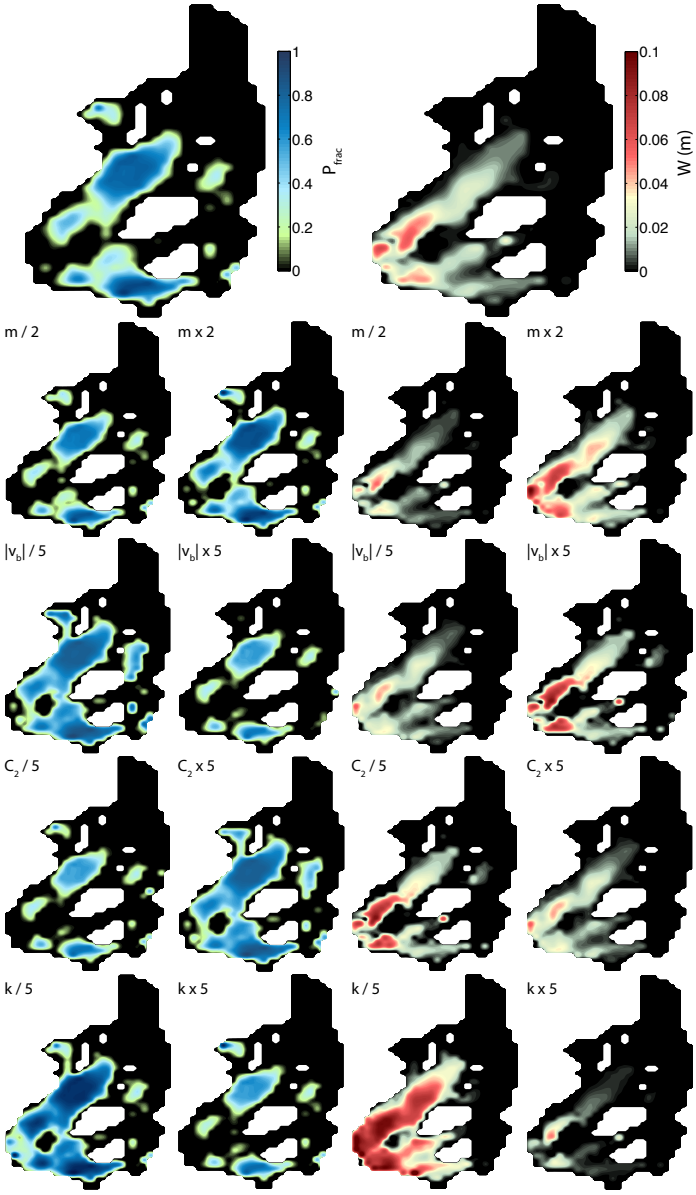

Figure 6.3: *Relative water pressure fraction $P_{frac} = P/P_0$ and water thickness W distributions for the unperturbed steady-state experiment (1^{st} row) and experiments with perturbed melt input m (2^{nd} row), sliding velocity $|\mathbf{v}_b|$ (3^{rd} row), creep closure coefficient C_2 (4^{th} row) and hydraulic conductivity k (5^{th} row).*

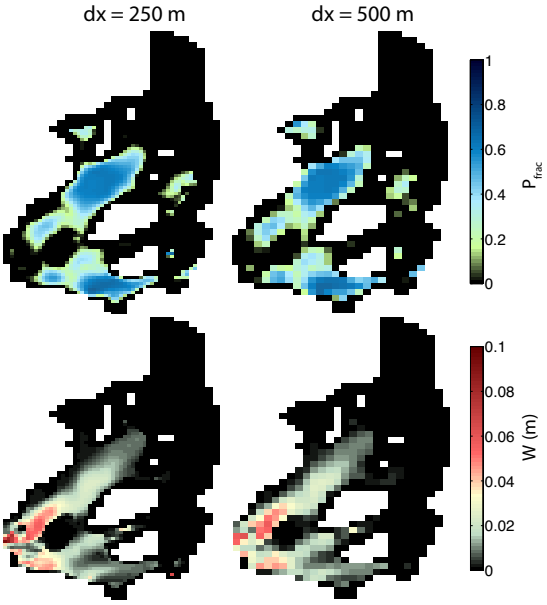

Figure 6.4: *Steady state fractional pressure P_{frac} and water thickness W at 250-m and 500-m resolution.*

6.5.3 Transient experiments

In a next step, we illustrate the role of englacial storage on the pressure and water thickness evolution. In steady state the englacial porosity ϕ does not directly influence steady-state pressures in Equation (6.23). Also, the water thickness W evolution from mass continuity (Equation (6.21)) is independent of ϕ in steady state. From this it can be understood that steady-state P and W are insensitive to changes in the englacial porosity ϕ. On the other hand, in non-steady conditions, enforced by varying the melt input m, Equation (6.20) applies and ϕ affects the pressure evolution. Here, we analyse the impact of ϕ on the pressure evolution by performing experiments with different values of ϕ, while forcing the model with idealised seasonal melt input (Figure 6.2b).

Snapshots of the fractional water pressure P_{frac}, water thickness W and hydraulic potential ψ for a run with $\phi = 0.001$ are shown in Figure 6.5. Corresponding times of the snapshots are indicated in Figure 6.2b.

Figure 6.5 illustrates that prior to the start of the melt season, water resides only in local minima of the fluid potential. Even without the small background melt input rate, some water would remain in the fluid potential minima as water concentrates in these areas (and does not reach the glacier boundary). Advective water flow is dominated by horizontal gradients in water pressure and surface height, with an additional weaker influence of gradients in basal

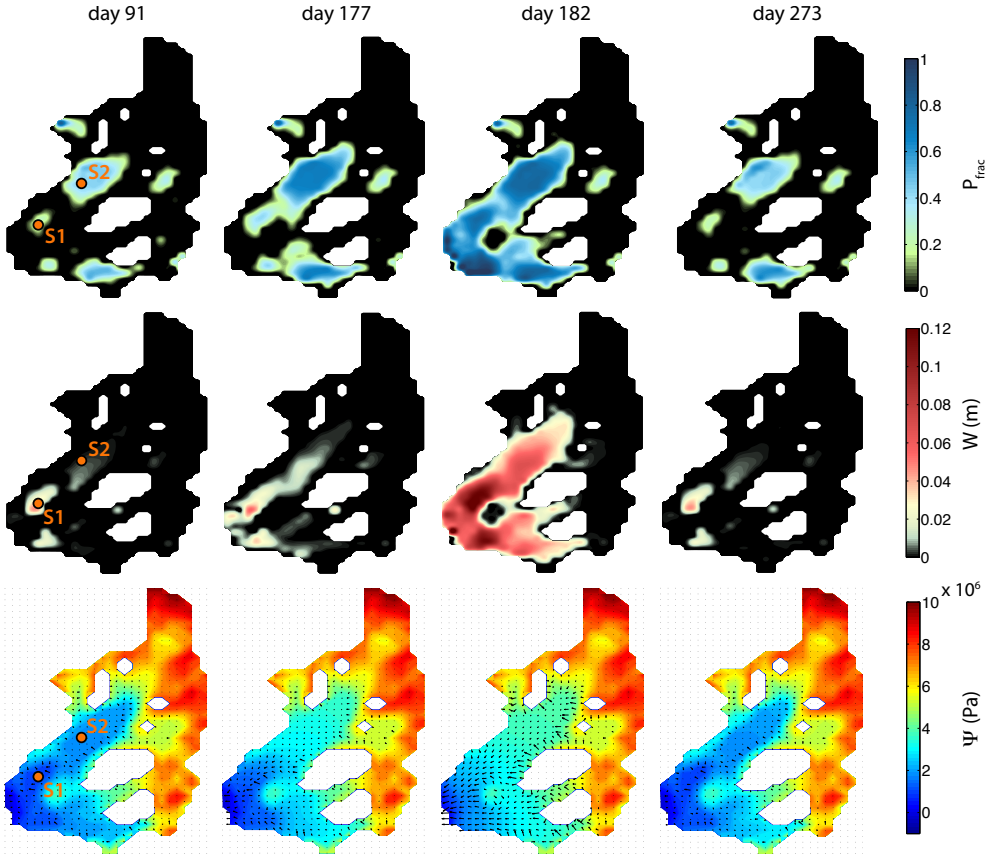

Figure 6.5: *Snapshots of the fractional water pressure (1st row), water thickness (2nd row) and hydraulic potential (3rd row) in the transient melt input experiment with* $\phi = 0.001$. *Arrows superposed on the hydraulic potential maps indicate advective water flow direction and speed (up to 0.25 m* s^{-1}*). The temporal evolution of water pressure and thickness is analysed in more detail at sites S1 and S2, marked in orange.*

topography. Shallow subglacial water levels in fluid potential minima cause substantial water pressures to persist outside the melting season. Substantial sliding and cavitational opening near the glacier front leads to relatively low water pressures even in case of a substantial water amount of subglacial water. During the melt season substantial variability in melt input induces strong changes in the subglacial water pressure and water thickness distributions, shown for a minimum in the melt input at day 177 and a maximum at day 182. Increasing melt input implies water accumulation and elevated water pressures to increase the system's capacity and to move more water out of the system. Conversely, a drop in the melt input induces a decrease in the subglacial water level and a lower water pressure reduces the system's

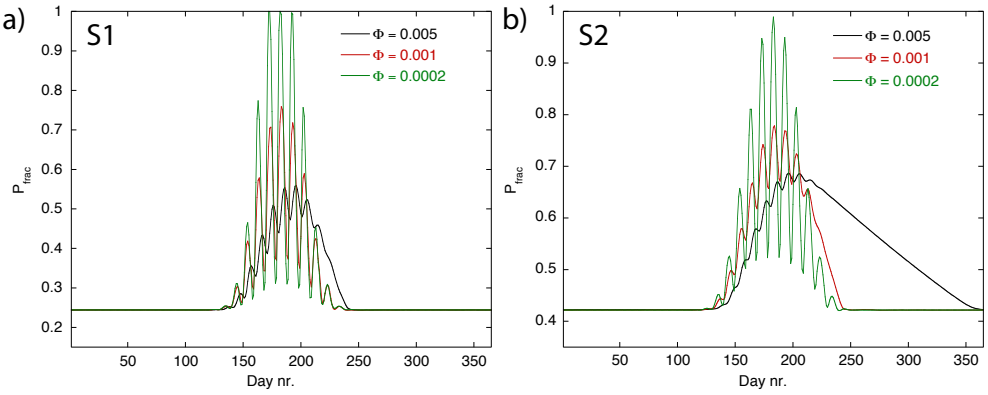

Figure 6.6: *Time-series of the fractional pressure at sites S1 (a) and S2 (b) for englacial porosity* $\phi = 0.0002$ *(green),* 0.001 *(red) and* 0.005 *(black).*

capacity and attracts more water from surrounding grid cells.

We repeated the experiment with smaller porosity ($\phi = 0.0002$) and larger porosity ($\phi = 0.005$). Time-series of the annual evolution of fractional pressure at sites S1 and S2 are shown in Figure 6.6. As discussed in Section 6.3 the englacial porosity is a measure for how rapid the water pressure responds to changes in the melt input. The englacial porosity regulates the rapidity of changes in the water pressure as it affects the rate of change of the englacial water level. With a high englacial porosity, a large flux from or to the englacial system is required to substantially change the englacial water level and water pressure. Figure 6.6 depicts the slow response of subglacial water pressures to melt variability for large ϕ. In case of large ϕ, short-term pressure variations are nearly absent during the melt season and it takes several months before the pressure relaxes back to steady-state pressures outside the melt season. Conversely, in case of a low englacial porosity, pressure responds very quickly to changes in melt input as only small changes in the englacial water amount are needed to change the englacial water level substantially. In addition to the choice of ϕ, the rapidity of pressure variations, reflecting changes in the englacial water level, are affected by local factors. For example, a relatively large ice thickness and slow water flow explain a longer response time at S2 in comparison to S1.

Time-stepping restrictions for advection and diffusion of water are usually much less severe than restrictions for the evolution of pressure. Nevertheless, the minimum time-step for stability of the pressure evolution depends linearly on the porosity ϕ, which implies computational cost generally reduces linearly with increasing ϕ. This means calculations for a highly porous medium, such as a fast-flowing temperate glacier, are much more efficient than for a slow and cold glacier with a low porosity. In case one is interested in simulating longer-term variations in water pressure one could decide to manually select a higher porosity to reduce

computational cost at the expense of short-term variations in water pressure. In that case, the porosity does no longer reflect the actual englacial pore space, but is rather used as a regularisation parameter to reduce stiffness of the pressure equation.

6.6 Conclusions & outlook

We have tested and analysed behaviour of a subglacial hydrology model, which combines a distributed linked-cavity model with an englacial model. The model simulates water transport and the evolution of water pressure under varying melt conditions. The model combines water flow along fluid potential gradients with a cavity opening/closure model, while the water pressure is linked to the englacial water level. A major advantage of accounting for englacial storage is that it reduces stiffness of the pressure evolution, thereby substantially easing numerical implementation and reducing computational cost. In this work, we analysed steady-state behaviour and the role of englacial transport under transient melt conditions.

In steady state, subglacial water pressure in a linked-cavity system can directly be related to the amount of subglacial water in the form of a power law. We find that steady state pressures are proportional to the magnitude of creep closure and the melt input, while pressures are inversely proportional to the conductivity of the drainage system and the magnitude of basal sliding. Furthermore, steady-state water pressure and thickness are independent of the englacial porosity and converge under grid refinement. The use of a direct relation between pressure and water amount, as is done by means of a parameterisation in *Flowers and Clarke* [2002]; *Bueler and Brown* [2009]; *Pimentel and Flowers* [2011], seems only appropriate when the system is close to steady state most of the time. The lack of dependence of pressure on sliding velocities in such parameterisations increases uncertainty in computed pressures when opening by cavitation is deemed as an important process.

Test results with a transient melt input, representing a typical seasonal melt cycle, on Nordenskiöldbreen, Svalbard, illustrate that the chosen englacial porosity strongly affects the rapidity of adjustment of the englacial water level and thereby the water pressure to changes in the melt input. In highly porous glaciers, such as fast-flowing temperate glaciers, pressure variability is strongly dampened. On the contrary, in slow-flowing cold ice with a low englacial porosity, water pressure reacts quickly to changes in melt input.

The main aim of this work was to present and test a hydrology model which is suitable for coupling to the thermo-mechanically coupled ice sheet model PISM. As mentioned, ice sheet models require a hydrology model that: 1) includes reasonable physics of water transport and drainage system evolution, 2) is applicable to a wide range of spatial and temporal scales, 3) has a limited number of poorly-constrained parameters that can be constrained given scarcely available data. We are somewhat reluctant to incorporate more detailed physics as this will interfere with goals 2) and 3). The addition of englacial storage is however very important when coupling the hydrology model to PISM as it introduces the englacial porosity as a

regularisation parameter. As a higher englacial porosity reduces runtime at the expense of detail in the pressure evolution, englacial porosity can be used as an adjustable parameter, whose value should reflect a tradeoff between computational effort and temporal accuracy. In long time-scale experiments a high value for the porosity parameter may be desired, whereas a lower value could be used in short time-scale experiments when more detail in computed pressures is required. Note that, as steady-state pressures are unaffected by englacial porosity, it is only the rate of convergence of water pressures towards a new steady state, which is affected by this parameter.

In this work, the hydrology model is used as a stand-alone model without interaction with ice flow dynamics and thermodynamics. Current work focuses on coupling the hydrology model to PISM. We further investigate possibilities to extend the hydrology model as this may be desired for specific applications. For example, a till model could be added, which accounts for exchange of water with a porous till layer at the base of the ice. Additionally, the current model does not account for a possible transition of the distributed drainage system into a channelised system. For example, when attempting to simulate the seasonal pressure evolution of fast-flowing outlet glaciers, such an extension may be relevant to model enhanced efficiency of the drainage system for high melt input rates. Recent studies attempting to couple distributed and channelised drainage yield promising results [*Schoof*, 2010; *Pimentel and Flowers*, 2011; *Hewitt et al.*, 2012; *Hewitt*, 2013], but require the positions of channels to be fixed, which together with the lack of data to constrain additional parameters limits the use of implementation in ice sheet models. We currently investigate alternative ways to account for the qualitative impact of fast channelised drainage on subglacial water pressures. It should be noted that all model extensions will go at the expense of adding more poorly-known parameters to a system, which is already poorly-constrained through the lack of direct observations of basal processes. Adding complexity to subglacial models is meaningless if calibration of model parameters yields infinite possible solutions given a shortage of observational data.

7

Conclusions & outlook

The main aim of this dissertation is to improve our understanding of both surface and basal conditions in the context of Svalbard glaciers. In this final chapter, a brief summary is given of the key results of this thesis and some directions for future work are discussed.

7.1 Surface processes

At the surface, interactions with the atmosphere and underlying firn determine the surface mass budget. In Chapter 2, the spatio-temporal evolution of the surface mass balance and the snow/firn pack of Nordenskiöldbreen has been analysed. For that purpose, a surface energy balance model has been coupled to a multi-layer snow model, forced with meteorological input from a regional climate model (RACMO) and nearby weather station data over the period 1989-2010. Regional climate model output provides valuable input for mass balance modelling, particularly in areas with scarce availability of meteorological records from weather stations. A wealth of in situ observations plays a decisive role in calibrating, initialising and validating the model. A mean negative surface mass balance of -0.39 m w.e. yr^{-1} was found for 1989-2010 and only two positive mass balance years could be identified. Variability in the annual mass balance is to a large extent explained by summer temperature variations. Refreezing of melt water contributes as much as 0.27 m w.e. yr^{-1} to the mass budget, constituting a substantial fraction of 69% of annual accumulation. Refreezing is most pronounced in the accumulation area, thereby raising annual mean subsurface temperatures at a few meters depth to melting point. These results importantly illustrate that for Arctic glaciers like Nordenskiöldbreen accounting for firn processes is crucial for accurate modelling of the surface mass balance. Additionally, accounting for the major impact of refreezing on subsurface temperatures and the timing and rate of melt water input into the englacial system, is of high relevance for ice dynamical modelling exercises, requiring prescribed surface conditions. Climate sensitivity experiments demonstrate that accounting for seasonally inhomogeneous climate change, with relatively modest warming in summer, substantially reduces the mass balance and refreezing sensitivity in a changing climate. The mass balance effect of a 1 K annual mean temperature increase of -0.21 m w.e. yr^{-1} is found to be balanced by a precipitation increase of 23%. As projected temperatures are expected to

increase by as much as 4-6 K for this region from 1961-1990 to 2071-2100, while precipitation is expected to rise by only 10-20% [*Førland et al.*, 2011], severe surface mass loss can be expected in the 21st century.

Substantial uncertainty in mass balance modelling as well as in the interpretation of local mass balance observations stems from the lack of detailed knowledge of how snow accumulation varies in space and time. In Chapter 3, a novel inverse approach is presented to extract annual accumulation along a transect from reflectivity contrasts in ground-penetrating radar (GPR) data. The method uses the coupled surface energy balance - snow model (Chapter 2) in an inverse approach and aims to find a match between simulated and observed radar travel times by iteratively adjusting accumulation, serving as input for the coupled model. This approach has distinct advantages over traditional methods. Firstly, since the model accounts for mass exchange between annual layers and runoff, we can distinguish between annual surface accumulation and mass stored in annual layers. In contrast to traditional approaches, this enables reconstructing accumulation from GPR in temperate firn with substantial melt percolation, refreezing and runoff. Secondly, explicit modelling of density variability and water content along the transect avoids the need to make rough assumptions on these variables as in traditional methods affecting reconstructed accumulation. Application of the method to infer accumulation along a 16-km transect on Nordenskiöldbreen results in annual accumulation patterns between 2007-2012. Accumulation is found to vary substantially in space and time with standard deviations of spatial variability ranging between 13 and 27% of the annual mean for the different years. Accounting for horizontal density variability along the transect is shown to reduce spatial variability in reconstructed accumulation by as much as 19% in comparison to traditional methods. Correlating the mean spatial accumulation pattern against terrain characteristics (slope, curvature and wind sheltering) reveals a strong prevalence of snow deposition on steep slopes in the lee of undulations. These findings may help in the development of new parameterisations linking accumulation variability to terrain features and wind characteristics. Finally, the effect of small-scale spatial variability on the mean surface mass balance is quantified, indicating a negligible effect in the accumulation area and a substantial mass loss of on average -0.08 m w.e. yr^{-1} in the ablation zone. The non-zero effect of spatial variability in accumulation on the mean mass budget is a direct consequence of nonlinearity of the mass balance response to changes in precipitation. Future studies involving mass balance modelling in environments with pronounced small-scale variability in accumulation should bear in mind that systematic errors in the estimated mean surface mass balance may arise when prescribing unrealistically smooth spatial accumulation patterns.

7.2 Subglacial conditions

At the ice-bed interface, the rate of basal motion depends crucially and in a complex manner on the interplay of stresses, thermodynamics and hydrology. Regardless of variability in

the external climate forcing, these internal interactions may lead to feedbacks inducing periodic changes in ice geometry and dynamics. In Chapter 4, we studied cyclic behaviour in a thermo-mechanically coupled 3-D ice sheet model (PISM) arising from internal feedbacks. An analysis has been given in which cyclic variations in the rate of basal sliding are linked to changes in ice geometry, the basal thermal structure and the distribution of subglacial water. Steady fast flow and two types of cyclic behaviour were identified when exploring a parameter space spanned by two sliding law parameters. High-frequency and low-frequency oscillations are identified and differ in terms of volume fluctuations and changes in the polythermal basal structure. The low-frequency cycles appear to be of similar origin as a previously proposed thermally-controlled mechanism for both surging of glaciers in Svalbard and Heinrich-type oscillations of large ice sheets. Cyclic behaviour is found to be more pronounced for low till strength and a more plastic sliding law. Accounting for the surface height dependence of the mass balance introduces an additional destabilising mechanism, possibly interfering with other internal feedbacks. Although Chapter 4 provides useful insight in possible oscillatory mechanisms and controls on cyclic behaviour, much remains to be learned about the processes involved. Clearly, the occurrence, magnitude and frequency of cyclic behaviour depends strongly on the choice of sliding law and prescribed material properties of the bed. When attempting to simulate surging of actual glaciers, detailed knowledge is hence required of site-specific basal conditions (such as sediment properties, basal topography, thermal structure and drainage system morphology), which is commonly infeasible given a lack of observational constraints. Additionally, more observational data, either directly or indirectly providing information on basal conditions, are inevitably needed to facilitate physical model development required to simulate surge-type behaviour of actual glaciers in more detail. For example, simulating surging of glaciers in Alaska, which has been linked to changes in drainage efficiency, requires a more detailed treatment of water pressure variations in response to transient behaviour of the drainage system. First steps towards a more complete subglacial hydrology model for PISM have been discussed in Chapter 6.

Detailed knowledge of basal topography is relevant both for estimating ice volume contained in ice masses as well as for accurate time-dependent modelling of glacier dynamics. As direct observations of basal topography are scarce, inverse methods in which more widely available surface data are used to learn about basal conditions have become of increasing interest. Chapter 5 evaluates an inverse modelling approach in which step-wise adjustments of bed heights, serving as a lower boundary in an ice dynamical model, are applied to minimise the discrepancy between modelled and measured surface heights. Following up on previous flowline modelling work, a simple regularisation technique is used in which the surface misfit is directly used to adjust bed heights. Chapter 5 provides a first application of the method in 3-D and initial experiments verify robustness/convergence of the approach in a synthetic framework with a constant climate forcing. In a next step, the approach is applied to the real glacier geometry of Nordenskiöldbreen, which involves additional complexity related to dealing with data errors and a height- and time-dependent climate forcing. A stopping criterion

is used to stop the iterative method before the bed gets too severely polluted by undesired noise. Validation against scarce radar data reveals successful reconstruction of bed heights. Remaining uncertainties can mainly be ascribed to uncertain model physics and in particular in the description of sliding. Further improving the description of sliding in response to changes in till properties and water pressures would help to improve the accuracy of derived bed heights. In addition to recovering basal topography, the method additionally provides a method for initialisation as modelled present-day surface heights match observed values and thermodynamics are consistent with past surface climate conditions. In future work, the approach may hence serve as a useful tool to spin-up ice dynamical models for forecasting experiments. As the bed-height correction method can be used with ice flow models of varying complexity, the inverse method can both be applied for accurate mapping of basal topography of individual glaciers (using more complete ice flow models) or to estimate the ice volume contained in a number of glaciers (using simpler ice flow models). Chapter 5 importantly considers the case where only surface height data and no surface velocity data are used in the bed-height reconstruction. In case distributed remotely-sensed surface velocity data would be available, an alternative mass conservation approach can be applied to reconstruct basal topography [*Morlighem et al.*, 2011; *McNabb et al.*, 2012]. Furthermore, with distributed surface velocity data, simultaneous inversion for both basal topography and slipperiness can potentially be done either by means of time-dependent adjoint-based inversions [*Goldberg and Heimbach*, 2013] or, in the case of ice-streams, using bayesian inference methods [*Gudmundsson and Raymond*, 2008; *Raymond Pralong and Gudmundsson*, 2011].

In Chapters 4 and 5, the urge for a more detailed treatment of subglacial hydrology to improve modelling accuracy has been stressed. In Chapter 6, ongoing work towards implementation of a new hydrology model in PISM is presented and discussed. The principle aim of a hydrology model is to compute water pressures, as sliding laws used in ice dynamical models commonly relate the degree of basal friction to the effective pressure of the ice. In order to model water pressures ice sheet models require a hydrology component that: 1) incorporates reasonable physics of water transport and drainage morphology, 2) is applicable at a wide range of spatial and temporal scales, 3) includes a limited number of poorly-constrained constants. Keeping this in mind, a linked-cavity drainage model is coupled to an englacial storage model, which enables simulating spatio-temporal water pressure variations, subglacial water transport and an evolving drainage system capacity. Steady-state experiments provide useful insight in the high sensitivity of computed water pressures to uncertain model parameters affecting cavity opening/closure and transmissivity of the drainage system as well as to changes in melt water sources. Steady-state pressures are found to be independent of englacial storage. Experiments with transient melt input illustrate the crucial role of accounting for englacial storage on the rapidity of variations in simulated water pressures. Incorporating englacial storage substantially eases numerical implementation by relaxing stiffness of the pressure evolution. At the same time, computational effort reduces substantially for larger englacial porosity. In Chapter 6, the use of the englacial porosity as an adjustable regularisation pa-

rameter, which value reflects a tradeoff between computational effort and temporal accuracy of the pressure evolution, has been suggested. This effectively facilitates application of a coupled ice dynamical / subglacial hydrology model at a wide range of spatial and temporal scales. Current work mainly focusses on implementing the hydrology model in the ice dynamical framework of PISM. This involves numerical choices in how to deal with processes acting at different characteristic time-scales and physical modelling choices, such as which sliding law is most appropriate to connect hydrology and basal shearing. Several further extensions of the hydrology model are currently being explored including adding a porous till layer and/or accounting for channelised drainage. The unstably concentrating character of channelised drainage remains challenging to model as channels are required to form at specified locations, which limits robustness of results under grid refinement. Alternative methods to include channelised drainage in a qualitative way without explicit modelling of channel formation and growth are currently being investigated.

Bibliography

ACIA (2005), *Arctic climate impact assessment*, Cambridge University Press.

Alley, R., S. Axandakrishxan, C. Bentley, and N. Lord (1994), A water-piracy hypothesis for the stagnation of Ice Stream C, Antarctica, *Annals of Glaciology*, *20*(1), 187–194.

Anandakrishnan, S., and R. Alley (1997), Stagnation of ice stream C, West Antarctica by water piracy, *Geophysical Research Letters*, *24*(3), 265–268.

Anandakrishnan, S., R. Alley, R. Jacobel, and H. Conway (2001), The flow regime of Ice Stream C and hypotheses concerning its recent stagnation, *The West Antarctic Ice Sheet: Behavior and Environment, AGU Antarctic Research Series*, *77*, 283–296.

Arcone, S., V. Spikes, and G. Hamilton (2005), Stratigraphic variation within polar firn caused by differential accumulation and ice flow: Interpretation of a 400 MHz short-pulse radar profile from West Antarctica, *Journal of Glaciology*, *51*(174), 407–422.

Arnold, N., I. Willis, M. Sharp, K. Richards, and W. Lawson (1996), A distributed surface energy-balance model for a small valley glacier. I. Development and testing for Haut Glacier d'Arolla, Valais, Switzerland, *Journal of Glaciology*, *42*(140), 77–89.

Arthern, R., and G. Gudmundsson (2010), Initialization of ice-sheet forecasts viewed as an inverse Robin problem, *Journal of Glaciology*, *56*(197), 527–533.

Arthern, R., D. Vaughan, A. Rankin, R. Mulvaney, and E. Thomas (2010), In situ measurements of Antarctic snow compaction compared with predictions of models, *Journal of Geophysical Research*, *115*(F3), F03,011.

Aschwanden, A., and H. Blatter (2009), Mathematical modeling and numerical simulation of polythermal glaciers, *Journal of Geophysical Research*, *114*(F1), F01,027.

Aschwanden, A., E. Bueler, C. Khroulev, and H. Blatter (2012), An enthalpy formulation for glaciers and ice sheets, *Journal of Glaciology*, *58*(209), 441–457.

Aster, R., B. Borchers, and C. Thurber (2005), Parameter estimation and inverse problems: Elsevier Academic Press, *Burlington, Massachusetts*.

Bales, R., Q. Guo, D. Shen, J. McConnell, G. Du, J. Burkhart, V. Spikes, E. Hanna, and J. Cappelen (2009), Annual accumulation for Greenland updated using ice core data developed during 2000–2006 and analysis of daily coastal meteorological data, *Journal of Geophysical Research: Atmospheres (1984–2012)*, *114*(D6).

Bartholomaus, T., R. Anderson, and S. Anderson (2007), Response of glacier basal motion to transient water storage, *Nature Geoscience*, *1*(1), 33–37.

Bartholomaus, T., R. Anderson, and S. Anderson (2011), Growth and collapse of the distributed subglacial hydrologic system of Kennicott Glacier, Alaska, USA, and its effects on basal motion, *Journal of Glaciology*, *57*(206), 985–1002.

Bartholomew, I., P. Nienow, D. Mair, A. Hubbard, M. King, and A. Sole (2010), Seasonal evolution of subglacial drainage and acceleration in a Greenland outlet glacier, *Nature Geoscience*, *3*(6), 408–411.

Bell, C., D. Mair, D. Burgess, M. Sharp, M. Demuth, F. Cawkwell, R. Bingham, and J. Wadham (2008), Spatial and temporal variability in the snowpack of a High Arctic ice cap: implications for mass-change measurements, *Annals of Glaciology*, *48*(1), 159–170.

Benestad, R. (2008), *Empirical-Statistical downscaled Arctic Temperature and Precipitation Series*, Met.no Report 12/2008.

Berthier, E., E. Schiefer, G. Clarke, B. Menounos, and F. Rémy (2010), Contribution of Alaskan glaciers to sea-level rise derived from satellite imagery, *Nature Geoscience*, *3*(2), 92–95.

Bindschadler, R., and P. Vornberger (1998), Changes in the West Antarctic ice sheet since 1963 from declassified satellite photography, *Science*, *279*(5351), 689–692.

Blaszcyk, M., J. Jania, and J. O. Hagen (2009), Tidewater glaciers of Svalbard: Recent changes and estimates of calving fluxes, *Polish Polar Research*, *30*(2), 85–142.

Blatter, H., and K. Hutter (1990), Polythermal conditions in Arctic glaciers, *Journal of Glaciology*, *37*, 261–269.

Bond, G., et al. (1992), Evidence for massive discharges of icebergs into the North Atlantic ocean during the last glacial period, *Nature*, *360*, 245–249.

Bougamont, M., S. Tulaczyk, and I. Joughin (2003), Response of subglacial sediments to basal freeze-on: 2. Application in numerical modeling of the recent stoppage of Ice Stream C, West Antarctica, *Journal of Geophysical Research*, *108*(B4).

Bougamont, M., J. Bamber, and W. Greuell (2005), A surface mass balance model for the Greenland Ice Sheet, *Journal of Geophysical Research*, *110*(F4), F04,018.

Bradford, J., J. Nichols, T. Mikesell, and J. Harper (2009), Continuous profiles of electromagnetic wave velocity and water content in glaciers: an example from Bench Glacier, Alaska, USA, *Annals of Glaciology*, *50*(51), 1–9.

Braithwaite, R. (1995), Positive degree-day factors for ablation on the Greenland ice sheet studied by energy-balance modelling, *Journal of Glaciology*, *41*(137), 153–160.

Braithwaite, R., and Y. Zhang (1999), Modelling changes in glacier mass balance that may occur as a result of climate changes, *Geografiska Annaler: Series A, Physical Geography*, *81*(4), 489–496.

Brown, J., J. Harper, W. T. Pfeffer, N. Humphrey, and J. Bradford (2011), High-resolution study of layering within the percolation and soaked facies of the Greenland Ice Sheet, *Annals of Glaciology*, *52*(59), 35–42.

Budd, W. (1975), A first simple model for periodically self-surging glaciers, *Journal of Glaciology*, *14*(70), 3–21.

Budd, W., P. Keage, and N. Blundy (1979), Empirical studies of ice sliding, *Journal of Glaciology*, *23*(89), 157–170.

Bueler, E., and J. Brown (2009), Shallow shelf approximation as a sliding law in a thermomechanically coupled ice sheet model, *Journal of Geophysical Research*, *114*(F3), F03,008.

Bueler, E., J. Brown, and C. Lingle (2007), Exact solutions to the thermomechanically coupled shallow-ice approximation: effective tools for verification, *Journal of Glaciology*, *53*(182), 499–516.

Bugnion, V., and P. Stone (2002), Snowpack model estimates of the mass balance of the Greenland ice sheet and its changes over the twentyfirst century, *Climate Dynamics*, *20*(1), 87–106.

Calov, R., A. Ganopolski, V. Petoukhov, M. Claussen, and R. Greve (2002), Large-scale instabilities of the Laurentide ice sheet simulated in a fully coupled climate-system model, *Geophysical Research Letters*, *29*(24), 2216.

Calov, R., R. Greve, A. Abe-Ouchi, E. Bueler, P. Huybrechts, J. Johnson, F. Pattyn, and L. Tarasov (2010), Results from the Ice-Sheet Model Intercomparison Project Heinrich Event INtercOmparison (ISMIP HEINO), *Journal of Glaciology*, *56*(197), 371–383.

Claremar, B., F. Obleitner, C. Reijmer, V. Pohjola, A. Waxegård, F. Karner, and A. Rutgersson (2012), Applying a mesoscale atmospheric model to Svalbard glaciers, *Advances in Meteorology*, *Article ID 321649*.

Clarke, G. (1976), Thermal regulation of glacier surging, *Journal of Glaciology*, *16*(74), 231–250.

Clarke, G. (1987), Fast glacier flow: Ice streams, surging, and tidewater glaciers, *Journal of Geophysical Research*, *92*(B9), 8835–8842.

Clarke, G. (2005), Subglacial processes, *Annu. Rev. Earth Planet. Sci.*, *33*, 247–276.

Clarke, G., U. Nitsan, and W. Paterson (1977), Strain heating and creep instability in glaciers and ice sheets, *Reviews of Geophysics*, *15*(2), 235–247.

Clarke, G., S. Collins, and D. Thompson (1984), Flow, thermal structure, and subglacial conditions of a surge-type glacier, *Canadian Journal of Earth Sciences*, *21*(2), 232–240.

Clarke, G., S. Marshall, C. Hillaire-Marcel, G. Bilodeau, and C. Veiga-Pires (1999), A glaciological perspective on

Heinrich events, *Geophysical Monograph Series*, *112*, 243–262.

Clarke, G., E. Berthier, C. Schoof, and A. Jarosch (2009), Neural networks applied to estimating subglacial topography and glacier volume, *Journal of Climate*, *22*(8), 2146–2160.

Clarke, G., F. Anslow, A. Jarosch, V. Radic, B. Menounos, T. Bolch, and E. Berthier (2013), Ice volume and subglacial topography for western Canadian glaciers from mass balance fields, thinning rates, and a bed stress model, *Journal of Climate*, *26*(12), 4282–4303.

Clifton, A., and M. Lehning (2008), Improvement and validation of a snow saltation model using wind tunnel measurements, *Earth Surface Processes and Landforms*, *33*(14), 2156–2173.

Colbeck, S. (1986), Classification of seasonal snow cover crystals, *Water Resources Research*, *22*(9S), 59S–70S.

Curry, J. A., J. L. Schramm, and E. E. Ebert (1995), Sea ice-albedo climate feedback mechanism, *Journal of Climate*, *8*(2), 240–247.

Dadic, R., R. Mott, M. Lehning, and P. Burlando (2010), Wind influence on snow depth distribution and accumulation over glaciers, *Journal of Geophysical Research*, *115*(F1), F01,012.

Davies, J., and D. McKay (1989), Evaluation of selected models for estimating solar radiation on horizontal surfaces, *Solar Energy*, *43*(3), 153–168.

Day, J., J. Bamber, P. Valdes, and J. Kohler (2012), The impact of a seasonally ice free Arctic Ocean on the temperature, precipitation and surface mass balance of Svalbard, *The Cryosphere*, *6*(1), 35–50.

De Rydt, J., G. Gudmundsson, H. Corr, and P. Christoffersen (2013), Surface undulations of Antarctic ice streams tightly controlled by bedrock topography, *The Cryosphere*, *7*(2), 407–417.

De Woul, M., and R. Hock (2005), Static mass-balance sensitivity of Arctic glaciers and ice caps using a degree-day approach, *Annals of Glaciology*, *42*(1), 217–224.

Den Ouden, M., C. Reijmer, L. Pohjola, R. van de Wal, J. Oerlemans, and W. Boot (2010), Stand-alone single-frequency GPS ice velocity observations on Nordenskiöldbreen, Svalbard, *The Cryosphere*, *4*(4), 593–604.

Divine, D., and C. Dick (2006), Historical variability of sea ice edge position in the Nordic Seas, *Journal of Geophysical Research*, *111*(C1), C01,001.

Divine, D., E. Isaksson, T. Martma, H. Meijer, J. Moore, V. Pohjola, R. van de Wal, and F. Godtliebsen (2011), Thousand years of winter surface air temperature variations in Svalbard and northern Norway reconstructed from ice core data, *Polar Research*, *30*(7379).

Dowdeswell, J., G. Hamilton, and J. Hagen (1991), The duration of the active phase on surge-type glaciers: contrasts between Svalbard and other regions, *Journal of Glaciology*, *37*(127), 388–400.

Dowdeswell, J., R. Hodgkins, A. Nuttall, J. Hagen, and G. Hamilton (1995), Mass balance change as a control on the frequency and occurrence of glacier surges in Svalbard, Norwegian High Arctic, *Geophysical Research Letters*, *22*(21), 2909–2912.

Dozier, J., and J. Frew (1990), Rapid calculation of terrain parameters for radiation modeling from digital elevation data, *Geoscience and Remote Sensing*, *28*(5), 963–969.

Dunse, T., O. Eisen, V. Helm, W. Rack, D. Steinhage, and V. Parry (2008), Characteristics and small-scale variability of GPR signals and their relation to snow accumulation in Greenland's percolation zone, *Journal of Glaciology*, *54*(185), 333–342.

Dunse, T., R. Greve, T. Schuler, and J. Hagen (2011), Permanent fast flow versus cyclic surge behaviour: numerical simulations of the Austfonna ice cap, Svalbard, *Journal of Glaciology*, *57*(202), 247–259.

Dunse, T., T. Schuler, J. Hagen, and C. Reijmer (2012), Seasonal speed-up of two outlet glaciers of Austfonna, Svalbard, inferred from continuous GPS measurements, *The Cryosphere*, *6*(2), 453–466.

Eisen, O., W. Harrison, and C. Raymond (2001), The surges of Variegated Glacier, Alaska, USA, and their connection to climate and mass balance, *Journal of Glaciology*, *47*(158), 351–358.

Eisen, O., F. Wilhelms, D. Steinhage, and J. Schwander (2006), Improved method to determine radio-echo sounding reflector depths from ice-core profiles of permittivity and conductivity, *Journal of Glaciology*, *52*(177), 299–310.

Ettema, J., M. van den Broeke, E. van Meijgaard, W. van de Berg, J. Box, and K. Steffen (2010), Climate of the Greenland ice sheet using a high-resolution climate model–Part 1: Evaluation, *The Cryosphere*, *4*(4), 511–527.

Fahnestock, M., T. Scambos, R. Bindschadler, and G. Kvaran (2000), A millennium of variable ice flow recorded by the Ross Ice Shelf, Antarctica, *Journal of Glaciology*, *46*(155), 652–664.

Farinotti, D., M. Huss, A. Bauder, M. Funk, and M. Truffer (2009), A method to estimate the ice volume and ice-thickness distribution of alpine glaciers, *Journal of Glaciology*, *55*(191), 422–430.

Flowers, G., and G. Clarke (2002), A multicomponent coupled model of glacier hydrology: 1. Theory and synthetic examples, *Journal of Geophysical Research*, *107*(B11).

Førland, E., R. Benestad, F. Flatøy, I. Hanssen-Bauer, J. Haugen, K. Isaksen, A. Sorteberg, and B. Ådlandsvik (2009), *Climate development in North Norway and the Svalbard region during 1900–2100*, Norsk Polarinstitutt Rapportserie nr. 128.

Førland, E., R. Benestad, I. Hanssen-Bauer, J. Haugen, and T. Skaugen (2011), Temperature and Precipitation Development at Svalbard 1900–2100, *Advances in Meteorology*, *Article ID 893790*.

Fountain, A. (1996), Effect of snow and firn hydrology on the physical and chemical characteristics of glacial runoff, *Hydrological Processes*, *10*(4), 509–521.

Fowler, A. (1987), Sliding with cavity formation, *Journal of Glaciology*, *33*(115), 255–267.

Fowler, A. (1997), *Mathematical models in the applied sciences*, Cambridge University Press.

Fowler, A. (2001), Modelling the flow of glaciers and ice sheets, *Continuum Mechanics and Applications in Geophysics and the Environment*, pp. 201–221.

Fowler, A., T. Murray, and F. Ng (2001), Thermally controlled glacier surging, *Journal of Glaciology*, *47*(159), 527–538.

Frezzotti, M., S. Urbini, M. Proposito, C. Scarchilli, and S. Gandolfi (2007), Spatial and temporal variability of surface mass balance near Talos Dome, East Antarctica, *Journal of Geophysical Research: Earth Surface (2003–2012)*, *112*(F2).

Fujita, S., et al. (2011), Spatial and temporal variability of snow accumulation rate on the East Antarctic ice divide between Dome Fuji and EPICA DML, *The Cryosphere*, *5*, 1057–1081.

Gagliardini, O., et al. (2013), Capabilities and performance of Elmer/Ice, a new generation ice-sheet model, *Geoscientific Model Development Discussions*, *6*(1), 1689–1741.

Gascoin, S., S. Lhermitte, C. Kinnard, K. Borstel, and G. E. Liston (2013), Wind effects on snow cover in Pascua-Lama, Dry Andes of Chile, *Advances in Water Resources*, *55*, 25–39.

Giesen, R. (2009), The ice cap Hardangerjøkulen in the past, present and future climate, Ph.D. thesis, IMAU, Utrecht University.

Giesen, R., and J. Oerlemans (2010), Response of the ice cap Hardangerjøkulen in southern Norway to the 20th and 21st century climates, *The Cryosphere*, *4*, 191–213.

Goldberg, D. (2011), A variationally derived, depth-integrated approximation to a higher-order glaciological flow model, *Journal of Glaciology*, *57*(201), 157–170.

Goldberg, D., and P. Heimbach (2013), Parameter and state estimation with a time-dependent adjoint marine ice sheet model, *The Cryosphere Discussions*, *7*, 2845–2890.

Greuell, W. (1992), Hintereisferner, Austria: mass-balance reconstruction and numerical modelling of the historical length variations, *Journal of Glaciology*, *38*(129), 233–244.

Greuell, W., and T. Konzelmann (1994), Numerical modelling of the energy balance and the englacial temperature of the Greenland Ice Sheet. Calculations for the ETH-Camp location (West Greenland, 1155 m asl), *Global and Planetary Change*, *9*(1-2), 91–114.

Greuell, W., and J. Oerlemans (1989), The evolution of the englacial temperature distribution in the superimposed ice zone of a polar ice cap during a summer season, in *Glacier fluctuations and climatic change: proceedings of the Symposium on Glacier Fluctuations and Climatic Change, held in Amsterdam, 1-5 June 1987*, vol. 6, p. 289,

Springer.

Greuell, W., W. Knap, and P. Smeets (1997), Elevational changes in meteorological variables along a midlatitude glacier during summer, *Journal of Geophysical Research*, *102*(D22).

Greve, R. (2005), Relation of measured basal temperatures and the spatial distribution of the geothermal heat flux for the Greenland ice sheet, *Annals of Glaciology*, *42*(1), 424–432.

Greve, R., R. Takahama, and R. Calov (2006), Simulation of large-scale ice-sheet surges: The ISMIP HEINO experiments, *Polar Meteorology and Glaciology*, *20*, 1–15.

Gudmundsson, G. (2003), Transmission of basal variability to a glacier surface, *Journal of Geophysical Research*, *108*(B5), 2253.

Gudmundsson, G. (2011), Inverse methods in glaciology, in *Encyclopedia of Snow, Ice and Glaciers*, Springer.

Gudmundsson, G., and M. Raymond (2008), On the limit to resolution and information on basal properties obtainable from surface data on ice streams, *The Cryosphere*, *2*, 167–178.

Habermann, M., D. Maxwell, and M. Truffer (2012), Reconstruction of basal properties in ice sheets using iterative inverse methods, *Journal of Glaciology*, *58*(210), 795–807.

Haeberli, W., and M. Hölzle (1995), Application of inventory data for estimating characteristics of and regional climate-change effects on mountain glaciers: a pilot study with the European Alps, *Annals of Glaciology*, *21*, 206–212.

Hagen, J., J. Kohler, K. Melvold, and J. Winther (2003), Glaciers in Svalbard: mass balance, runoff and freshwater flux, *Polar Research*, *22*(2), 145–159.

Hagen, J. O. (1993), *Glacier atlas of Svalbard and Jan Mayen*, vol. 129, Norsk polarinstitutt.

Hagen, J. O., T. Eiken, J. Kohler, and K. Melvold (2005), Geometry changes on Svalbard glaciers: mass-balance or dynamic response?, *Annals of Glaciology*, *42*(1), 255–261.

Hamilton, G., and J. Dowdeswell (1996), Controls on glacier surging in Svalbard, *Journal of Glaciology*, *42*(140), 157–168.

Hanssen-Bauer, I., and E. Førland (1998), Long-term trends in precipitation and temperature in the Norwegian Arctic: can they be explained by changes in atmospheric circulation patterns?, *Climate Research*, *10*(2), 143–153.

Hanssen-Bauer, I., E. Førland, K. Johansen, and Ø. Nordli (2009), The Climate of Svalbard and Jan Mayen. Analyses of time-series data from 1911 to 2007, *Tech. rep.*, met.no.

Harrison, W., and A. Post (2003), How much do we really know about glacier surging?, *Annals of Glaciology*, *36*(1), 1–6.

Heining, C. (2011), Velocity field reconstruction in gravity-driven flow over unknown topography, *Physics of Fluids*, *23*(032101).

Heinrich, H. (1988), Origin and consequences of cyclic ice rafting in the northeast Atlantic Ocean during the past 130,000 years, *Quaternary Research*, *29*(2), 142–152.

Hewitt, I. (2011), Modelling distributed and channelized subglacial drainage: the spacing of channels, *Journal of Glaciology*, *57*(202), 302–314.

Hewitt, I. (2013), Seasonal changes in ice sheet motion due to melt water lubrication, *Earth and Planetary Science Letters*, *371*, 16–25.

Hewitt, I., C. Schoof, and M. Werder (2012), Flotation and free surface flow in a model for subglacial drainage. Part 2. Channel flow, *Journal of Fluid Mechanics*, *702*, 157–187.

Hindmarsh, R., and E. Le Meur (2001), Dynamical processes involved in the retreat of marine ice sheets, *Journal of Glaciology*, *47*(157), 271–282.

Hock, R. (1999), A distributed temperature-index ice-and snowmelt model including potential direct solar radiation, *Journal of Glaciology*, *45*(149), 101–111.

Hock, R., and B. Holmgren (2005), A distributed surface energy-balance model for complex topography and its

application to Storglaciaren, Sweden, *Journal of Glaciology*, *51*(172), 25–36.

Hock, R., V. Radic, and M. De Woul (2007), Climate sensitivity of Storglaciaren, Sweden: an intercomparison of mass-balance models using ERA-40 re-analysis and regional climate model data, *Annals of Glaciology*, *46*(1), 342–348.

Houghton, H. (1954), On the annual heat balance of the Northern Hemisphere, *Journal of Atmospheric Sciences*, *11*, 1–9.

Huss, M., and D. Farinotti (2012), Distributed ice thickness and volume of all glaciers around the globe, *Journal of Geophysical Research*, *117*(F4), F04,010.

Huss, M., A. Bauder, M. Werder, M. Funk, and R. Hock (2007), Glacier-dammed lake outburst events of Gornersee, Switzerland, *Journal of Glaciology*, *53*(181), 189–200.

Huss, M., D. Farinotti, A. Bauder, and M. Funk (2008), Modelling runoff from highly glacierized alpine drainage basins in a changing climate, *Hydrological Processes*, *22*(19), 3888–3902.

Hutter, K. (1983), *Theoretical glaciology: material science of ice and the mechanics of glaciers and ice sheets*, Springer.

Huybrechts, P., and J. de Wolde (1999), The dynamic response of the Greenland and Antarctic ice sheets to multiple-century climatic warming, *Journal of Climate*, *12*(8), 2169–2188.

IPCC (2001), *Climate Change 2001: The Scientific Basis. Contribution of Working Group I to the Third Assessment Report of the Intergovernmental Panel on Climate Change*, Cambridge University Press.

IPCC (2007), *Climate Change 2007: The physical science basis: Working group I contribution to the fourth assessment report of the IPCC*, Cambridge University Press.

Isaksson, E., et al. (2001), A new ice-core record from Lomonosovfonna, Svalbard: viewing the 1920-97 data in relation to present climate and environmental conditions, *Journal of Glaciology*, *47*(157), 335–345.

Iverson, N., T. Hooyer, and R. Baker (1998), Ring-shear studies of till deforrn. ation: Coulomb-plastic behavior and distributed strain in glacier beds, *Journal of Glaciology*, *44*, 634–642.

Jacobel, R., T. Scambos, N. Nereson, and C. Raymond (2000), Changes in the margin of Ice Stream C, Antarctica, *Journal of Glaciology*, *46*(152), 102–110.

James, T., T. Murray, N. Barrand, H. Sykes, A. Fox, and M. King (2012), Observations of enhanced thinning in the upper reaches of Svalbard glaciers, *The Cryosphere*, *6*(6), 1369–1381.

Jania, J., D. Mochnacki, and B. Gadek (1996), The thermal structure of Hansbreen, a tidewater glacier in southern Spitsbergen, Svalbard, *Polar Research*, *15*(1), 53–66.

Jansson, P., R. Hock, and T. Schneider (2003), The concept of glacier storage: a review, *Journal of Hydrology*, *282*(1-4), 116–129.

Jiskoot, H., T. Murray, and P. Boyle (2000), Controls on the distribution of surge-type glaciers in Svalbard, *Journal of Glaciology*, *46*(154), 412–422.

Joughin, I., D. MacAyeal, and S. Tulaczyk (2004), Basal shear stress of the Ross ice streams from control method inversions, *Journal of Geophysical Research*, *109*(B9).

Joughin, I., J. Bamber, T. Scambos, S. Tulaczyk, M. Fahnestock, and D. MacAyeal (2006), Integrating satellite observations with modelling: basal shear stress of the Filcher-Ronne ice streams, Antarctica, *Philosophical Transactions of the Royal Society A: Mathematical, Physical and Engineering Sciences*, *364*(1844), 1795–1814.

Kamb, B. (1987), Glacier surge mechanism based on linked cavity configuration of the basal water conduit system, *Journal of Geophysical Research*, *92*(B9), 9083–9100.

Kamb, B., C. Raymond, W. Harrison, H. Engelhardt, K. Echelmeyer, N. Humphrey, M. Brugman, and T. Pfeffer (1985), Glacier surge mechanism: 1982-1983 surge of Variegated Glacier, Alaska, *Science*, *227*(4686), 469–479.

Kanagaratnam, P., S. P. Gogineni, V. Ramasami, and D. Braaten (2004), A wideband radar for high-resolution mapping of near-surface internal layers in glacial ice, *Geoscience and Remote Sensing*, *42*(3), 483–490.

Kellogg, W. (1975), Climatic feedback mechanisms involving the polar regions, *Climate of the Arctic*, pp. 111–116.

Klok, E., and J. Oerlemans (2002), Model study of the spatial distribution of the energy and mass balance of Morteratschgletscher, Switzerland, *Journal of Glaciology*, *48*(163), 505–518.

Koerner, R. (1970), Some observations on superimposition of ice on the Devon Island ice cap, NWT Canada, *Geografiska Annaler. Series A. Physical Geography*, pp. 57–67.

Kohler, J., J. Moore, M. Kennett, R. Engeset, and H. Elvehøy (1997), Using ground-penetrating radar to image previous years' summer surfaces for mass-balance measurements, *Annals of Glaciology*, *24*, 355–360.

Kondratyev, K. (1969), *Radiation in the Atmosphere*, 912 pp., Academic Press Inc.

Konzelmann, T., R. van de Wal, W. Greuell, R. Bintanja, E. Henneken, and A. Abe-Ouchi (1994), Parameterization of global and longwave incoming radiation for the Greenland ice sheet, *Global and Planetary change*, *9*(1-2), 143–164.

Korona, J., E. Berthier, M. Bernard, F. Rémy, and E. Thouvenot (2009), SPIRIT. SPOT 5 stereoscopic survey of Polar Ice: Reference Images and Topographies during the fourth International Polar Year (2007-2009), *ISPRS Journal of Photogrammetry and Remote Sensing*, *64*(2), 204–212.

Kovacs, A., A. Gow, and R. Morey (1995), The in-situ dielectric constant of polar firn revisited, *Cold Regions Science and Technology*, *23*(3), 245–256.

Kuipers Munneke, P., C. Reijmer, M. van den Broeke, P. Stammes, G. König-Langlo, and W. Knap (2008), Analysis of clear-sky Antarctic snow albedo using observations and radiative transfer modeling, *Journal of Geophysical Research*, *113*(D17118).

Leclercq, P., P. Pitte, R. Giesen, M. Masiokas, and J. Oerlemans (2012), Modelling and climatic interpretation of the length fluctuations of Glaciar Frías (north Patagonian Andes, Argentina) 1639-2009 AD, *Climate of the Past*, *8*, 1385–1402.

Lehning, M., H. Löwe, M. Ryser, and N. Raderschall (2008), Inhomogeneous precipitation distribution and snow transport in steep terrain, *Water Resources Research*, *44*(7).

Lenaerts, J., M. Van den Broeke, S. Déry, G. König-Langlo, J. Ettema, and P. K. Munneke (2010), Modelling snowdrift sublimation on an Antarctic ice shelf, *The Cryosphere*, *4*(2), 179–190.

Li, H., F. Ng, Z. Li, D. Qin, and G. Cheng (2012), An extended "perfect-plasticity" method for estimating ice thickness along the flow line of mountain glaciers, *Journal of Geophysical Research*, *117*(F1).

Ligtenberg, S., M. Helsen, and M. van den Broeke (2011), An improved semi-empirical model for the densification of Antarctic firn, *The Cryosphere*, *5*, 809–819.

Liston, G. E., and M. Sturm (1998), A snow-transport model for complex terrain, *Journal of Glaciology*, *44*(148), 498–516.

Liston, G. E., R. B. Haehnel, M. Sturm, C. A. Hiemstra, S. Berezovskaya, and R. D. Tabler (2007), Instruments and methods simulating complex snow distributions in windy environments using SnowTran-3D, *Journal of Glaciology*, *53*(181), 241–256.

Looyenga, H. (1965), Dielectric constants of heterogeneous mixtures, *Physica*, *31*(3), 401–406.

Luthi, M., M. Funk, A. Iken, S. Gogineni, and M. Truffer (2002), Mechanisms of fast flow in Jakobshavn Isbrae, West Greenland: Part III. Measurements of ice deformation, temperature and cross-borehole conductivityin boreholes to the bedrock, *Journal of Glaciology*, *48*(162), 369–385.

MacAyeal, D. (1989), Large-scale ice flow over a viscous basal sediment- Theory and application to ice stream B, Antarctica, *Journal of Geophysical Research*, *94*(B4), 4071–4087.

MacAyeal, D. (1992), The basal stress distribution of Ice Stream E, Antarctica, inferred by control methods, *Journal of Geophysical Research*, *97*, 595–603.

MacAyeal, D. (1993), Binge/purge oscillations of the Laurentide ice sheet as a cause of the North Atlantic's Heinrich events, *Paleoceanography*, *8*(6), 775–784.

Machguth, H., O. Eisen, F. Paul, and M. Hoelzle (2006), Strong spatial variability of snow accumulation observed with helicopter-borne GPR on two adjacent Alpine glaciers, *Geophysical Research Letters*, *33*, L13,503.

Mangerud, J., and J. Landvik (2007), Younger Dryas cirque glaciers in western Spitsbergen: smaller than during the Little Ice Age, *Boreas*, *36*(3), 278–285.

Marshall, S., and G. Clarke (1997), A continuum mixture model of ice stream thermomechanics in the Laurentide ice sheet. 1. Theory, *Journal of Geophysical Research*, *102*(B9), 20,615–20,637.

Maxwell, D., M. Truffer, S. Avdonin, and M. Stuefer (2008), An iterative scheme for determining glacier velocities and stresses, *Journal of Glaciology*, *54*(188), 888–898.

McDonald, J. (1960), Direct absorption of solar radiation by atmospheric water vapor, *Journal of Atmospheric Sciences*, *17*, 319–328.

McNabb, R., et al. (2012), Using surface velocities to calculate ice thickness and bed topography: a case study at Columbia Glacier, Alaska, USA, *Journal of Glaciology*, *58*(212), 1151–1164.

Meier, M. (1965), Glaciers and climate, *The Quaternary of the United States*, pp. 795–804.

Michel, L., M. Picasso, D. Farinotti, A. Bauder, M. Funk, and H. Blatter (2013), Estimating the ice thickness of mountain glaciers with an inverse approach using surface topography and mass-balance, *Inverse Problems*, *29*(3).

Miège, C., R. Forster, J. Box, E. Burgess, J. McConnell, D. Pasteris, and V. Spikes (2013), Southeast Greenland high accumulation rates derived from firn cores and ground-penetrating radar, *Annals of Glaciology*, *54*(63), 322–332.

Morland, L., and I. Johnson (1980), Steady motion of ice sheets, *Journal of Glaciology*, *25*, 229–246.

Morlighem, M., E. Rignot, H. Seroussi, E. Larour, H. Dhia, and D. Aubry (2011), A mass conservation approach for mapping glacier ice thickness, *Geophysical Research Letters*, *38*(19), L19,503.

Mott, R., M. Schirmer, M. Bavay, T. Grünewald, and M. Lehning (2010), Understanding snow-transport processes shaping the mountain snow-cover, *The Cryosphere*, *4*(4), 545–559.

Murray, T., G. Stuart, P. Miller, J. Woodward, A. Smith, P. Porter, and H. Jiskoot (2000), Glacier surge propagation by thermal evolution at the bed, *Journal of Geophysical Research*, *105*(B6), 13,491–13,507.

Murray, T., T. Strozzi, A. Luckman, H. Jiskoot, and P. Christakos (2003), Is there a single surge mechanism? Contrasts in dynamics between glacier surges in Svalbard and other regions, *Journal of Geophysical Research*, *108*(B5), 2237.

Nakicenovic, N., et al. (2000), Special report on emissions scenarios: a special report of Working Group III of the Intergovernmental Panel on Climate Change, *Tech. rep.*, Pacific Northwest National Laboratory, Richland, WA (US), Environmental Molecular Sciences Laboratory (US).

Nuth, C., G. Moholdt, J. Kohler, J. O. Hagen, and A. Kääb (2010), Svalbard glacier elevation changes and contribution to sea level rise, *Journal of Geophysical Research*, *115*(F1), F01,008.

Nuth, C., J. Kohler, M. König, A. von Deschwanden, J. Hagen, A. Kääb, G. Moholdt, and R. Pettersson (2013), Decadal changes from a multi-temporal glacier inventory of Svalbard, *The Cryosphere Discussions*, *7*, 2489–2532.

Nuttall, A.-M., and R. Hodgkins (2005), Temporal variations in flow velocity at Finsterwalderbreen, a Svalbard surge-type glacier, *Annals of Glaciology*, *42*(1), 71–76.

Nye, J. (1951), The flow of glaciers and ice-sheets as a problem in plasticity, *Proceedings of the Royal Society of London. Series A. Mathematical and Physical Sciences*, *207*(1091), 554–572.

Nye, J. (1969), A calculation on the sliding of ice over a wavy surface using a Newtonian viscous approximation, *Proceedings of the Royal Society of London. A. Mathematical and Physical Sciences*, *311*(1506), 445–467.

Obleitner, F., and M. Lehning (2004), Measurement and simulation of snow and superimposed ice at the Kongsvegen glacier, Svalbard (Spitzbergen), *Journal of Geophysical Research*, *109*(D4), D04,106.

Oerlemans, J. (1983), A numerical study on cyclic behaviour of polar ice sheets, *Tellus A*, *35*(2), 81–87.

Oerlemans, J. (1997), Climate sensitivity of Franz Josef Glacier, New Zealand, as revealed by numerical modeling, *Arctic and Alpine Research*, *29*(2), 233–239.

Oerlemans, J. (2001), *Glaciers and climate change*, Taylor & Francis.

Oerlemans, J., and B. Grisogono (2002), Glacier winds and parameterisation of the related surface heat fluxes, *Tellus*

A, *54*(5), 440–452.

Oerlemans, J., and W. Knap (1998), A 1 year record of global radiation and albedo in the ablation zone of Morteratschgletscher, Switzerland, *Journal of Glaciology*, *44*(147).

Oerlemans, J., and B. Reichert (2000), Relating glacier mass balance to meteorological data by using a seasonal sensitivity characteristic, *Journal of Glaciology*, *46*(152), 1–6.

Oerlemans, J., and C. van der Veen (1984), *Ice sheets and climate*, Springer.

Oerlemans, J., et al. (1998), Modelling the response of glaciers to climate warming, *Climate Dynamics*, *14*(4), 267–274.

Oerlemans, J., R. Giesen, and M. Van den Broeke (2009), Retreating alpine glaciers: increased melt rates due to accumulation of dust (Vadret da Morteratsch, Switzerland), *Journal of Glaciology*, *55*(192), 729–736.

Pälli, A., J. Kohler, E. Isaksson, J. Moore, J. Pinglot, V. Pohjola, and H. Samuelsson (2002), Spatial and temporal variability of snow accumulation using ground-penetrating radar and ice cores on a Svalbard glacier, *Journal of Glaciology*, *48*(162), 417–424.

Papa, B., L. Mysak, and Z. Wang (2006), Intermittent ice sheet discharge events in northeastern North America during the last glacial period, *Climate Dynamics*, *26*(2), 201–216.

Paterson, W. (1994), *The physics of glaciers*, Pergamon, New York.

Pattyn, F. (2010), Antarctic subglacial conditions inferred from a hybrid ice sheet/ice stream model, *Earth and planetary science letters*, *295*(3), 451–461.

Paul, F., and F. Svoboda (2010), A new glacier inventory on southern Baffin Island, Canada, from ASTER data: II. Data analysis, glacier change and applications, *Annals of Glaciology*, *50*(53), 22–31.

Payne, A. (1995), Limit cycles in the basal thermal regime of ice sheets, *Journal of Geophysical Research*, *100*(B3), 4249–4263.

Payne, A. (1999), A thermomechanical model of ice flow in West Antarctica, *Climate Dynamics*, *15*(2), 115–125.

Payne, A., and P. Dongelmans (1997), Self-organization in the thermomechanical flow of ice sheets, *Journal of Geophysical Research*, *102*(B6), 12,219–12,233.

Pettersson, R. (2004), Dynamics of the cold surface layer of polythermal Storglaciären, Sweden, *PhD diss. Stockholm University. Department of Physical Geography and Quaternary Geology. Stockholm University Dissertation Series*.

Pettersson, R., P. Jansson, and H. Blatter (2004), Spatial variability in water content at the cold-temperate transition surface of the polythermal Storglaciären, Sweden, *Journal of Geophysical Research: Earth Surface (2003–2012)*, *109*(F2).

Pfeffer, W., and N. Humphrey (1998), Formation of ice layers by infiltration and refreezing of meltwater, *Annals of Glaciology*, *26*, 83–91.

Pfeffer, W., M. Meier, and T. Illangasekare (1991), Retention of Greenland runoff by refreezing: implications for projected future sea level change, *Journal of Geophysical Research*, *96*(C12), 22,117–22,124.

Pham, Q. (1995), Comparison of general-purpose finite-element methods for the Stefan problem, *Numerical Heat Transfer*, *27*(4), 417–435.

Pimentel, S., and G. E. Flowers (2011), A numerical study of hydrologically driven glacier dynamics and subglacial flooding, *Proceedings of the Royal Society A: Mathematical, Physical and Engineering Science*, *467*(2126), 537–558.

Plassen, L., T. Vorren, and M. Forwick (2004), Integrated acoustic and coring investigation of glacigenic deposits in Spitsbergen fjords, *Polar Research*, *23*, 89–110.

Pohjola, V., T. Martma, H. Meijer, J. Moore, E. Isaksson, R. Vaikmae, and R. Van De Wal (2002a), Reconstruction of three centuries of annual accumulation rates based on the record of stable isotopes of water from Lomonosovfonna, Svalbard, *Annals of Glaciology*, *35*(1), 57–62.

Pohjola, V., J. Moore, E. Isaksson, T. Jauhiainen, R. van de Wal, T. Martma, H. Meijer, and R. Vaikmäe (2002b),

Effect of periodic melting on geochemical and isotopic signals in an ice core from Lomonosovfonna, Svalbard, *Journal of Geophysical Research*, *107*(10.1029).

Pollard, D., and R. DeConto (2012), A simple inverse method for the distribution of basal sliding coefficients under ice sheets, applied to Antarctica, *The Cryosphere*, *6*, 953–971.

Pomeroy, J., and D. Gray (1990), Saltation of snow, *Water Resources Research*, *26*(7), 1583–1594.

Press, W., B. Flannery, S. Teukolsky, and W. Vetterling (1992), Secant method, false position method, and ridders method, *Numerical Recipes in FORTRAN: The Art of Scientific Computing*, pp. 347–352.

Rachlewicz, G., W. Szczucinski, and M. Ewertowski (2007), Post-Little Ice Age retreat rates of glaciers around Billefjorden in central Spitsbergen, Svalbard, *Polish Polar Research*, *28*(3), 159–186.

Raper, S., and R. Braithwaite (2006), Low sea level rise projections from mountain glaciers and icecaps under global warming, *Nature*, *439*(7074), 311–313.

Raymond, M., and G. Gudmundsson (2005), On the relationship between surface and basal properties on glaciers, ice sheets and ice streams, *Journal of Geophysical Research*, *110*(B8), B08,411.

Raymond, M., and G. Gudmundsson (2009), Estimating basal properties of ice streams from surface measurements: a non-linear Bayesian inverse approach applied to synthetic data, *The Cryosphere*, *3*, 265–278.

Raymond Pralong, M., and G. Gudmundsson (2011), Bayesian estimation of basal conditions on Rutford Ice Stream, West Antarctica, from surface data, *Journal of Glaciology*, *57*(202), 315–324.

Reichert, B. K., L. Bengtsson, and J. Oerlemans (2001), Midlatitude forcing mechanisms for glacier mass balance investigated using general circulation models, *Journal of Climate*, *14*(17), 3767–3784.

Reijmer, C., and R. Hock (2008), Internal accumulation on Storglaciaren, Sweden, in a multi-layer snow model coupled to a distributed energy-and mass-balance model, *Journal of Glaciology*, *54*(184), 61–72.

Retzlaff, R., and C. Bentley (1993), Timing of stagnation of Ice Stream C, West Antarctica, from short-pulse radar studies of buried surface crevasses, *Journal of Glaciology*, *39*(133).

Richardson, C., E. Aarholt, S.-E. Hamran, P. Holmlund, and E. Isaksson (1997), Spatial distribution of snow in western Dronning Maud Land, East Antarctica, mapped by a ground-based snow radar, *Journal of Geophysical Research*, *102*(B9), 20,343–20,353.

Robin, G. (1955), Ice movement and temperature distribution in glaciers and ice sheets, *Journal of Glaciology*, *2*(18), 523–532.

Robin, G. d. Q., S. Evans, and J. T. Bailey (1969), Interpretation of radio echo sounding in polar ice sheets, *Philosophical Transactions for the Royal Society of London. Series A, Mathematical and Physical Sciences*, pp. 437–505.

Rose, K. (1979), Characteristics of ice flow in Marie Byrd Land, Antarctica, *Journal of Glaciology*, *24*, 63–75.

Rye, C. J., N. S. Arnold, I. C. Willis, and J. Kohler (2010), Modeling the surface mass balance of a high Arctic glacier using the ERA-40 reanalysis, *Journal of Geophysical Research*, *115*(F2).

Schneider, T., and P. Jansson (2004), Internal accumulation in firn and its significance for the mass balance of Storglaciaren, Sweden, *Journal of Glaciology*, *50*(168), 25–34.

Schoof, C. (2005), The effect of cavitation on glacier sliding, *Proceedings of the Royal Society A: Mathematical, Physical and Engineering Science*, *461*(2055), 609–627.

Schoof, C. (2006), Variational methods for glacier flow over plastic till, *Journal of Fluid Mechanics*, *555*, 299–320.

Schoof, C. (2010), Ice-sheet acceleration driven by melt supply variability, *Nature*, *468*(7325), 803–806.

Schoof, C., I. J. Hewitt, and M. A. Werder (2012), Flotation and free surface flow in a model for subglacial drainage. Part 1. Distributed drainage, *Journal of Fluid Mechanics*, *702*, 126–156.

Schytt, V. (1949), Re-freezing of the melt-water on the surface of glacier ice, *Geografiska Annaler*, *31*, 222–227.

Sergienko, O., R. Bindschadler, P. Vornberger, and D. MacAyeal (2008), Ice stream basal conditions from block-wise surface data inversion and simple regression models of ice stream flow: Application to Bindschadler Ice Stream, *Journal of Geophysical Research*, *113*(F4), F04,010.

Serreze, M., A. Barrett, J. Stroeve, D. Kindig, and M. Holland (2009), The emergence of surface-based Arctic amplification, *The Cryosphere*, *3*(1), 11–19.

Serreze, M. C., and J. A. Francis (2006), The Arctic amplification debate, *Climatic Change*, *76*(3-4), 241–264.

Sevruk, B. (1997), Regional dependency of precipitation-altitude relationship in the Swiss Alps, *Climatic Change*, *36*(3-4), 355–369.

Sinisalo, A., A. Grinsted, J. C. Moore, E. Karkas, and R. Pettersson (2003), Snow-accumulation studies in Antarctica with ground-penetrating radar using 50,100 and 800 MHz antenna frequencies, *Annals of Glaciology*, *37*(1), 194–198.

Sole, A., P. Nienow, I. Bartholomew, D. Mair, T. Cowton, A. Tedstone, and M. A. King (2013), Winter motion mediates dynamic response of the Greenland Ice Sheet to warmer summers, *Geophysical Research Letters*, *40*(15), 3940–3944.

Spikes, V. B., G. S. Hamilton, S. A. Arcone, S. Kaspari, and P. A. Mayewski (2004), Variability in accumulation rates from GPR profiling on the West Antarctic plateau, *Annals of Glaciology*, *39*(1), 238–244.

Stacheder, M. (2005), TDR and low-frequency measurements for continuous monitoring of moisture and density in a snow pack, *Int. Agrophysics*, *19*, 75–78.

Steen-Larsen, H. C., E. D. Waddington, and M. R. Koutnik (2010), Formulating an inverse problem to infer the accumulation-rate pattern from deep internal layering in an ice sheet using a Monte Carlo approach, *Journal of Glaciology*, *56*(196), 318–332.

Sturm, M., J. Holmgren, M. König, and K. Morris (1997), The thermal conductivity of seasonal snow, *Journal of Glaciology*, *43*(143), 26–41.

Sundal, A. V., A. Shepherd, P. Nienow, E. Hanna, S. Palmer, and P. Huybrechts (2011), Melt-induced speed-up of Greenland ice sheet offset by efficient subglacial drainage, *Nature*, *469*(7331), 521–524.

Svendsen, J. I., and J. Mangerud (1997), Holocene glacial and climatic variations on Spitsbergen, Svalbard, *The Holocene*, *7*(1), 45–57.

Taurisano, A., T. V. Schuler, J. O. Hagen, T. Eiken, E. Loe, K. Melvold, and J. Kohler (2007), The distribution of snow accumulation across the Austfonna ice cap, Svalbard: direct measurements and modelling, *Polar Research*, *26*(1), 7–13.

Thorsteinsson, T., C. Raymond, G. Gudmundsson, R. Bindschadler, P. Vornberger, and I. Joughin (2003), Bed topography and lubrication inferred from surface measurements on fast-flowing ice streams, *Journal of Glaciology*, *49*(167), 481–490.

Tiuri, M., A. Sihvola, E. Nyfors, and M. Hallikaiken (1984), The complex dielectric constant of snow at microwave frequencies, *IEEE Journal of Oceanic Engineering*, *9*(5), 377–382.

Trabant, D., and L. Mayo (1985), Estimation and effects of internal accumulation on five glaciers in Alaska, *Annals of Glaciology*, *6*, 113–117.

Tulaczyk, S., W. Kamb, and H. Engelhardt (2000a), Basal mechanics of ice stream B, West Antarctica 1. Till mechanics, *Journal of Geophysical Research*, *105*(B1), 463–481.

Tulaczyk, S., W. Kamb, and H. Engelhardt (2000b), Basal mechanics of ice stream B, West Antarctica 2. Undrained plastic bed model, *Journal of Geophysical Research*, *105*(B1), 483–494.

Van Angelen, J., J. M Lenaerts, M. van den Broeke, X. Fettweis, and E. Meijgaard (2013), Rapid loss of firn pore space accelerates 21st century Greenland mass loss, *Geophysical Research Letters*, *40*, 2109–2113.

Van de Wal, R., R. Mulvaney, E. Isaksson, J. Moore, J. Pinglot, V. Pohjola, and M. Thomassen (2002), Reconstruction of the historical temperature trend from measurements in a medium-length borehole on the Lomonosovfonna plateau, Svalbard, *Annals of Glaciology*, *35*(1), 371–378.

Van de Wal, R., W. Boot, M. van den Broeke, C. Smeets, C. Reijmer, J. Donker, and J. Oerlemans (2008), Large and rapid melt-induced velocity changes in the ablation zone of the Greenland Ice Sheet, *Science*, *321*(5885), 111–113.

Van den Broeke, M., D. van As, C. Reijmer, and R. van de Wal (2004), Assessing and improving the quality of unattended radiation observations in Antarctica, *Journal of Atmospheric and Oceanic Technology*, *21*(9), 1417–1431.

Van den Broeke, M., C. Reijmer, D. van As, and W. Boot (2006), Daily cycle of the surface energy balance in Antarctica and the influence of clouds, *International Journal of Climatology*, *26*(12), 1587–1605.

Van Meijgaard, E., L. van Ulft, W. van den Berg, F. Bosveld, B. van den Hurk, G. Lenderink, and A. Siebesma (2008), The KNMI regional atmospheric climate model RACMO version 2.1, *Tech. rep.*, Royal Netherlands Meteorological Institute.

Van Pelt, W., and J. Oerlemans (2012), Numerical simulations of cyclic behaviour in the Parallel Ice Sheet Model (PISM), *Journal of Glaciology*, *58*(208), 347–360.

Van Pelt, W., J. Oerlemans, C. Reijmer, V. Pohjola, R. Pettersson, and J. van Angelen (2012), Simulating melt, runoff and refreezing on Nordenskiöldbreen, Svalbard, using a coupled snow and energy balance model, *The Cryosphere*, *6*(3), 641–659.

Van Pelt, W., R. Pettersson, V. Pohjola, S. Marchenko, B. Claremar, and J. Oerlemans (2013a), Inverse estimation of snow accumulation variability along a snow radar transect on Nordenskioldbreen, Svalbard, *submitted to Journal of Geophysical Research: Earth Surface*.

Van Pelt, W., J. Oerlemans, C. Reijmer, R. Pettersson, V. Pohjola, E. Isaksson, and D. Divine (2013b), An iterative inverse method to estimate basal topography and initialize ice flow models, *The Cryosphere*, *7*(3), 987–1006.

Waddington, E. D., T. A. Neumann, M. R. Koutnik, H.-P. Marshall, and D. L. Morse (2007), Inference of accumulation-rate patterns from deep layers in glaciers and ice sheets, *Journal of Glaciology*, *53*(183), 694–712.

Wadham, J., and A. Nuttall (2002), Multiphase formation of superimposed ice during a mass-balance year at a maritime high-Arctic glacier, *Journal of Glaciology*, *48*(163), 545–551.

Walczowski, W., and J. Piechura (2006), New evidence of warming propagating toward the Arctic Ocean, *Geophysical Research Letters*, *33*(L12), L12,601.

Waldner, P., C. Huebner, M. Schneebeli, A. Brandelik, and F. Rau (2001), Continuous measurements of liquid water content and density in snow using TDR, in *Second International Symposium and Workshop on Time Domain Reflectometry for Innovative Geotechnical Applications*, pp. 446–456.

Weertman, J. (1957), On the sliding of glaciers, *Journal of Glaciology*, *3*(21), 33–38.

Weis, M., R. Greve, and K. Hutter (1999), Theory of shallow ice shelves, *Continuum Mechanics and Thermodynamics*, *11*(1), 15–50.

Winkelmann, R., M. Martin, M. Haseloff, T. Albrecht, E. Bueler, C. Khroulev, and A. Levermann (2011), The Potsdam Parallel Ice Sheet Model (PISM-PIK)–Part 1: Model description, *The Cryosphere*, *5*(3), 715–726.

Winstral, A., K. Elder, and R. E. Davis (2002), Spatial snow modeling of wind-redistributed snow using terrain-based parameters, *Journal of Hydrometeorology*, *3*(5), 524–538.

Wright, A., J. Wadham, M. Siegert, A. Luckman, and J. Kohler (2005), Modelling the impact of superimposed ice on the mass balance of an Arctic glacier under scenarios of future climate change, *Annals of Glaciology*, *42*(1), 277–283.

Yen, Y. (1981), Review of thermal properties of snow, ice and sea ice, *Tech. rep.*, DTIC Document.

Zuo, Z., and J. Oerlemans (1996), Modelling albedo and specific balance of the Greenland ice sheet: calculations for the Søndre Strømfjord transect, *Journal of Glaciology*, *42*, 305–317.

Zwally, H., W. Abdalati, T. Herring, K. Larson, J. Saba, and K. Steffen (2002), Surface melt-induced acceleration of Greenland ice-sheet flow, *Science*, *297*(5579), 218–222.

Publications

Van Pelt, W.J.J. and J. Oerlemans (2012). Numerical simulations of cyclic behaviour in the Parallel Ice Sheet Model (PISM), *Journal of Glaciology*, *58*(208), 347–360, doi:10.3189/2012JoG11J217.

Van Pelt, W.J.J., J. Oerlemans, C.H. Reijmer, V.A. Pohjola, R. Pettersson and J.H. van Angelen (2012). Simulating melt, runoff and refreezing on Nordenskiöldbreen, Svalbard, using a coupled snow and energy balance model, *The Cryosphere*, *6*(3), 641–659, doi:10.5194/tc-6-641-2012.

Van Pelt, W.J.J., J. Oerlemans, C.H. Reijmer, R. Pettersson, V.A. Pohjola, E. Isaksson and D. Divine (2013). An iterative inverse method to estimate basal topography and initialize ice flow models, *The Cryosphere*, *7*(3), 987–1006, doi:10.5194/tc-7-987-2013.

Van Pelt, W.J.J., R. Pettersson, V.A. Pohjola, S. Marchenko, B. Claremar and J. Oerlemans (2013). Inverse estimation of snow accumulation variability along a snow radar transect on Nordenskiöldbreen, Svalbard, *submitted to Journal of Geophysical Research: Earth Surface*.

Oerlemans, J. and W.J.J. van Pelt (2013). A model study of Abrahamsenbreen (northern Spitsbergen), *submitted to Polar Research*.

Bueler, E.L., W.J.J. van Pelt and J. Oerlemans (2013). A distributed numerical model of subglacial hydrology in tidewater glaciers and ice sheets, *in preparation*.

Dankwoord

Hoewel je als onderzoeker regelmatig op jezelf bent aangewezen, had dit werk nooit tot stand kunnen komen zonder de hulp en onvoorwaardelijke steun van begeleiders, collega's, vrienden en familie. Een woord van dank is daarom zeker op zijn plaats!

Ten eerste gaat mijn dank uit naar Hans, mijn dagelijkse begeleider en promotor. Je grote enthousiasme over alles wat met ijs en klimaat te maken werkt erg aanstekelijk en heeft me vele malen geïnspireerd. De vrijheid die je me gaf om eigen ideeën te ontwikkelen en onderzoeken heb ik als bijzonder leerzaam en prettig ervaren. Op momenten dat ik vastliep en feedback nodig had, heeft je waardevolle inbreng me vaak tot nieuwe inzichten gebracht.

De krenten in de pap tijdens mijn promotietijd waren de jaarlijkse veldwerktrips naar Spitsbergen. Carleen en Wim, het was een groot plezier om het veldwerk samen met jullie voor te bereiden en mee te mogen maken. Veijo, Rickard and all others participating in the field campaigns on Nordenskiöldbreen since 2011, the wonderful and unforgettable memories I have of the field trips are mainly because of you. I certainly hope we will stay in touch and keep collaborating in the future.

De aangename werksfeer op het IMAU is een belangrijk ingrediënt geweest voor het succesvol voltooien van mijn PhD. Ik ben alle collega's binnen het IMAU dankbaar voor de gezellige tijd. Tussen het soms taaie modelleerwerk door, vormen de koffie- en lunchpauzes een welkome afwisseling. Dat geldt zeker ook voor de wekelijkse badmintonsessies. In het bijzonder wil ik mijn kamergenoten Jan en Jan bedanken voor de gezelligheid en de (meestal) geduchte tegenstand bij UT en NFS. Daarnaast waren de afgelopen jaren op het IMAU lang niet zo fijn geweest zonder Stefan, Bas, Paul, Rianne, Michiel Helsen, Michiel van den Broeke, Roderik, Willem Jan, Carina, Melchior, Lennert, Malou, Peter, Thomas, Aimée, Dewi, Lisa, Maria, Arjan, Niels, Erik, Abdel en Wim. Mijn dank gaat zeker ook uit naar het secretariaat (Yvonne en Wanda) en Sandra voor de administratieve hulp en Marcel en Michael voor technische bijstand bij computerproblemen. Carleen, bedankt voor je adviezen en eerste kritische blik op mijn papers.

Much of the work presented in this thesis has been done in collaboration with foreign colleagues. I especially would like to acknowledge partners at the University of Uppsala, Sweden, and the University of Fairbanks, Alaska. I am very grateful to Ed Bueler, who has helped me to learn about and work with the ice flow model PISM. Our useful discussions have helped me a great deal to improve my understanding of complex numerical issues and in the end I believe we have made important progress towards a novel hydrology model for PISM.

Zeker niet te verwaarlozen is de bijdrage die vrienden hebben geleverd aan dit proefschrift. Tim, als huisgenoot heb je me regelmatig uitgeteld op de bank zien neerploffen na een lange dag. Bedankt voor de gezelligheid, vriendschap, interesse en de goede discussies. Jorrick, Thomas en Thijs, ik weet zeker dat er nog veel legendarische avonden en weekenden met slechte grappen zullen volgen. Robbin en Michou, zonder jullie had ik in mijn eentje op de tennis-/squashbaan gestaan. Jeroen, Bas, Rutger, Sander, Joris, Wim en Joost, na de vele borrels, uitstapjes en vakanties wordt het misschien tijd dat we weer eens gaan roeien? Cintia en Hans, ik kan me geen leukere en gezelligere uitvalsbasis in Berlijn voorstellen. Luc, het wordt wel weer eens tijd voor een goed feestje!

Waar zou ik zijn zonder mijn familie? Pap en mam, ik ben jullie heel dankbaar voor de onvoorwaardelijke steun door de jaren heen. Jullie interesse heeft me gestimuleerd om mijn werk in begrijpelijke taal uit te leggen. Renske, mijn grote zus, als respectievelijk psycholoog en natuurkundige kunnen we het eigenlijk verrassend goed met elkaar vinden!

Tot slot, Anna-Carolina, als geen ander heb je de positieve en negatieve aspecten van het PhD-bestaan meegekregen. Je hebt me leren relativeren en trots te zijn op eigen werk. Ik weet zeker dat onze gedeelde passie voor reizen en avontuur ons nog op hele mooie plekken in de wereld gaat brengen!

Curriculum Vitae

Ward van Pelt was born on the 10th of March 1985 in the coastal town of Vlissingen in the southwest of the Netherlands. This is where he grew up and obtained his high school diploma at the Scheldemond College in 2003. He decided to leave the coast and move to Utrecht to study Physics and Astronomy at the University of Utrecht. In 2006, he obtained his Bachelor degree and stayed in Utrecht to do a Master in Meteorology, Physical Oceanography and Climate. As part of the Master programme he, together with two classmates, spent a semester in Oklahoma in the United States of America to attend courses at the School of Meteorology at the University of Oklahoma. Back in Utrecht, he wrote a Master thesis on the mass balance of the Morteratsch glacier, Switzerland. He graduated cum laude in August 2009 and a few days later he started his PhD project on modelling of glaciers in Svalbard at the Institute for Marine and Atmospheric research Utrecht (IMAU). In collaboration with colleagues from the University of Uppsala, Sweden, Ward participated in three field campaigns to Nordenskiöldbreen, Svalbard, between 2011 and 2013. The results of his PhD research are presented in this thesis.

Ward van Pelt werd geboren op 10 maart 1985 in de kustplaats Vlissingen in het zuidwesten van Nederland. Hier groeide hij op en behaalde in 2003 zijn VWO-diploma aan het Scheldemond College. Ward besloot de kust te verlaten en te verhuizen naar Utrecht om daar Natuur- en Sterrenkunde aan de Universiteit Utrecht te gaan studeren. In 2006 behaalde hij zijn bachelordiploma en besloot in Utrecht te blijven voor een Master in Meteorologie, Fysische Oceanografie en Klimaat. Als onderdeel van het masterprogramma verbleef Ward samen met twee mede-studenten een semester lang in Oklahoma in de Verenigde Staten om aldaar vakken te volgen aan de School of Meteorology aan de Universiteit van Oklahoma. Weer terug in Utrecht schreef hij zijn masterthesis over de massabalans van de Morteratschgletsjer in Zwitserland. Hij behaalde cum laude zijn masterdiploma in augustus 2009 en startte een paar dagen later met zijn promotieonderzoek over het modelleren van gletsjers in Spitsbergen aan het Instituut voor Marien en Atmosferisch onderzoek Utrecht (IMAU). In samenwerking met collega's van de Universiteit van Uppsala, Zweden, heeft Ward deelgenomen aan drie veldwerkcampagnes op Nordenskiöldbreen, Spitsbergen, tussen 2011 and 2013. Het resultaat van zijn promotiewerk is gepresenteerd in dit proefschrift.